Catalytic properties and interface interaction of platinum subnano-clusters on graphene nano sheets

Rikson Asman Fertiles Siburian

February 2013

Catalytic properties and interface interaction of platinum subnano-clusters on graphene nano sheets

Rikson Asman Fertiles Siburian

February 2013

Catalytic properties and interface interaction of platinum subnano-clusters on graphene nano sheets

Rikson Asman Fertiles Siburian
Doctoral Program in Frontier Science

Submitted to the Graduate School of
Pure and Applied Sciences
in Partial Fulfillment of the Requirements
for the Degree of Doctor of Philosophy in
Engineering

at the
University of Tsukuba

Abstract

Fuel cells are widely considered to be efficient and non-polluting power sources offering much higher energy densities and energy efficiencies compared to other current/conventional systems. The main objective in fuel cell technologies is to develop low-cost, high performance and durable materials. From viewpoints of Pt electrocatalyst, it is required to reduce electrocatalyst loading of Pt in fuel cell electrodes, to decrease electrocatalyst nanoparticle sizes, and to improve the performance of catalyst support materials. Further, the performance of fuel cells system is directly related to the material properties. Therefore, material technology plays a pivotal role in the development of electrochemical energy conversion and storage systems. Among the various materials, which have been investigated in these electrochemical devices, carbon materials are of great interest owing to their abundance, stability and relative environmental friendliness. Graphene, as a new carbon material has attractive great interest from both fundamental science and applied research. It has large surface area, high conductivity, unique graphitized basal plane structure, and potential low manufacturing cost. Therefore, graphene is a promising candidate as fuel cell catalyst support.

This study was performed to evaluate the possibility of graphene as the support material. I have tried to control the particle size of Pt on graphene nano sheets (GNS) in a region from sub-nanometer to a few nanometers. The controlling of Pt particle size was realized by changing Pt loading on GNS. Then, I can clarify relationships among the Pt particle size, catalytic activity, and the electronic structure of Pt on GNS. Interestingly, Pt subnano-clusters are formed on GNS, which has never been observed for the other graphitic supports. Furthermore, I found that Pt subnano-clusters (0.8 nm) with an extremely large surface area (170 $m^2\ g^{-1}$) are formed on the GNS support at a low loading of 10 wt % Pt/GNS catalyst. In addition, it also exhibits the best performance in the electro-oxidation of adsorbed CO. Therefore, Pt subnano-clusters can be expected as excellent electro-oxidation catalysts. An increase in loading of Pt leads to an increase in particle size of Pt, resulting in the lower activities for electro-oxidation of adsorbed CO. The core level of Pt 4f in the electronic structure for Pt subnano-clusters is shifted to higher binding energies, indicating chemical interaction between Pt and graphene. The modification of catalytic properties and the electronic structure is ascribed to the interface interaction between Pt and graphene via π–d hybridization. It is thus clearly shown in this study that the Pt subnano-clusters exhibit the outstanding properties, namely large surface area, high electrocatalytic activity, and strong interaction between Pt and graphene.

Next, I have tried to clarify the mechanism of formation for Pt subnano-clusters on GNS. The formation mechanism of Pt subnano-clusters composed of 5–40 Pt atoms on GNS has been studied by X-ray diffraction (XRD), X-ray photoelectron spectroscopy (XPS), and transmission electron microscope (TEM). It was found that the mechanism for the Pt subnano-cluster formation includes two pivotal surface reactions: the reduction of Pt^{2+} particles into isolated Pt atoms by H_2 on the GNS surface, followed by the formation of Pt subnano-clusters by collision of the Pt single atom migrating on GNS. The driving factors for the Pt subnano-clusters formation are ascribed to intense π–d hybridization between carbon and Pt as well as the large surface area of graphene.

Finally, N-doped graphene (N-G) and graphene were used in order to clarify the effect of defect graphene and support material for properties of Pt catalyst especially for oxygen reduction reaction (ORR). The defect of graphene was carried out by varying annealing temperature of GNS in ammonia. I found that the ORR electrocatalytic activity of N-G 900 (0.63 V versus RHE) is higher than that of GNS. It indicates that an incorporation of nitrogen in N-G may affect the ORR activities of N-G 900. XPS results exhibit that pyridinic N is the majority in N-G, where pyridinic N refers to N atom binding with two C atoms at the edges or defects of graphene and supply one p-electron to the π-system of graphene. Subsequently, Pt particles were deposited on N-G and GNS in order to know the effect of the support material for Pt catalytic activity at cathode. Interestingly, Pt subnano-clusters were formed in Pt/N-G catalysts with Pt particle size (0.7–1.0 nm). It also exhibits a strong interaction between Pt and N-G. However, the ORR activity of Pt/N-G is lower than that of Pt/GNS catalysts. It clearly indicates that the doping of nitrogen significantly influence the π–d hybridization in terms of electronic structures.

Contents

List of Figures

List of Tables

Chapter 1

Introduction

1.1 General Introduction

Nowadays, the population is approximately seven billions and is estimated to grow to nine billion by 2050, and about ten billion by 2100 [1]. With the rapid increase in population and economic development around the world, the demand for energy is surging [2]. Energy is the lifeblood of technological and economic development. Therefore, the secure, reliable and affordable energy supplies are fundamental to economic stability and development.

The world's energy demand will increase from about twelve billion tons oil equivalents (t.o.e.) in 2009 to either eighteen billion or seventeen billion t.o.e. by 2035. The total global energy use exceeds 350 quadrillion British thermal units (Btus) per year, which is equivalent to over 170 million barrels of oil each day. The global energy consumption main draws from 86 % three primary fossil fuels sources; those are 33 % petroleum oil, 23 % natural gas, and 30 % coal [3]. They are responsible for much of the world's electric power and total energy demands. For instance, the electricity generation provides 18,000 terawatt-hours of energy a year, corresponding to around 40 % of humanity's total energy use [4]. However, there are some disadvantages of fossil fuels (i) pollution, they give off carbon dioxide when burned, thereby causing a greenhouse effect. The carbon dioxide emissions are estimated to increase from twenty nine gigatonnes (Gt) per year to 43 Gt yr^{-1} or 36 Gt yr^{-1} under the current and new policies, respectively [5]. This is also the main contributory factor to the global warming experienced by the earth today and (ii) the fossil fuels are not renewable resources. The fossil fuels take million years to form and thus have limited reserves. In addition, their consumption rate is much faster than their generation rate in the age of industry [6]. The amount of fossil fuel (coal, oil, natural gas) is finite, and any extrapolation in our present rate of consumption will lead to the exhaustion of readily available reserves in about 100 years (or somewhere between 30 and 300 years) [7]. It means they will deplete one day. The cheaper alternative energy has become more important especially at a time where we are facing a global recession. Therefore, lowering the fuel consumption of transportation vehicles could decrease both emissions of greenhouse gases and our dependence on fossil fuels [8]. Natural gas as one kind of fossil fuel source seemly could provide a secure economical alternative to petroleum. Proven reserves of natural gas have doubled in the last decade [9]. Hydrogen gas (H_2) seems to be capable of solving major environmental problems [10]. When H_2 is burned in a fuel cell, directly producing electricity to power a vehicle, the exhaust contains none of the odd nitrogen

compounds $(NO)_x$ associated with combustion. Furthermore, if the H_2 is generated from non-fossil energy, it could eliminate the CO_2 emissions from the transport sector.

Recently, polymer electrolyte membrane fuel cells (PEMFCs) have increasingly received worldwide attention because of their potential application in transportation and in stationary and portable electronics. Commercialization of fuel cells and deployment in these early market applications is expected to lead to further improvement in performance, durability, and cost [11]. For operation with hydrogen as the fuel, the only chemical byproduct is water; thus, the process is clean. The fuel cell is also more efficient in its conversion of chemical energy to electrical energy than present technologies. Together, these features suggest that fuel cells can reduce the problems associated with petroleum based energy production, which include air pollution, greenhouse gas emissions, and economic dependence on petroleum. For this reason, industrial developers and world governments have shown great interest in developing fuel cell power sources [12]. Fundamentally, the performance of fuel cells system is directly related to the material properties. Therefore, material technology plays a pivotal role in the development of electrochemical energy conversion and storage systems. Among the various materials, which have been investigated in these electrochemical devices, carbon materials are of great interest owing to their abundance, stability and relative environmental friendliness. In particular, the excellent chemical stability across a wide temperature range in either acidic or basic media makes carbon materials extremely attractive for use as electrodes in electrochemical energy devices [13]. The graphene as a carbon material has fascinated many researchers, especially as based material for fuel cells and capacitors. Graphene, a single layer of two dimensional honeycomb carbon lattices, is emerged as exciting novel material [14] due to it has been demonstrated to possess a high specific surface area, good chemical stability and outstanding electrical properties [15]. It is thus expected to be one of the best suitable base materials for developing alternative energy sources. In this study, I reported a recent significant progress of graphene as a new supported material for Pt based fuel cell catalyst. The Pt subnano-clusters were formed on graphene nano sheets (GNS) exhibit the superior catalytic activity and strong interaction between Pt and graphene probably via π–d interaction.

The aims of this study are (i) to control the Pt particle size on GNS in a region from sub-nanometer to a few nanometers and also to clarify relationship among Pt particle size, catalytic activity and electronic structure of Pt on GNS, (ii) to study the formation process of Pt subnano-clusters on GNS, (iii) to know effect of annealing temperature of GNS in ammonia for Pt/N-GNS catalysts properties, and (iv) to clarify support material effect for oxygen reduction activity based on Pt catalyst. Base on the results of this study, I can improve electrocatalytic activity of Pt catalyst and reduce Pt usage by using GNS as a supporting material.

1.2 Carbon materials as support materials for fuel cell

Carbon materials such as activated carbons, carbon blacks, and graphitic materials have been wide used in heterogeneous catalysis, as either catalysts or catalyst supports. Carbon is a versatile and fascinating material that can be used in a number of technological processes, including high technology processes. This is due to the ability of carbon atoms to bond with each other in various ways to form linear, planar, and tetrahedral bonding arrangements, thus producing materials with a large range of properties. Physicochemical characteristics such as electrical conductivity, surface area and porosity, and surface chemistry may be tuned for specific applications. The potential market growth of the carbons in catalysis depends on (i) better understanding of the chemistry of carbon surfaces and fine tuning of the microstructure of these materials, which could then be exploited in the design of truly unique catalysts and (ii) improvements in quality control and production methods, to supply constant quality materials (synthetic carbons) [16].

Since the catalysts are bonded to the support, the support material can potentially influence the activity of the catalyst. It is well known that supported metal catalysts show improvement stability and higher activity compared to unsupported bulk metal catalysts. The underlying support affects the catalytic properties due to a variety of reasons including: (i) influencing the shape, size and dispersion of the catalyst nanoparticles and (ii) electronic interactions between support and catalyst [17,18]. This interaction effect can be explained in two distinct ways. First, the support material can modify the electronic character of the catalyst particles. This electronic effect could affect the reaction characteristics of the active sites present on the catalyst surface. The second is a geometric effect. The support material could also modify the shape of the catalyst particles. Those effects could change the activity of catalytic sites on the metal surface and modify the number of active sites [19].

Commonly, carbons are widely used as catalyst supports for precious metals in low temperature fuel cells. The main requirements of suitable supports for fuel cell catalysts are (i) large surface area and good crystallinity, providing a high dispersion of Pt nanoparticles and contributing low loading catalyst for fuel cell operation, (ii) good electrical conductivity, facilitating electron transfer to produce the better device performance [20,21], (iii) good catalyst-support interaction, (iv) meso-pore structure enabling the ionomer and polymer electrolyte to bring the catalyst nanoparticles close to the reactants, i.e. to maximize the triple-phase boundary (TPB), (v) good water handling capability to avoid flooding, (vi) good corrosion resistance, (vii) easy recovery of the catalyst, (viii) assist in sufficiently enhancing the catalyst performance and durability by reducing catalyst poisoning (e.g. CO, S, etc.), and (ix) it affects the catalyst particle size [22,23]. Base on the surface area, the activity of a catalyst increases as the reaction surface area of the catalyst increases, catalyst particles should be reduced in the diameter to increase the active surface. In this sense, the specific activity of the metal nanoparticles can decrease with decreasing the particle size (particle

size effect) [24,25]. Therefore, the development of new carbon and non-carbon supports, which could improve the electrochemical activity of the catalysts are needed. Besides the high surface area, porosity and electrical conductivity, corrosion resistance is also an important factor in the choice of a good catalyst support due to it influences the stability of PEMFCs [26]. Thereby, the choice of support material is vital and highly influential in determining the behavior, performance, longevity and cost effectiveness of the catalyst and the overall fuel cell.

1.2.1 Carbon black

Carbon black (CB) is widely used as a catalyst support in low temperature fuel cells. They were manufactured by the pyrolysis of hydrocarbon such as natural gas or oil fractions from petroleum processing [27]. For instance, the Vulcan XC-72 has been used widely as the support for platinum (Pt) catalyst. Carbon blacks are usually submitted to chemical activation to increase anchoring centers for metal catalysts and also to increase metal loading and dispersion. The high availability and low cost make carbon blacks the most used support for fuel cell catalysts. The disadvantage of these carbons is the presence of a high amount of micro-pore, which can hinder the reactant flow. Moreover, these materials present low stability at temperatures higher than 100 °C. The catalyst supports of various CB are shown in Table 1.1 [28].

Table 1.1 Catalyst support of various CB.

Types of carbon black	Surface area ($m^2 g^{-1}$)	Particle size (nm)
3950 FB	1500	16
Black pearls 2000 FB	1475	15
Exp. sample AB	835	30
Vulcan XC-72R FB	254	30
Conductex 975 FB	250	24
Shavinigan AB	70–90	40–50
Denka black AB	58	40

AB: acetylene black; FB: oil-furnace black.

As shown in Table 1.1, the surface area of AB is smaller than FB type. The Pt particle size supported on AB is larger than FB [24]. It indicates that the Pt particle size decreases with increasing the specific surface area of carbon black [29]. The Vulcan XC-72 presented a higher Pt dispersion than that on the other carbon black. The high Pt dispersion was attributed to the high internal porosity [30].

In order to increase metal dispersion and catalytic activity on CB, it is needed to activate. The activation of carbon materials may be done by using physical (thermal treatment) and chemical activation

(oxidative treatment). The aim of physical activation to remove the impurities present on the carbon surface. It was carried out by heat treatments under argon atmosphere at 850 ^{o}C for 5 h or in air steam at 500 ^{o}C for 2.5 h [31]. On the other hand, chemical activation was performed by oxidation of the carbon surface with oxidants (HNO_3, H_2O_2, O_2 or O_3). Thereby, the functionalities present on the carbon surface (e.g. carboxylic, phenolic, lactonic, and etheric groups). They are responsible to form the acidic sites and destruct basic sites surface of carbon [32]. The effect of oxidative treatment of the carbon on Pt catalyst are believed be able to increase Pt dispersion on support [33] and providing the stronger interaction of the metallic precursor with the carbon of low acidity (like those treated with H_2O_2 or O_3) than with the most acidic carbon (treated with HNO_3) [34]. Regarding the effect of chemical activation of the carbon on the electrocatalytic activity of supported catalysts, generally, as expected, carbon treatments, which increase metal dispersion, also increase their electrocatalytic activity [35,36].

Although widely used as catalyst-support, CB still suffer from problems such as (i) the presence of organo-sulphur impurities and (ii) deep micro-pore or recesses which trap the catalyst nanoparticles making them inaccessible to reactants thus leading to reduced catalytic activity. The pore size and pore distribution also affect the interaction between Nafion® ionomer and the catalyst nanoparticles. Since the size of Nafion® micelles (> 40 nm) is larger than the recesses in the CB, any metal nanoparticles in pore with diameter lower than the micelle size are not accessible to Nafion® and provide no contribution to the electrochemical activity. Furthermore, CB is thermo-chemically unstable. It is required under acidic conditions of fuel cell and the absence of this leads to corrosion of the carbon support resulting in disintegration of catalyst layer. Therefore, the other carbon materials are needed [22].

1.2.2 Carbon nanostructures

The carbon blacks have high specific surface area but they are difficult to be fully accessible due to their pores are less than 1 nm. The presence of micro-pore (< 2 nm) is a disadvantage of carbon when used as catalyst support, because supplying a fuel may not occur smoothly and the activity of the catalyst may be limited. Moreover, it is known that micro-pore of these types of amorphous carbon particles are poorly connected. Compared with CB, generally meso-pore carbons (MCs) presented higher surface area and lower amount or absence of micro-pore. In a meso-pore carbon-supported catalyst, the metal catalyst particles are distributed and supported on the surface or in pores of the meso-pore carbon. A large meso-pore surface area, particularly with pore size > 20 nm, gives rise to a high dispersion of Pt particles, which resulted in a large effective surface area of Pt with a high catalytic activity. The meso-pore structure facilitated smooth mass transportation to give raises a high limiting current [28].

Recently, the novel non-conventional carbon materials have attracted much interest as electrocatalyst support because of their good electrical and mechanical properties and their versatility in pore size and pore distribution tailoring. These materials present a different morphology than CB both at the nanoscopic level in

terms of their pore texture (for example meso-pore carbon) and at the macroscopic level in terms of their form (for example microsphere). The examples are supports produced from ordered meso-pore carbon (OMC) [37], carbon nanotube (CNT) [38,39], carbon nanocoil (CNC) [20], graphite nanofiber [40], and carbon nanofiber (CNF) [41].

Among the new carbon materials, CNT is the most investigated as catalyst support for low temperature fuel cells. The CNT is unique compare to the others carbon due to it has tubular structure, high chemical stability, excellent electronic conductivity, and high surface area. Moreover, CNT has a positive effect on Pt structure, resulting in a higher catalytic activity and a higher stability than CB. A problem for the commercialization of CNT is its higher cost compared to that of CB [42–44]. The CNT is 2-D nanostructures, typically tubes formed by rolled-up single sheets of hexagonally arranged carbon atoms. They may be single walled (SWCNT) or multi-walled (MWCNT). Depending on the structure, SWCNT can be conducting, i.e. metallic as well as semi-conducting in nature. SWCNT structure is characterized by a chiral vector (m, n) which defines its metallic or semi-conducting properties [42,45,46]. When compared to Pt supported on Vulcan XC-72, CNT based catalyst showed higher retention of electrochemical area, smaller increment in interfacial charge transfer resistance and a slower degradation of the fuel cell performance. This conclusively confirmed the higher corrosion resistance of MWCNT and also a stronger interaction with the Pt nanoparticles. It was also observed that highly corrosion-resistant MWCNT prevented the cathode catalyst layer from severe water flooding by maintaining the electrode structure and hydrophobicity for a long period under continuous anodic potential stress. Loss in catalytic sites available for oxygen reduction reaction (ORR) was found to be a major contributor to the overall over potential [47].

Since CNT is rolled-up co-axial sheets of graphene, oxygen atoms find it hard to attack this structure. It has been previously proposed that carbon supports with a higher graphitic component are much more thermally and electrochemically stable due to their higher corrosion resistance [48]. One distinct advantage offered by MWCNT is their significantly resistance towards corrosion compared to CB. The stability of the underlying carbon support affects the loss of Pt surface area following both Pt particle sintering and Pt release from the carbon support. On the other hand, CB contains mainly plane graphite carbon and amorphous carbon, which has an abundance of dangling bonds and defects [49]. The dangling bonds can easily form surface oxides, which results in a higher corrosion rate under electrochemical oxidation. Although CNT also contain dangling bonds and defects, but these are much less than CB consequently CNT is more stable in strongly oxidizing conditions [50]. However, further oxidation must attack the intact basal planes beneath the defect carbons, which is difficult. In contrast, amorphous carbons and discontinuous graphite crystallites in CB provide ample sites for the electrochemical oxidation [51]. The architecture of the CNT also gives rise to specific edge sites where the Pt crystallites can easily anchor. The specific Pt crystallites sites anchored on CNT provide active sites which are much more active.

Further, it is well known that the stability of Pt/C catalyst was affected by behavior of carbon support. The formation of partial graphitization made the surface of carbon more resistant to air oxidation due to the π-complex structures (π-sites) in the carbon basal planes [52]. In addition, the degree of graphitization increases with increasing strength of π-sites (sp^2-hybridized carbon) on the support, which act as anchoring centers for Pt, thus, strengthens the metal-support interaction. The higher graphitic content has also been linked to a stronger interaction between metal and carbon support [53]. However, despite all the advantages offered by CNT, its application to fuel cells is still faced by many challenges. The current synthesis techniques for CNT are not suitable for large scale production and suffer from cost limitations. Although the costs of CNT have reduced significantly over the last few years there is still a need to develop cost effective methods for its large scale production [22]. The main characteristic of carbon materials and carbon-supported catalysts are reported in Table 1.2 [28]. Briefly, the properties of carbonaceous and non-carbonaceous support materials are shown in Table 1.2 and 1.3, respectively [22].

Table 1.2 Properties of carbonaceous support materials.

Types of carbon material	**Support properties**	**Catalysts (particle size); loading**	**ECSA ($m^2 g^{-1}$)**	**Power density ($mW cm^{-2}$)**	**Electrode**	**Observation/ comments**
CNT (SWCNT, MWCNT)	• sp^2 carbon • hydrophobic • high conductivity • N-doped CNT for ORR	Pt (2–5 nm) 0.04 mg cm^{-2}, Pt-Ru (3–4 nm); 2.5 mg cm^{-2}; Pt-Co (5–10 nm), Pt-Fe, Pt-Ni, Pt-WO_3; Pt-Ru-Ir, Pt-Ru-Ni, Ru-Se, etc. Mono, binary and tertiary alloys	Up to 44.3 (anode)	39.3–62 (anode) 595 (cathode)	Anode, cathode	Larger catalyst particles without surface treatment, good metal dispersion in case of SWCNT, high metal stability for MWCNT
CNF	• sp^2 carbon • High conductivity	Pt (3–8 nm, recently, < 5 nm), Pt-Ru	20–80	93 (anode) 900 (cathode)	Anode, cathode	• Long term stability and durability

	• 3.9 S cm^{-1} • High durability • N-doping for ORR	(< 5 nm)				• Increased graphitization enhances ORR
OMC, DOMC	• sp^2/sp^3carbon • High SA • 0.3 S cm^{-1} • Good pore structure and size distribution • Few O-functional groups	Pt (0.5 mg cm^{-2}) < 8 nm Pt-Ru; Fe 2 mg cm^{-2}	62.96–208.2 ~ 28 μg cm^{-2}	80 (anode)–500 (cathode)	Anode, cathode	• Easier mass transportation with desired pore morphology • Lack of good contact between Pt and Nafion buried inside large pore DOMC
ND, BDD	• sp^3 carbon • Low surface area (SA) • High stability • Low conductivity • Doped • High resistance to poisoning	Pt (avg. 4.6 nm, 10–150 nm), Pt-Ru, Au, Pt-RuO_2, Pt-RuO_2-RhO_2 ,Pt-SnO_2 (avg. 5 nm) and Pt-Ta_2O_5 (avg. 9.1 nm)	–	–	Cathode	• Low metal stability and dispersion hence agglomeration and large NP size variation
Graphene, FLG	• sp^2 carbon, rippled sheet structure • Hydrophobic • High conductivity • 10^3–10^4 S cm^{-1} • N-doping for ORR	Pt, Pd, Pt-Ru, Pt-Pd	44.6–81.6	390–440 (cathode)	Anode, cathode	• Often produced from reduced GO • Can also be prepared as vertically aligned 1–3 layers graphene (FLG) • High resistance to CO-poisoning • Properties

						depend on synthesis method used
GO/RGO	• sp^2/sp^3 carbon • Variable conductivity • $\leq 10^4$ S cm^{-1} • Hydrophilic • O-functional groups	Pt (2–6 nm), Pt-Ru	≤ 113	128	Anode	• O-defects promote uniform dispersal of NPs • Allows high loading with small particle size • O-species appear to increase CO-tolerance
Vulcan XC-72R	• sp^3 carbon • Good metal dispersion • 254 (m^2 g^{-1}) SA • Low conductivity 4.0 (S cm^{-1}) • Micro-pore	Pt (2–5 nm)	40–50 (cathode) 60–70 (anode)	152 at 200 mA cm^{-2} 402 at 0.6 V	Anode, cathode	• CB helps reduce the overall cost of the fuel cell • CB still suffer from problem such as (i) the presence of organo-sulphur impurities and (ii) deep micro-pore or recesses which trap the catalyst nanoparticles making them inaccessible to reactants thus leading to reduced catalytic activity

						• CB is thermodynamically instability.

CBs (carbon blacks); CNT (carbon nanotubes); CNF (carbon nanofibers); OMC (ordered meso-pore carbons); DOMC (disordered meso-pore carbons); ND (nano diamonds); BDD (boron doped diamonds); FLGs (graphene nanoflakes); GO (graphene oxide); RGO (reduced graphene oxide).

Table 1.3 Properties of non-carbonaceous support materials.

Types of carbon material	**Support properties**	**Catalysts (particle size); loading**	**ECSA ($m^2 g^{-1}$)**	**Power density ($mW cm^{-2}$)**	**Electrode**	**Observation/ comments**
$TiO_{2-}x$ or Ti_nO_{2n-1}	•Semiconductor/ conductor/proton conductor • Low SA, highly durable	Pt, Pd, PANI-Fe	233	560–1000 (cathode)	Anode, cathode	• Up to 10-fold higher ORR for Pt/C • Nb/Ru doping increases conductivity (1.11 S cm^{-1})
TiN	• High electrical conductivity • 4000 S cm^{-1} • Resistant to CO poisoning	Pt (3.2–20 nm); 0.02–0.03 mg cm^{-2}	70	–	Anode, cathode	• Low rate of corrosion under fuel cell conditions • Electrically passive in sulfuric acid media at temperatures > 60 °C, due to the formation of -OH groups on surface
TiB_2	• Good conductivity • Excellent	Pt 3.4 nm	34.7	–	Cathode	• High electrochemical stability

	thermal stability • Corrosion resistance in acid medium					
ITO	• Semiconductor • 1000 S cm^{-1} • High oxidation resistance	Pt (5–30 nm), Au (30 nm), Au-Pt (60 nm)	–	–	Anode, cathode	• Faster electron kinetics or lower charge transfer resistance • Agglomeration
SiO_2	• Semiconductor • High oxidation resistance	Pt, Pt-Ru 2.2 nm	32–89.6	≤ 90	Anode, cathode	• Significantly reduced methanol crossover and control fuel feeding • Long-term durability in high methanol conc. • High mass activity
WO NPs, microspheres and NWs	•Semiconductor/ proton conductor • 2.58 S cm^{-1} • Low surface area • CO tolerant	Pt (1–3 nm) 0.18 mg cm^{-2} Pt-Ru	63.5	–	Anode, cathode	• Forms tungsten trioxide hydrates to enable enhanced proton transfer
WC NPs, NWs, nanofibers, meso-Porous	• Catalytic properties like Pt, synergistic effects • CO tolerant	Pt, Au, Pd, Ag	182	~ 200 (cathode)	Anode, cathode	• Crystallinity and porous structure of WC are affected by the temp. for the carburization • WC not stable at oxidation voltages above

						0.8 V • Stability of WC can be improved by the presence of sub monolayer coverage of Pt
SZ	• Proton conductor • Highly hydrophilic • 10^{-2} S m^{-1}	Pt ~ 8 nm	80	–	Cathode	• Better than Pt/C in absence of Nafion • 50–100 nm SZ particles • High stability in fuel cell conditions
SnO_2 NPs, NWs	• High corrosion resistance • 10 S cm^{-1}	Pt 2–6 nm ≤ 50 wt %	–	≤ 740 (cathode)	Anode, cathode	• Oxidation resistant • High tolerance to voltage cycling • High stability in fuel cell conditions • Sb doping improves corrosion resistance and electrochemical stability

Titanium oxides (TiO_{2-x} or Ti_nO_{2n-1}); TiN (titanium nitride); TiB_2(titanium diboride); SnO_2(Tin oxide); ITO (Indium tin oxide); SiO_2 (Silicon dioxide); W (Tungsten); WO_x (Tungsten oxide); WC (Tungsten carbide); SZ (Sulfated zirconia); NPs (nano particles); NWs (nano wires).

1.3 Graphene

Carbon is the *materia prima* for life and the basis of all organic chemistry. Because of the flexibility of its bonding, carbon-based systems show an unlimited number of different structures with an equally large variety of physical properties. These physical properties are, in great part, the result of the dimensionality of these structures. Among systems with only carbon atoms, graphene, a two-dimensional (2D) allotrope of carbon plays an important role since it is the basis for the understanding of the electronic properties in other allotropes [54].

Graphene is a flat monolayer of sp^2-bonded carbon atoms into a two-dimensional (2D) honeycomb lattice [14]. It is the basic building block of all the "graphitic" materials such as fullerene (0D), carbon nanotube (1D) and graphite (3D) (Figure 1.1). Graphene consists of an atom-thick sp^2-hybridized carbon sheet, in which each carbon atom is bonded to three carbon atoms, thus forming a hexagonal framework with bond lengths of 1.42 Å. The 2-D planar structure of the carbon sheet allows both the edge planes and basal planes to interact with the catalyst nanoparticles. The rippled but planar sheet structure also provides a very high surface area for the attaching catalyst nanoparticles [22].

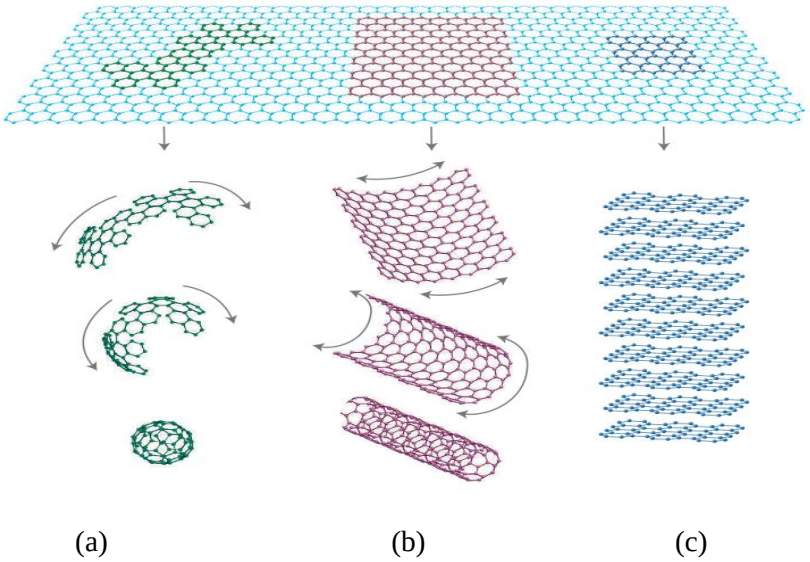

Figure 1.1 Mother of all graphitic forms. Graphene is a 2D building material for carbon materials of all other dimensionalities. It can be wrapped up into (a) 0D buckyballs, rolled into (b) 1D nanotubes, and stacked into (c) 3D graphite [55].

In fact, 2D like graphene was predicted theoretically not exists because strictly 2D crystals were thought to be thermodynamically unstable at finite temperature [55]. This is a reason to an explosion of

interest, and much research has been conducted on the structure and property characterization of graphene. The properties of graphene and the other carbon materials are shown in Table 1.4 [15].

Tab1e 1.4 Properties of graphene and the other carbon material.

Type of carbon materials	**Properties**				
	Specific surface area ($m^2 g^{-1}$)	**Thermal conductivity ($W m^{-1} K^{-1}$)**	**Intrinsic mobility ($cm^2 V^{-1} s^{-1}$)**	**Young's modulus (TPa)**	**Optical transparency (%)**
Graphene	2630	~ 5000	~ 15,000 (in-plane values onto SiO_2 surface) ~ 200,000 (free-standing)	~ 1.0	~ 97.7
Graphite	~ 10	~ 3000 (in-plane values)	13,000 (in-plane values)	1.06	–
Activated carbon	1200	0.15–0.5	–	0.138	–
Carbon nanotubes	1315	> 3000 (multi-walled carbon nanotube)	~ 100,000	0.64	–
Fullerenes	5	0.4	0.56	0.01	–

Table 1.4 shows that the graphene is a good base material due to it have a good electrical conductivity and large surface area. The high electrical conductivity is caused by its unique electronic structure. Intrinsically, graphene is a zero-gap conductor and charge carriers of graphene behave as massless Dirac fermions [55]. The surface area of one hexagon and calculated the specific surface area (SSA) by dividing the weight of two carbon atoms, which is 1315 $m^2 g^{-1}$, corresponding to one side of hexagonal surface. In the case of graphene, the SSA should be considered as two sides of hexagonal surface. Therefore, the SSA of graphene is calculated to be 2630 $m^2 g^{-1}$ [56]. Compared to the graphite (~ 10 $m^2 g^{-1}$) [13] and CNT (1315 $m^2 g^{-1}$), graphene has outstanding theoretical SSA.

The structural flexibility of graphene is reflected in its electronic properties. The sp^2-hybridization between one s-orbital and two p-orbitals leads to a trigonal planar structure with a formation of a σ-bond between carbon atoms that are separated by 1.42 Å. The σ-band is responsible for the robustness of the lattice structure in all allotropes. Due to the Pauli principle, these bands have a filled shell and, hence, form a

deep valence band. The unaffected p-orbital, which is perpendicular to the planar structure, can bind covalently with neighboring carbon atoms, leading to the formation of a π-band. Since each p-orbital has one extra electron, the π-band is half filled. Half-filled bands in transition elements have played an important role in the physics of strongly correlated systems, due to their strong tight-binding character and the Coulomb energies are large, leading to strong collective effects, magnetism, and insulating behavior due to correlation gaps [54].

1.3.1 Synthesis graphene

The development of various methods for producing graphene, a single layer of carbon atoms bonded together in a hexagonal lattice has stimulated a vast amount of research in recent years [55]. Graphene can be prepared by two approaching, those are top-down and bottom-up. The top-down approach implies graphite was exfoliated into the mixture of a single and a few layer graphele platelets. Graphite was oxidized to be graphite oxide and sonicated onto water to form graphene oxide (GO) is the most representative example of the top-down approach [57]. This approach can produce scalable and low cost graphene. Unfortunately, it is hard to obtain single layer graphene with high quality due to during its exfoliation defect was created. In particular, reduction of GO into graphene results in a graphitic structure that is also one-atom thick, but it still contains large number of defects, such as nanoholes and Stone-Wales defect (heptagon/pentagon bonded carbon atom network) [58]. On the other hand, bottom-up approaches, which are directly growing graphene from organic precursors such as methane and other hydrocarbon sources [59], include epitaxial growth [60] and chemical vapor deposition (CVD) [61]. Bottom-up approach is one of the most attractive methods for high-quality and large-area graphene production. Particularly, CVD grown graphene has been demonstrated to be of promise for potential applications as transparent electrodes [62]. However, bottom-up approaches are extremely difficult to control manufacturing process, and thus they result in high manufacturing cost. Table 1.5 shows comparison of the synthetic methods and properties of graphene [63].

Tab1e 1.5 Comparison of the synthetic methods and properties of graphene and its derivatives.

Category	Synthesis	Conditions	Properties
Bottom-up	Chemical vapor deposition (CVD)	Pd(111) with ethylene in STM	Monolayer graphene islands 200–2000 Å in size
		Thermal cycling of a Ru(0001) single crystal in UHV	Single crystal domains > 200 μm
		Ir(111) with ethylene	Large-scale continuity and low defects

		Cu foils at 1000 °C	4050 $cm^2 V^{-1} s^{-1}$ mobility centimeter order size
		Cu foils role-to-role process	30-inch graphene films
	Epitaxial growth	Thermal decomposition on (0001) 6 H-silicon carbide (SiC)	1100 $cm^2 V^{-1} s^{-1}$ mobility
		Vacuum graphitization of single SiC	> 25,000 $cm^2 V^{-1} s^{-1}$ mobility
		Ex-situ graphitization of Si-terminated SiC(0001)	Large grains 2000 $cm^2 V^{-1} s^{-1}$ mobility
Top-down	Mechanical exfoliation	Wet ball milling in NMP	0.8–1.8 nm thickness ~ 1.2×10^3 S m^{-1}
		Wet ball milling in DMF	~ 0.096 mg mL^{-1} in DMF Yield > 32 wt%
		Dry ball milling with melamine	Dry ball milling with melamine
	Chemical exfoliation	Alkali metal intercalation and ethanol exfoliation	Scaled up to 70 g quantities of graphite nanoplatelets
		Oxidation of natural graphite followed by reduction with N_2H_4	~ 200 S m^{-1} electrical conductivity
		Reduction with N_2H_4 in DMF/water (9/1) mixture	~ 16,000 S m^{-1}
		Reduction with phenylhydrazine	~ 21,000 S m^{-1}, high dispersion
		Solvothermal reduction with NMP	21,600 S m^{-1} 1.4 g mL^{-1} in NMP
		Reduction with Vitamin C	14.1 S m^{-1}, non-toxic
		Reduction with Fe catalyst	2300 S m^{-1}, non-toxic

UHV = ultra-high vacuum; NMP = N-methylpyrrolidone; DMF, dimethylformamide; STM, scanning tunneling microscope.

Table 1.5 shows that chemically exfoliated graphenes have been effectively used in fuel cell applications because of the versatility of their surface modifications, unique defect behaviors, functional groups, and advantages associated with low cost, easy scale up and wide range of applications [57]. The chemically

modified graphene was prepared by using graphite oxide. There are three methods to produce graphite oxide, namely Hummers [64], Brodie [65], and Staudenmaier methods [66]. All of these methods oxidized graphite with strong acids and oxidants. The chemical structure of graphite oxide is shown in Figure 1.2.

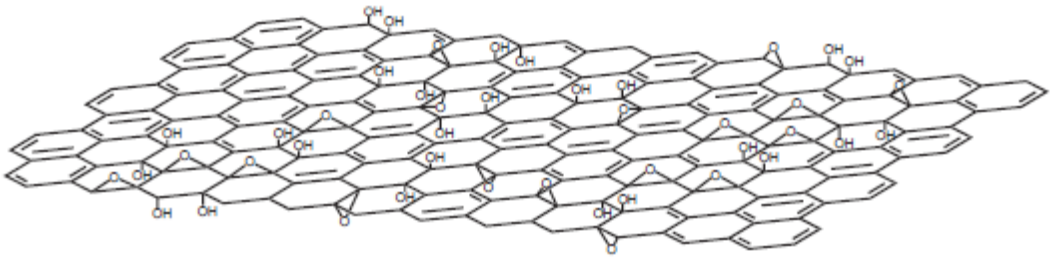

Figure 1.2 Chemical structure of graphite oxide [67].

As shown in Figure 1.2, the sp^2-bonded carbon network of graphite is strongly disrupted, resulting carbon is bonded to hydroxyl or epoxide groups and carboxylic or carbonyl in the edges of graphite oxide layers [68–70]. Then, graphite oxide can be completely exfoliated to produce aqueous colloidal suspensions of graphene oxide sheets by simple sonication [71] and the mixture graphite oxide/water was stirred for a long enough time [72]. The graphene oxide can be easily dispersed on water due to it is hydrophilic. Based on the surface charge of graphene oxide sheets, they have negative charges when dispersed in water [73]. This suggests that electrostatic repulsion between negatively charged graphene oxide sheets could generate a stable aqueous suspension of them. However, the chemical modified graphene (CMG) are electrically insulating owing to disruption of the graphitic networks. In order to produce electrically conducting CMG, graphene oxide can be reduced by using reductants such as hydrazine [74–77]. The properties of CMG with different chemical approaches are described in Table 1.6 [57].

Table 1.6 Properties of CMG with different chemical approaches.

Starting materials	**Dispersible solvents**	**Concentration (mg ml^{-1})**	**Lateral size**	**Thickness (nm)**
GO/MH	Water	1	–	–
GO/MH	Water	0.5	Several hundred nm	~ 1
GO/MH	Water	0.1	–	~ 1.7
GO/MH	Water	7	Several hundred nm	~ 1
GO/H	Water/methanol, acetone, acetonitrile mixed solvents	3–4	Several hundred nm	~ 1.2

GO/MH	DMF, NMP, DMSO, HMPA	1	~ 560 nm	~ 1
GO/H	Water, acetone, ethanol, 1-propanol, ethylene glycol, DMSO, DMF, NMP, pyridine, THF	0.5	100–1,000 nm	1.0–1.4
GO/O	DMF, THF, CCl_4, DCE	0.5	–	0.5–2.5
Graphite fluoride	DCB, MC, THF	0.002–0.54	1,600 nm	~ 0.95
GO/S	DMF, DMAc, NMP	1	Several hundred nm	1.8–2.2
GO/MH	Hydrazine	1.5	Up to 20 μm × 40 μm	~ 0.6
GO/S	THF	< 0.48	–	1–2
GO/S	NMP, DMF, DCB, THF, nitromethane	0.1	100–2,500 nm	1.1–3.5 (ave. 1.75)
GO/H	Ethanol	1	Several hundred nm	~ 2
Graphite powder	NMP, DMAc, GBL, DMEU	0.01	Several μm	1–5
GIC	NMP	0.15	Several hundred nm	~ 0.35
EG	DCE	0.0005	Nanoribbon (width < 10 nm)	1–1.8
EG	DMF	–	~ 250 nm	~ 1
EG	Water, DMF, DMSO	0.015–0.020	Several hundred nm to a few μm	2–3 (2–3 layers of graphene)
Graphite rod	DMF, DMSO, NMP	1	500–700 nm	~ 1.1

GO = graphite oxide; MH = modified Hummers method; H = Hummers method; O = their own method; S = Staudenmaier method; EG = expandable graphite; GIC = graphite intercalation compound; DMF = dimethylformamide; DMAc = N,N′-dimethylacetamide; DMSO = dimethylsulphoxide; NMP = N-methylpyrrolidone; THF = tetrahydrofuran; MC = dichloromethane; DCE = 1,2-dichloroethane; DCB =

1,2-dichlorobenzene; HMPA = hexamethylphosphoramide; GBL = γ-butyrolactone; DMEU = 1,3-dimethyl-2-imidazolidinone.

The chemical route to produce aqueous suspension of reduced graphene oxide consists of (i) oxidation of graphite to synthesize graphite oxide, (ii) exfoliation of graphene oxide in water by sonication of graphite oxide, and (iii) controlled reduction of graphene oxide sheets by hydrazine yielding a colloidal suspension of conductive CMG sheets, which are stabilized by electrostatic repulsion [73]. The chemical reduction of graphene oxide route is very important in order to produce graphene. There are a large number of oxygen containing functional groups and structure defects on the surface of graphene oxide. The oxygen-containing functional groups were partially reduced by hydrazine (Figure 1.3) [78].

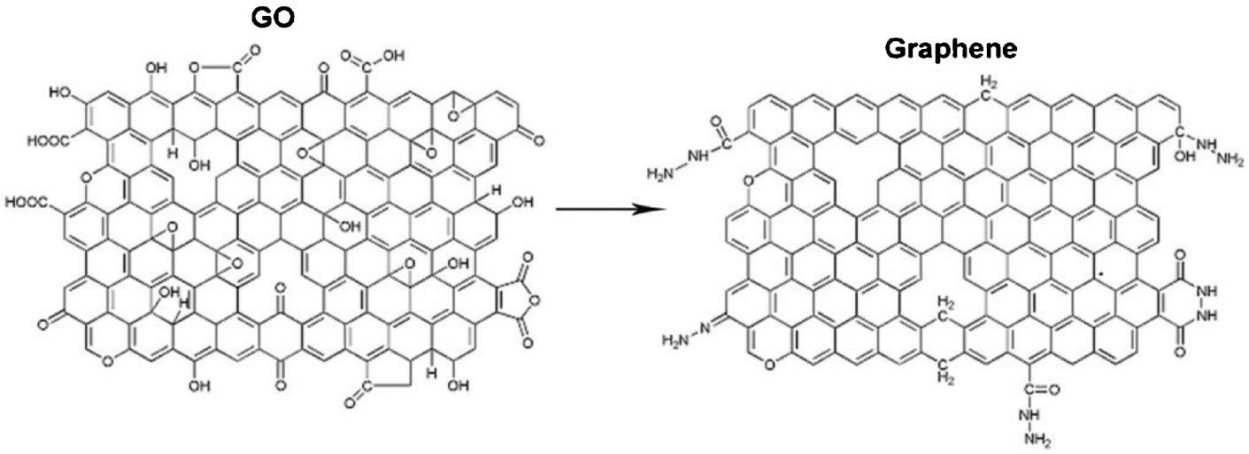

Figure 1.3 Schematic structure of graphene oxide (GO) was reduced by hydrazine.

Furthermore, the route of reduction process of graphene oxides by hydrazine was described in Figure 1.4.

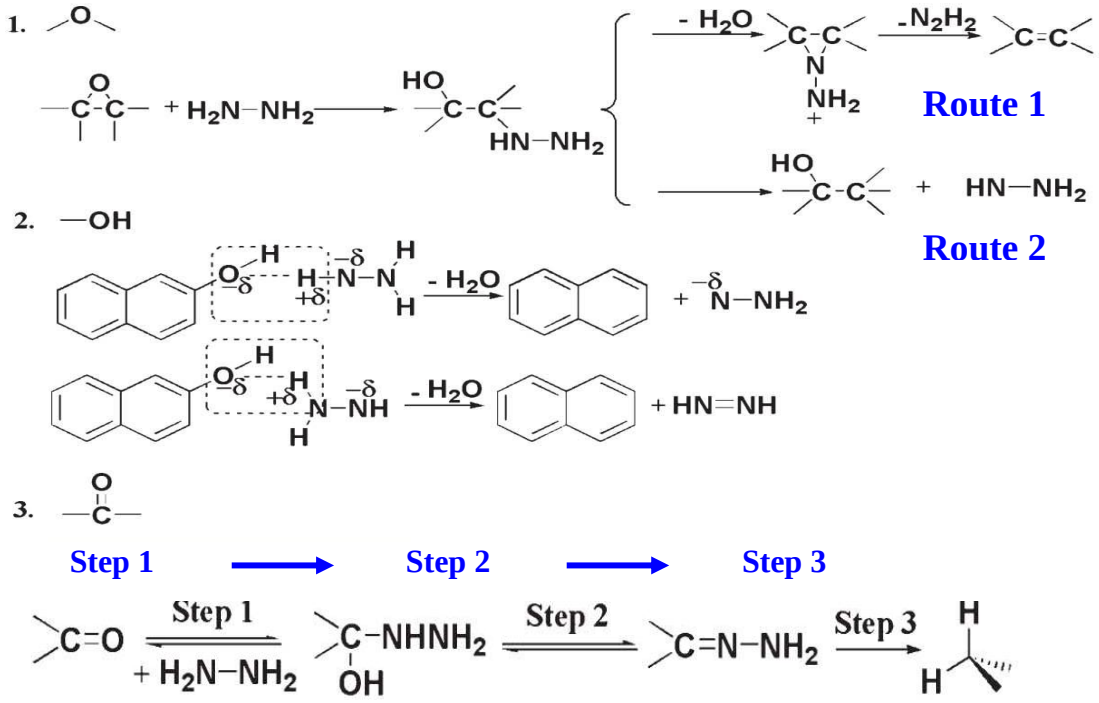

Figure 1.4 Mechanism of graphene oxide (GO) reduction.

Figure 1.4 shows the reduction of graphene oxides by using hydrazine. It confirmed that hydrazine (N_2H_4) molecules can react with epoxides (Route 1) [79]. However, it was proposed theoretically that $NHNH_2$ can escape without the second H abstraction during epoxide reduction with hydrazine [80] (Route 2). Therefore, the intermediate structure of hydrazine could be generated for the appearance of metastable phases. Metastable $NHNH_2$, which is more active than N_2H_4, can also act as a source of hydrogen to reduce the epoxide through ring opening. In this way, epoxy groups could be reduced more thoroughly. It can provide further insights into the open question of how the hydroxyl oxygen is removed by hydrazine. It is deduced that all three H atoms in $NHNH_2$ are able to react with the hydroxyl groups owing to the electrostatic attraction [81], thereby yielding NH = NH or N–NH_2 along with H_2O.

On the other hand, for carbonyl groups, the lone pair electrons on the nitrogen atom can act as a nucleophile to participate in a nucleophilic addition reaction with the electrophilic carbonyl group and form a hydrazino alcohol, as expressed in step 1. However, the hydrazino alcohol is thermally unstable in nature and is prone to dehydration via step 2, yielding hydrazone which results in the removal of oxygen [74,82].

Additionally, hydrazine is known to react with carboxylic acid groups to form hydrazides through an amidation process and with anhydrides and lactones to form hydrazides. These newly generated hydrazino alcohols, hydrazides and hydrazones on RGO (Figure 1.4) are expected to be responsible for the C-N and C=N bonds. Therefore, the reduction process is effective in eliminating oxygen-containing groups and re-establishing the conjugated graphene network [78].

1.3.2 Applications of graphene in fuel cells

Graphene can be used for fuel cell as catalyst support or metal free catalyst and ionomer after proper chemical modification as summarized at Table 1.7.

Tab1e 1.7 Applications of graphene in fuel cells.

Applications	Materials and conditions	Properties
Catalyst support	Fuctionalized graphene sheet	Higher electrochemical surface area and oxygen reduction activity compared with the commercial E-TEK catalyst or Pt/MWCNT
	Poly(diallyl-dimethyl-ammonium chloride)-coated GNP	Improved durability than Pt/CNT and E-TEK Pt/C in ORR
	One pot reduction of H_2PtCl_6 and GO using $NaBH_4$	Higher current density and better electrocatalytic stability over Pt/Vulcan
	Perfluorosulfonic acid	Improved durability, proton transfer and CO tolerance

	fuctionalized graphene	
	Nitrogen doped graphene using melamine	Improved electrocatalytic activity toward ORR in alkaline electrolytes
	Microwave-heating of graphene in a NH_3 atmosphere	High electrochemical active surface area high methanol catalytic activity, strong CO tolerance
Metal free catalyst	CVD in the presence of NH_3 (N-doped graphene)	Better electrocatalytic activity, long-term operation stability, and CO tolerance than the commercially Pt catalysts
	Direct annealing of graphene oxide and benzyl disulfide in argon (S-doped graphene)	Excellent catalytic activity, long-term stability, and high methanol tolerance in alkaline media for ORR
	Thermal annealing GO in the presence of B_2O_3 (B-doped graphene)	Excellent electrocatalytic activity toward ORR and high CO tolerance
Others	Sulfonic acid-functionalized GO (ionomer)	Four times higher proton conductivity than that of the unmodified membrane
	Hybrid supports composed of functionalized GO and MWCNT	Less restacking of GO improved fuel cell performance
	Hybrid supports composed of functionalized GO and carbon black	Larger electrochemical surface area and faster interfacial oxygen kinetics

GNP = graphene nanoplatelet; GO = graphite oxide; ORR = oxygen reduction reaction; CVD = chemical vapor deposition; MWCNT = multi-walled carbon nanotubes.

The most important role of graphene as a supporting material for metal catalysts is the provision of anchoring sites to obtain a uniform distribution of nano-sized metal particles, which results in high catalytic activity [83]. The other applications of graphene are shown in Table 1.8 [84].

Table 1.8 Electronics applications of graphene.

Application	Drivers	Issues to be addressed
E-paper	High transmittance of monolayer graphene could provide visibility	Requires better control of contact resistance
Foldable	Graphene of high electronic	Requires better control of contact resistance, the sheet

light-emitting diodes (OLEDs)	quality has a bendability of below 5 mm, improved efficiency due to graphene's work function tunability, and the atomically flat surface of graphene helps to avoid electrical shorts and leakage current	resistance needs to be reduced, and conformal coverage of three-dimensional structures is needed
High-frequency transistor	No manufacturable solution for InP high-electron-mobility transistor (low noise)	Need to achieve current saturation, and f_T = 850 GHz, f_{max} = 1,200 GHz should be achieved
Logic transistor	High mobility	New structures need to resolve the bandgap-mobility trade-off and an on/off ratio larger than 10^6 needs to be achieved
Touch screen	Graphene has better endurance than benchmark materials	Requires better control of contact resistance, and the sheet resistance needs to be reduced (possibly by doping)

1.4 Fuel cell

Today, fuel cells are widely considered to be efficient and non-polluting power sources offering much higher energy densities and energy efficiencies compared to other current/conventional systems. A fuel cell is an electrochemical device that converts the chemical energy of a fuel (e.g. hydrogen, methanol, etc.) and an oxidant (air or pure oxygen) in the presence of a catalyst into electricity, heat and water [22].

The main objective in fuel cell technologies is to develop low-cost, high-performance and durable materials. Many efforts have been done to reduce the cost and increase the performance of a fuel cell, such as: (i) reducing the electrocatalyst loading in fuel cell electrodes, (ii) decreasing the electrocatalyst nanoparticle size, (iii) improving the performance of carbonaceous electrocatalyst support and exploring novel non-carbonaceous electro catalyst support materials, (iv) improving electrocatalyst dispersion by using novel fabrication methods, (v) developing membrane electrode assembly (MEA) fabrication methods to enable better catalyst dispersion and utilization, and (vi) using new techniques to increase mass-transport at the fuel cell electrode surface [22,85]. Currently, there are six main types of fuel cells, namely: (i) polymer electrolyte membrane fuel cell (PEMFC) including direct methanol fuel cell (DMFC), (ii) alkaline fuel cell (AFC), (iii) phosphoric acid fuel cell (PAFC), (iv) molten carbonate fuel cell (MCFC), (v) solid oxide fuel

cell (SOFC) and (vi) microbial fuel cell (MFC). PEMFC, DMFC, AFC, PAFC, and MFC operate at low temperatures (50–200 °C) and MCFC and SOFC at high temperatures (650–1000 °C) [86,87].

Among the family of fuel cell technologies, PEMFC have some uniquely attractive features [88–90] and gained international attention as candidates for alternative automotive and stationary power sources. They provide high power density, low operating temperature, high chemical to electrical energy conversion efficiency, and fast and easy start-up [91]. Additionally, they are very reliable and are constructed from durable and benign materials. A large number of successful applications of PEMFCs and DMFCs like passenger vehicles, generators (APU), chargers and other portable and hand held devices including mobile phones and laptops are currently commercially available [86,92]. However, the large-scale application of PEMFC technology for transportation and utility or stand-alone power generation was considered to be too expensive (mainly due to the catalyst) and sensitive to the low levels of carbon monoxide present in reformed carbonaceous fuel feed streams (CO poison) [93]. The type of fuel cells and their characteristics are listed in Table 1.9 [86].

Table 1.9 Comparison of different fuel cells and their operating characteristics.

Type of fuel cell	Operating temperature (^{o}C)	Electrolyte	Efficiency (%)	Applications
AFC	660–250	Liquid	50–70	Transportation, space, military, energy storage systems, portable power systems, and decentralized stationary systems
DMFC	50–90	Solid	35–40	
PEMFC	80–100	Solid	35–60	
MCFC	≈ 650	Liquid	40–55	Combined heat and power for decentralized stationary systems and transportation
PAFC	160–250	Liquid	35–50	
SOFC	750–1000	Solid	45–60	

1.4.1 Application of fuel cell

Fuel cell technologies have performed in some sectors such as military, industrial, space, portable, residential, transportation and trading due to better power quality, reliability, portability and ecological constraints. Hydrogen energy utilization at residences is an alternative method especially for supply power demand of stationary or portable devices. Among the various next generation power plants, the fuel cell power plants (FCPPs) has been found to be one of the most promising energy sources due to high efficiency and environment-friendly operation [94]. FCPPs are electrochemical devices that convert the chemical

energy of a reaction directly into the electrical energy. The use of FCPPs is expected to become more widespread in the near future, in spite of their high current capital cost [95], e.g. for cogeneration of heat and power, and as a substitute for batteries in portable devices, e.g. for laptops [96]. In the future, fuel cells will run on gas derived from biomass or pure hydrogen extracted from water using wind or solar energy, thus playing a key role in ushering in a sustainable energy future. A fuel cell system worked by hydrogen can be used to distribute sources of energy for meeting the power demand instead of constructing new conventional power plants [86]. In this context, the hydrogen can be used to replace the present fossil fuels [97] for transportation and a source for electricity and heating [98]. Because hydrogen is the lightest, simplest, one of the most abundant element in nature, and also hydrogen energy system is a continuous, renewable, sustainable and efficient system in harmony with the environment [97].

A FCPP mainly consists of a fuel-processing unit (reformer), fuel cell stack and power-conditioning unit. The fuel cell uses hydrogen as input and produces direct current (dc) power at the output of the stack. A simple representation of a fuel cell system is shown in Figure 1.5.

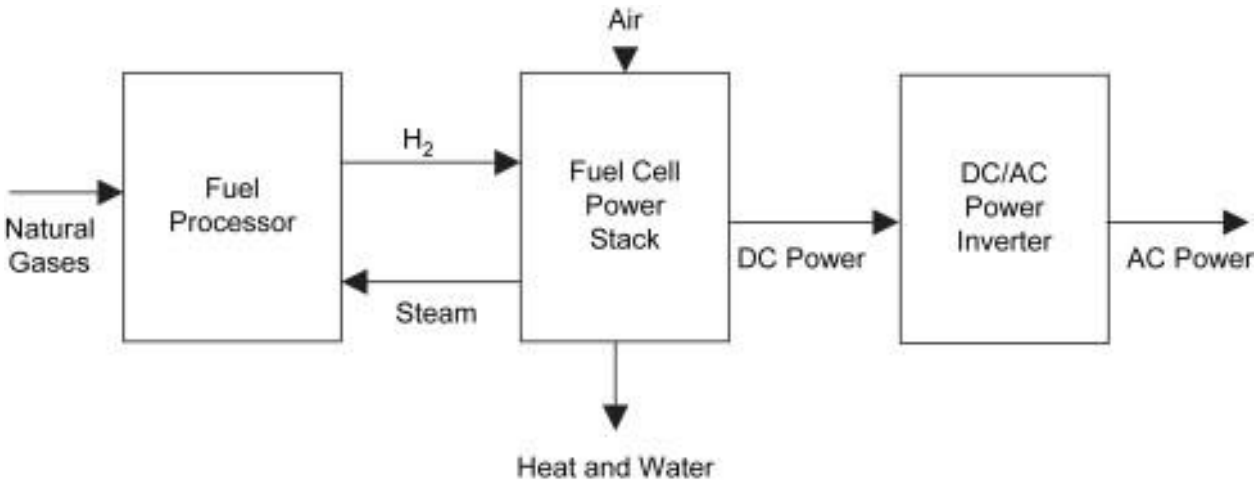

Figure 1.5 Basic fuel cell components [86].

The performance of a fuel cell is generally characterized by using the polarization curve, which is a plot of the fuel cell output voltage as a function of load current. The polarization curve is computed by using the Tafel equation [99], which subtracts the various voltage losses from the open circuit dc voltage, and is expressed as

$$V_{stack} = V_{open} - V_{ohmic} - V_{activation} - V_{concentration} \quad (1\text{–}1)$$

where,

$$V_{open} = N_0 \ (E^0 + E^1) = N_0 \left[- \frac{\Delta_f^{-0}}{2F} + \frac{RT}{2F} \ ln \left(\frac{pH_2 \sqrt{pO_2}}{pH_2O} \right) \right] \quad (1\text{–}2)$$

$$V_{ohmic} = (i + i_n) R_{FC} = I_{dc} R_{FC} \quad (1\text{–}3)$$

$$V_{activation} = \left(N_0 \frac{RT}{2\alpha F} ln \left(\frac{I_{dc}}{I_0} \right) \right) \quad (1–4)$$

$$V_{concentration} = -c \ln \left(1 - \left(\frac{I_{dc}}{I_{Lim}} \right) \right) \quad (1–5)$$

N_0 = the cell number, V_0 = the open cell voltage, R = the universal gas constant, T = the temperature of the fuel cell stack, F = the Faraday's constant, $p\mathrm{H_2}$ = the hydrogen partial pressure, $p\mathrm{H_2O}$ = the water partial pressure, $p\mathrm{O_2}$ = the oxygen partial pressure, pO = the standard pressure, α = the charge transfer coefficient of the electrodes, I_{dc} = the current of the fuel cell stack, I_{Lim} = the limiting current of fuel cell stack, I_0 = the exchange current of fuel cell stack and c is the empirical coefficient for concentration voltage. The steady state voltage for one cell (N_0 = 1) and power versus cell current density is obtained based on Eq. 1-1 [95].

Fuel cells are very useful as power sources in remote locations, such as spacecraft, remote weather stations, parks, rural locations, and in certain military applications. A fuel cell system running on hydrogen can be compact, lightweight and has no major moving parts. Because fuel cells have no moving parts, and do not involve combustion, in ideal conditions they can achieve up to 99.99 % reliability [100]. There are wide ranges applications of fuel cells namely [86,101] (i) stationary power applications: power generating stations, auxiliary units, distributed power generation, and residential use as combined heat and power generation system, (ii) transportation applications: buses, track, cars, and airport intra-terminal vehicles, and (iii) portable applications: laptops and cellular phones.

1.4.2 Operation of fuel cell

Fuel cell is an electrochemical device which converts chemical energy of reaction into the electrical energy. It consists of an electrolyte with anode (negative electrode) and cathode (positive electrode) on either side. When H_2 gas is fed to anode, the H_2 is split into protons and electrons on anode catalyst layer, where the protons is allow to flow through the electrolyte to the cathode side but electrons are not allow to flow through the electrolyte so electrons are flow through the external circuit where electricity (discharge) are produced. The electrons and protons flow from anode to cathode simultaneously. On the other side, the O_2 (from air) gas is fed to cathode after then electrons, proton and O_2 react at cathode catalyst layer and produce water and heat as a byproduct. The fuel cell is work till the fuel is supplied continuously. Figure 1.6 shows the schematic diagram of PEMFC [102].

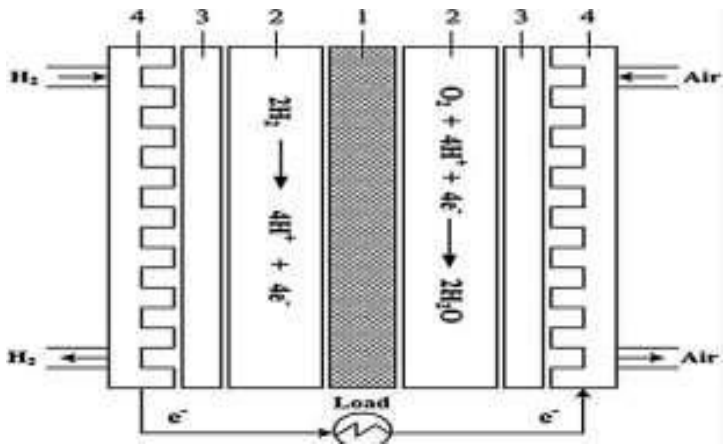

1 = polymer membrane; 2 = catalyst layer; 3 = gas diffusion layer (GDL); 4 = current collector

Figure 1.6 Schematic of PEMFC.

The advantages of PEMFC is highly efficient, more electricity per unit of fuel is produce, low CO_2 emission, low operating temperature, and quick startup. As shown in Figure 1.6, the components of PEMFC consist of below as:

(a) *Electrolyte membrane*

Fuel cell membrane have relatively high proton conductivity, it provides a barrier to mixing of fuel and reactant gases. It is made of perfluorocarbon-sulfonic acid ionomer (PSA). The main property of the membrane is proton conductivity which is the function of water content and temperature.

(b) *Electrode*

Electrode is essentially made of a thin catalyst layer pressed between the ionomer membrane and a porous electrically conductive substrate. In this electrode catalyst layer electrochemical reaction take place.

(c) *Gas diffusion layer (GDL)*

GDL plays crucial role in PEMFC, it distributes the reactant gases homogeneously from the flow field to the catalyst layer through it for the electrochemical reaction. It prevents local hotspot and catalyst flooding by removing heat and excess water from the electrode. It is made of carbon fiber material such as carbon fiber paper and woven cloths.

(d) *Bipolar plates*

The bipolar separator/collector connect the cell electrically in series in fuel cell stack, it also separates the gases in adjacent cell. It is generally made of two families of material which are graphite composite and metallic.

1.4.3 PEMFC performance [102]

1. Efficiency

The fuel cell efficiency, defined as a ratio between the electricity produced and hydrogen consumed is directly proportional to its potential:

$$\eta = V / 1.482 \quad (1–6)$$

Where V is cell potential and 1.482 is the thermo neutral potential corresponding to hydrogen's higher heating value. Sometimes, the efficiency is expressed in terms of the lower heating value (LHV).

$$H_{LHV} = V / 1.254 \quad (1–7)$$

In addition, if some hydrogen is lost (i_{loss}) either due to hydrogen diffusion through the membrane, or due to combining with oxygen that diffused through the membrane or due to internal currents, hydrogen consumption will be higher than that corresponding to generated current, and consequently, the fuel cell efficiency would be somewhat lower than given by equation.

$$\eta = V / 1.482 \times i / (i + i_{loss}) \quad (1–8)$$

If hydrogen is supplied to the cell in excess of that required for the reaction stoichiometry, this excess will leave the fuel cell unused. In case of pure hydrogen this excess may be recirculated back into the stack so it does not change the fuel cell efficiency (not accounting for the power needed for hydrogen recirculation pump), but if hydrogen is not pure (such as in reformate gas feed) unused hydrogen leaves the fuel cell and does not participate in the electrochemical reaction. Then, the fuel cell efficiency is

$$\eta = V / 1.482 \times \eta_{fu} \quad (1–9)$$

Where, η_{fu} is fuel utilization, which is equal to $1/SH_2$, where SH_2 is the hydrogen stoichiometric ratio, i.e., the ratio between the amount of hydrogen actually supplied to the fuel cell and that consumed in the electrochemical reaction. Where, η_{fu} is fuel utilization, which is equal to $1/SH_2$,where SH_2 is the hydrogen stoichiometric ratio, i.e., the ratio between the amount of hydrogen actually supplied to the fuel cell and that consumed in the electrochemical reaction. The comparison of efficiency between fuel cell and conventional electricity generating unit is shown in Figure 1.7.

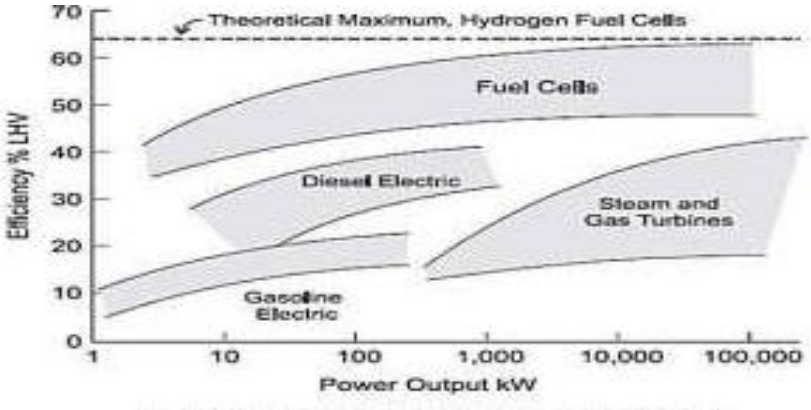

Figure 1.7 Comparison of efficiency fuel cell with conventional electricity generating unit [102].

2. Polarization characteristics

The theoretical optimum fuel cell voltage of 1.23 V would be realized at all operating current but the actual cell potential decrease from its optimum value because of irreversible losses. The losses which often called polarization over potential and overvoltage, these are arise from three sources namely (a) activation polarization, (b) ohmic polarization, and (c) concentration polarization. Further, the polarization curve for PEMFC is shown in Figure 1.8.

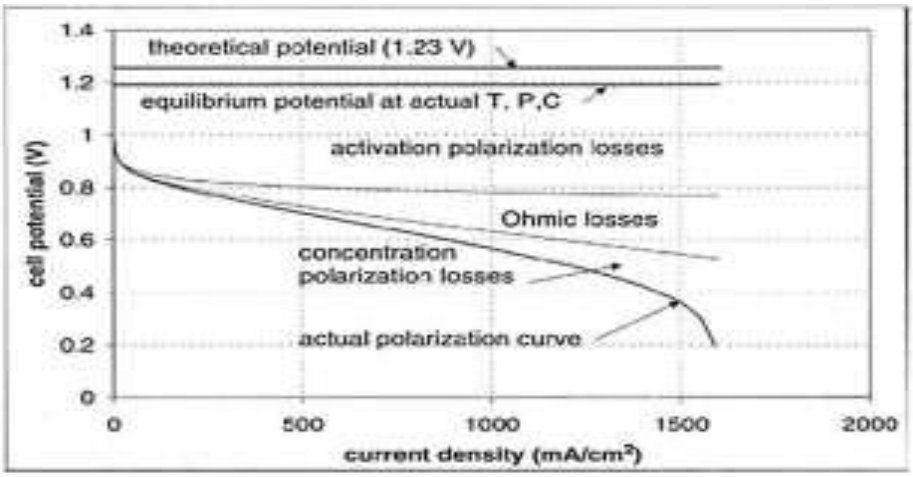

Figure 1.8 Polarization curve for PEMFC.

(a) Activation polarization

Activation polarization is present when the rate of an electrochemical reaction at an electrode surface is controlled by sluggish electrode kinetics. In other words, activation polarization is directly related to the rates of electrochemical reactions. There is a close similarity between electrochemical and chemical reactions in that both involve an activation barrier that must be overcome by the reacting species. In the case of an electrochemical reaction with $\eta_{act} > 50–100$ mV,

$$H_{act} = RT/\alpha nF \ln i / i_o \qquad (1–10)$$

Where the electron is transfer coefficient of the reaction at the electrode being addressed, and α is the exchange current density.

(b) Ohmic polarization

Ohmic losses occur because of resistance to the flow of ions in the electrolyte and resistance to flow of electrons through the electrode materials. The dominant Ohmic losses, through the electrolyte, are reduced by decreasing the electrode separation and enhancing the ionic conductivity of the electrolyte. Because both the electrolyte and fuel cell electrodes obey Ohm's law, the Ohmic losses can be expressed by the equation

$$\eta_{ohm} = iR \qquad (1–11)$$

Where *i* is the current flowing through the cell, and *R* is the total cell resistance, which includes electronic, ionic, and contact resistance.

(c) *Concentration polarization*

As a reactant is consumed at the electrode by electrochemical reaction, there is a loss of potential due to the inability of the surrounding material to maintain the initial concentration of the bulk fluid. That is, a concentration gradient is formed. Several processes may contribute to concentration polarization: slow diffusion in the gas phase in the electrode pores, solution/dissolution of reactants/products into/out of the electrolyte, or diffusion of reactants/products through the electrolyte to/from the electrochemical reaction site. At practical current densities, slow transport of reactants/products to/from the electrochemical reaction site is a major contributor to concentration polarization

$$\eta_{conc} = RT/nF \ln i / i_L \qquad (1–12)$$

Where, i_L is the limiting current.

3. Power characteristic

It is a product of voltage and current (P = VI), the maximum power is obtain at approximate 0.5 to 0.6 V corresponding to relatively high current. At the peak point, the internal resistance of the cell is equal to the electrical resistance of the external circuit. Designer must be selected the desire operating range according to whether high efficiency or high power are require for application. It is never desirable to operate in the range beyond where the power curve drops off. Figure 1.9 shows the power characteristic curve with polarization curve for PEMFC.

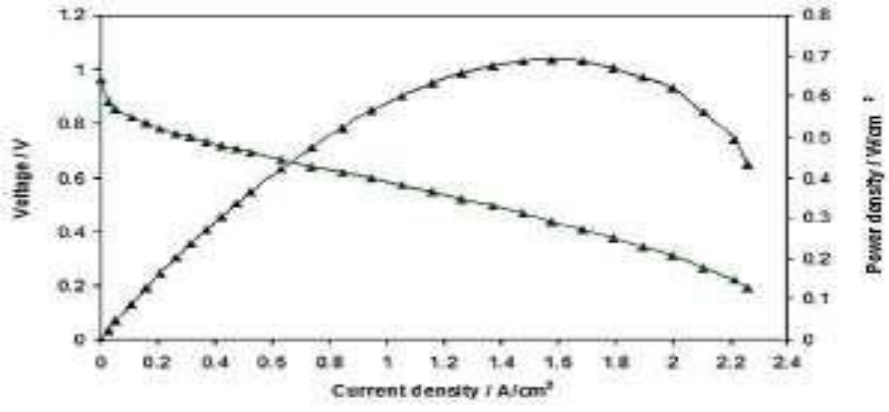

Figure 1.9 Power characteristic curve with polarization curve for PEMFC.

There are several parameters which affect the performance of fuel cell, such as (i) Pressure. The rate of electrochemical reaction is proportional to the partial pressure of oxygen and hydrogen because the higher

pressure forces the reactant gases in to contact with the electrolyte thus the polarization curve increases with increasing the pressure of reactant gases and decreases with decreasing with the pressure of reactant gases. But higher pressure require power to compress the reactant gases and create the problem of leakage, the optimum range of pressure is near the atmospheric pressure 1 atm to 3 atm; (ii) Temperature. Higher temperature improve the reaction rate because at higher temperature improve the mass transfer within the cell resulting decrease in cell resistance thus the polarization curve increases with increasing in temperature and decrease with decreasing in temperature. But the accumulation of water in oxidant stream limits the operating temperature bellow 100 ^{o}C, i.e. at boiling temperature. At the boiling point of water the water boil and resulting steam severely reduce the partial pressure of oxygen thus reduces the cell performance due to oxygen starvation. The fuel cell voltage increases with increasing the operating temperature until the temperature approaches the boiling point further increases in temperature result decreases the voltage. The optimum temperature is obtaining 80 ^{o}C where the two affect balance each other. Typically operating temperature is 70 to 90 ^{o}C with increases the boiling point of water by increasing the pressure; (iii) Stoichiometry ratio. It is the ratio of the amount of gas present relative to the amount of gas that is needed to exactly complete the reaction, thus stoichiometry ratio 1.0 provides exact amount of gas molecule for theoretically complete the reaction below this ratio provides insufficient gas for reaction and above this ratio provide excessive gas for reaction. Higher stoichiometry ratio increases the chance that sufficient number of hydrogen and oxygen interact with electrolyte thus polarization curve increases with increasing the stoichiometry ratio and decreases with decreasing in stoichiometry ratio. The optimum value of stoichiometry ratio is 1.4 for the hydrogen and 2 for the oxygen at rated load; and (iv) Humidity. Humidity is typically measure as “relative humidity”. When a gas has absorbed as much water as it is physically able at a given pressure and temperature, it is said to be saturated and has a relatively humidity of 100 %. With increase the temperature of the saturated gases relative humidity drops (4 % decrease in relative humidity with each degree Celsius of temperature). Humidification is essential for the operation of PEMFC because the water molecule moves with the hydrogen ion during the ion exchange reaction. Insufficient humidification of the membrane leads the cracks and holes in the membrane resulting chemical short circuit, hot spot, local gas mixing and possibility of fire occur. Excessive humidification leads the condensation and flooding within the flow field resulting the phenomenon known as cell reversal where the affected cell produce zero or negative voltage. By proper humidification of reactant gases can improve the performance of fuel cell. However, the others important factors, those are durability and cost is still remain as the major barriers to fuel cell commercialization. In the past two years, more than 35 % cost reduction has been achieved in fuel cell fabrication; the current status of $ 61/kW (2009) for transportation fuel cell is still over 50 % higher than the target of the US Department of Energy (DOE), i.e. $ 30/kW by 2015, in order to compete with the conventional technology of internal-combustion engines. The applications of PEMFC in cars are listed in Table 1.10.

Table 1.10 PEMFC cars.

Automaker	**Fuel cell size type/ Range (mile/km)**	**Fuel Type**	**Commercial Introduction**
BMW	5 kw/180 mile per 300 km	Gasoline/Liquid hydrogen	Munich Airport Hydrogen Vehicle Project
Daimler	90 kw/239 mile per 385 km	Compress hydrogen	Small series production starts in 2009. The seventy to be deployed in Los Angeles and San Francisco by 2012
Ford Motor	85 kw/180 mile per 290 km	8.8 lb. (4 kg) Compress. H_2 @ 5,000 psi	3 year demonstration in Vancouver beginning late 2004. The thirty fleet vehicles in Sacramento, Orlando and Detroit
Honda	100 kw/354 mile per 570 km	Compress hydrogen	Small scale production of 200 vehicles between 2008–2010. Leasing in Southern California and Japan.
Hyundai	80 kw/185 mile per 300 km	Compress. H_2 @ 350 bar	Demonstrating 33 Hyundai Tucsons and Kia Sportage FCVs in the US between 2004–2009 and in Korea between 2006–2010.

1.4.4 Hydrogen (H_2)-PEMFC

Hydrogen is now widely regarded as one key element of a potential energy solution for the twenty-first century, capable of assisting in issues of environmental emissions, sustainability and energy security. Hydrogen has the potential to provide for energy in transportation, distributed heat and power generation and energy storage systems with little or no impact on the environment, both locally and globally [103]. At present, hydrogen is produced in large quantities from fossil fuels by steam reforming of natural gas and partial oxidation of coal or heavy hydrocarbons [104]. Hydrogen is an attractive alternative fuel. However, unlike coal, gas or oil, hydrogen is not a primary energy source. Hydrogen can be obtained from diverse resources, both renewable (hydro, wind, wave, solar, biomass and geothermal) and non-renewable (coal, natural gas and nuclear). It can be stored as a fuel and used in transportation and distributed heat and power generation systems using fuel cells, internal combustion engines or turbines, with the only byproduct at the point of use being water. The ability of hydrogen to replace fossil fuels in the transportation sector could address one of the world's major environmental problems [105].

A schematic of a H_2-PEMFC is shown in Figure 1.10. Hydrogen is oxidized at the anode (left), and protons travel across the membrane to the cathode (right) where oxygen is reduced to water [106].

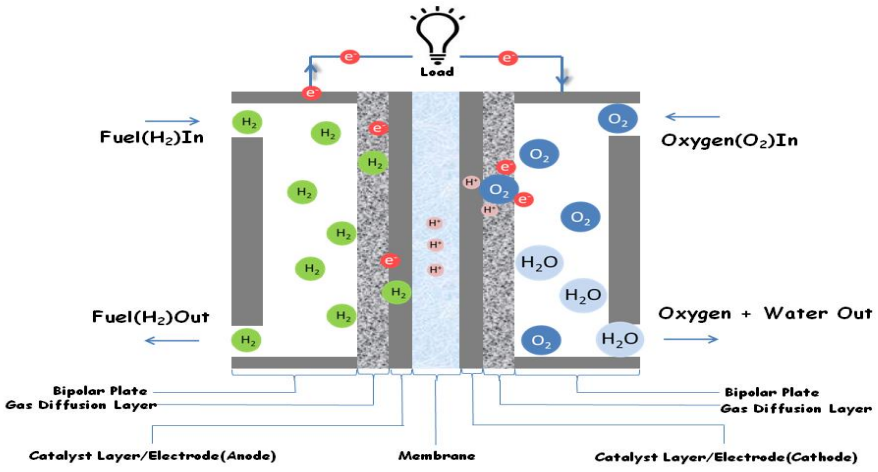

Figure 1.10 Schematic of a hydrogen/air fuel cell.

A fuel cell consists of two electrodes where are separated by an electrolyte or membrane. At one electrode, the anode, a fuel is oxidized. Typical fuels include hydrogen, methanol, ethanol, or formic acid. Of these, the fuels are usual easily oxidized by platinum-based [12]. For hydrogen fuel, the half reaction is

$$\text{Anode} : \quad H_2\,(g, 1\ \text{atm}) \longrightarrow 2H^+\,(aq,\ 1\ M) + 2e^-, \quad E^0 = 0.0\ V \qquad (1\text{–}13)$$

At the other electrode, the cathode, a reduction must occur to ensure electro neutrality of the fuel cell. Regardless of the fuel, the species to be reduced is almost always oxygen. Desired is the four-electron reduction of oxygen to water, the oxygen reduction reaction (ORR):

$$\text{Cathode} : \quad O_2\,(g, 1\ atm) + 4e^- + 4H^+\,(aq, 1\ M) \longrightarrow 2H_2O, \quad E^0 = 1.23\ V \qquad (1\text{–}14)$$

The combination reaction then is

$$\text{Overall} : \quad H_2 + \tfrac{1}{2}\,O_2 \longrightarrow 2H_2O, \quad \Delta E = 1.23\ V \qquad (1\text{–}15)$$

The first half reaction, involving hydrogen oxidation, is facile with present Pt-based catalysts. However, the ORR is not facile, even with platinum catalyst. The difficulty in oxygen reduction stems from exceptionally strong O=O bond (498 kJ/mol). Thus, activation of this bond is typically kinetically slow. At both the anode and cathode, the catalyst is supported on carbon usually found as a felt onto which the catalyst has been impregnated. The separator between the two electrodes is a polymer electrolyte now commonly made from the conductive fluoropolymer Nafion. The combined polymer electrode assembly is known as a membrane electrode assembly (MEA) [106].

The H_2-PEMFC has been recognized as a potential future power source for zero-emission vehicles [107]. However, to become commercially viable, H_2-PEMFC has to overcome the barrier of high catalyst cost caused by the exclusive use of Pt and Pt-based catalysts [108]. Precious-metal catalysts, predominantly Pt supported on carbon, are used for both the oxidation of the fuel and reduction of the oxygen in a typical temperature range of 80–100 °C. Pt and Pt based alloys are the most commonly used catalysts for H_2-PEMFC as Pt offers: (i) highest catalytic activity, (ii) chemical stability, (iii) high exchange current density (i_o), and (iv) superior work function [109–111]. However, the global scarcity of Pt and its high cost demand for an urgent need to reduce the use of Pt and to improve the efficiency in PEMFC.

Apart from the issue of the high cost of catalyst and other fuel cell system components (polymer electrolyte membrane, bipolar plates, the rest of the power system, and so on), H_2-PEMFC suffer from insufficient performance durability, arising mainly from cathode catalyst oxidation, catalyst migration, loss of electrode active surface area, and corrosion of the carbon support [112]. Consequently, much of the past research has been focused on determining whether automotive Pt loading targets (< 0.2 gPt/kW), driven by cost and Pt supply considerations, could be met with currently known catalyst technology [113]. In fact, it may be said that the approaches have been adopted to achieve better catalyst efficiency can broadly be divided into the following categories: (i) employing Pt based bimetallic and ternary catalyst systems and other nonprecious metals to decrease Pt dependency and (ii) improving the catalyst support. It has been realized that the catalytic activity of the Pt based catalyst is strongly dependent on the composition, structure, morphology, particle size, alloyed degree [114] and catalyst supports [115,116]. In addition, the proton conducting membrane is the vital component of a PEMFC, which it makes possible to attain high power densities. The quantum jumps in PEMFC performance, due to the transition from phenol sulfonic acid and polystyrene sulfonic acid membranes to Nafion (Table 1.11).

Table 1.11 Quantum jumps in the development of proton conducting membranes [117].

Time	Membrane	Power density (kW m^{-2})	Lifetime (thousands of hours)
1959–1961	Phenol sulfonic	0.05–0.1	0.3–1
1962–1965	Polystyrene sulfonic	0.4–0.6	0.3–2
1966–1967	Polytrifluorostyrene sulfonic	0.75–0.8	1–10
1968–1970	Nafion experimental	0.8–1	1–100
1971–1980	Nafion production	6–8	10–100

It was due to two reasons: (i) Nafion is a perfluoro sulfonic acid, with a structure similar to that of teflon, except that it has side chains with ether linkages, followed by CF_2 groups prior to the sulfonic acid (Figure 1.11).

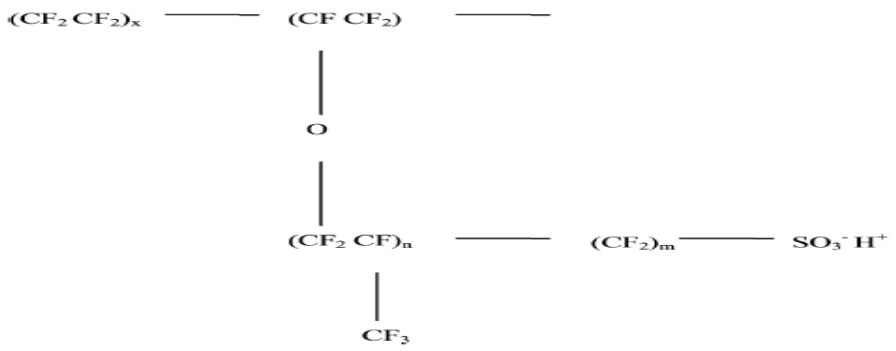

Figure 1.11 Structure of nafion.

The high electronegativity (i.e. electron affinity) of the fluorine atom, bonded to the same carbon atom as the SO_3H group, makes the sulfonic acid be a super acid (e.g. like the trifluoromethane sulfonic acid). Thus, there was at least a two-fold increasing in the specific conductivity of this membrane, as compared with the polystyrene sulfonic acids (Table 1.11), and (ii) the CF_2 groups are highly stable at the potential of the oxygen cathode and also at the anode, which may contain small amounts of hydrogen peroxide, as stated above. The most dramatic result by using Nafion, was that it extended the lifetime of PEMFCs at least by four orders of magnitude (Table 1.11). The Dow Chemical Company and Asahi Chemical Company synthesized advanced perfluorosulfonic acid membranes with shorter side chains and a higher ratio of SO_3H to CF_2 groups [117].

1.4.5 Thermodynamic and Kinetic Considerations of Fuel Cells [118]

The energy storage and power characteristics of electrochemical energy conversion systems follow directly from the thermodynamic and kinetic formulations for chemical reactions as adapted to electrochemical reactions. First, the basic thermodynamic considerations are treated. The basic thermodynamic equations for a reversible electrochemical transformation are given as

$$\Delta G = \Delta H - T\Delta S \tag{1–16}$$

and

$$\Delta G^o = \Delta H^o - T\Delta S^o \tag{1–17}$$

where ΔG is the Gibbs free energy, or the energy of a reaction available (= free) for useful work, ΔH is the enthalpy, or the energy released by the reaction, ΔS is the entropy, and T is the absolute temperature, with TΔS being the heat associated with the organization/disorganization of materials. Because ΔG represents the net useful energy available from a given reaction, in electrical terms, the net available electrical energy from a reaction in a cell is given by

$$\Delta G = - nFE \tag{1–18}$$

and

$$\Delta G^o = - nFE^o \tag{1–19}$$

where *n* is the number of electrons transferred per mole of reactants, *F* is the Faraday constant, being equal to the charge of one equivalent of electrons, and *E* is the voltage of the cell with the specific chemical reactions; in the other words, *E* is the electromotive force (emf) of the cell reaction. Spontaneous processes have a negative free energy and a positive emf. The van't Hoff isotherm identifies the free energy relationship for bulk chemical reactions as

$$\Delta G = \Delta G^o + RT \ln (A_P/A_R) \tag{1–20}$$

where *R* is the gas constant, *T* is the absolute temperature, A_P the activity product of the products and A_R the activity product of the reactants. Combining equations (1–16) and (1–17) with the van't Hoff isotherm, the Nernst equation for electrochemical reactions as below:

$$E = E^o + (RT/nF) \ln (A_P/A_R) \tag{1–21}$$

Faraday's laws, as summarized in equation (1–19), give the direct relationship between the amount of reaction and the current flow.

$$g = It(MW) / nF \tag{1–22}$$

g is the grams of material transformed, I is the current flow (amps), t is the time of current flow (seconds, hours), MW is the molecular or atomic weight of the material being transformed, and n is the number of electrons in the reaction. Thus, the reversible heat effect can be obtained below as

$$\Delta G = - nFE = \Delta H - T\Delta S \tag{1–23}$$

$$= \Delta H - nFT (dE/dT) \tag{1–24}$$

Finally, the fuel cells as aforementioned have many benefits such as (i) Efficient. They convert hydrogen and oxygen directly into electricity and water, with no combustion in the process. The resulting efficiency is between 50 and 60 %, about double that of an internal combustion engine, (ii) Clean. If hydrogen is the fuel, there are no pollutant emissions from a fuel cell itself, only the production of pure water. In contrast to an internal combustion engine, a fuel cell produces no emissions of sulphur dioxide, which can lead to acid rain, or nitrogen oxides which produce smog or dust particulates, (iii) Quiet**.** A fuel cell has no moving parts, although a fuel cell system may have pumps and fans. As a result, electrical power is produced relatively silently. Many hotels and resorts in quiet locations, for example, could replace diesel engine generators with fuel cells for both main power supply or for backup power in the event of power outages, (iv) Modular. That is, fuel cells of varying sizes can be stacked together to meet a required power demand. As mentioned earlier, fuel cell systems can provide power over a large range, from a few watts to megawatts, and (v) Environmentally safe. They produce no hazardous waste products, and their only byproduct is water (or water and carbon dioxide in the case of methanol cells) and fuel cells may give us the opportunity to provide the world with sustainable electrical power. However, at present there are still remain many obstacles to develop fuel cells, namely (i) At present platinum is a key component to fuel cells. Platinum is a scarce natural resource; the largest supplies to the world platinum market are from South Africa, Russia and Canada. Shortages of platinum are not anticipated; however changes in government policies could affect the supply, (ii) At present, a large portion of the investment in fuel cells and hydrogen technology has come from auto manufacturers. However, if fuel cells prove unsuitable for automobiles, new sources of investment for fuel cells and the hydrogen industry will be needed, (iii) Fuel cells must obtain mass-market acceptance to succeed. This acceptance depends largely on price, reliability, longevity of fuel cells and the accessibility and cost of fuel. Compared to the price of present day alternatives e.g. diesel engine generators and batteries, fuel cells are comparatively expensive. In order to be competitive, fuel cells need to be mass produced less expensive materials developed, and (iv) An infrastructure for the mass-market availability of hydrogen, or methanol fuel initially, must also develop. At present there is no infrastructure in place for either of these fuels. Unless motorists are able to obtain fuel conveniently and affordably, a mass market for motive applications will not develop [119].

1.5 Pt deposition on support material

The important step in the catalyst synthesis procedure is the deposition of Pt onto the support materials, such as CNT for which a wide variety of methods have been reported, which have been discussed in a recent review article [120]. Although some methods that can be categorized as variation of vapor phase deposition processes have been employed, synthesis methods based on liquid-phase precursors are preferred because they allow particle size control. For catalysis and electrocatalysis, the goal is to keep the catalysts size as

small as possible because it equates into large catalytic surface area per mass of catalyst; although consideration must be given to long term stability. There are four commonly employed liquid-phase precursor methods are impregnation method, precipitation method, colloidal method and ion exchange method for synthesis of metal nanoparticles. The fundamental mechanism for nanosize metal synthesis of each method is not fully understood, although a general understanding of the differences methods are as shown in the Figure 1.12.

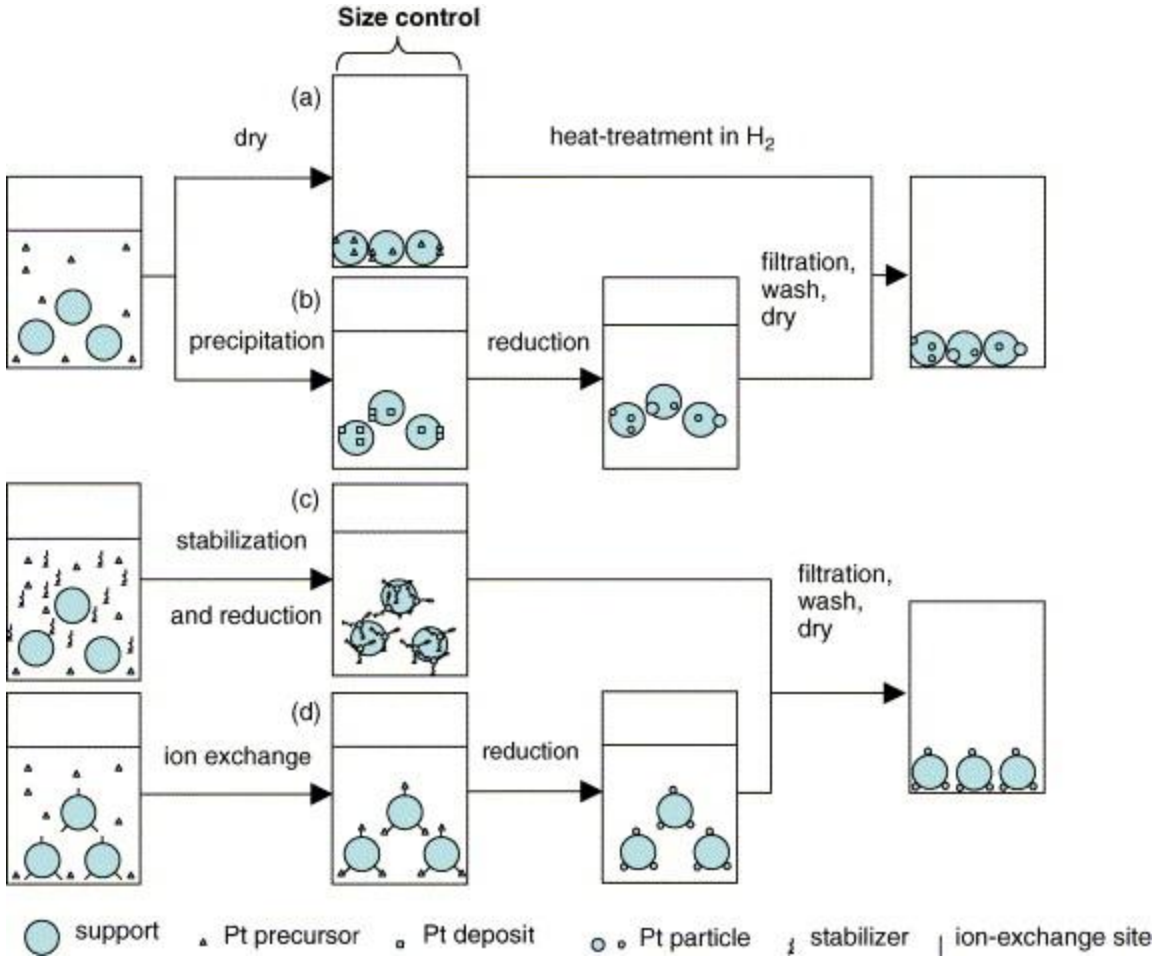

Figure 1.12 Schematic illustrations of (a) impregnation, (b) precipitation, (c) colloidal, and (d) ion exchange methods.

As shown in Figure 1.12, the impregnation method involves introduction of the liquid precursor into the catalyst support powder which upon drying leaves metal catalyst salt and with subsequent heating under reducing conditions generates Pt catalysts. In the case of precipitation method, the catalyst support is introduced into a liquid medium containing the Pt precursor to form a suspension. The precipitant, usually a hydroxide, is added slowly to precipitate out the metal-containing complex and subsequently subjected to a

reduction step to generate the metal particles. For the colloidal method, the catalyst metal as colloid is stabilized by the addition of a stabilizer, where stabilizer can act as a bridge between the catalyst support and the precipitated catalyst. Then, the reduction step is achieved simultaneously by reductants, such as ethylene glycol (EG) [121,122]. Finally, at the ion exchange method, the Pt is introduced as an ion (salt) in a liquid medium, an ion exchange reaction of the following type may occur between the functional group of carbon support material and the catalyst metal ion [120].

1.6 Physical characterization methods

The common methods for physical characterization of PEMFC catalyst are X-ray diffraction (XRD), transmission electron microscope (TEM), and X-ray photon spectroscopy (XPS). Both XRD and TEM can be used to determine the Pt particle size and also the morphology of Pt particles may be observed through TEM images. On the other hand, XPS can be used to evaluate Pt electronic structure.

XRD is a rapid analytical technique primarily used for phase identification of a crystalline material and can provide information on unit cell dimensions. Because the wavelength of the X-rays is comparable to the size of the atoms, they are ideally suited for the probing the structure arrangement of atoms and molecules in a wide range of materials. Each crystal has its unique characteristic X-ray powder pattern based on Bragg's law (Equations 1–25 and 1–26), which can be used for the identification of the materials. The catalyst particle average diameter D can be calculated from diffraction peaks in the XRD patterns using Scherrer's equation.

$$\lambda = 2d \sin \theta \tag{1–25}$$

$$D = 0.9 \lambda / B_{2\theta} \cos \theta_{\max} \tag{1–26}$$

where d is the d-spacing, λ is the wavelength of the X-ray (1.54056 Å), θ is the angle at the maximum of the peak, and $B_{2\theta}$ is the width of the peak at half height.

XPS is a surface sensitive spectroscopy technique that allows chemical identification of the elements in the top atomic layers of a sample by recording the binding energies of the electrons associated with these atoms. Furthermore, because the binding energies differ, not only from chemical species to species, but also with the bonding conditions in which the element is found, this technique also provides information on the actual compounds present on the surface. In essence, it probes the electronic structure of the surface. The elemental information including the content and the valence state can be analyzed based on the peak intensities and the peak values in the XPS spectra.

TEM is used to identify imperfections in the atomic level structure of materials by analysis of microscopy surfaces. A very thin slice of the material to be tested is exposed to a beam of electrons. When the electrons interact with a consistent material structural, a constant fraction of electrons is transmitted back from the sample to detector. Once a structural imperfection if encountered, the fraction of transmitted

electrons changes, resulting in change of contrast. Diffraction contrast is useful in identifying large structure and crystallographic features. Phase contrast used for high magnification imaging of atomic columns. The samples were dispersed in ethanol under sonication and dropped on the carbon coated grid and then imaged.

1.7 Electrochemical Kinetics Characterization of PEMFC Catalysis

The electrochemically active surface area (ECSA) of Pt catalyst is determined by cyclic voltammetry (CV). The CV is an electrochemical method that allows determination of the real surface area of noble metal catalysts such as platinum by measuring the coulombic charge associated with the deposition or removal of a chemisorbed monolayer of a species, usually hydrogen. For hydrogen, 210 micro coulombs (μC) of charge correspond to coverage of 1 cm^2 of Pt area. When Pt electrode (electrocatalyst) is exposed to an aqueous acidic medium (electrolyte), the hydrated proton discharges with the formation of electro adsorbed hydrogen are formed according to the following reaction [123].

$$M\,(Pt) + H^+ + e^- \longrightarrow M\text{–}H_{ads} \qquad (1\text{–}27)$$

By altering the potential of the electrode, the reaction can be affected in the forward or reverse direction. In cyclic voltammetry, the electrode potential is cycled between two potentials and the current is measured. The electrochemical characterization is depicted in Figure 1.13.

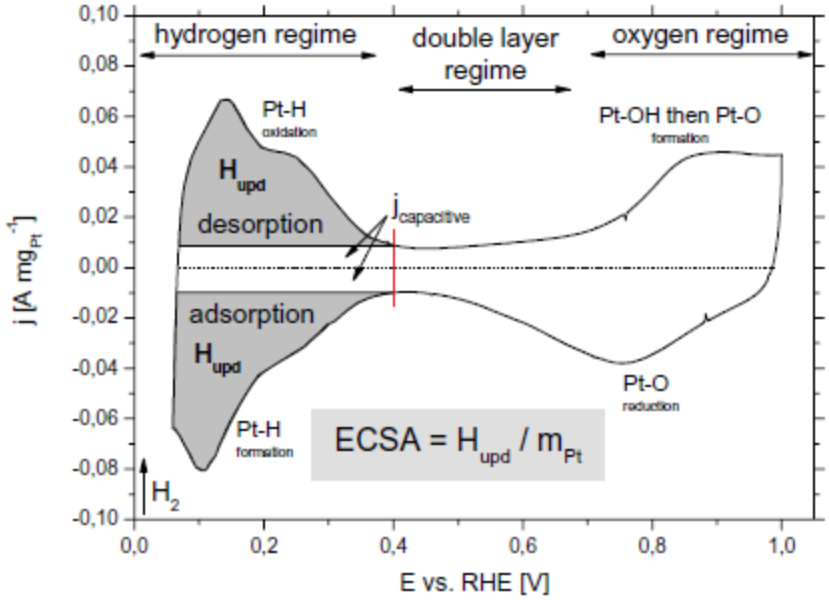

Figure 1.13 Analysis of a cyclic voltammogram for Pt/C, recorded in N_2 saturated, 0.1 M $HClO_4$ at room temperature [124,125].

To estimate the ECSA of Pt, CV profiles were recorded between 0.06 and 1.00 V versus reversible hydrogen electrode (RHE). The platinum ECSA was calculated using the mean integral charge of the hydrogen

adsorption/desorption area with double layer current corrected at 0.4 V versus RHE and with 210 μC cm_{Pt}^{-2}, assuming one hydrogen atom observed to one platinum atom (Figure 1.13).

The activity for the oxygen reduction reaction (ORR) can be determined by linear sweep voltammetry (LSV) measurements which conducted using the RDE technique. The intrinsic kinetic current at 0.9 V versus RHE was corrected with the mass transport diffusion limiting current between 0.2 and 0.5 V versus RHE (Figure 1.14).

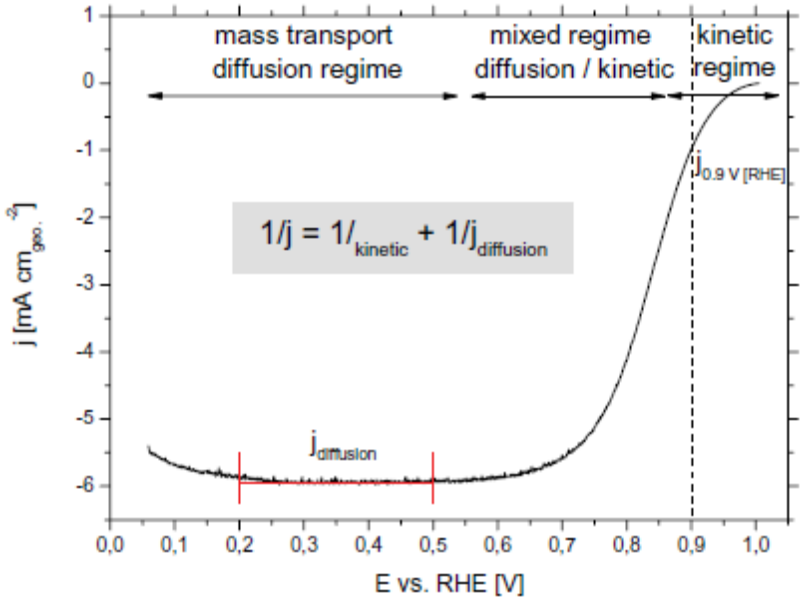

Figure 1.14 Analysis of a linear sweep voltammogram (Pt/C, 0.06–1.00 V versus RHE in O_2 saturated, 0.1 M $HClO_4$, and room temperature) [124].

1.8 Objectives

The objectives of this thesis are:

(i) To preparing Pt subnano-clusters and to control the Pt particle size on GNS in a region from sub-nanometer to a few nanometers.

(ii) To study formation process of Pt subnano-clusters on GNS.

(iii) To study effect of annealing temperatures of ammonia on GNS for Pt/N-GNS catalysts properties.

(iv) To study support materials effect for oxygen reduction activity of Pt catalysts.

(v) Enhancement electrocatalytic activity of Pt catalyst and reducing Pt usage on GNS.

In order to achieve the above objectives, GNS and N-doped GNS have been used as support materials for Pt catalysts. The support material effect and properties of Pt catalysts have been examined by electrochemical measurement, XPS, XRD and TEM, respectively.

1.9 Thesis Outline

In this thesis, there are seven chapters. Chapter 1 contains general introduction, basic concept about support materials, fuel cells, objectives and thesis outline. The principle and basic theory about XPS, XRD, electrochemistry, and electro-catalysis are described in Chapter 2. Then, in Chapter 3, controlling the Pt particle size on GNS in a region from sub-nanometer to a few nanometers is described. In this chapter also includes explanation how to prepare Pt subnano-clusters on GNS, and clearly clarify the relationship among Pt particle size, catalytic activity and electronic structure of Pt on GNS. Subsequently, the formation process of Pt subnano-clusters on GNS is clearly exhibited in Chapter 4. I explain step by step for formation process Pt subnano-clusters on GNS. Next, Chapter 5 discusses the effect of N-doped GNS (N-G) prepared at different temperature dopant for Pt/N-GNS properties. In this chapter, the properties of Pt/N-G catalysts as a function of varying annealing temperatures and also preparation N-G at various annealing temperature of GNS in ammonia, respectively are explained. Furthermore, Chapter 6 contains the support material effect for oxygen reduction activity based on Pt catalyst. In this chapter, I focus to know the support material effect for Pt catalytic activity at cathode. Finally, Chapter 7 contains conclusions and future works.

References

[1] R. Lee, Science, **333**, 569–573 (2011).

[2] Y. Cheng, C. H. Wang, Ind. Eng. Chem. Res., **51**, 9919–9920 (2012).

[3] International Energy Agency in World Energy Outlook 2011, 546–547, http://www.worldenergyoutlook.org.

[4] Q. Schiermeier, J. Tollefson, T. Scully, A. Witze, O. Morton, Nature, **454**, 816–823 (2008).

[5] S. Chu, A. Majundar, Nature, **488**, 294–302 (2012).

[6] G. Fischer, L. Schrattenholzer, Biomass and bioenergy, **20**, 151–152 (2001).

[7] L. W. Jones, Science, **174**, 367–370 (1971).

[8] F. Veld, Energy Fuels, **26**, 3882–3890 (2012).

[9] E. M. Farland, Science, **338**, 340–341 (2012).

[10] M. J. Prather, Science, **302**, 581–582 (2003).

[11] H. Zhang, P. K. Shen, Chem. Rev., **112**, 2780–2832 (2012).

[12] R. Borup, et.al., Chem. Rev., **107**, 3904–3951 (2007).

[13] J. B. Hou, Y. Y. Shao, M. W. Ellis, R. B. Moore, B. L. Yi, Phys. Chem. Chem. Phys., **13**, 15384–15402 (2011).

[14] K. S. Novoselov, A. K. Geim, S. V. Morozov, D. Jiang, Y. Zhang, S. V. Dubonos, I. V. Grigorieva, A. A. Firsov, Science, **306**, 666–669 (2004).

[15] H. J. Choi, S. M. Jung, J. M. Seo, D. W. Chang, L. Dai, J. B. Baek, Nano Energy, **4**, 534–551 (2012).

[16] P. Serp, J. L. Figueiredo, Carbon Materials for Catalysis, John Wiley and Sons, New Jersey, 2009.

[17] X. Yu, S. Ye, J. Power Sources, **172**, 133–144 (2007).

[18] M. Kim, J. N. Park, H. Kim, S. Song, W. H. Lee, J. Power Sources, **163**, 93–97 (2006).

[19] R. L. Augustine, Heterogeneous Catalysis for the Synthetic Chemists, Marcel Dekker, New York, 1996.

[20] K. W. Park, Y. E. Sung, S. Han, Y. Yun, T. Hyeon, J. Phys. Chem. B, **108**, 939–940 (2004).

[21] Y. Takasu, T. Kawaguchi, W. Sugimoto, Y. Murakami, Electrochim. Acta, **48**, 3861–3862 (2003).

[22] S. Sharma, B. G. Pollet, J. Power Sources, **208**, 96–119 (2012).

[23] N. Jha, A. L. M. Reddy, M. M. Shaijumon, N. Rajalakshmi, S. Ramaprabhu, Int. J. Hydrogen Energy, **33**, 427–433 (2008).

[24] M. Watanabe, H. Sei, P. Stonehart, J. Electroanal. Chem., **261**, 375–376 (1989).

[25] K. Yahikozawa, Y. Fujii, Y. Matsuda, K. Nishimura, Y. Takasu, Electrochim. Acta, **36**, 973–974 (1991).

[26] D. A. Stevens, J. R. Dahn, Carbon, **43**, 179–188 (2005).

[27] K. Kinoshita, Carbon, electrochemical and physicochemical properties, Wiley-Interscience publication, California, 1987.

[28] E. Antolini, Appl. Catal. B: Environ., **88**, 1–24 (2009).

[29] M. Uchida, Y. Aoyama, M. Tanabe, N. Yanagihara, N. Eda, A. Ohta, J. Electrochem. Soc., **142**, 2572–2573 (1995).

[30] J. McBreen, H. Olender, S. Srinivasan, K. Kordesch, J. Appl. Electrochem., **11**, 787–788 (1981).

[31] A. L. N. Pinheiro, A. Oliveira-Neto, E. C. de Souza, J. Perez, V. A. Paganin, E. A. Ticianelli, E. R. Gonzalez, J. New Mater. Electrochem. Syst., **6**, 1–5 (2003).

[32] D. S. Cameron, S. J. Cooper, I. L. Dodgson, B. Harrison, J. W. Jenkins, Catal. Today, **7**, 113–115 (1990).

[33] G. C. Torres, E. I. Jablonski, G. T. Baronetti, A. A. Castro, S. R. de Miguel, O. A. Scelza, M.D. Blanco, M. A. P. Jimenez, J. L. G. Fierro, Appl. Catal. A, **161**, 213–215 (1997).

[34] A. S. Escribano, F. Coloma, F. R. Reinoso, Appl. Catal. A, **173**, 247–248 (1998).

[35] C. K. Poh, S. H. Lim, H. Pan, J. Lin, J. Y. Lee, J. Power Sources, **176**, 70–71 (2008).

[36] S. Kim, S. J. Park, Electrochim. Acta, **52**, 3013–3015 (2007).

[37] R. Ryoo, S. H. Joo, M. Kruk, M. Jaroniec, Adv. Mater., **13**, 677–681 (2001).

[38] K. I. Han, J. S. Lee, S. O. Park, S. W. Lee, Y. M. Park, H. Kim, Electrochim. Acta, **50**, 791–792 (2004).

[39] W. Z. Li, C. H. Liang, J. S. Qiu, W. J. Zhou, H. M. Han, Z. B. Wie, G. Q. Sun, Q. Xin, Carbon, **40**, 791–803 (2002).

[40] C. A. Bessel, K. Laubernds, N. M. Rodriguez, R. T. K. Baker, J. Phys. Chem. B, **105**, 1115–1118 (2001).

[41] E. S. Steigerwalt, G. A. Deluga, C. M. Lukehart, J. Phys. Chem. B, **106**, 760–766 (2002).

[42] G. Che, B. B. Lakshmi, E. R. Fisher, C. R. Martin, Nature, **393**, 346–347 (1998).

[43] T. Matsumoto, T. Komatsu, H. Nakano, K. Arai, Y. Nagashima, E. Yoo, T. Yamazaki, M. Kijima, H. Shimizu, Y. Takasawa, J. Nakamura, Catal. Today, **90**, 277–278 (2004).

[44] C. Wang, M. Waje, X. Wang, J. M. Tang, C. R. Haddon, Y. Yan, Nano Lett., **4**, 345–346 (2004).

[45] P. V. Dudin, P. R. Unwin, J. V. Macpherson, J. Phys. Chem. C, **114**, 13241–13248 (2010).

[46] D. B. Mawhinney, V. Naumenko, A. Kuznetsova, J. T. Yates Jr., J. Liu, R. Smalley, J. Am. Chem. Soc., **122**, 2383–2384 (2000).

[47] S. Park, Y. Shao, R. Kou, V. V. Viswanathan, S. A. Towne, P. C. Rieke, J. Liu, Y. Lin, Y. Wang, J. Electrochem. Soc., **158**, B297–B302 (2011).

[48] J. Wang, G. Yin, Y. Shao, Z. Wang, Y. Gao, J. Phys. Chem. C, **112**, 5784–5789 (2008).

[49] Y. Shao, G. Yin, J. Zhang, Y. Gao, Electrochim. Acta, **51**, 5853–5857 (2006).

[50] H. T. Fang, C. G. Liu, C. Liu, F. Li, M. Liu, H. M. Cheng, Chem. Mater., **16**, 5744–5750 (2004).

[51] L. Li, Y. Xing, J. Electrochem. Soc., **153**, A1823–A1828 (2006).

[52] F. Coloma, A. S. Escribano, J. Fierro, F. R. Reinoso, Langmuir, **10**, 750–755 (1994).

[53] M. Kang, Y. S. Bae, C. H. Lee, Carbon, **43**, 1512–1516 (2005).

[54] A. H. C. Neto, F. Guinea, N. M. R. Peres, K. S. Novoselov, A. K. Geim, Rev. Modern Phys., **81**, 110–155 (2009).

[55] A. K. Geim, K. S. Novoselov, Nature Materials, **6**, 183–191 (2007).

[56] A. Peigney, C. Laurent, E. Flahaut, R. R. Bacsa, A. Rousset, Carbon, **39**, 507–514 (2001).

[57] S. Park, R. S. Ruoff, Nature Nanotechnology, **4**, 217–224 (2009).

[58] Y. Q. Sun, Q. O. Wu, G. Q. Shi, Energy and Environ. Sci., **4**, 1113–1132 (2011).

[59] M. J. Allen, V. C. Tung, R. B. Kaner, Chem. Rev., **110**, 132–145 (2010).

[60] C. Berger, Z. Song, X. Li, X. Wu, N. Brown, C. Naud, D. Mayou, T. Li, J. Hass, A. N. Marchenkov, Science, **312**, 1191–1196 (2006).

[61] K. S. Kim, Y. Zhao, H. Jang, S. Y. Lee, J. M. Kim, J. H. Ahn, P. Kim, J. Y. Choi, B. H. Hong, Nature, **457**, 706–710 (2009).

[62] S. Bae, H. Kim, Y. Lee, X. F. Xu, J. S. Park, Y. Zheng, J. Balakrishnan, T. Lei, H. R. Kim, Y. I. Song, Y. J. Kim, K. S. Kim, B. Ozyilmaz, J. H. Ahn, B. H. Hong, S. Iijima, Nature Nanotech., **5**, 574–578 (2010).

[63] S. H. Hur, J. N. Park, Asia-Pac. J. Chem. Eng., (2012).

[64] W. S. Hummers, R. E. Offeman, J. Am. Chem. Soc., **80**, 1339 (1958).

[65] B. C. Brodie, Ann. Chim. Phys., **59**, 466 (1860).

[66] L. Staudenmaier, Ber. Deut. Chem. Ges., **31**, 1481 (1898).

[67] H. He, J. Klinowski, M. Forster, A. Lerf, Chem. Phys. Lett., **287**, 53–56 (1998).

[68] W. Cai, R. D. Piner, F. J. Stadermann, S. Park, M. A. Shaibat, Y. Ishii, D. Yang, A. Velamakanni, S. J. An, M. Stoller, J. An, D. Chen, R. S. Ruoff , Science, **321**, 1815–1817 (2008).

[69] A. Lerf, H. Heyong, M. Forster, J. Klinowski, J. Phys. Chem. B, **102**, 4477–4482 (1998).

[70] H. He, T. Riedl, A. Lerf, J. Klinowski, J. Phys. Chem., **100**, 19954–19958 (1996).

[71] S. Stankovich, R. D. Piner, X. Chen, N. Wu, S. B. T. Nguyen, R. S. Ruoff, J. Mater. Chem., **16**, 155–158 (2006).

[72] I. Jung, M. Pelton, R. Piner, D. A. Dikin, S. Stankovich, S. Watcharotone, M. Hausner, R. S. Ruoff, Nano Lett., **7**, 3569–3575 (2007).

[73] D. Li, M. B. Muller, S. Gilje, R. B. Kaner, G. G. Wallace, Nature Nanotech., **3**, 101–105 (2008).

[74] S. Stankovich, D. A. Dikin, R. D. Piner, K. A. Kohlhaas, A. Kleinhammes, Y. Jia, Y. Wu, S. B. T. Nguyen, R. S. Ruoff, Carbon, **45**, 1558–1565 (2007).

[75] V. C. Tung, M. J. Allen, Y. Yang, R. B. Kaner, Nature Nanotechnology, **4**, 25–29 (2009).

[76] Y. Si, E. T. Samulski, Nano Lett., **8**, 1679–1682 (2008).

[77] R. Muszynski, B. Seger, P. V. Kamat, J. Phys. Chem. C, **112**, 5263–5266 (2008).

[78] R. Wang, Y. Wang, C. Xu, J. Sun, L. Gao, RSC Advances, **3**, 1194–1200 (2013).

[79] S. T. Nguyen, S. Stankovich, D. A. Dikin, R. D. Piner, K. A. Kohlhaas, A. Kleinhammes, Y. Jia, Y. Wu, R. S. Ruoff, Carbon, **45**, 1558–1565 (2007).

[80] M. C. Kim, G. S. Hwang, R. S. Ruoff, J. Chem. Phys., **131**, 064704, 1–5 (2009).

[81] X. Zhou, J. Zhang, H. Wu, H. Yang, J. Zhang, S. Guo, J. Phys. Chem. C, **115**, 11957–11961 (2011).

[82] P. G. Ren, D. X. Yan, X. Ji, T. Chen, Z. M. Li, Nanotechnology, **22**, 055755 (2011).

[83] B. Seger, V. P. Kamat, J. Phys. Chem. C. **19**, 7990–7995 (2009).

[84] K. S. Novoselov, V. I. Fal'ko, L. Colombo, P. R. Gellert, M. G. Schwab, K. Kim, Nature, **490**, 192–200 (2012).

[85] A. Hermann, T. Chaudhuri, P. Spagnol, Int. J. Hydrogen Energy, **30**, 1297–1302 (2005).

[86] M. T. Gencoglu, Z. Ural, Int. J. Hydrogen Energy, **34**, 5242–5248 (2009).

[87] C. Mandil, Prospects for hydrogen and fuel cells, International Energy Agency, Publication, France (2005).

[88] S. Wasmus, A. Kuver, J. Electroanal. Chem., **461**, 14–31 (1999).

[89] A. H. C. Sirk, J. M. Hill, S. K. Y. Kung, V. I. Birss, J. Phys. Chem. B., **108**, 689–695 (2004).

[90] S. Du, J. Power Sources, **195**, 289–292 (2010).

[91] K. S. Dhathathreyan, P. Sridhar, G. Sasikumar, K. K. Ghosh, G. Velayutham, N. Rajalakshmi, C. K. Subramaniam, M. Raja, K. Ramya, Int. J. Hydrogen Energy, **24**, 1107–1115 (1999).

[92] P. Agnolucci, Int. J. Hydrogen Energy, **32**, 4319–4328 (2007).

[93] S. J. C. Cleghorn, X. Ren, T. E. Springer, M. S. Wilson, C. Zawodzinski, T. A. Zawodzinski, S. Gottesfeld, Int. J. Hydrogen Energy, **22**, 1137–1144 (1997).

[94] M. Uzunoglu, O. C. Onar, M. S. Alam, J. Power Sources, **168**, 40–50 (2007).

[95] M. Tanrioven, M. S. Alam, J. Power Sources, **157**, 401–410 (2006).

[96] Z. Lemes, A. Vath, Th. Hartkopf, H. Mancher, J. Power Sources, **154**, 386–393 (2006).

[97] M. Momirlan, T. N. Veziroglu, Int. J. Hydrogen Energy, **30**, 795–802 (2005).

[98] E. Yuzugullu, J. P. Deason, Energy Policy, **35**, 452–460 (2007).

[99] D. Thirumalai, R. E. White, J. Electrochem. Soc., **144**, 1717–1723 (1997).

[100] The online Fuel Cell Information Resource. Fuel cell basics and benefits, http://www.fuelcells.org/basics/benefits.

[101] A. L. Dicks, Fuel Cells and Hydrogen Tech., **4**, 203–245 (2012).

[102] S. Bhatta, B. Guptaa, V. K. Sethib, M. Pandey, Int. J. Curr. Eng. Tech., **2**, 219–226 (2012).

[103] P. P. Edwards, V. L. Kuznetsov, W. I. F. David, Phil. Trans. R. Soc. A, **365**, 1043–1056 (2007).

[104] T. I. Sigfusson, Phil. Trans. R. Soc. A, **365**, 1025–1042 (2007).

[105] M. Z. Jacobson, W. G. Colella, D. M. Golden, Science, **308**, 1901–1905 (2005).

[106] A. A. Gewirth, M. S. Thorum, Inorg. Chem., **49**, 3557–3566 (2010).

[107] B. C. H. Steele, A. Heinzel, Nature, **414**, 345–352 (2001).

[108] D. J. Berger, Science, **286**, 49–50 (1999).

[109] A. Halder, S. Sharma, M. S. Hegde, N. Ravishankar, J. Phys. Chem. C, **113**, 1466–1473 (2009).

[110] J. Chen, M. Wang, B. Liu, Z. Fan, K. Cui, Y. Kuang, J. Phys. Chem. B, **110**, 11775–11779 (2006).

[111] Y. Lin, X. Cui, C. Yen, C. M. Wai, J. Phys. Chem. B. Conden. Phase, **109**, 14410–14415 (2005).

[112] R. Bashyam, P. Zelenay, Nature, **443**, 63–66 (2006).

[113] P. J. Ferreira, G. J. la O', Y. S. Horn, D. Morgan, R. Makharia, S. Kocha, H. A. Gasteigerc, J. Electrochem. Soc., **152**, A2256–A2271 (2005).

[114] L. Zhang, J. Zhang, D. P. Wilkinson, H. Wang, J. Power Sources, **156**, 171–182 (2006).

[115] Y. Shao, G. Yin, Y. Gao, P. Shi, J. Electrochem. Soc. **153**, A1093– A1097 (2006).

[116] Z. Q. Tian, S. P. Jiang, Y. M. Liang, P. K. Shen, J. Phys. Chem. B, **110**, 5343–5350 (2006).

[117] M. Wakizoe, O. A. Velev, S. Srinivasan, Electrochim. Acta, **40**, 335–336 (1995).

[118] M. Winter, R. J. Brodd, Chem. Rev. **104**, 4248–4249 (2004).

[119] B. Cook, An Introduction to fuel cells and hydrogen technology, Heliocentris, Vancouver, Canada. 2001.

[120] K. Lee, J. Zhang, H. Wang, D. Wilkinson, J. Applied Electrochem., **36**, 507–522 (2006).

[121] R. Yu, L. Chen, Q. Liu, J. Lin, K. L. Tan, S. Ng, H. Chan, G. Q. Xu, T. S. Hor, Chem. Mat., **10**, 718–722 (1998).

[122] W. Chen, Y. Lee, Z. Liu, Chem. Commun., **21**, 2588–2589 (2002).

[123] M. W. Smith, J. Friedrich, S. Rigby, T. Ralph, F. Walsh, J. Phys. D. Apply. Phys., **41**, 174004–174005 (2008).

[124] Y. Garsany, Anal. Chem., **82**, 6321–6328 (2010).

[125] K. Cooper, Fuel Cell Testing and Diagnostics: Theory and Application, Scribner Associates Incorporated, North Carolina, USA. www. scribner.com.

Chapter 2

Method of Study

2.1 X-ray Photoelectron Spectroscopy

X-ray photoelectron spectroscopy (XPS) is a widely used for investigating the elemental and chemical composition of solid surface. The photoelectron spectrum provides much information on electron binding energy, shift in binding energy (chemical shift), and concentration of elements. XPS is thus extensively applied to research in solid state physics and solving the problems related to surfaces and interfaces [1]. Surface analysis by XPS involves irradiating a solid in vacuum with mono-energetic soft X-rays and analyzing the emitted electrons by energy. The spectrum is obtained as a plot of the number of detected electrons per energy interval versus their kinetic energy. Each element has a unique spectrum. The spectrum from a mixture of elements is approximately the sum of the peaks of the individual constituents. Because the mean free path of electrons in solids is very small, the detected electrons originate from only the top few atomic layers, making XPS a unique surface sensitive technique for chemical analysis. Quantitative data can be obtained from peak heights or peak areas, and identification of chemical states often can be made from exact measurement of peak positions and separations, as well as from certain spectral features [2].

2.1.1 Principle of XPS

The surface analysis by XPS is accomplished by irradiating a sample with mono-energetic soft X-rays and analyzing the energy of the detected electrons. The principle of XPS is based on the interaction between an electromagnetic wave and a material (atoms). Since the XPS spectrum directly reflects the electronic structure of a material, it provides information on electron configuration and energy levels within atoms. The process of photoelectron emission from a solid is divided into three stages (three steps model) [1]:

(1) First, X-rays are absorbed by atoms, and photoelectrons are emitted (photoelectron emission process).
(2) Next, part of the photoelectrons generated within a solid move toward the surface (electron attenuation length (escape depth)).
(3) Then, the photoelectrons which have reached the surface are emitted into a vacuum (work function).

In XPS, the energy conservation rule is hold between the energy of the excitation X-rays *hv*, the electron binding energy E_b, the kinetic energy of emitted photoelectrons E_k, and the work function Ø, depending on both material and spectrometer. Therefore, the photoelectrons have kinetic energies as the following

equation) (2-1):

$$E_k = h\nu - E_b - Ø \qquad (2–1)$$

Further, the energy diagram of photoelectron emission on carbon atom is shown in Figure 2.1.

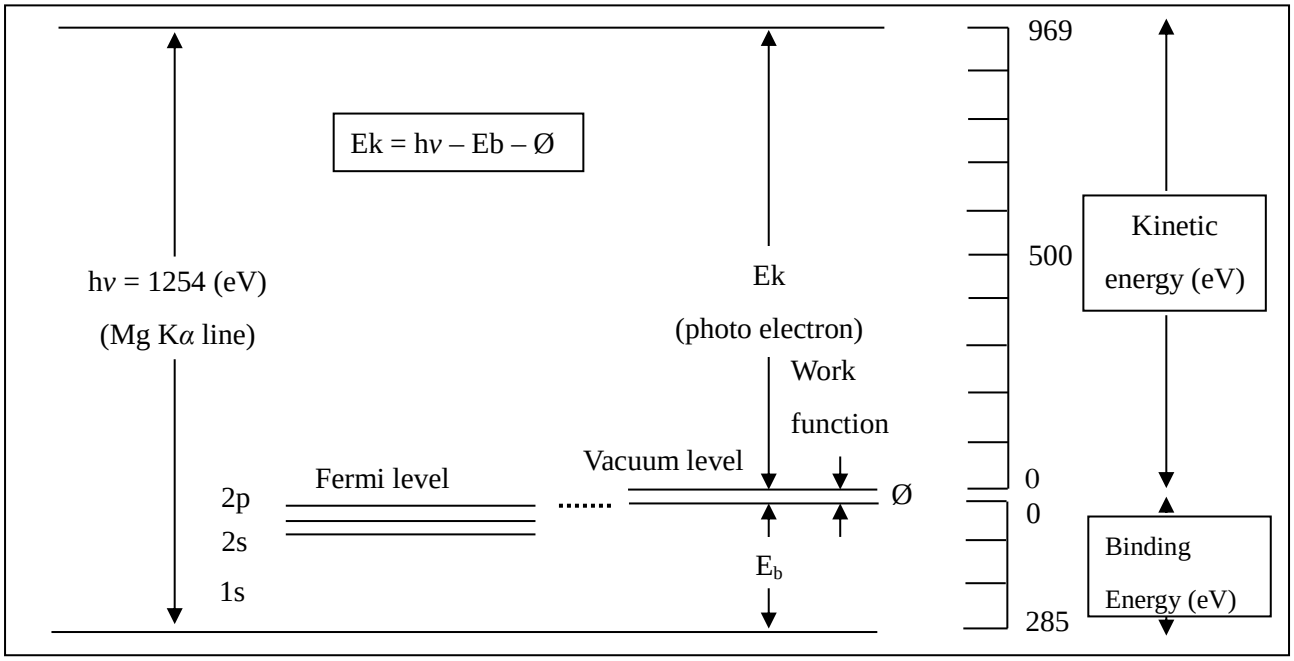

Figure 2.1 Energy diagram of photoelectron emission on carbon atom [1].

Where, the Fermi level corresponds to zero binding energy. E_b is defined by the difference between the total energy at the initial state and that at the final state of photoelectron emission process. The E_b is therefore determined by measuring the kinetic energy of the emitted photoelectrons. It slightly differs depending on the chemical environment of atoms, thus XPS allows the chemical state analysis of a material.

The XPS technique yields quantitative and qualitative information. Quantitative information arises from the element specificity of the binding energies and the relation between the intensity of the photoelectron peaks and the element concentration. Qualitative information is obtained from the energy position of a photoelectron peak with respect to the energy position of the same level in a reference compound (chemical shift) [3]. Chemical shifts of binding energies for a certain element level are due to different oxidation states and chemical environments. The energy of atom is divided into two terms, one associated with the net charge on the probe atom and the other term associated with the charge distribution of the surrounding atoms. Both terms are considered as “initial state effect” since they refer only to the electrostatic potential experienced by the core electron in the ground state before ionization [4].

2.1.2 Experimental apparatus

XPS is one of number surface analytical techniques that bombard the sample with photons, electrons or ions in order to excite the emission of photons, electrons or ions. In XPS, the sample is irradiated with low energy (~ 1.5 keV) X-rays, in order to provoke the photoelectric effect. The schematic diagram of the XPS apparatus is shown in Figure 2.2. The energy spectrum of the emitted photoelectrons is determined by means of a high resolution electron spectrometer.

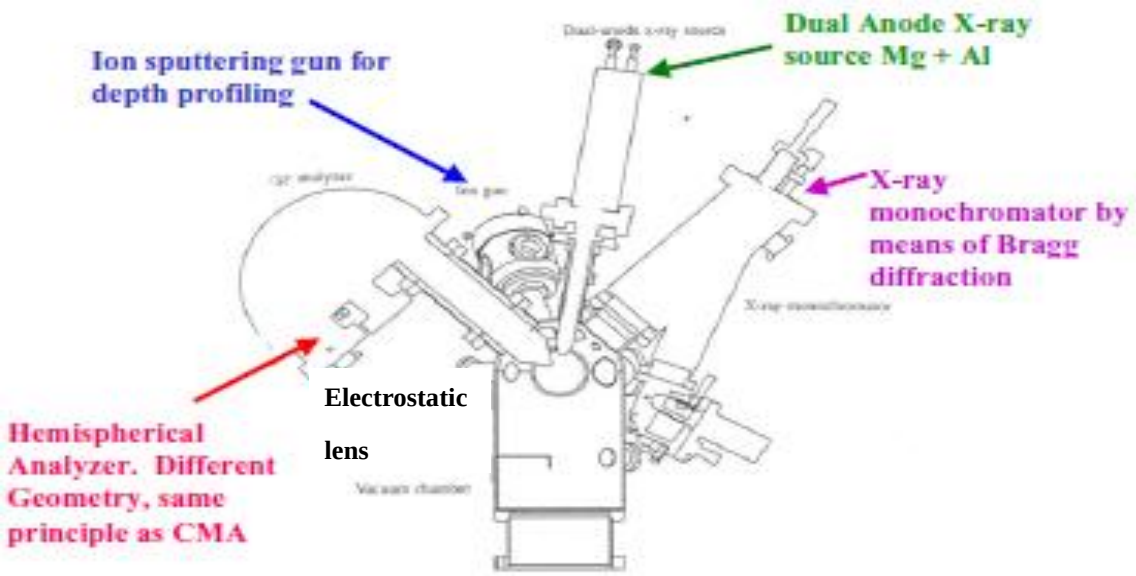

Figure 2.2 A schematic diagram of the PHI Model 5600 Multi Technique system [2].

The main components of a XPS instrument are the X-ray source, the electron energy analyzer, the electron detector and an efficient pumping system for the high vacuum requirement (Figure 2.3). The sample analysis is conducted in a vacuum chamber, under the best vacuum conditions achievable, typically ~ 10^{-10} torr. A photoelectron spectrometer, used to acquire the spectra, is composed of two chambers; an analyzing chamber and a preparation chamber (Figure 2.2). The analyzing chamber consists of an electron optic system to detect photoelectrons, an Mg/Al dual target X-ray tube, and a 4-axis stage (X, Y, Z, and T). The preparation chamber is equipped with a Kaufman type ion gun. A sample is transferred between the analyzing chamber and preparation chamber by a magnetic loader. The electron optic system consists of an electrostatic lens with a large incident solid angle, and electrostatic hemispherical analyzer with a center trajectory radius of 100 mm, and a multi-detection system with micro-channel plates. Electrons emitted from the surface of a sample are collected by electrostatic lens and then energy analyzed by the hemispherical analyzer. Two operating methods are available; one is to hold constant analyzer pass energy (E_0, CAE mode),

and the other is to hold constant the ratio between the kinetic energy (E) of electrons and the pass energy (E_0/E, CRR mode). In XPS, the CAE mode is normally used since it maintains a constant energy resolution of the analyzer across the entire energy region in the spectrum. In this mode, however, the analyzer transmission, which varies according to the energy of electrons, must be taken into consideration when making quantitative analysis [1]. The laboratory conventional source consists of an X-ray tube where X-rays are generated by electron bombardment of magnesium (Mg) or aluminium (Al) from which the K_α radiation is produced [3]. Typical diagram structure of an X-ray source (dual Mg and Al K_α source) can be seen in Figure 2.3.

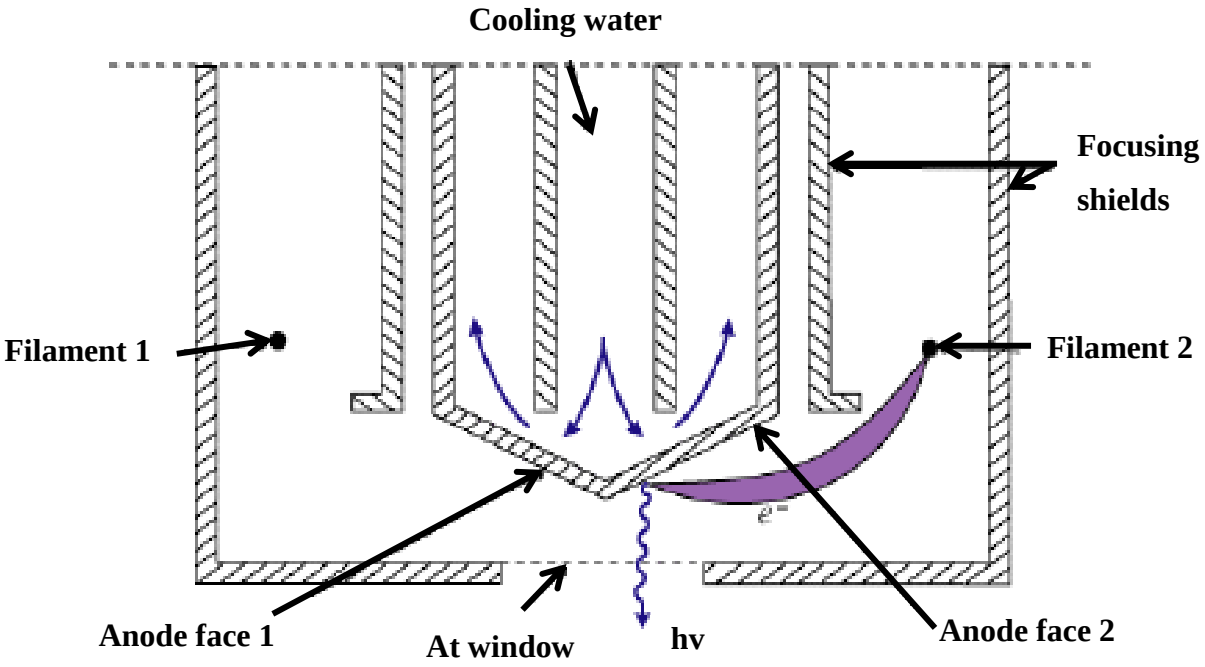

Figure 2.3 X-ray sources [5].

The end of the Cu supported anode has two angled faces. One of the faces is coated by a film of Al and the other is coated by that of Mg (typically ~ 10 μm in thickness). Beside the anodes, two filaments can be found in Figure 2.3. These filaments and the surrounding shields are at the ground potential. A high accelerating potential (up to + 15 kV) is applied to the anode during operation. The bombarding current (or emission current) on the anode is typically 5, 10, or 20 mA. Electrons of the filament bombard the anode face. Then soft X-rays will be generated. The X-rays pass through an aperture in the surrounding cylindrical shield, covered with a thin (~ 2 μm) sheet of Al foil. It is necessary to screen the sample from stray electrons, in order to minimize any heating effects and contamination originating in the source [6,7].

2.2 Analysis of XPS spectra [1]

2.2.1 Qualitative analysis

In qualitative analysis, attention is first directed to the positions of photoelectron peaks with relatively high intensities in an element. Other peaks with minor intensities, Auger electron peaks, and satellite peaks are then examined to identify the element. Where, the Auger electron peaks (KLL and LMM) as well as photoelectron peaks corresponding to various energy levels (1s, 2s, 2p, etc). Qualitative analysis is often made easier when the features of photoelectron, Auger electron, and satellite peaks are known in advance. The auger electron peaks are generally broader than photoelectron peaks. This is mainly due to the overlapping of several transitions and a very short relaxation process. Auger electron peaks shift relative to the energy of the X-ray source on the binding energy scale, since the kinetic energy of Auger electron is determined by energy levels within an atom, and is not dependent on the energy of the X-ray source. For example, when the source is changed from Mg K_α to Al K_α, Auger peaks shift to the high binding energy side by 233 eV.

The photoelectron peaks often give rise to chemical shifts and sometimes accompany satellite peaks, reflecting differences in the chemical environment of atoms. The chemical shifts in a photoelectron spectrum are frequently used to estimate the chemical state of elements. If the chemical shift is large enough to distinguish between peaks, each peak is identified by the peak position. When the chemical shift and full width half maximum (FWHM) are almost identical, the spectrum often has overlapping peaks. In such a case, peaks are separated to represent different chemical states. The chemical shift can be interpreted qualitatively by effective charge on an atom. When the atom bonded to another with larger electronegativity, its effective charge becomes positive to enlarge the binding energy, while the binding energy of the counterpart atom shifts to lower energy.

2.2.2 Quantitative analysis

Peak intensity in photoelectron spectrum due to an element is generally determined by three major factors: photoionization cross section (σ), electron mean free path (λ), and analyzer transmission (T). The peak intensity (I_i) of element *i* in a uniform sample is expressed in the following equation.

$$I_i = C_i \times \sigma \times (\sigma_0, \alpha, \beta) \times \lambda\,(s, E_i) \times T\,(E_i) \qquad (2\text{–}2)$$

where C_i is the concentration of element *i*, σ_0 the total photoionization cross section, α is the angle between the directions of photon (X-ray) incidence and photoelectron emission, β is the asymmetry parameter

indicating the angle dependence of emitted photoelectrons, and E_i the kinetic energy of electrons from element *i*.

2.3 X-ray diffraction (XRD)

XRD is a rapid analytical technique primarily used for phase identification of a crystalline material and can provide information on unit cell dimensions. Because the wavelength of the X-rays is comparable to the size of the atoms, they are ideally suited for the probing the structure arrangement of atoms and molecules in a wide range of materials. Diffraction of X-rays or neutrons by polycrystalline samples is one of the most important, powerful and widely used analytical techniques available to materials scientists. For most crystalline substances of technological importance, the bulk properties of a powder or a polycrystalline solid, averaged throughout the sample, are required; in general a single-crystal data, even if they can be obtained, are usually of little interest except for determination of the crystal structure or for studying some other fundamental physical property. In the main, powder diffraction is part of a wider investigation of physical, chemical or mechanical properties of materials. It is also interdisciplinary in nature, a technique which is equally applicable to a study of the behavior of semiconductors and superconductors, for example, as metal alloys, catalysts, minerals, pharmaceutical substances or polymers. Of the many applications of powder diffraction, the most significant advance in recent years has been the determination of crystal structures from powder data. XRD is a versatile, non-destructive analytical technique that reveals detailed information about the chemical composition and type of molecular bond of crystalline phase. It is an efficient technique to expose the crystallographic structure of natural and manufactured materials and a technique in which analytical results are correlated with references and standards of International Centre for Diffraction Data (ICDD). In addition, the other advantages of XRD are precise phase determination of solid materials; the X-ray spectra generated provide a structural fingerprint of the unknown, determination of material characteristic and the highest quality and reproducibility [8].

2.3.1 Principle of XRD

Diffraction is a scattering phenomenon. When X-rays are incident on crystalline solids, they are scattered in all directions. In some of these directions, the scattered beams are completely in phase and reinforce one another to form the diffracted beams. The Bragg's law describes the conditions under which this would occur. It is assumed that a perfectly parallel and monochromatic X-ray beam, of wavelength λ, is incident on a crystalline sample at an angle θ. The concept of X-ray diffraction can be described by the Bragg's law [9]:

$$n\lambda = 2d \sin\theta \qquad (2–3)$$

where *n* is a numeric constant known as the order of the diffracted beam, λ is the wavelength of the beam, *d* denotes the distance between lattice planes, and θ represents the angle of the diffracted wave.

This law relates the wavelength of electromagnetic radiation to the diffraction angle and the lattice spacing in a crystalline sample. These diffracted X-rays are then detected, processed and counted. By scanning the sample through a range of 2θ angles, all possible diffraction directions of the lattice should be attained due to the random orientation of the powdered material. Conversion of the diffraction peaks to d-spacing allows identification of the mineral because each mineral has a set of unique d-spacing. Typically, this is achieved by comparison of d-spacing with standard reference patterns.

2.3.2 XRD instrumentation and application [10,11]

X-ray diffractometers consist of three basic elements: an X-ray tube, a sample holder, and an X-ray detector. X-rays are generated in a cathode ray tube by heating a filament to produce electrons, accelerating the electrons toward a target by applying a voltage, and bombarding the target material with electrons. When electrons have sufficient energy to dislodge inner shell electrons of the target material, characteristic X-ray spectra are produced. These spectra consist of several components, the most common being K_α and K_β. K_α consists, in part, of $K_{\alpha 1}$ and $K_{\alpha 2}$. $K_{\alpha 1}$ has a slightly shorter wavelength and twice the intensity as $K_{\alpha 2}$. The specific wavelengths are characteristic of the target material (Cu, Fe, Mo, Cr). Filtering, by foils or crystal monochromators, is required to produce monochromatic X-rays needed for diffraction. $K_{\alpha 1}$ and $K_{\alpha 2}$ are sufficiently close in wavelength such that a weighted average of the two is used. Copper is the most common target material for single-crystal diffraction, with Cu K_α radiation = 1.5418 Å. These X-rays are collimated and directed onto the sample. As the sample and detector are rotated, the intensity of the reflected X-rays is recorded. When the geometry of the incident X-rays impinging the sample satisfies the Bragg's equation, constructive interference occurs and a peak in intensity occurs. A detector records and processes this X-ray signal and converts the signal to a count rate which is then output to a device such as a printer or computer monitor. The geometry of an X-ray diffractometer is such that the sample rotates in the path of the collimated X-ray beam at an angle θ while the X-ray detector is mounted on an arm to collect the diffracted X-rays and rotates at an angle of 2θ. The instrument used to maintain the angle and rotate the sample is termed a *goniometer*. For typical powder patterns, data is collected at 2θ from ~ 5 to 90 °, angles that are preset in the X-ray scan.

XRD is most widely used for the identification of unknown crystalline materials (e.g. minerals, inorganic compounds). Determination of unknown solids is critical to studies in geology, environmental science, material science, engineering and biology. The other applications include: characterization of crystalline materials, identification of fine-grained minerals such as clays and mixed layer clays that are

difficult to determine optically, determination of unit cell dimensions and measurement of sample purity. With specialized techniques, XRD also can be used to determine crystal structures using Rietveld refinement determine of modal amounts of minerals (quantitative analysis) characterize thin films samples by (determining lattice mismatch between film and substrate and to inferring stress and strain; determining dislocation density and quality of the film by rocking curve measurements; measuring superlattices in multilayered epitaxial structures, and determining the thickness, roughness and density of the film using glancing incidence X-ray reflectivity measurements) and make textural measurements, such as the orientation of grains, in a polycrystalline sample. Thereby, the XRD has several strengthens, such as (i) powerful and rapid (< 20 min) technique for identification of an unknown mineral, (ii) in most cases, it provides an unambiguous mineral determination, (iii) minimal sample preparation is required, (iv) XRD units are widely available and (v) data interpretation is relatively straight forward. However, XRD still has the limitations properties, namely (i) homogeneous and single phase material is best for identification of an unknown, (ii) must have access to a standard reference file of inorganic compounds (d-spacing, *hkl*), (iii) requires tenths of a gram of material which must be ground into a powder, (iv) for mixed materials, detection limit is ~ 2 % of sample, (v) for unit cell determinations, indexing of patterns for non-isometric crystal systems is complicated, and (vi) peak overlay may occur and worsens for high angle reflections.

2.4 Transmission electron microscope (TEM) [12]

Microscopy involves the study of objects that are too small to be examined by the unaided eye. In the SI (metric) system of units, the sizes of these objects are expressed in terms of sub-multiples of the meter, such as the micrometer (1 μm = 10^{-6} m, also called a micron) and also the nanometer (1 nm = 10^{-9} m). In a TEM, electrons penetrate a thin specimen and are then imaged by appropriate lenses. The TEM has proved invaluable for examining the ultrastructure of metals. For example, crystalline defects known as dislocations were first predicted by theorists to account for the fact that metals deform under much lower forces than calculated for perfect crystalline array of atoms. With a modern TEM (resolution ≈ 0.2 nm), it is even possible to image individual atomic planes or columns of atoms. The TEM has been equally useful in the life sciences, for example examining plant and animal tissue, bacteria, and viruses. The TEM is capable of displaying magnified images of a thin specimen, typically with a magnification in the range 10^3 to 10^6. In addition, the instrument can be used to produce electron-diffraction patterns, useful for analyzing the properties of a crystalline specimen. This overall flexibility is achieved with an electron-optical system containing an electron gun (which produces the beam of electrons) and several magnetic lenses, stacked vertically to form a lens column. It is convenient to divide the instrument into three sections, which we first define and then study in some detail separately. Those are (i) the illumination system comprise the electron

gun, together with two or more condenser lenses that focus the electrons onto the specimen. Its design and operation determine the diameter of the electron beam (often called the "illumination") at the specimen and the intensity level in the final TEM image, (ii) the specimen stage allows specimens to either be held stationary or else intentionally moved, and also inserted or withdrawn from the TEM. The mechanical stability of the specimen stage is an important factor that determines the spatial resolution of the TEM image, and (iii) the imaging system contains at least three lenses that together produce a magnified image (or a diffraction pattern) of the specimen on a fluorescent screen, on photographic film, or on the monitor screen of an electronic camera system. How this imaging system is operated determines the magnification of the TEM image, while the design of the imaging lenses largely determines the spatial resolution that can be obtained from the microscope. The schematic diagram of a TEM instrument is shown in Figure 2.4.

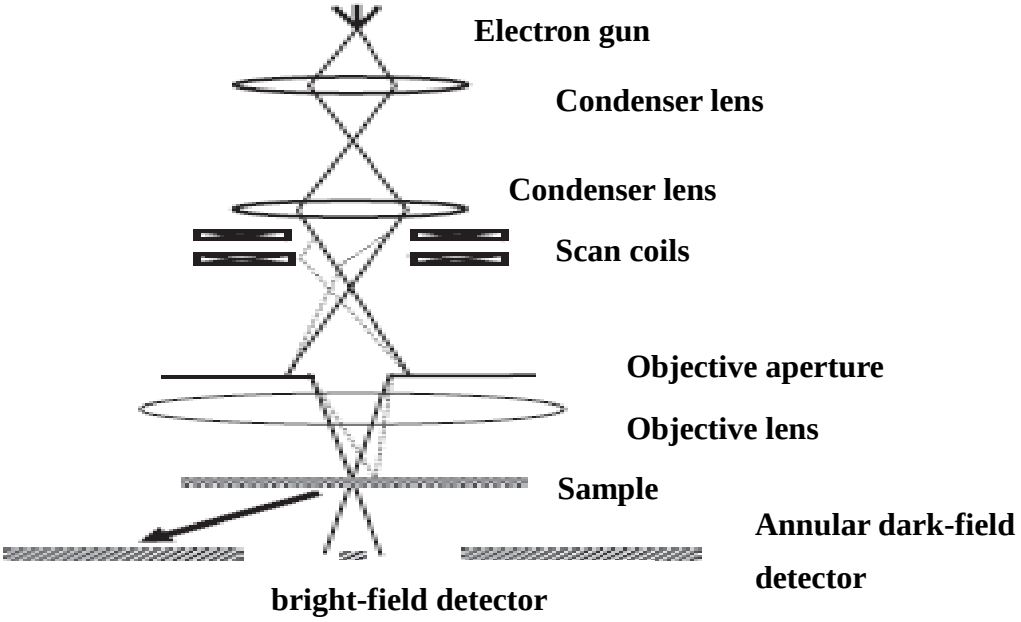

Figure 2.4 TEM instrument diagram.

2.4.1 TEM instrument

(1) Electron gun

The electron gun produces a beam of electrons whose kinetic energy is high enough to enable them to pass through thin areas of the TEM specimen. The gun consists of an electron source, also known as the cathode because it is at a high negative potential, and an electron-accelerating chamber. There are several types of electron source and operating on different physical principles. The electron source is a V-shaped (hairpin) filament made of tungsten (W) wire, spot-welded to straight-wire leads that are mounted in a ceramic or glass socket, allowing the filament assembly to be exchanged easily when the filament eventually burns out. A direct current (dc) heats the filament to about 2700 K, at which temperature tungsten emits

electrons into the surrounding vacuum by the process known as thermionic emission. The process of thermionic emission can be illustrated using electron energy diagram (Figure 2.5).

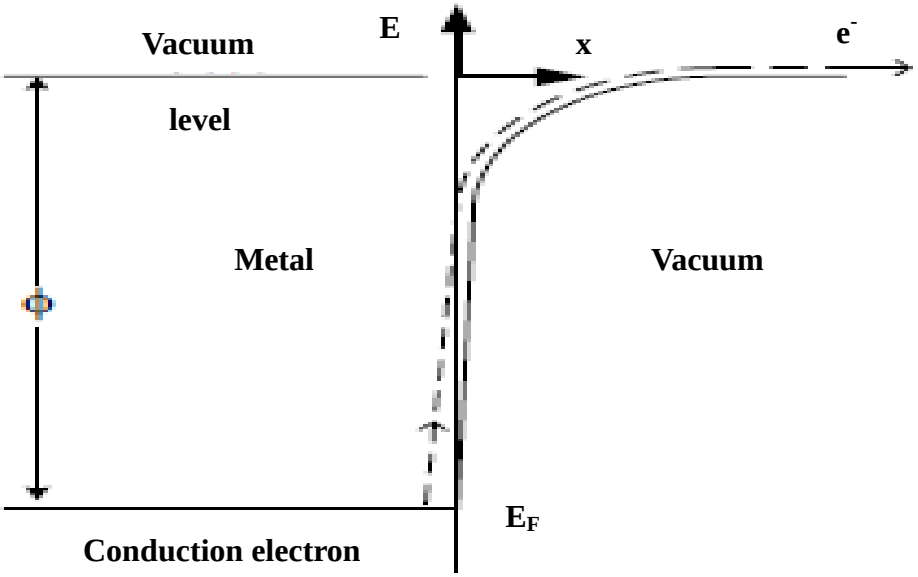

Figure 2.5 Electron energy-band diagram of a metal, for the case where no electric field is applied to its surface. The process of thermionic emission of an electron is indicated by the dashed line.

In which the vertical axis represents the energy *E* of an electron and the horizontal axis represents distance *z* from the tungsten surface. Within the tungsten, the electrons of highest energy are those at the top of the conduction band, located at the Fermi energy E_F. These conduction electrons carry the electrical current within a metal; they normally cannot escape from the surface because E_f is an amount Ø (the work function) below the vacuum level, which represents the energy of a stationary electron, located a short distance outside the surface. As shown in Figure 2.5, the electron energy does not change abruptly at the metal/vacuum interface; when an electron leaves the metal, it generates lines of electric field that terminate on positive charge (reduced electron density) at the metal surface. This charge provides an electrostatic force toward the surface that weakens only gradually with distance. Therefore, the electric field involved and the associated potential (and potential energy of the electron) also fall off gradually outside the surface. Raising the temperature of the cathode causes the nuclei of its atoms to vibrate with increasing amplitude. Because the conduction electrons are in thermodynamic equilibrium with the atoms, they share this thermal energy, and a small proportion of them achieve energies above the vacuum level, enabling them to escape across the metal/vacuum interface.

(2) Electron acceleration

After emission from the cathode, electrons are accelerated to their final kinetic energy E_0 by means of an electric field parallel to the optic axis. This field is generated by applying a potential difference V_0 between the cathode and an anode, a round metal plate containing a central hole (vertically below the cathode) through which the beam of accelerated electrons emerges. Many of the accelerated electrons are absorbed in the anode plate and only around 1 % passes through the hole, so the beam current in a TEM is typically 1 % of the emission current from the cathode. To produce electron acceleration, it is only necessary that the anode be positive relative to the cathode.

(3) Condenser lens system

The TEM may be required to produce a highly magnified (e.g. M = 10^5) image of a specimen on a fluorescent screen, of diameter typically 15 cm. To ensure that the screen image is not too dim, most of the electrons that pass through the specimen should fall within this diameter, which is equivalent to a diameter of (15 cm)/M = 1.5 μm at the specimen. For viewing larger areas of specimen, however, the final-image magnification might need to be as low as 2000, requiring an illumination diameter of 75 μm at the specimen. In order to achieve the required flexibility, the condenser-lens system must contain at least two electron lenses. The first condenser (C_1) lens is a strong magnetic lens, with a focal length (f) that may be as small as 2 mm. To use the virtual electron source (diameter d_s) as its object, C_1 produces a real image of diameter d_1. The second condenser (C_2) lens is a weak magnetic lens (f ≈ several centimeters) that provides little or no magnification (M ≈ 1) but allows the diameter of illumination (d) at the specimen to be varied continuously over a wide range. The C_2 lens also contains the condenser aperture (the hole in the condenser diaphragm) whose diameter d can be changed in order to control the convergence semi-angle α of the illumination, the maximum angle by which the incident electrons deviate from the optic axis.

(4) Specimen stage

The specimen stage is designed to hold the specimen as stationary as possible, as any drift or vibration would be magnified in the final image, impairing its spatial resolution (especially if the image is recorded by a camera over a period of several seconds). But in order to view all possible regions of the specimen, it is also necessary to move the specimen horizontally over a distance of up to 3 mm if necessary. To allow observation in different brands or models of microscope, TEM specimens are always made circular with a diameter of 3 mm. Perpendicular to this disk, the specimen must be thin enough (at least in some regions) to allow electrons to be transmitted to form the magnified image. The design of the stage must also allow the

specimen to be inserted into the vacuum of the TEM column without introducing air. This is achieved by inserting the specimen through an airlock, a small chamber into which the specimen is placed initially and which can be evacuated before the specimen enters the TEM column. Not surprisingly, the specimen stage and airlock are the most mechanically complex and precision machined parts of the TEM. There are two basic designs of the specimen stage: side-entry and top-entry. In a side-entry stage, the specimen is clamped (for example, by a threaded ring) close to the end of a rod-shaped specimen holder and is inserted horizontally through the airlock. One advantage of this side-entry design is that it is easy to arrange for precision motion of the specimen. A further advantage of the side-entry stage is that heating of a specimen is easy to arrange, by installing a small heater at the end of the specimen holder, with electrical leads running along the inside of the holder to a power supply located outside the TEM. In a top-entry stage, the specimen is clamped to the bottom end of a cylindrical holder that is equipped with a conical collar**.** The holder is loaded into position through an airlock by means of a sliding and tilting arm, which is then detached and retracted.

(5) TEM imaging system

The imaging lenses of a TEM produce a magnified image or an electron diffraction pattern of the specimen on a viewing screen or camera system. The spatial resolution of the image is largely dependent on the quality and design of these lenses, especially on the first imaging lens: the objective. As in the case of a light-optical microscope, the lens closest to the specimen is called the objective. It is a strong lens, with a small focal length; because of its high excitation current, the objective must be cooled with temperature controlled water, thereby minimizing image drift that could result from thermal expansion of the specimen stage. Because focusing power depends on lens excitation, the current for the objective lens must be highly stabilized, using negative feedback within its *dc* power supply. The power supply must be able to deliver substantially different lens currents, in order to retain the same focal length for different electron-accelerating voltages. The TEM also has fine controls that enable the operator to make small fractional adjustments to the objective current, to allow the specimen image to be accurately focused on the viewing screen. The other parts of TEM imaging system are (i) Objective aperture. An objective diaphragm can be inserted located at the back-focal plane (BFP) of the post-field of the objective lens, the plane at which a diffraction pattern of the specimen is first produced. In this plane, distance from the optic axis represents the direction of travel (angle relative to the optic axis) of an electron that has just left the specimen, (ii) Objective stigmator. The stigmator controls are adjusted to minimize this streaking effect, (iii) Selected-area aperture**.** This selected-area diffraction (SAD) diaphragm is used to limit the region of specimen from which an electron diffraction pattern is recorded, (iv) Intermediate lens. The intermediate serves two purposes. First of all, by changing its focal length in small steps, its image magnification can be

changed, allowing the overall magnification of the TEM to be varied over a large range, typically 10^3 to 10^6. Second, by making a larger change to the intermediate lens excitation, an electron diffraction pattern can be produced on the TEM viewing screen, (v) Projector lens. The purpose of projector lens is to produce an image or a diffraction pattern across the entire TEM screen, with an overall diameter of several centimeters, and (vi) TEM screen and camera. To permanently record a TEM image or diffraction pattern, photographic film can be used. This film has a layer of a silver halide (AgI and/or AgBr) emulsion, similar to that employed in black and white photography; both electrons and photons produce a subtle chemical change that can be amplified by immersion in a developer solution. In regions of high image intensity, the developer reduces the silver halide to metallic silver, which appears dark. The recorded image is a therefore a photographic negative, whose contrast is reversed relative to the image seen on the TEM screen. An optical enlarger can be used to make a positive print on photographic paper, which also has a silver-halide coating.

(6) Vacuum system

It is essential to remove most of the air from the inside of a TEM column, so that the accelerated electrons can follow the principles of electron optics, rather than being scattered by gas molecules. In addition, the electron gun requires a sufficiently good vacuum in order to prevent a high voltage discharge and to avoid oxidation of the electron-emitting surface. A mechanical rotary pump (RP) is used in many vacuum systems. This pump contains a rotating assembly, driven by an electric motor and equipped with internal vanes separated by a coil spring so that they press against the inside cylindrical wall of the pump, forming an airtight seal. To produce a high vacuum ($\approx 10^{-3}$ Pa), a diffusion pump (DP) can be added. It consists of a vertical metal cylinder containing a small amount of a special fluid, a carbon or silicon-based oil having very low vapor pressure and a boiling point of several hundred degrees Celsius. Sometimes a turbo molecular pump (TMP), essentially a high speed turbine fan, is used in place of (or to supplement) a diffusion pump. Usually an ion pump (IP) is used to achieve pressures below 10^{-4} Pa, as required to operate a LaB_6, or field-emission electron source. By applying a potential difference of several kilovolts between large electrodes, a low pressure discharge is set up (aided by the presence of a magnetic field) which removes gas molecules by burying them in one of the electrodes. These different pumps must work together in the correct sequence. If the TEM column has been at atmospheric pressure (perhaps for maintenance), most of the air is removed by a rotary pump, which can then function as a backing pump for the DP, TMP, or IP. The pumping sequence is controlled by opening and closing vacuum valves in response to the local pressure, monitored by vacuum gauges located in different parts of the system. In a modern TEM, the vacuum system is automated and under electronic control; in fact, its circuit board can be the most complicated in the entire electronics of the microscope.

2.5 Electrochemistry

Electrochemistry is the science which deals with the consequences of the transfer of electric charge from one phase to another. An electrochemical reaction is a heterogeneous process which involves electron transfer across a phase boundary or interface. It is a heterogeneous process which involves electron transfer across a phase boundary or interface. Electron transfer occurs at interfaces between a metallic conductor (an electrode) and an ionic conductor (an electrolyte). Electrode contains mobile electrons. It acts as source or sink of electrons, such as metals: Pt, Au, Ni, Cu, Hg, non-metals: glassy carbon, graphite, semiconductors, metal oxides, and electroactive polymers: polypyrrole, polyaniline. On the other hand, electrolyte contains mobile ions, i.e. solvents and salts, aqueous solutions, non-aqueous solutions, solid electrolytes, and polymer electrolytes [13].

Electrochemical reactions are labeled as redox (oxidation/reduction) processes. The oxidation is the loss of electrons and reduction is the gain of electrons. The basic reaction in electrochemistry is denoted as below [14].

$$O_x + ne^- \longleftrightarrow \text{Red} \qquad (2\text{–}4)$$

where *Red*, *Ox* and *n* are reduced, oxidized species, and number of electrons in the reaction, respectively. The potential electrode (*E*) can be calculated by using Nernst equation (Equation 2-5), E_0 is redox standard potential, *R* (gas constant, 8.314 J mol^{-1} K), *F* is Faraday constant, *T*, absolute temperature (K) and the chemical activity is a product between concentration and activity coefficient (*aOx* and *aRed*).

$$E = E^0 + \frac{RT}{nF}\ln\frac{aO_x}{aRed} \qquad (2\text{–}5)$$

2.5.1 Basic principles

Electrochemical phenomena and processes are useful for the quantitative and qualitative chemical analysis of various substances and media, including liquids, gases, and solids. It is very convenient that electrical signals are used for the perturbation: current, potential, and that the result again is obtained as an electrical signal. The major groups of electrochemical methods for chemical analysis consist of (i) Conductometry, which measures the electrical conductivity of the electrolyte solution being examined, (ii) Coulometry, which measures the amount of charge (Q) consumed for the complete conversion (oxidation or reduction) of the substance being examined, (iii) Potentiometry, which measures the open circuit equilibrium potential of an indicator electrode, for which the substrate being examined is potential determining, and (iv) Voltammetry, which determines the steady state or transient polarization characteristics of electrodes in

reactions involving the substance being examined. Electrochemical methods of analysis are distinguished by their high sensitivity, selectivity, speed of the measurements, and other advantages [15].

Voltammetry is a widely electrochemical technique to measure the current as a function of the varied potential, i.e. cyclic voltammetry (CV) and linear sweep voltammetry (LSV) [15]. CV has the further attraction of providing information not only on the thermodynamics of redox processes but also on the kinetics of heterogeneous electron-transfer reactions and coupled chemical reactions. The characteristic shapes of the voltammetric waves and their unequivocal position on the potential scale virtually finger print the individual electrochemical properties of redox systems. For this reason the method has been labeled electrochemical spectroscopy. In cyclic voltammetry, mass transport of the reducible or oxidizable electroactive species occurs only by diffusion. This is measured with suitable equipment and recorded as a characteristic current-voltage curve for a cyclic voltammogram (Figure 2.6).

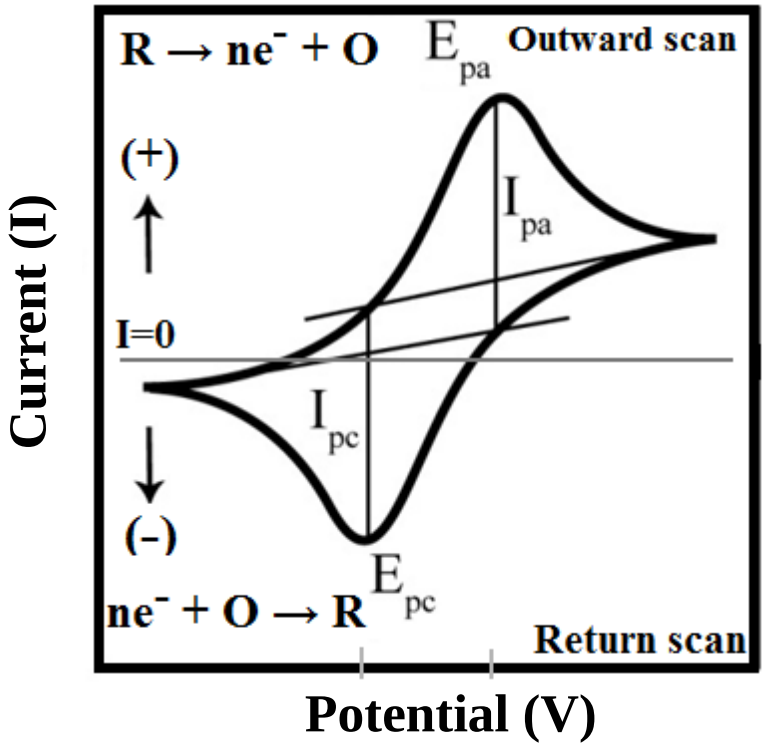

Figure 2.6 Cyclic voltammogram for a reversible charge transfer; E_{pc}: cathodic peak potential, E_{pa}: anodic peak potential, $\mathbf{i}_{pc}$: cathodic peak current, and $\mathbf{i}_{pa}$: anodic peak current [16].

As it is impossible to monitor absolute single electrode potentials, the working electrode (WE) potential ***E*** always refers to a non-polarized reference electrode (RE), e.g. Ag/AgCl or the saturated calomel electrode (SCE). If the currents are low and the solvent-electrolyte system has a high conductivity, this type of two-electrode cell is sufficient for voltammetric measuring. Its usage is well-known from classical polarography.

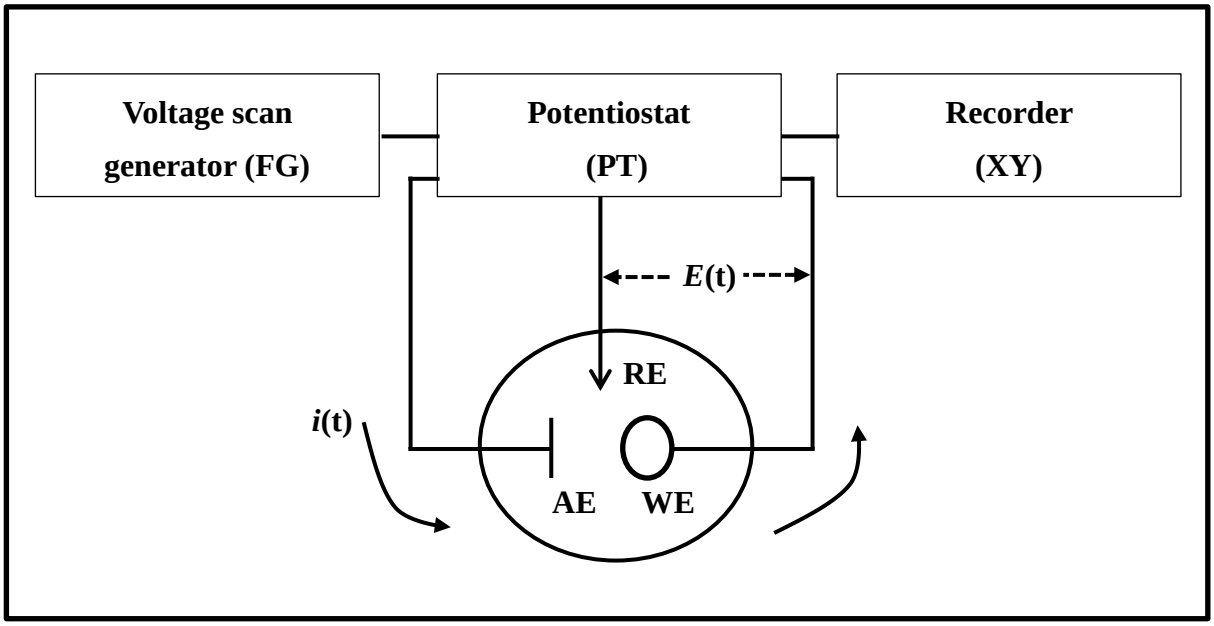

Figure 2.7 Schematic experimental setup for cyclic voltammetry. RE: reference electrode, WE: working electrode, AE: auxiliary electrode [16].

As shown in Figure 2.7, in this technique current is passed through the working and an additional auxiliary electrode (AE), while almost no current flows through the RE on account of its high impedance. In order to keep the existing uncompensated ***iR*** drop as small as possible, the reference electrode is placed as close as possible to the WE using a Luggin's capillary. Potentiostatic control ensures that the real potential ***E(t)*** at the WE with respect to the RE is, by and large, the same as the applied cell voltage generated by the function generator. Operational amplifiers in the control circuit adjust the current passing through the WE and AE until the potential ***E(t)*** corresponds to E_{appl} (applied cell voltage). Besides potentiostats with the electrochemical cell arrangement, the standard device for voltammetric experiments comprises a voltage scan generator, which supplies the desired potential program, as well as an **XY** recorder (or a suitable fast transient recorder) which registers the current-voltage curve.

2.5.2 Electrode reactions in CV experiment

The simplest Faradaic electrode reaction is the heterogeneous charge transfer from an electro-active species **A** to the electrode or vice versa, in which, dependent on the given electrode potential, **A** is either oxidized or reduced to **B** (electron-transfer mechanism : E mechanism).

$$A + e^- \overset{E}{\longleftrightarrow} B \qquad (2\text{–}6)$$

In order to simplify the theoretical analysis, only reduction processes will be discussed. Two processes determine the shape of the voltammetric current-voltage curve. These are heterogeneous charge transfer and diffusional mass transport. The heterogeneous charge-transfer at the electrode interface is described by the Butler-Volmer equation (Equation 2-7), the basic equation in electrochemical kinetics.

$$j_A(0,t) = \frac{i}{n\,FA} = C_A(0,t)k^0 exp\left[-\alpha\frac{nF}{RT}(E-E^0)\right] - C_B(0,t)k^0 exp\left[(1-\alpha)\frac{nF}{RT}(E-E^0)\right] \quad (2\text{–}7)$$

where k^0 = heterogeneous standard rate constant, α = transfer coefficient, E^0 = standard potential, A = electrode area, j = flux at the electrode interface, and F = Faraday constant. The equation 2-7 indicates that the measurable current density depends on the surface concentration of the redox partners involved the electrode potential (E_t), and the heterogeneous standard rate constant k^0. The standard potential E^o characterizes a situation in which the surface concentrations of the oxidized and reduced forms are equal under conditions of thermodynamic equilibrium. Because of the difference between the resulting potential-dependent surface concentrations C_A(O,t) and C_B(O,t) and the concentrations in the rest of the solution, a gradient emerges, along which diffusion controlled mass transport occurs. The time-dependent concentration distribution in the expanding diffusion layer can be derived from Fick's second law (Equation 2-8).

$$\frac{\partial c_i}{\partial t} = D_i\frac{\partial^2 C_i}{\partial x^2} \quad (2\text{–}8)$$

where i = A, B

If voltammetry is used for analytical purposes, an extremely large electrode area/volume ratio is often chosen to increase sensitivity, e.g., in inverse voltammetry or when working with thin-layer cells. Under these conditions, diffusion is no longer semi-infinite but finite, i.e. the thickness of the diffusion layer is limited by the volume, and this changes the characteristics of the diffusion gradient. The concentration gradient at the electrode surface is directly proportional to the charge flux (Equation 2-9).

$$j_A(0,t) = -D_A\left(\frac{\partial C_A}{\partial x}\right)_{x=0} = D_B\left(\frac{\partial C_B}{\partial x}\right)_{x=0} \quad (2\text{–}9)$$

Comparison of equations (2-7) and (2-9) shows that the measurable current at the WE has two components; one for the heterogeneous charge transfer and one for the mass transport [16].

2.5.3 CO stripping

The Pt surface area can be estimated by electrochemical stripping of carbon monoxide (CO) for an adsorbed monolayer. It is generally assumed that CO is bonded linearly to a single metal surface atom. Thus,

the electro-oxidation of an adsorbed monolayer of CO may be used for Pt surface area measurement. The electrochemically active surface area (ECSA) was determined by a Faradic charge of 420 μC cm^{-2} for CO adsorbs monolayer [17].

$$Pt_{ECSA}(cm^2 g^{-1}) = \frac{Q_{CO\ (\mu C)}}{420(\mu C\ cm^2)\cdot Pt\ loading(g)} \quad (2\text{–}10)$$

2.6 Electrocatalysis

Catalysis is a changing the reaction rate at which that equilibrium is approached, by promoting an alternative molecular reaction path (mechanism) with a lower activation energy (Figure 2.8).

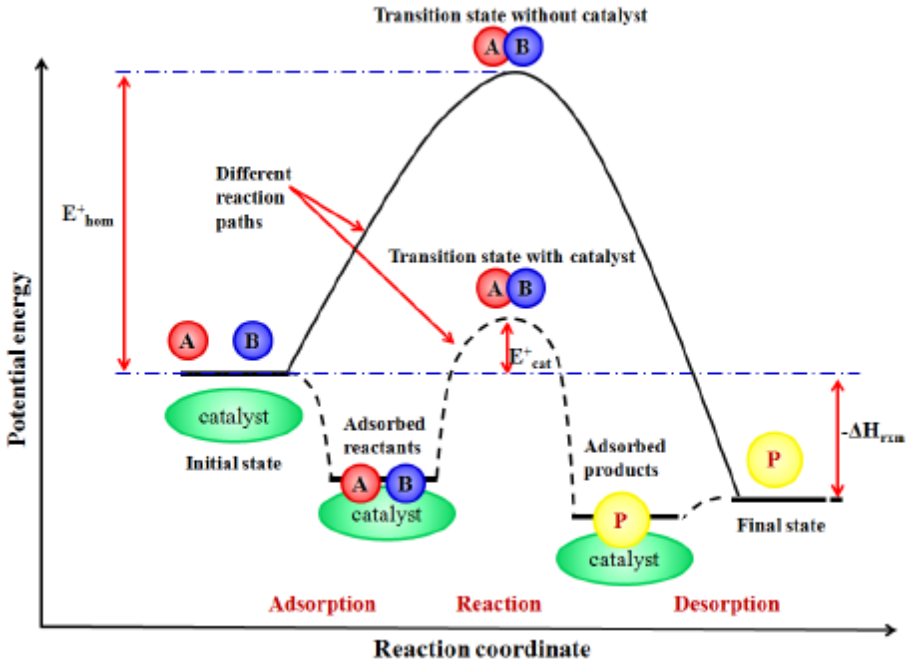

Figure 2.8 Schematic illustration of potential-energy diagram characterizing a simple chemical reaction in the presence or absence of a catalyst [18].

Figure 2.8 shows that the initial and final energies of reactant and product, respectively, are unaffected by the presence of catalyst (i.e. no change in enthalpy of reaction). In heterogeneous catalysis, the catalyst and reagents are in different phases.

The electrocatalysis means designing surfaces to obtain a high current density (i.e. high rate of conversion) close to the equilibrium potential (i.e. at low overpotential), and materials that allow practical current densities at low overpotential. Electrocatalysis is an important topic for electrochemical reactions; the electrode plays a catalytic role, being the donor of electrons for the cathodic reaction or the acceptor of electrons for the anodic reaction. Electrocatalysts are mainly metals and can commonly be an alloy, a metal

oxide, or a transition metal complex (either adsorbed or bonded to the substrate). Most electrode reactions require a substantial overpotential to drive them at a practical current density. In these cases, it may be that a new, low energy of activation route, from reactant to product, can be created by designing an appropriate surface that optimally stabilizes an adsorbed species. The catalysts for FCs are usually precious metals dispersed over a high surface area form of carbon and poisoned by the adsorption of an unwanted species on the surface. It is important to recognize that practical electrocatalysts must meet more criteria than simply giving a high current density at low overpotential The practical electrocatalysts/substrates should be considered: (i) no competing reactions (selectivity), (ii) availability as a high area coating on a substrate, (iii) stable (to corrosion) on-load, off-line and during switching, (iv) high mechanical stability, (v) performance maintained over long periods, and (vi) acceptable cost. Even now, electrocatalysts are still being developed and improved using guiding principles and largely empirical approaches. The general concepts are clear: the dominant role of adsorbed intermediates; selecting the catalyst material and using the environment of the surface atoms to tailor the electronic levels within the catalyst to give the optimum strength of adsorption; recognizing the importance of particular surface sites; geometric factors such as the spacing of active sites; and the importance of creating sites where the nearest neighbors are different atoms and creating surfaces with the highest number of active sites/unit area, thereby introducing cost efficiency into the use of the electrocatalyst [19].

References

[1] N. Ikeo, Y. Iijima, N. Niimura, M. Sigematsu, T. Tazawa, S. Matsumoto, K. Kojima, Y. Nagasawa, Handbook of X-ray Photoelectron Spectroscopy, JEOL, 1991.

[2] J. F. Moulder, W. F. Stickle, P. E. Sobol, K. D. Bomben, Handbook of X-ray Photoelectron Spectroscopy, Perkin Elmer Corporation, Minnesota, USA, 1992.

[3] A. M. Venezia, Catal. Today, **77**, 359–370 (2003).

[4] D. W. Davis, D. A. Shirley, J. Electron Spectr. Relat. Phenom., **3**, 137–138 (1974).

[5] K. Yates, A. Barrie, F. J. Street, J. Phys. E. Sci. Inst., **6**, 130 (1973).

[6] J. C. Vickerman, Surface analysis-the principal techniques, John Wiley and Sons, 1997.

[7] D. Briggs, M. Seah, Practical surface analysis, John Wiley and Sons, 1990.

[8] J. I. Langford, D. Louer, Rep. Prog. Phys., **59**, 131–234 (1996).

[9] A. R. Barron, Physical Methods in Chemistry and Nano Science, Houston, Rice University, USA, 2012.

[10] D. M. Moore, R. C. Reynolds, Jr., X-Ray diffraction and the identification and analysis of clay minerals, second edition, Oxford University Press, New York, 1997.

[11] H. P. Klug, L. E. Alexander, X-ray diffraction procedures for polycrystalline and amorphous materials, second edition, Wiley, New York, 1974.

[12] R. F. Egerton, Physical Principles of Electron Microscopy, An Introduction to TEM, SEM, and AEM, Springer, United States of America, 2005.

[13] P. Atkins, L. Jones, Chemical Principles, the quest for insight, fifth edition, W. F. Freeman, 2007.

[14] A. J. Bard, L. R. Faulkner, Electrochemical Methods: Fundamentals and Applications, second edition, John Wiley and Sons, New York, 2001.

[15] V. S. Bagotsky, Fundamentals of Electrochemistry, second edition, John Wiley and Sons, New Jersey, 2006.

[16] J. Heinze, Angewandte Chemie, **23**, 839–918 (1984).

[17] J. Zhang, H. Liu, Electrocatalysis of Direct Methanol Fuel Cells: From Fundamentals to Applications, Wiley-VCH, Weinheim, 2009.

[18] P. Atkins, J. D. Paula, Physical Chemistry, eight edition, Oxford University Press, Oxford, 2006.

[19] D. Pletcher, A First Course in Electrode Processes, second edition, RSC Publishing, Cambridge, 2010.

Chapter 3

Size Control to a Sub-Nanometer Scale in Platinum Catalysts on Graphene

In this chapter, size controlled Pt catalysts supported by graphene nano sheets (GNS) are prepared by changing loading of Pt at 10–70 wt % using an impregnation method was investigated. It is found that Pt subnano-clusters (0.8 nm) with an extremely large surface area (170 m^2 g^{-1}) are formed on the GNS support in a 10 wt % Pt/GNS catalyst. An increase in loading of Pt leads to an increase in the particle sizes of Pt, which results in lower activities for electro-oxidation of adsorbed CO. A core level shift of Pt 4f in XPS indicates that Pt is chemically interacted with graphene. The modification of catalytic properties and the electronic structure is ascribed to the interface interaction between Pt and graphene via π–d hybridization.

3.1 Introduction

Graphene, a flat monolayer of carbon atoms tightly packed into a two-dimensional honeycomb lattice, has attracted great interests from both fundamental science and applied research, because of its unusual electronic properties and unique character due to one-atom-thick planar sheet structure [1]. Recently, graphene nano sheets (GNS) have been applied to a support material for low temperature fuel cell catalysts [2]. The combination of the large surface area (theoretical value of 2630 m^2 g^{-1}), high conductivity (1250 S m^{-1}), unique graphitized basal plane structure, and potential low manufacturing cost makes GNS a promising candidate as low temperature fuel cell catalyst support [2].

The GNS-supported catalysts have mostly been evaluated for a potential application as anode materials in direct methanol and hydrogen fuel cells [2]. Generally, Pt and Pt-based catalysts supported on GNS present higher catalytic activities for methanol oxidation reaction (MOR) [3–5] and hydrogen oxidation reaction (HOR) [6] than those of catalysts supported on carbon blacks.

Platinum clusters on graphene have attracted considerable attention in theoretical studies [7–12] because modification in the electronic structure of Pt is expected, which may lead to an enhancement in the catalytic activity. The adsorption sites of Pt atoms, geometric structure of Pt clusters, the adsorption energy of Pt atoms, the magnetic properties, and the electronic structure of Pt have been reported on defect-free graphene, defective graphene [7,9], strained graphene, and nitrogen-doped graphene [9]. Stabilization of Pt clusters by graphene has been reported, which modifies the d-band structure and the magnetic properties [10] of Pt. Although small clusters of Pt have been extensively studied in theoretical studies, experimental works have not been studied in detail so far because the sizes of Pt particles of Pt/GNS catalysts in the literature are generally large as 2–5 nm [2]. On the other hand, in our group, Pt subnano-clusters are found to be formed on GNS [5], which are composed of 5–40 Pt atoms. They showed a high CO tolerance as an anode catalyst in H_2-O_2 polymer electrolyte fuel cells (PEFCs) [6]. The high CO tolerance has been ascribed to the interface interaction between Pt and graphene [5,6]. The reason why our group can synthesize Pt subnano-clusters is due to the preparation method. I have prepared Pt/GNS catalysts by an impregnation method, in which weak and strong reductions of platinum catalysts precursors are combined properly using ethanol and hydrogen. As has been reported previously, the proposed mechanism for the formation of Pt subnano-clusters includes the following pivotal surface reactions: the reduction into PtO_x particles (Pt^{2+}), the formation of isolated Pt atoms by H_2 reduction, followed by the formation of Pt subnano-clusters by the collision of the Pt single atoms migrating on GNS [13].

The importance in the study of graphene supported Pt catalysts lies in a control in the electronic structure of Pt by taking advantage of the Pt-C interaction, which probably varies as a function of Pt particle size. It is thus an interesting subject in experimental studies how to control the particle size of Pt on graphene at a sub-nanometer scale, which may further control the catalytic activity of Pt. If it is possible, the Pt

subnano-clusters on graphene will be a new type of Pt catalyst, whose electronic structure can be controlled by the Pt-C interaction.

In this study, I have first tried to control the particle size of Pt on GNS in a region from sub-nanometer to a few nanometers. I have successfully controlled the average particle size of Pt by changing loading of Pt on GNS. Then, I have studied the relationship among the Pt particle size, the catalytic activity, and the electronic structure of Pt on GNS by X-ray diffraction (XRD), transmission electron microscope (TEM), electrochemical measurements, and X-ray photoelectron spectroscopy (XPS).

3.2 Experimental

3.2.1 Synthesis of GNS

GNS were prepared from graphite powder (particle size pass 45 μm, Wako Pure Chemical Industries). First, graphite was oxidized to form graphite oxide [14]. Secondly, it was ultrasonicated into distilled water to form graphene oxide sheets. Finally, graphene oxide sheets were reduced by using hydrazine hydrate to produce GNS. The schematic of synthesis GNS is depicted in Figure 3.1.

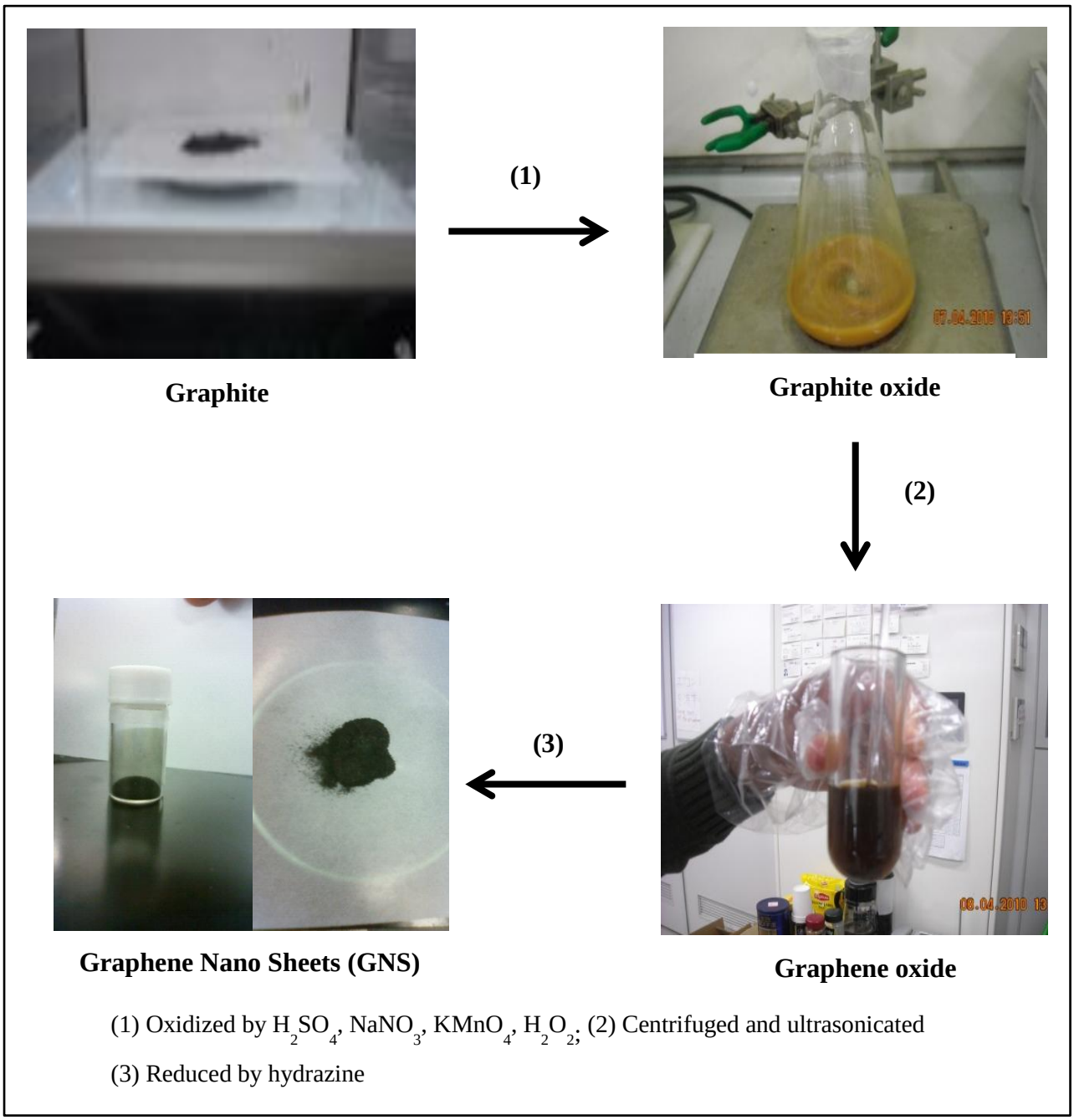

Figure 3.1 Schematic of GNS synthesis.

The formation of GNS is confirmed by XRD, XPS, and TEM, respectively. The XRD patterns of GNS are shown in (Figure 3.2).

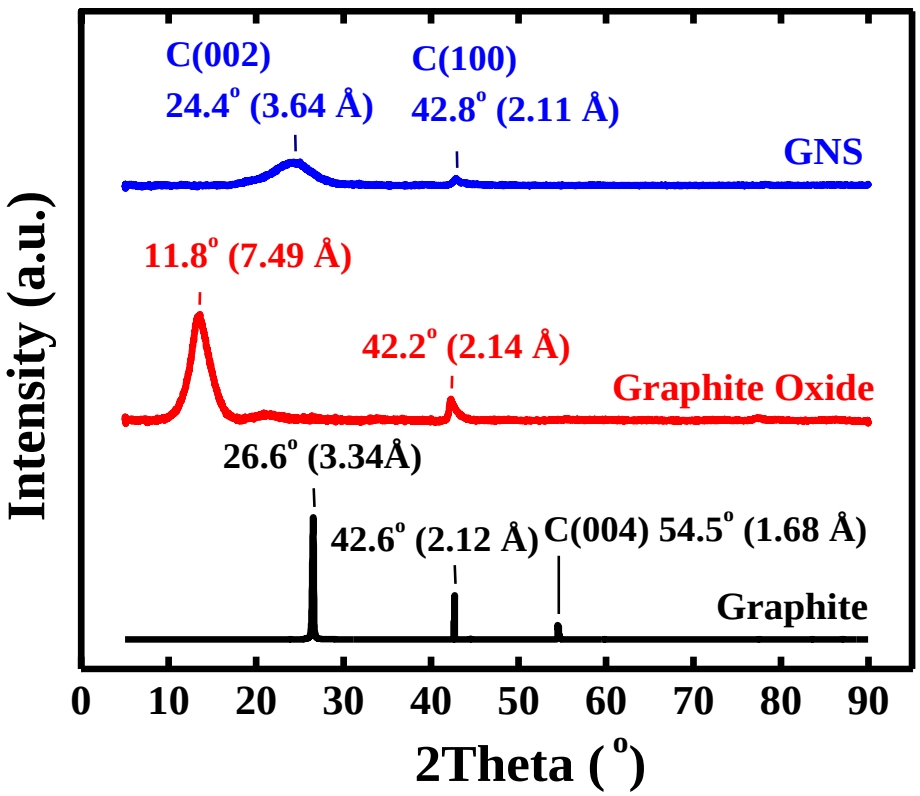

Figure 3.2 XRD patterns of graphite, graphite oxide and GNS, respectively.

Figure 3.2 shows XRD patterns exhibit C(002) peaks at various positions, meaning that the distances between graphene layers vary depending on the chemical treatments. The C(002) peak of graphite appeared at 2θ = 26.6° (3.34Å) as shown in Figure 3.2 in agreement with literature data. As for graphite oxide and GNS, C(002) peaks at 2θ = 11.8° (7.49 Å) and 2θ = 24.4° (3.64 Å) indicate a significant increase in the interlayer distance. After the reduction of graphite oxide by hydrazine, the graphite (002) peak turned to be very weak and broad, indicating graphene formation. Further, the binding energy of graphite, graphite oxide, and GNS, respectively, are obtained by XPS measurement. There is a difference in binding energy between graphite oxide and GNS. The peak at 284.6 eV is characteristic for graphite C 1s, while the peak at 286.6 eV indicates the formation of oxygen-containing carbon species such as carboxyl (COOH), carbonyl (C = O) or ether (C–O–C) species [15] (Figure 3.3).

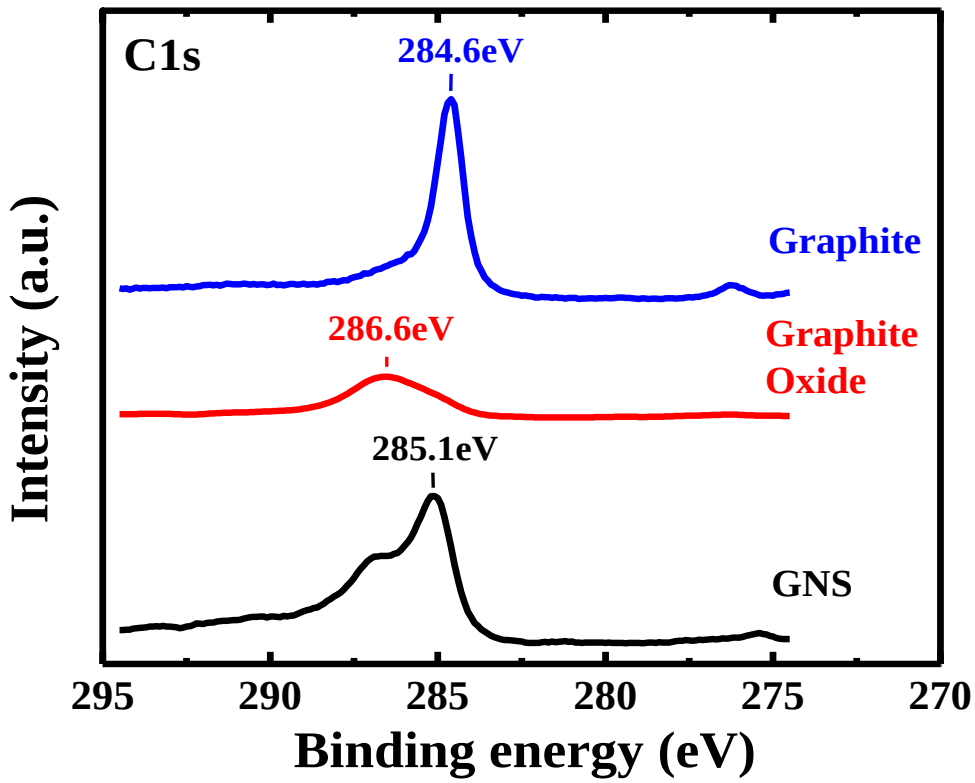

Figure 3.3 XPS spectra of C 1s graphite, graphite oxide, and GNS.

These XRD and XPS data indicate the π–π stacking became weak by oxidation of graphite. In our reduction condition using hydrazine, GNS includes some remaining oxygen species although the hydrazine reduction eliminates oxygen atoms in the functional groups [16,17]. However, it is considered that GNS are successfully prepared through the chemical reduction of graphite oxide. The surface area of GNS was measured to be 318 m^2 g^{-1} by Brunauer-Emmett-Teller (BET) method. It is much larger than the BET area of carbon black (64–120 m^2 g^{-1}) [18]. The large surface area of GNS is also evidence for the formation of graphene. The structure of graphite oxide and GNS can be observed by TEM measurement. The TEM images of graphite oxide and GNS, respectively are shown in Figure 3.4.

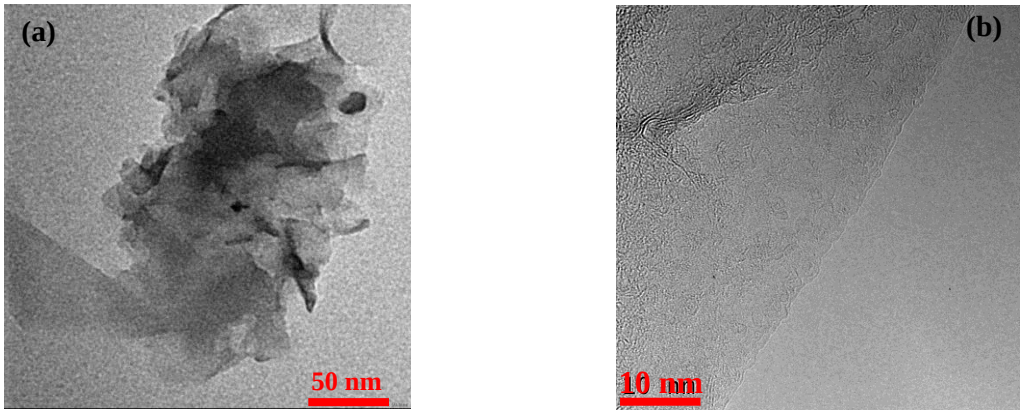

Figure 3.4 TEM images of (a) graphite oxide and (b) GNS.

Figure 3.4 shows TEM images of graphite oxide and GNS. The TEM image (Figure 3.4 (a)) of the graphite oxide exhibits coalesces and a wrinkle structure. On the other hand, the GNS image (Figure 3.4 (b)) shows an intricate long-range array of fold and ripple without coalesces sheets into overlapped region. Therefore, a significant reduction in the intensity of C(002) peak in XRD and a clear thin-sheet structure with wrinkle in TEM, clearly indicating single or a few layers of GNS.

3.2.2 Catalyst preparation and characterization

The 10–70 wt % Pt/GNS catalysts were prepared by using impregnation method with controlling the amount of Pt precursor of [$H_2PtCl_6 \cdot 6H_2O$] (Alfa Aesar, A Johnson Matthey Company) on GNS, respectively. An ethanol solution of the Pt precursor was mixed with the ethanol solution of GNS and was stirred for 3 hours. The product was then collected by filtration and dried in air at 60 ^oC for 12 h. Finally, the product was reduced by heat treatment in a hydrogen (H_2) stream (25 mL/min) at 400 ^oC for 2 h in a furnace. The heat treatment process can be seen in Figure 3.5. Finally, the collected product was used as Pt/GNS catalyst.

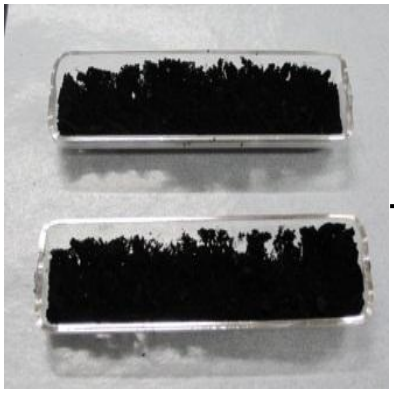

10–70 wt % Pt/GNS catalysts powder, respectively

(1) →

Tube furnace

(2) →

Heat treatment in tube furnace

(1) Catalyst powder was put into tube furnace.

(2) Catalyst was reduced by heat treatment. The temperature programs were set below as:

- Program 1 (Flowing N_2) (400 ^oC, 2h) (100 mL/min)
- Program 2 (Flowing H_2) (400 ^oC, 2h) (25 mL/min)
- Program 3 (Flowing N_2) (cooling until below 50 ^oC)
- Samples were taken out.

Figure 3.5 The diagram of reduction process for Pt/GNS catalyst by using heat treatment.

Then, the 10–70 wt % Pt/GNS catalysts were characterized by thermogravimetric/differential thermal analysis (TG/DTA), XRD, TEM, XPS and electrochemical measurements. TG/DTA measurements were carried out using TG/DTA6300, Seiko Instruments Inc. (Reference: Pt-pan; Air 200 mL/min; T measurement: 50–1000 ^oC; Rate: 10 ^oC/min, respectively). XRD measurements were performed at room temperature employing a two circle diffractometer (PANalytical PW 3050 Philips X'Pert Pro, Cu K_α radiation of 1.541 Å, without monochromator), installed at a line focus X-ray generator. A reflection free Si plate was used as a sample stage. Cu K_α radiation obtained by reflection from a singly bent HOPG crystal was used as the incident X-ray. Diffraction pattern was recorded using a solid state detector (PANalytical X'Celerator) with a scan speed of 0.005 deg. (in 2θ)/sec up to 90 degrees. XPS measurements were carried out using JEOL, JPS 9010 TR (X-ray source Al K_α, 1486.6 eV, pass energy 50 eV, energy resolution 1.88 eV which was calibrated using Ag $3d_{5/2}$ by measuring a clean Ag sample, the uncertainty of binding energy ± 0.05 eV). The electrochemical measurements were conducted using PGSTAT PG12, AUTOLAB Potentiostat/Galvanostat. The electrochemical measurements were carried out in a three electrodes system in nitrogen saturated 0.1 M $HClO_4$ at 60 °C, with Pt-wire, Ag/AgCl, and glassy carbon disk as counter electrode

(CE), reference electrode (RE), and working electrode (WE), respectively (Figure 3.6).

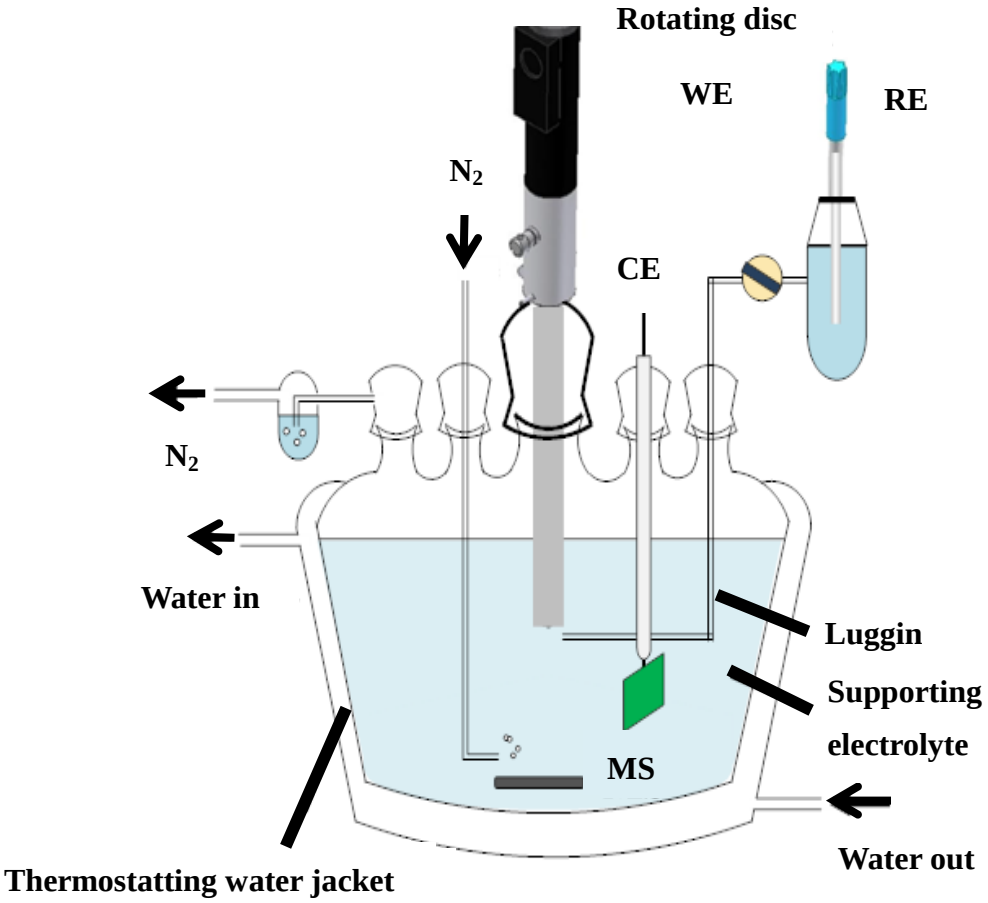

Figure 3.6 Illustrating cell for cyclic voltammetric experiments with three-electrode configuration.

The cyclic voltammograms (CVs) were obtained at - 0.25 to 0.8 V versus Ag/AgCl with scan rate of 10 mV s^{-1}. The electrochemical active surface area (ECSA) for each of 10–70 wt % Pt/GNS catalysts was measured by using hydrogen adsorption/desorption ($ECSA_H$) and CO stripping voltammogram ($ECSA_{CO}$), respectively. Commonly, hydrogen adsorption/desorption cyclic voltammetry is carried out to evaluate $ECSA_H$ [16,19].

For the $ECSA_H$ measurements, 1 mg Pt/GNS catalyst was firstly diluted into 500 µl Nafion solution (1:50 in methanol, 5 wt % Nafion (Aldrich)). Then, 10 µl catalyst ink solution was loaded onto a clean glassy carbon disk electrode (0.28 cm^2). The Pt loadings of catalysts on working electrode are then calculated as 2.0, 3.0, 4.0, 5.0, 6.0, 7.0, 8.0, 9.0, 10.0, 11.0, 12.0, 13.0, and 14.0 µg for 10, 15, 20, 25, 30, 35, 40, 45, 50, 55, 60, 65, and 70 wt % Pt/GNS catalysts, respectively. For example, Pt loading of 10 wt % Pt/GNS is calculated by 1 mg × (10 wt %/100 wt %) × (10 µl/500 µl).

For CO-stripping measurements, the amounts of Pt set on the working electrode are the same as those measured in $ECSA_H$. Each of catalyst ink solutions for 10–70 wt % Pt/GNS catalysts was loaded onto a glassy carbon disk electrode (0.28 cm^2) with diluted (1:50 in methanol) 5 wt % Nafion solution (Aldrich),

respectively. Prior to the measurements, the working electrode was firstly purged by bubbling nitrogen through the electrolyte solution of 0.1 M $HClO_4$ for 20 minutes, and then it was scanned at - 0.2 to 0.8 V versus Ag/AgCl for 50 cycles in nitrogen with scan rate 10 mV s^{-1} and rotation rate 500 rpm for cleaning and de-oxygenates the environment. Subsequently, CO was adsorbed to the surface of the working electrode by bubbling 3 % CO/H_2 into the electrolyte solution of 0.1 M $HClO_4$ at 60 ^oC for 1 hour, while holding the working electrode potential at - 0.15 V versus Ag/AgCl. After 3 % CO/H_2 bubbling, the gas was switched to nitrogen for 30 minutes and the potential was scanned from - 0.2 to 0.8 V versus Ag/AgCl to record the CO-stripping voltammogram at 60 ^oC with a scan rate of 10 mV s^{-1} [20–22].

For the comparison, every measurement was also done for the commercial catalysts of 20 and 40 wt % Pt/carbon black (CB) (Johnson Matthey).

3.3 Results

3.3.1 TG/DTA

The amounts of Pt on GNS for 10–70 wt % Pt/GNS catalysts were measured by TG/DTA (see the Supporting Information, Appendix 1, Figure 1S). As shown in Figure 3.7, the amounts of Pt are exactly the same as those calculated in the catalyst preparation procedure.

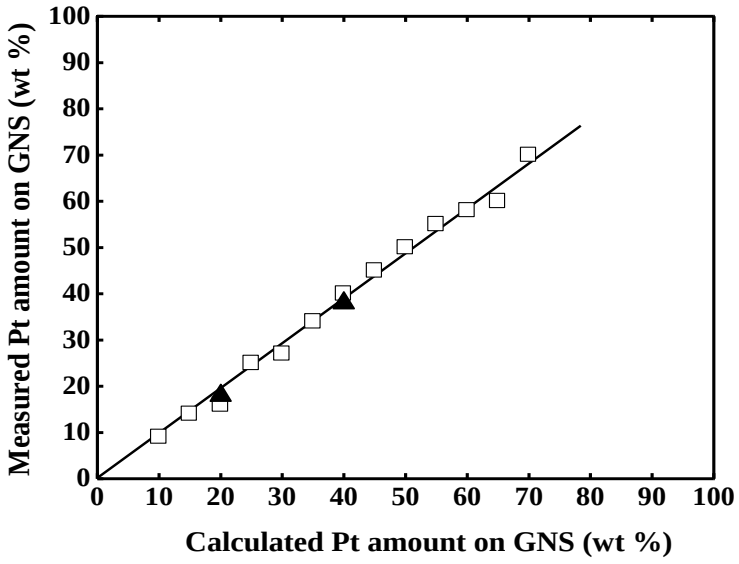

Figure 3.7 Pt amount on GNS (wt %) measured by TG/DTA versus calculated Pt amount on GNS (□). The results for 20 and 40 wt % Pt/CB commercial catalysts are also shown (▲).

The results indicate that all the Pt atoms in the catalyst precursors are included in the Pt/GNS catalysts. I can thus control the amount of Pt on GNS exactly so that one can evaluate the relationship among the particle size, the electronic structure, and the catalytic activity as a function of the Pt amount.

3.3.2 TEM

TEM measurements were carried out to examine the Pt particle size and the size distribution as well as the dispersion character for Pt/GNS and Pt/CB catalysts. Figure 3.8 shows the TEM images for 10–70 wt % Pt/GNS and 20 and 40 wt % Pt/CB catalysts with histograms of particle size distributions by measuring the size of 650 particles for 10–70 wt % Pt/GNS and 20 and 40 wt % Pt/CB catalysts, respectively. The TEM images clearly show high dispersions of Pt particles on GNS and carbon black.

It should be noted that Pt subnano-clusters are seen for Pt/GNS catalyst with low loadings of Pt below 40 wt %. For 10 wt % Pt/GNS catalyst, the average Pt particle size is estimated to be 0.87 nm. That is, Pt subnano-clusters were mostly formed on GNS. They seem to be homogenously distributed on GNS without aggregation even after heating treatment in N_2/H_2 (4:1 v/v) at 400 ^oC in the catalyst preparation procedure. A large surface area of Pt is thus expected, which may reduce Pt usage in fuel cells. With increasing amount of Pt for 10–50 wt % Pt/GNS catalysts, the average Pt particle sizes tend to become large as shown in Figure 3.8.

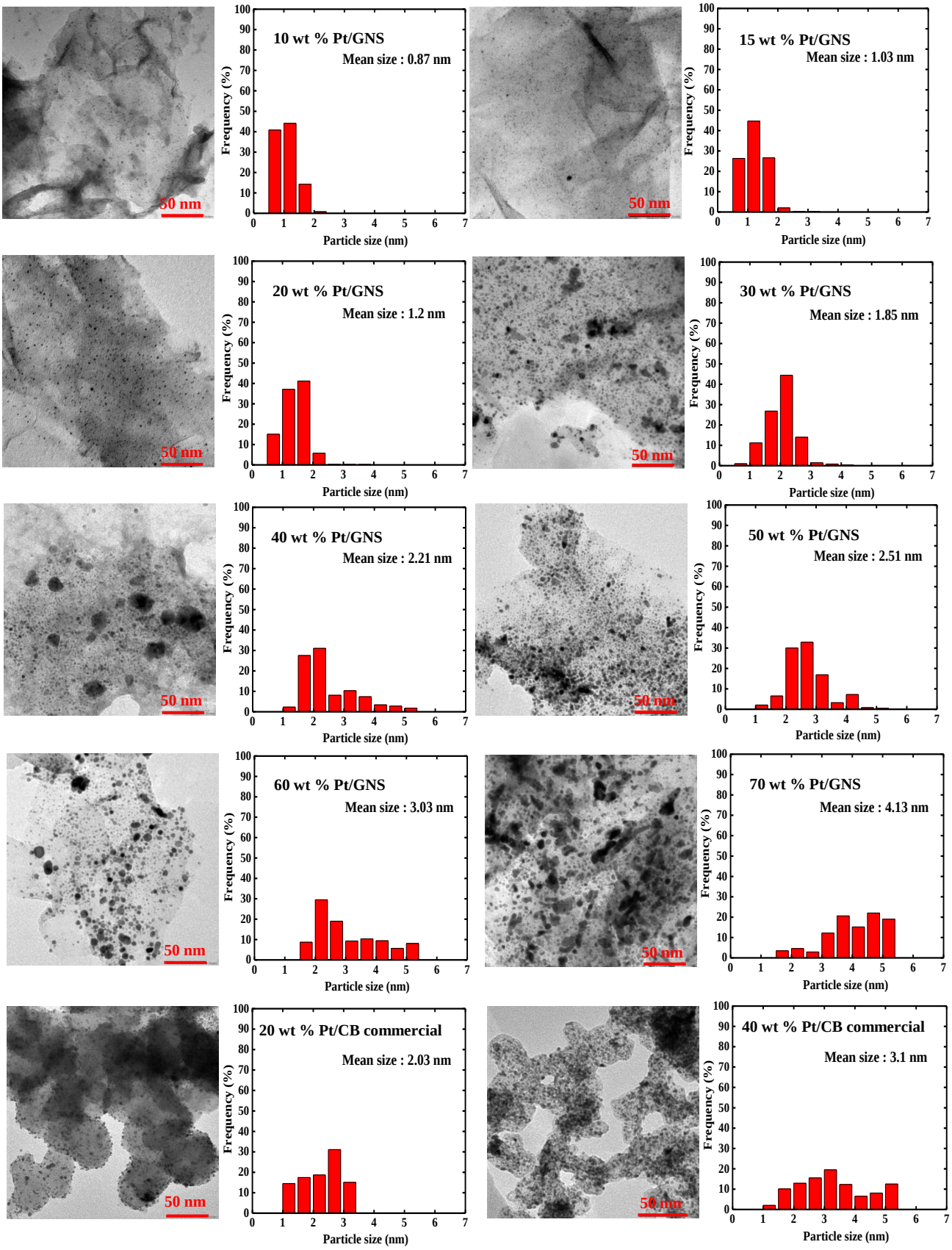

Figure 3.8 TEM images and histograms of 10–70 wt % Pt/GNS. The results for 20 and 40 wt % Pt/CB commercial catalysts are also shown.

Further, Figure 3.9 shows the average Pt particle size estimated by TEM as a function of Pt loading.

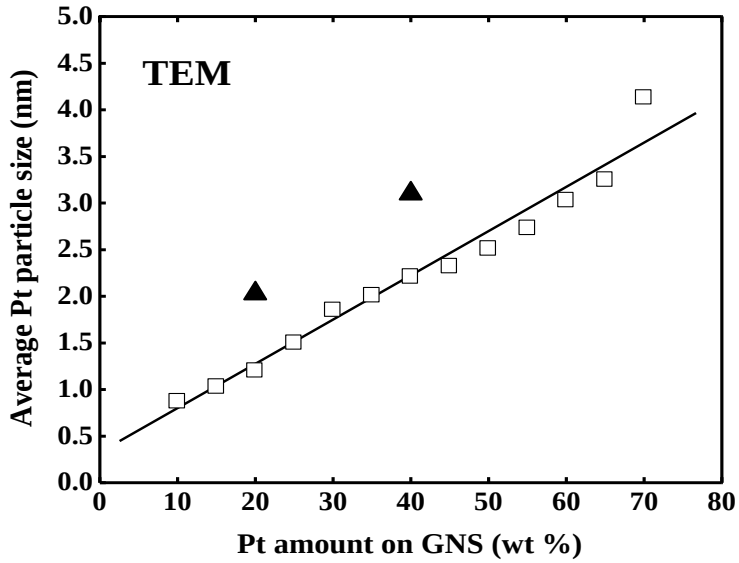

Figure 3.9 Average Pt particle size (nm) estimated by TEM versus Pt amount on GNS (□). The results for 20 and 40 wt % Pt/CB commercial catalysts (▲) are also shown.

It is clearly shown that the average particle size of Pt linearly increases with increasing amount of Pt. For 10–20 wt % Pt/GNS, the average size of Pt is about 1 nm. On the other hand, for 55–70 wt % Pt/GNS catalysts, the Pt subnano-clusters are not seen and the average Pt particle sizes are estimated to be 2.7–3.8 nm. Moreover, larger Pt particles (> 10 nm) are present on those catalysts as shown in the Appendix 1, Supporting Information (Figure 2S and 3S).

In comparison, 20 and 40 wt % Pt/CB commercial catalysts were observed by TEM (Figure 3.8). The average particle sizes of Pt for 20 and 40 wt % Pt/CB (2.0 and 3.1 nm) are larger than 20 and 40 wt % Pt/GNS catalysts (1.2 and 2.2 nm), indicating that the small Pt particles are much more deposited on GNS compared to CB.

3.3.3 XRD

The XRD patterns for 10–70 wt % Pt/GNS and 20 and 40 wt % Pt/CB commercial catalysts are shown in Figure 3.10. All the patterns gave peaks at 2θ Bragg angles around 25^{o} and 39^{o} corresponding to C(002) and Pt(111), respectively. The C(002) peak appears weak and broad for Pt/GNS catalysts. Note that the C(002) peak usually appears sharp at 26.5^{o} for graphite [16] corresponding to the interlayer distance of d = 3.4 Å and a broad peak at 10^{o} for graphite oxide (GO) [23] corresponding to that of d = 8.4 Å. In Figure 3.10, weak and broad peaks at around 25^{o} (d = 3.5 Å) are seen, meaning that graphene sheets are formed

successfully. However, some graphitic (stacked graphene) species should remain due to the weak peak at 25° suggesting a stacking of graphene to some extent.

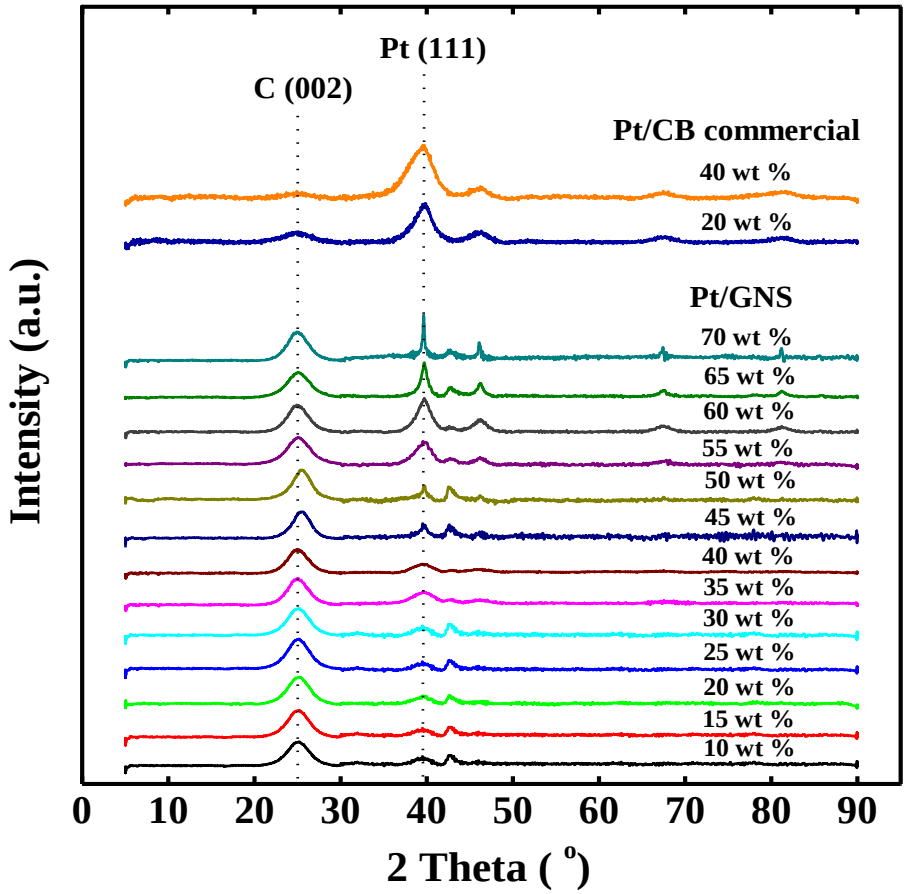

Figure 3.10 XRD patterns of 10–70 wt % Pt/GNS and 20 and 40 wt % Pt/CB commercial catalysts.

As shown in Figure 3.10, Pt(111) peaks for 10–50 wt % Pt/GNS catalysts are very weak and broad, and then gradually become intense and sharp for 55–70 wt % Pt/GNS catalysts. The weak XRD peaks of Pt are characteristic for Pt/GNS catalysts [13], in contrast to the Pt/CB catalysts showing intense XRD peaks of Pt (Figure 3.10). The weak and broad peaks of Pt(111) for the Pt/GNS catalysts indicate that very small particles of Pt (< 2 nm) were formed on graphene. I thus estimated the particle size by XRD using Scherrer equation [24] as shown in Figure 3.11. The average Pt particle size is not so different at 2.8–4.0 nm below 45 wt %, while the intensity of XRD peak gradually increases with Pt loading. It is noted that the average size distribution of Pt is not the real one because XRD patterns are not obtained for the Pt subnano-clusters as observed by TEM. The average size distribution of relatively large Pt particles is thus measurable by XRD. This is the reason why the average particle size of Pt estimated by XRD is very different from that estimated by TEM.

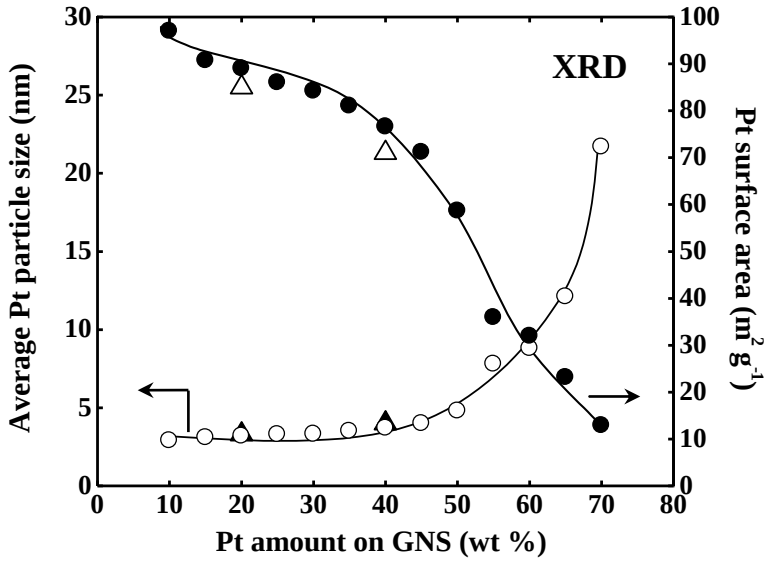

Figure 3.11 Average Pt particle size (nm) (○, left axis) and Pt surface area (m^2 g^{-1}) (●, right axis) estimated by XRD as a function of 10–70 wt % Pt/GNS. The results for the 20 and 40 wt % Pt/CB commercial catalysts are also shown (▲ and △).

As for 20 and 40 wt % Pt/CB commercial catalysts, Pt(111) peaks are relatively large in intensity, suggesting that the crystallinity of Pt is higher than those of Pt/GNS. The particles sizes of 20 and 40 wt % Pt/CB commercial catalysts are estimated to be 3.3 and 4.0 nm, respectively (Figure 3.11).

3.3.4 $ECSA_H$ and $ECSA_{CO}$

Cyclic voltammetry (CV) has been performed on Pt/GNS and Pt/CB catalysts to measure the electrochemical surface area (ECSA) of Pt and to evaluate electrocatalytic activities for the oxidation of adsorbed CO. $ECSA_H$ and $ECSA_{CO}$ were measured by hydrogen desorption and the electro-oxidation of CO to CO_2 as shown in Figures 3.12 and 3.13, respectively.

The $ECSA_H$ was calculated as reported in the literature [16,19]. The cyclic voltammograms for Pt/GNS and Pt/CB catalysts (Figure 3.12) show three characteristic regions: the hydrogen adsorption potential region between - 0.2 and 0.1 V versus Ag/AgCl is followed by the double layer potential region, while above 0.45 V versus Ag/AgCl, first OH adsorption and then oxide formation can be observed [25]. It seems that the oxide formation peaks are relatively weak for Pt/GNS catalysts compared to the Pt/CB catalysts.

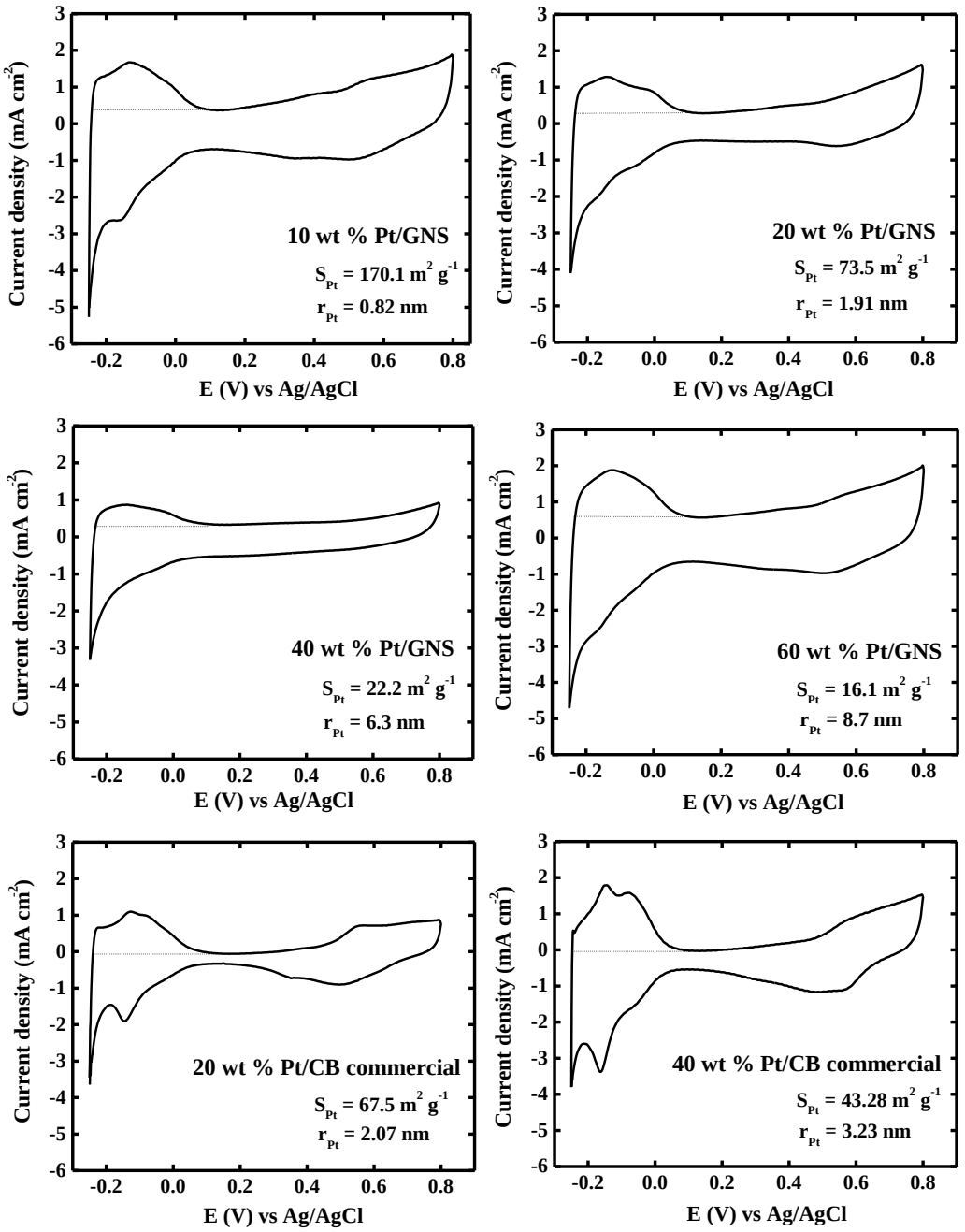

Figure 3.12 Cyclic voltammograms of 10–70 wt % Pt/GNS and 20 and 40 wt % Pt/CB commercial catalysts.

The CO stripping voltammetry was carried out in a N_2-saturated 0.1 M $HClO_4$ solution at 60 ^oC. The CO stripping curves were obtained from two consecutive scan cycles. Figure 3.13 shows CO stripping voltammograms for 10–70 wt % Pt/GNS and 20 and 40 wt % Pt/CB catalysts, respectively. It is clearly shown that the CO electro-oxidation peaks are large and sharp for 10–30 wt % Pt/GNS. $ECSA_{CO}$ was then

obtained by calculating CO stripping charge area under the CO stripping peak in potential region from 0.3 to 0.7 V versus Ag/AgCl (Figure 3.13) [20–22].

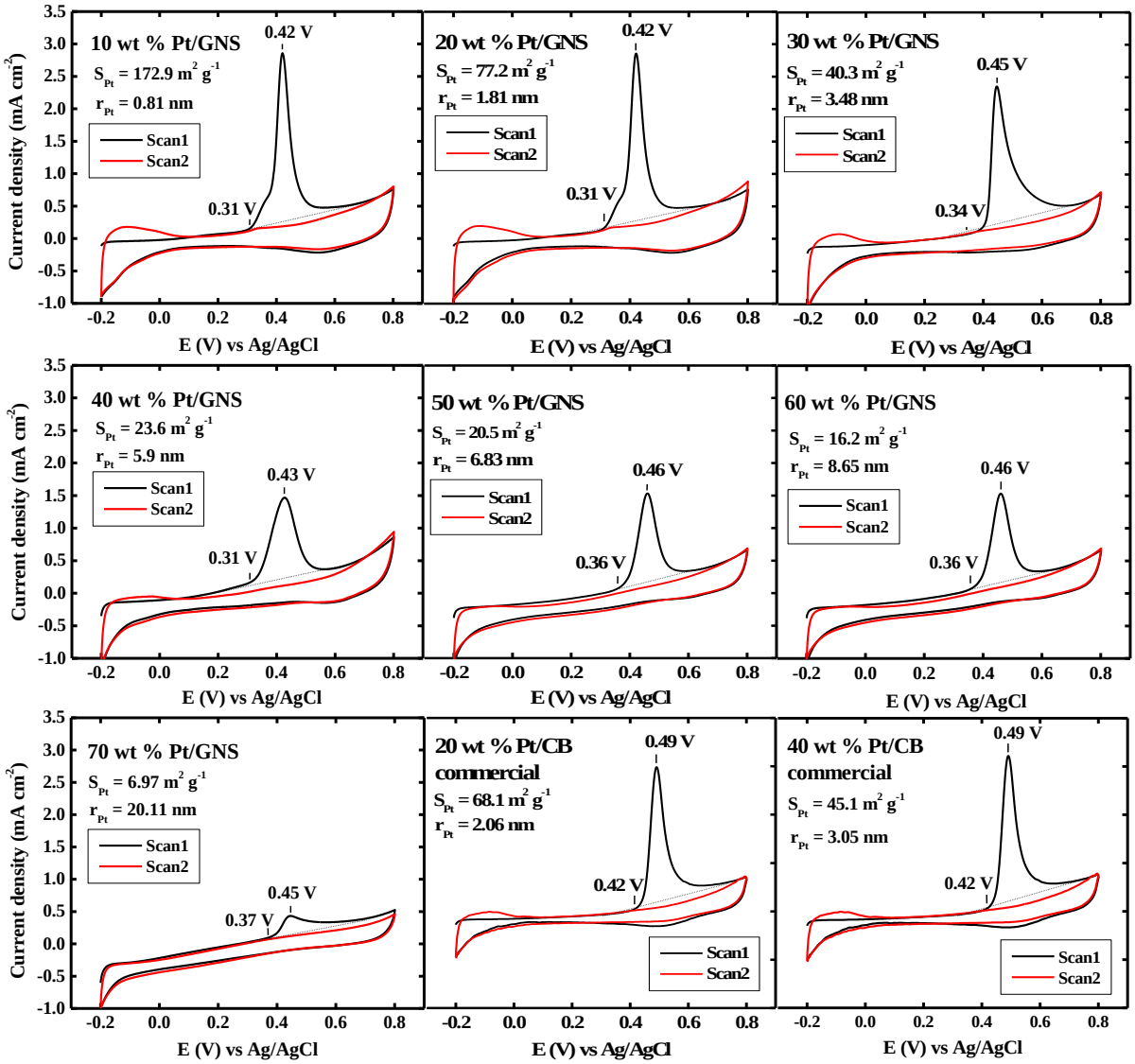

Figure 3.13 CO stripping voltammograms of 10–70 wt % Pt/GNS and 20 and 40 wt % Pt/CB commercial catalysts measured in 0.1 M $HClO_4$ at 60 ^oC with the scan rate of 10 mV s^{-1}.

Both $ECSA_H$ and $ECSA_{CO}$ for 10–70 wt % Pt/GNS and 20 and 40 wt % Pt/CB are shown in Figure 3.14a. It is clear that the $ECSA_H$ is in good agreement with $ECSA_{CO}$. This indicates that the electrochemical-surface area of Pt is accurately estimated as a function of Pt loading by the electrochemical measurements. Note that the Pt surface area (S_{Pt}) is extremely large as 170.1 $m^2 g^{-1}$ for 10 wt % Pt/GNS, corresponding to an average size of 0.82 nm. The estimated size of Pt cluster is consistent with that measured by TEM in terms of the formation of Pt subnano-clusters. It is thus concluded that the majority of Pt particles in 10 wt % Pt/GNS is Pt subnano-clusters.

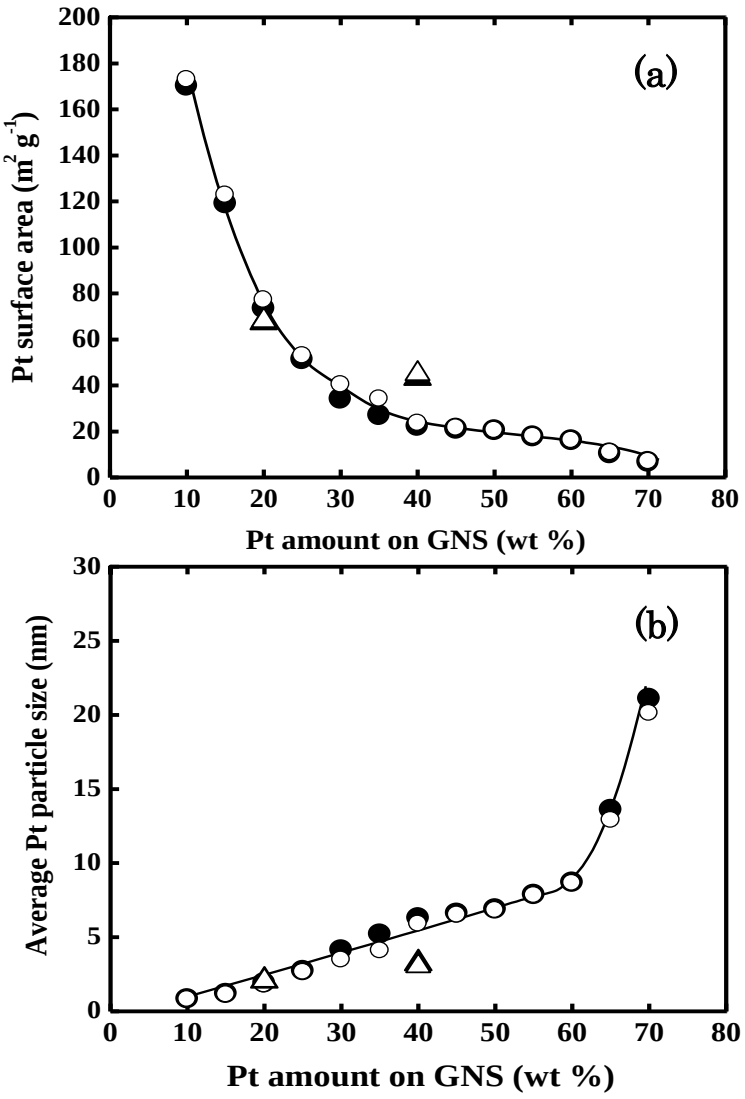

Figure 3.14 (a) Pt surface area (m^2 g^{-1}) estimated by ECSA versus Pt amount on GNS (wt %): $ECSA_H$ (●), $ECSA_{CO}$ (○). The results for the 20 and 40 wt % Pt/CB commercial catalysts are also shown: $ECSA_H$ (▲), $ECSA_{CO}$ (△). (b) Average Pt particle size (nm) estimated by ECSA versus Pt amount on GNS (wt %): $ECSA_H$ (●), $ECSA_{CO}$ (○). The results for the 20 and 40 wt % Pt/CB commercial catalysts are also shown: $ECSA_H$ (▲), $ECSA_{CO}$ (△).

Generally, the surface area of Pt is in the ranges of 60–80 m^2 g^{-1} for Pt/CB commercial catalysts [24]. That is, the surface area of 10 wt % Pt/GNS is 2–3 times larger than ordinal Pt/CB catalysts. The surprisingly large area of electro-chemically active surface means a possibility to reduce Pt usage in fuel cells if the catalytic activity is as high as those for larger Pt particles. As described later, the catalytic activity of Pt/GNS is superior to commercial catalysts in the electro-oxidation of adsorbed CO.

As for higher Pt loadings, 20–70 wt % Pt/GNS, $ECSA_H$ and $ECSA_{CO}$ significantly drop as shown in

Figure 3.14a. The average size of Pt nanoparticles increased up to 10 nm at 60 wt % of Pt (Figure 3.14b). The sizes of 8–20 nm at 55–70 wt % Pt/GNS measured by ECSA agree with those measured by XRD. However, the Pt average size measured by TEM is relatively smaller than those measured by ECSA and XRD. This is explained by the coexistence of small and large Pt particles with different size distribution. In fact, Pt subnano-clusters coexisting with larger nanoparticles are observed in TEM images for 15–40 wt % Pt/GNS catalysts (Figure 3.8). However, the Pt subnano-clusters are not formed on 50–70 wt % Pt/GNS catalysts. Here, the average particle sizes estimated by TEM, XRD, and ECSA are compared as shown in Table 3.1.

Table 3.1 Average Pt particle size of samples.

Samples	**Average Pt particle size (nm)**			
	XRD measurement	**TEM measurement**		**ECSA measurement**
		< 5 nm	**> 5 nm**	
10 wt % Pt/GNS	2.9	0.87	–	0.82
15 wt % Pt/GNS	3.1	1.03	–	1.18
20 wt % Pt/GNS	3.2	1.2	–	1.91
25 wt % Pt/GNS	3.3	1.5	–	2.74
30 wt % Pt/GNS	3.3	1.85	5.23	4.12
35 wt % Pt/GNS	3.5	2.01	5.3	5.2
40 wt % Pt/GNS	3.7	2.21	5.38	6.3
45 wt % Pt/GNS	4.0	2.32	5.54	6.6
50 wt % Pt/GNS	4.8	2.51	5.6	6.9
55 wt % Pt/GNS	7.8	2.73	5.74	7.87
60 wt % Pt/GNS	8.8	3.03	6.13	8.7
65 wt % Pt/GNS	12.1	3.25	7.96	13.6
70 wt % Pt/GNS	21.7	4.13	8.48	21.1
20 wt % Pt/CB (commercial)	3.3	2.03	6.11	2.07
40 wt % Pt/CB (commercial)	4.0	3.1	6.54	3.23

The average sizes measured by TEM are comparable with those measured by ECSA for low Pt loadings of 10–20 wt % for Pt/GNS. On the other hand, the average sizes measured by XRD are comparable with those measured by ECSA for high Pt loadings of 50–70 wt % for Pt/GNS. Those agreements are explained by the presence of subnano-clusters and larger particles of Pt with two different size-distributions,

which is due to the formation mechanism of Pt subnano-clusters as has been reported elsewhere [13]. As shown in Figure 2S, Appendix 1, Supporting Information, larger particles over 5 nm were frequently observed for 30–70 wt % Pt/GNS.

In comparison, 20 and 40 wt % Pt/CB commercial catalysts, the average particle sizes of Pt measured by TEM, XRD, and ECSA are comparable as 2–4 nm although XRD overestimate the particle size due to the presence of small particles with the size of ca. 1 nm. In the case of Pt/CB, the size distribution is normal in the absence of large Pt particles over 5 nm as observed for Pt/GNS.

3.3.5 Electro-oxidation of adsorbed CO

The electro-oxidation of adsorbed CO on Pt/GNS in Figure 3.13 shows characteristic features different from those for Pt/CB in terms of the electro-oxidation potential and width of the peak. As for 10–20 wt % Pt/GNS, the threshold voltages of the electro-oxidation peaks are very low as 0.31 V versus Ag/AgCl and the electro-oxidation peak is located at 0.42 V, which is in contrast with the results of Pt/CB catalysts with the threshold of 0.42 V and the peak of 0.49 V versus Ag/AgCl. That is, the lower shift in potential is about 1 V. It is clear that the catalytic properties of Pt supported by GNS are very different from those of Pt/CB catalysts. With increasing Pt loading on GNS, however, the electro-oxidation peaks are shifted to higher voltages as shown in Figure 3.13. The tendency is clearly shown in Figure 3.15, in which the threshold of electro-oxidation peak is shifted to higher voltages with increasing Pt loading.

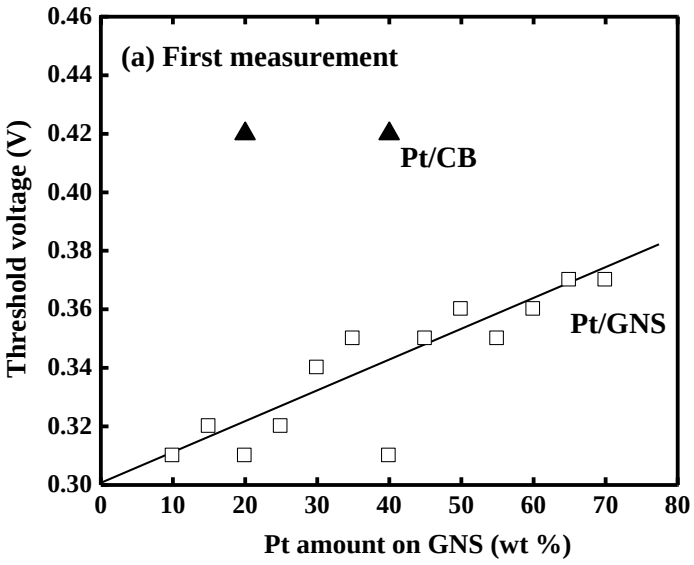

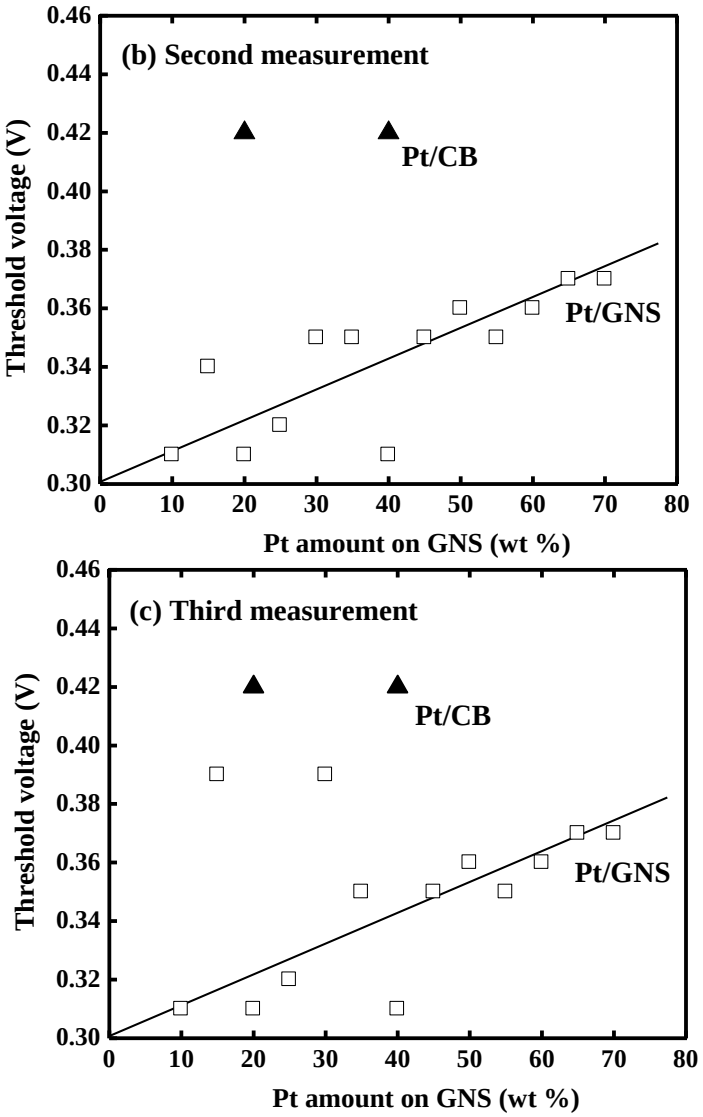

Figure 3.15 Threshold voltages of CO electro-oxidation peak in CO stripping voltammogram as a function of Pt amount on GNS (wt %) (□), (a) first measurement, (b) second measurement, and (c) third measurement. The results for the 20 and 40 wt % Pt/CB commercial catalysts are also shown (▲).

Considering that Pt subnano-clusters are formed at low loadings of 10–20 wt %, the shift of voltages in the electro-oxidation of adsorbed CO is due to a superior catalytic activity of Pt subnano-clusters on GNS. That is, the shift to higher voltages for Pt/GNS catalysts is explained by the particle size effect of Pt. It is also noticed that the width of the electro-oxidation peaks for Pt/GNS gradually increases with increasing Pt loading from 10 to 70 wt %. This is explained by the coexistence of Pt subnano-clusters and larger Pt particles, where two characters of high and low activities are probably mixed in the CO electro-oxidation.

On the other hand, no significant effect of the particle size was observed for Pt/CB catalysts. As shown in Figures 3.13 and 3.15, the thresholds and the peak maxima of the CO electro-oxidation peaks are comparable between 20 and 40 wt % Pt/CB catalysts, although the particle sizes are different as 2.1 and 3.3

nm, respectively. Furthermore the width of the peaks for Pt/CB is relatively sharp compared to those for Pt/GNS, indicating the homogeneous catalytic activity of Pt in Pt/CB. Those results indicate that the catalytic properties of Pt/CB are identical independent of the particle size, further suggesting that the support effect of CB is weak. In addition, the threshold voltages of Pt/CB in Figure 3.15, 0.42 V, seem to be high compared to those of Pt/GNS, 0.33–0.37 V, although the particle size for 30–70 wt % Pt/GNS (4–21 nm) is much larger than those of Pt/CB (2–3 nm) shown in Table 3.1. For large Pt particles on GNS, the electronic modification of Pt via Pt-graphene interface interaction should be insignificant. The difference in the electro-oxidation activity between Pt/GNS and Pt/CB is thus explained by the difference in the morphology of Pt particles or the surface geometrical structure of Pt particles as described in discussion section.

3.3.6 XPS

The electronic structures of Pt for Pt/GNS and Pt/CB catalysts were examined by XPS. Figure 3.16 shows XPS spectra of Pt 4f for 10–70 wt % Pt/GNS and 20 and 40 wt % Pt/CB catalysts.

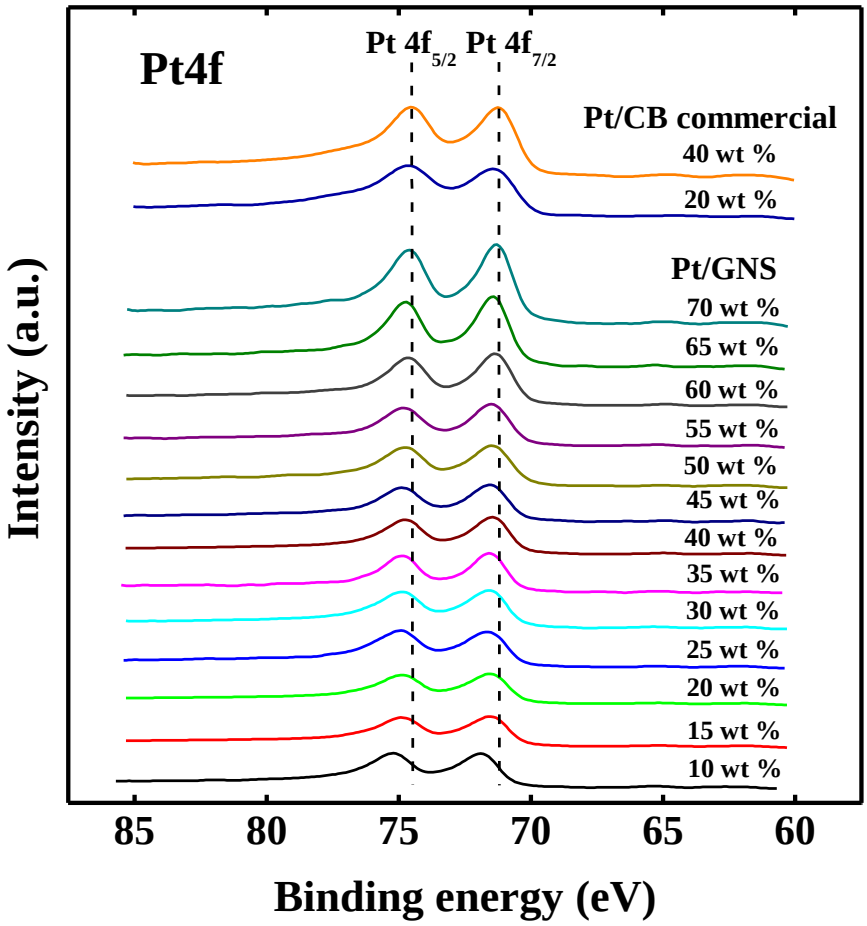

Figure 3.16 XPS spectra of 10–70 wt % Pt/GNS and 20 and 40 wt % Pt/CB commercial catalysts in the Pt 4f region. The results for the 20 and 40 wt % Pt/CB commercial catalysts are also shown.

It is found that the Pt 4f peak of Pt/GNS is shifted to higher binding energies with decreasing Pt loading. The peak maximum of Pt $4f_{7/2}$ for 10 wt % Pt/GNS is located at 71.8 eV, which is much higher than that of bulk Pt, 71.2 eV [15]. The tendency of the binding energy shift in Pt $4f_{7/2}$ with Pt loading is clearly shown in Figure 3.17, in which the peak maxima shift to higher energies with decreasing Pt loading. Even at 70 wt % of Pt loading, the peak maximum at 71.3 eV is a little high compared to the bulk value at 71.2 eV. The energy shift should be related to the particle size of Pt on GNS. That is, modification in the electronic state of Pt should become significant due to the interface interaction between Pt and graphene when Pt subnano-clusters are the majority on GNS. The interface interaction is considered to be π–d hybridization of graphene and Pt, respectively, which will be discussed in section 3.4.4.

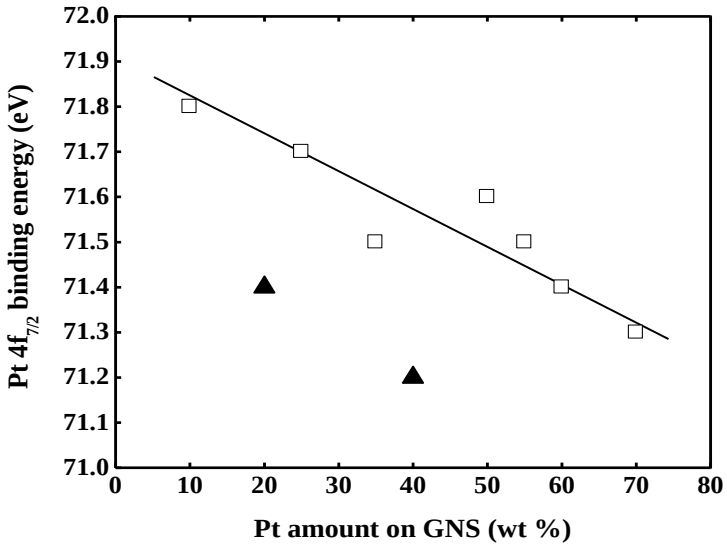

Figure 3.17 Pt $4f_{7/2}$ binding energy (eV) versus Pt amount on GNS (wt %) of 10–70 wt % Pt/GNS (□). The results for the 20 and 40 wt % Pt/CB commercial catalysts are also shown (▲).

On the other hand, binding energies (BEs) of Pt $4f_{7/2}$ for 20 and 40 wt % Pt/CB at 71.4 and 71.2 eV are close to the bulk value of 71.2 eV, although the particle sizes of Pt in Pt/CB are small as 2.1 and 3.3 nm. For the comparable particle sizes in Pt/GNS, the high BE shifts correspond to 0.3–0.5 eV, which is greater than those for Pt/CB. The absence of significant BE shift of Pt $4f_{7/2}$ in Pt/CB suggests that no significant interface interaction between Pt and CB. The difference in the modification in the electronic states of Pt between Pt/GNS and Pt/CB as a function of Pt loading well corresponds to that in electro-catalytic activity of CO oxidation described in section 3.3.5. That is, the catalytic activity and the BE of Pt $4f_{7/2}$ are increased in parallel with decreasing particle size of Pt on GNS. The relationship among the catalytic activity, the BE shift, and the particle size is thus ascribed to the interface interaction between Pt and graphene. As for Pt/CB, no significant change in both catalytic activity and BE of Pt $4f_{7/2}$ was observed when the particle size is changed. That is due to the absence of the interface interaction between Pt and CB.

There are two possible factors contributing to the core level shift: initial state effect associated to

changes in the local electronic structure (valence electron configuration), final state effect due to changes in the relaxation process (extra-atomic response to the positively charged hole) [26]. The final state effect is discarded because the core level shift was observed for Pt/GNS, while no peak shift was observed for Pt/CB at the same Pt loading or particle size.

The atomic ratio of Pt to C estimated by XPS for 10–70 wt % Pt/GNS and Pt/CB catalysts are summarized in Appendix 1, Supporting Information (Table 1S). It is shown that the atomic ratio of Pt to C increases with increasing Pt loading. Here, the Pt/C ratio of Pt/GNS is comparable with that of Pt/CB at the same Pt loading.

3.4 Discussion

3.4.1 Distribution of particle size

Table 3.1 shows the average Pt particle sizes estimated by XRD, TEM, and ECSA, respectively. Apparently, differences in the estimation of average Pt particle size are seen, which can be ascribed to the difference in the definition of "average particle size". The estimation by TEM is made on the basis of particle number although large particles include many Pt atoms. In XRD measurements, crystallinity is evaluated, in which information on the large crystallite can be obtained without detecting small particles below 1 nm. It is thus impossible to estimate the size of Pt subnano-clusters. On the other hand, ECSA obtained from cyclic voltammetry (CV) measurements give the average particle size on the basis of Pt amount because ECSA (m^2 g^{-1}) is the surface area on the basis of Pt amount. In Table 3.1, the estimations by TEM agree with those by ECSA if the loading of Pt is less than 15 %. That is because the particles are mostly composed of very small clusters so that the average size based on particle number is comparable with that based on Pt amount. Here, XRD cannot evaluate the size of Pt subnano-clusters. On the other hand, for larger loadings over 55 wt % Pt, the average sizes evaluated by XRD agrees with those by ECSA. This can be explained by the majority of large Pt crystallites. However, small particles always coexist with large particles as shown in TEM images (Figure 3.8). That is why TEM measurements underestimate the average size of Pt particles if Pt loading is larger than 20 wt %.

Interestingly, the average particle sizes of Pt catalysts at 25–50 wt % estimated by XRD, TEM, and ECSA are very different. In XRD, the intensities of Pt(111) peak are very weak although ECSA estimates relatively large particles as 4–7 nm, indicating that the Pt particles have low crystallinity. One possible explanation of the low crystallinity is the formation of Pt clusters with a raft-like structure because of the strong interface interaction between Pt and graphene forming the subnano-clusters of Pt.

3.4.2 Subnano-clusters

The results of XRD, TEM, and ECSA experiments clearly indicate that many Pt subnano-clusters were formed for 10 wt % Pt/GNS, in which the surface area is found to be extremely high as 170 $m^2 g^{-1}$. However, Pt subnano-clusters coexist with Pt nanoparticles (2–5 nm) for 15–50 wt % Pt/GNS. Although Pt catalysts supported by graphene have been extensively studied in the application of electrocatalysts, the formation of the Pt subnano-clusters have not frequently reported so far. The reason may be due to the preparation methods. In our preparation method of the Pt subnano-clusters, the combination of weak and strong reductions using ethanol and hydrogen are adopted, respectively, where Pt subnano-clusters are formed during the hydrogen reduction as reported elsewhere [13]. That is, Pt oxides particles formed by the ethanol reduction on graphene are then reduced to Pt atoms by hydrogen, which migrate on GNS to form Pt clusters by their collision. In this study, I found that the size of Pt clusters increase with increasing loading of Pt. The relationship between the cluster size and the Pt loading can be explained by an entropy effect that chance in the collision of Pt with each other depends on the relative surface area of GNS to an amount of Pt atoms. That is, an increase in the amount of Pt causes high probability of the collision between Pt atoms leading to the formation of larger Pt particles.

3.4.3 Particle size effect on catalytic properties

In this study, particle size effects on the catalytic properties of Pt have been observed in electro-oxidation of adsorbed CO. For smaller Pt particles or subnano-clusters, so-called ignition voltages shift to be lower. That is, their catalytic activity in the electro-oxidation of adsorbed CO is higher compared to those of larger Pt particles on graphene. The high catalytic activity and large ECSA of the Pt subnano-clusters is promising as a cost-effective Pt catalyst.

Question arises as to why smaller Pt particles on graphene are more active for the electro-oxidation of adsorbed CO. The particle size dependence of Pt catalysts on the catalytic performances has been extensively studied for electro-oxidation of adsorbed CO and methanol oxidation reaction [22,25,27]. However, the size effect is not straight forward because it is known that the electro-oxidation of adsorbed CO is structure-sensitive on Pt and defects of Pt surface play significant role in the electro-oxidation of CO or methanol [25,28,29]. It has been reported that the least active is the (111) terrace site of Pt, while step or kink sites are considered to dissociate water and stabilize OH adspecies as a reactive intermediates [25]. Arenz et al. have clearly reported the importance of defects on Pt nanoparticles supported by carbon using infrared reflection-absorption spectroscopy (IRAS) [25]. In their results of CO stripping experiments, the rate of CO_2 formation increased with increasing particle size ($1 \leq 2 < 5 << 30$ nm), which is the reverse order for the present Pt/GNS catalysts. They consider that large particles have “rougher” surfaces than small particles,

which have some fairly smooth (111) facets. They also showed that the electro-oxidation activity of Pt particles is sensitively changed if the catalyst is annealed in CO-saturated solution by cycling of the electrode potential between $0.05 < E < 1.2$ V for 5 min. The CO-annealing removes surface irregularities of Pt. Anyway, Arenz et al. consider that defects are active sites for CO electro-oxidation. I also consider that edge Pt atoms at kink or step sites are active in Pt subnano-clusters on GNS. Note that the number of Pt atoms in the Pt subnano-clusters is very few below ~ 40 [13]. In the case of small Pt subnano-clusters, many Pt atoms with low coordination numbers should be there at the edges of clusters, which are probably reactive for the dissociation of H_2O_a or the reaction between CO_a and OH_a. That is, the increase in the amount of Pt atoms with low coordination numbers on GNS for smaller Pt clusters such as for Pt subnano-clusters on GNS is probably the main origin of the promoted catalytic activity for the electro-oxidation of adsorbed CO. The specific character of the Pt subnano-clusters is probably due to the support effect, i.e. strong interface interaction between Pt atoms with the graphene sheet as described below.

3.4.4 Support effects

The formation of Pt subnano-clusters as well as the superior catalytic properties for the electro-oxidation of CO can be ascribed to the support effect or the interface interaction between Pt and graphene. There have been many theoretical reports concerning the support effect of graphene on the properties of Pt electrocatalysts although the experimental works on the support effect of graphene and the size dependence of Pt are scarce. To the best of our knowledge, the present study is the first experimental report concerning the size dependence of Pt clusters supported by GNS on the catalytic properties and the electronic structure. The present results clearly indicate that the support effects are more significant for smaller Pt clusters in terms of the catalytic activity of the electro-oxidation of adsorbed CO as well as the core level of Pt 4f.

The interaction between Pt and graphene is considered to be π–d hybridization. Even for graphite supported Pt catalysts, the interface interaction has been observed between Pt and graphitic carbon. Our groups have studied the support effect of graphite on Pt catalysts by surface science methods using a Pt-deposited graphite model catalyst [30–35]. We have found the formation of Pt monolayer clusters, which promote activity for H_2-D_2 exchange reaction and CO desorption [30,31]. It has been also found that the Pt monolayer clusters are more stable on nitrogen-doped graphite [32]. This suggests that π states in the conjugated system determine the properties of the interaction between Pt and carbon. As a modified π state, non-bonding π states may be responsible for the π–d hybridization [33]. We have thus studied the local electronic structure in the vicinity of vacancies and doped-nitrogen by scanning tunneling spectroscopy (STS), and found that the non-bonding local states propagate from the vacancies or the doped-nitrogen [34,35]. I thus consider that the support effect observed in the graphene case is also ascribed to the π–d

hybridization. However, the interaction between Pt and graphene seems to be more significant compared to that of graphite because the formation of Pt subnano-clusters seen in Pt/GNS catalysts has never been observed on graphite or nitrogen-doped graphite. I assume that the difference between graphite and graphene is ascribed to the presence and absence of weak hybridization of p_z orbitals between graphene layers.

As described in section 3.3.6, the large core level shift of Pt 4f is observed towards higher BE for smaller Pt clusters on GNS, which clearly indicates larger interface interactions between Pt and GNS for smaller Pt clusters. This is probably due to the increase in the amount of Pt atoms with low coordination numbers for smaller Pt clusters on GNS. That is, low coordinated Pt atoms such as edge Pt atoms in the Pt subnano-clusters make the strong π–d hybridization with carbon atoms of GNS. As a result, smaller Pt clusters on GNS shows large core level shifts in Pt 4f. The π–d hybridization in Pt clusters on graphene has been reported in theoretical reports. Basically the π–d hybridization is weak compared with the Pt-Pt bonding in Pt clusters. The interaction between Pt and graphene is more significant for smaller Pt_n clusters (n = 1–5), in which edge Pt atoms in Pt clusters interact with graphene more strongly [10,11]. In addition, a raft-like structure of Pt clusters has been reported as a stable geometry [10,11]. In this sense, the results in the present study are consistent with those of theoretical reports in terms of more significant interactions between Pt and graphene for smaller Pt subnano-clusters.

3.5 Conclusion

I have successfully controlled the average size of Pt particles by changing Pt loading on GNS from 10 to 70 wt %. At a low loading of 10 wt %, Pt subnano-clusters are formed showing large surface area of 170 $m^2\ g^{-1}$. The 10 wt % Pt/GNS catalyst exhibits the best performance in the electro-oxidation of adsorbed CO. Therefore, Pt subnano-clusters can be expected as excellent electro-oxidation catalysts. An increase in loading of Pt leads to an increase in particle size of Pt, resulting in the lower activities for electro-oxidation of adsorbed CO. Core level of Pt in the electronic structure for Pt subnano-clusters are shifted to higher binding energies, indicating chemical interaction between Pt and graphene. The interaction is explained by π–d hybridization.

References

[1] A. K. Geim, K. S. Novoselov, Nat. Mater., **6**, 183–190 (2007).

[2] E. Antolini, Applied Catalysis B: Environmental, **123–124**, 52–68 (2012).

[3] L. Dong, R. R. S. Gari, Z. Li, M. M. Craig, S. Hou, Carbon, **48**, 781–787 (2010).

[4] S. Bong, Y. R. Kim, I. Kim, S. Woo, S. Uhm, J. Lee, H. Kim, Electrochem. Commun., **12**, 129–131 (2010).

[5] E. J. Yoo, T. Okada, T. Akita, M. Kohyama, J. Nakamura, I. Honma, Nano Lett., **9**, 2255–2259 (2009).

[6] E. J. Yoo, T. Okada, T. Akita, M. Kohyama, I. Honma, J. Nakamura, J. Power Sources, **196**, 110–115 (2011).

[7] Y. Tang, Z. Yang, X. Dai, Phys. Chem. Chem. Phys., **14**, 16566–16572 (2012).

[8] A. Rochefort, D. Q. Yang, E. Sacher, Carbon, **47**, 2233–2238 (2009).

[9] G. Kim, S. Jhi, ACS Nano, **5**, 805–810 (2011).

[10] P. Blonski, J. Hafner, J. Chem. Phys., **134**, 154705, 1–12 (2011).

[11] G. Kim, Y. Kawazoe, K. Lee, J. Phys. Chem. Lett., **3**, 1989–1996 (2012).

[12] K. O. Maeda, Y. Morikawa, S. Tanaka, M. Kohyama, Surf. Sci., **604**, 144–154 (2010).

[13] R. Siburian, J. Nakamura, J. Phys. Chem. C, **116**, 22947–22953 (2012).

[14] E. J. Yoo, J. Kim, E. Hosono, H. S. Zhou, T. Kudo, I. Honma, Nano Lett., **8**, 2277–2282 (2008).

[15] J. Moulder, W. F. Stickle, P. E. Sobol, K. D. Bomben, Handbook of X-ray Photoelectron Spectroscopy, Perkin Elmer Corporation, Minnesota, USA, 1992.

[16] B. Seger, P. V. Kamat, J. Phys. Chem. C, **113**, 7990–7995 (2009).

[17] Y. Si, E. T. Samulski, Nano Lett., **8**, 1679–1682 (2008).

[18] G. Attard, C. Barnes, Surfaces, third edition, Oxford Science Publications, Oxford, 2004.

[19] M. Sogaard, M. Odgaard, E. M. Skou, Solid State Ionics, **145**, 31–35 (2001).

[20] J. B. Joo, P. Kim, W. Kim, Y. Kim, J. Yi, J Appl. Electrochem., **39**, 135–140 (2009).

[21] T. Vidakovic, M. Christov, K. Sundmacher, Electrochim. Acta, **52**, 5606–5613 (2007).

[22] O. V. Cherstiouk, P. A. Simonov, E. R. Savinova, Electrochim. Acta, **48**, 3851–3860 (2003).

[23] V. A. Murugan, T. Muraliganth, A. Manthiram, Chem. Mater., **21**, 5004–5006 (2009).

[24] A. Pozio, M. De Francesco, A. Cemmi, F. Cardellini, L. Giorgi, J. Power Sources, **105**, 13–19 (2002).

[25] M. Arenz, K. J. J. Mayrhofer, V. Stamenkovic, B. B. Blizanac, T. Tomoyuki, P. N. Ross, N. M. Markovic, J. Am. Chem. Soc., **127**, 6819–6829 (2005).

[26] C. Bittencourt, M. Hecq, A. Felten, J. J. Pireaux, J. Ghijsen, M. P. Felicissimo, P. Rudolf, W. Drube, X. Ke, G. V. Tendeloo, Chem. Phys. Lett., **462**, 260–264 (2008).

[27] F. Maillard, E. R. Savinova, P. A. Simonov, V. I. Zaikovskii, U. Stimming, J. Phys. Chem. B, **108**, 17893–17904 (2004).

[28] G. Garcia, M. T. M. Koper, Phys. Chem. Chem. Phys., **10**, 3802–3811 (2008).

[29] S. W. Lee, S. Chen, J. Suntivich, K. Sasaki, R. R. Adzic, Y. S. Horn, J. Phys. Chem. Lett., **1**, 1316–1320 (2010).

[30] T. Kondo, K. Izumi, K. Watahiki, Y. Iwasaki, T. Suzuki, J. Nakamura, J. Phys. Chem. C, **112**, 15607–15610 (2008).

[31] J. Oh, T. Kondo, D. Hatake, Y. Iwasaki, Y. Honma, Y. Suda, D. Sekiba, H. Kudo, J. Nakamura, J. Phys. Chem. Lett., **1**, 463–466 (2010).

[32] T. Kondo, T. Suzuki, J. Nakamura, J. Phys. Chem. Lett., **2**, 577–580 (2011).

[33] T. Kondo, W. Iwasaki, Y. Honma, Y. Takagi, S. Okada, J. Nakamura, Phys. Rev. B, **80**, 233408, 1–4 (2009).

[34] T. Kondo, Y. Honma, J. Oh, T. Machida, J. Nakamura, Phys. Rev. B, **82**, 153414, 1–4 (2010).

[35] T. Kondo, S. Casolo, T. Suzuki, T. Shikano, M. Sakurai, Y. Harada, M. Saito, M. Oshima, M. I. Trioni, G. F. Tantardini, J. Nakamura, Phys. Rev. B, **86**, 035436, 1–6 (2012).

Chapter 4

Formation Process of Pt Subnano-Clusters on Graphene Nano Sheets

The formation mechanism of Pt subnano-clusters composed of 5–40 Pt atoms on graphene nano sheets (GNS) has been studied by X-ray diffraction (XRD), X-ray photoelectron spectroscopy (XPS), and transmission electron microscope (TEM). The exchange of Cl^- ion by OH^- ion and the reduction of Pt^{4+} to Pt^{2+} are examined by XPS in the reduction of an H_2PtCl_6 catalyst precursor by ethanol at different pH. XPS and TEM results show that particles of Pt^{2+}-containing compounds with the sizes of 2–7 nm are first formed on GNS by the reduction of H_2PtCl_6 with ethanol, which are then fully reduced to Pt subnano-clusters by H_2 at 400 ^oC. The proposed mechanism for the Pt subnano-clusters formation includes two pivotal surface reactions: the reduction of Pt^{2+}-particles into isolated Pt atoms by H_2 on the GNS surface, followed by the formation of Pt subnano-clusters by collision of the Pt single atom migrating on GNS.

4.1 Introduction

Graphene nano sheets (GNS) exhibit a unique structure of two-dimensional sheet composed of sp^2-bonded carbon atoms with one-atomic thickness. Recently, graphene has fascinated many researchers because of its unique electronic properties [1], excellent mechanical properties [2], superior thermal properties [3] and specific surface area (2630 $m^2 g^{-1}$) [4]. The application of graphene to catalysts has been reported in the research area of electrocatalysts for fuel cells [5–7]. Platinum (Pt) catalysts supported by GNS have been applied for methanol oxidation reaction (MOR) [5,8–10], hydrogen oxidation reaction (HOR) [11], and oxygen reduction reaction (ORR) [12–14]. In the case of MOR [5,8–10], HOR [11] and ORR [9,12], Pt/GNS catalysts exhibited higher catalytic activities compared to Pt/carbon black (CB). In contrast, some groups have reported that Pt deposited onto graphene sheets showed lower catalytic activities compared to Pt/CB [13]. It has been also reported that the CO-tolerance of Pt/GNS anode catalysts is superior to that of Pt/CB [11]. The improved catalytic performance of Pt/GNS can be explained by the interface interaction between graphene and Pt, probably, via π–d hybridization [15]. It should be noted that Pt subnano-clusters are found to be formed on GNS, which have never been observed for the other graphitic supports [5]. That is, the sizes of Pt particles for Pt/CB range from 1 to 10 nm. The Pt subnano-cluster formation suggests that the interface interaction seems to be intense for graphene compared to the other graphitic carbon. However, the formation mechanism of the Pt subnano-clusters on GNS has not been clarified yet.

The approach taking advantage of the interface interaction for the preparation of Pt catalysts electrode is promising from viewpoints of reducing Pt usages. To this end, novel nanocarbons such as carbon nanotubes or carbon nanohorns have been studied as catalyst supports [16–20]. Concerning the mechanism of the interface interaction, the model studies of Pt-deposited HOPG (highly oriented pyrolitic graphite) have been carried out, in which monolayer Pt clusters are formed and they show a high catalytic activity for H_2–D_2 exchange reaction [21]. The Pt catalysts on HOPG also show a significant reduction in the adsorption energy of CO [22]. Based on the results of electrode catalysts using nanocarbons and the model study using HOPG, one can regard that the interface interaction causes a modification in the electronic structure of Pt particles on carbon, resulting in the modification of catalytic properties.

In the preparation of Pt catalysts supported by nanocarbons such as carbon nanotube and graphene, the choice of preparation method is very important because the surface of nanocarbons is composed of chemically inactive π–conjugated carbons. Many techniques have been reported for preparing highly dispersed Pt catalysts on carbon, namely, colloid methods [23–25] or alcohol reduction methods [26–30]. Herein, I prepared Pt/GNS catalysts by an impregnation method with ethanol as a reduction agent as well as sodium hydroxide solvent. By this method, one can prepare the stable and narrow size distribution of Pt colloids by controlling pH of catalyst solution [31–35].

The aim of this study is to clarify the formation process of Pt subnano-clusters on GNS during the

catalyst preparation. I prepared Pt/GNS catalysts using an H_2PtCl_6 precursor at different pH, in which the formation process of Pt subnano-clusters on GNS was examined by X-ray diffraction (XRD), X-ray photoelectron spectroscopy (XPS), transmission electron microscope (TEM), and thermogravimetric/differential thermal analysis (TG/DTA).

4.2 Experimental

GNS was obtained via a solution-based route, involving the chemical oxidation of graphite to hydrophilic graphite oxide [36]. Graphite oxides were made by the Hummers method [37]. Graphite oxides were easily exfoliated to form individual graphene oxide sheets by ultra-sonication in water. The graphene oxide sheets were then reduced to GNS by using hydrazine hydrate. The characterization results of GNS have been reported in Chapter 3 (Figures 3.2, 3.3, and 3.4).

The 30 wt % Pt catalysts were deposited onto GNS using the precursor of [$H_2PtCl_6 \cdot 6H_2O$] (Alfa Aesar, A Johnson Matthey Company). An ethanol solution of the precursor was mixed with an ethanol solution of GNS. The pH of the mixed solution was adjusted at pH 1, 6 and 12.5 by dropping 1M NaOH aqueous solution. The pH was measured by using a pH meter. After stirring solution for 3 h, the product was collected by filtration and was dried in air at 60 ^oC for 12 h. It was then reduced by a hydrogen stream 25 mL/min at 400 ^oC for 2h in a furnace. Finally, the catalyst was collected and characterized by XRD, XPS, TEM and TG/DTA. XRD measurements were performed at room temperature employing a two circle diffractometer (PANalytical PW 3050 Philips X'pert Pro, Cu K_α radiation of 1.541 Å, without monochromator), installed at a line focus X-ray generator. A reflection free Si plate was used as a sample stage. Cu K_α radiation obtained by reflection from a singly bent HOPG crystal was used. Diffraction pattern was recorded using a solid state detector (PANalytical X'Celerator) with a scan speed of 0.05 deg. (in 2θ)/sec up to 90 degrees. XPS measurements were carried out using JEOL JPS 9010 TR (X-ray source Al K_α, 1486.6 eV; pass energy 50 eV, energy resolution 1.88 eV which was calibrated using Ag $3d_{5/2}$ by measuring a clean Ag sample, the uncertainty of binding energy ± 0.05 eV). TEM (JEOL JEM-1400 electron microscope was operated at 80 kV, resolution lattice image 0.20 nm, and resolution point image 0.38 nm. TG/DTA measurements were carried out using TG/DTA6300, Seiko Instruments Inc. (Reference: Pt; Air 200 mL/min; T measurement: 50–1000 ^oC; Rate: 10 ^oC/min), respectively.

4.3 Results and Discussion

4.3.1 Formation of Pt subnano-clusters

The physical properties of Pt/GNS catalysts were examined by XRD, XPS and TEM. Figure 4.1 shows the XRD patterns for the Pt/GNS catalysts prepared at pH 1, 6, and 12.5, respectively. The Pt(111) peak was very weak for all the Pt/GNS catalysts. This suggests the formation of very small Pt clusters below 1.5 nm. Here, I confirmed that 25–28 wt % Pt is supported on GNS by TG/DTA measurements (see Appendix 1, Supporting Information, Figure 4S).

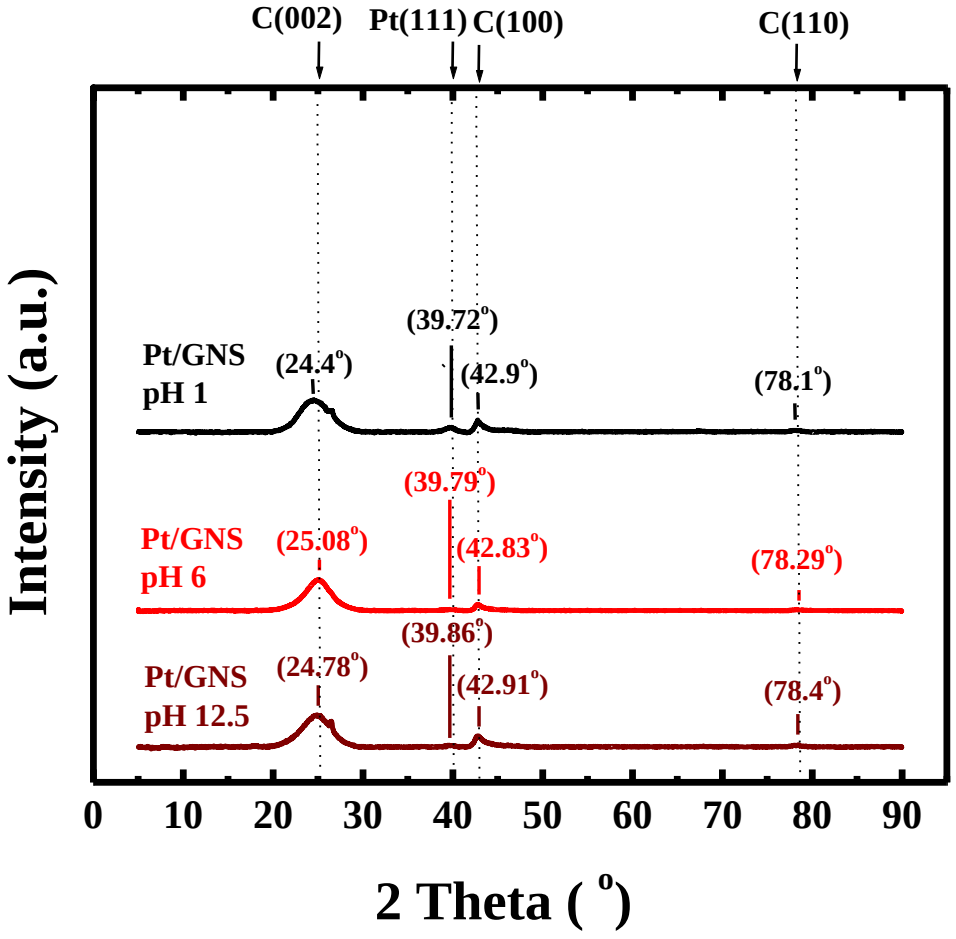

Figure 4.1 XRD patterns of 30 wt % Pt/GNS prepared at pH 1, 6, and 12.5.

The cluster size of Pt was then estimated by TEM. The TEM images and the histogram of the size distribution are shown in Figure 4.2 for Pt/GNS prepared with different pH.

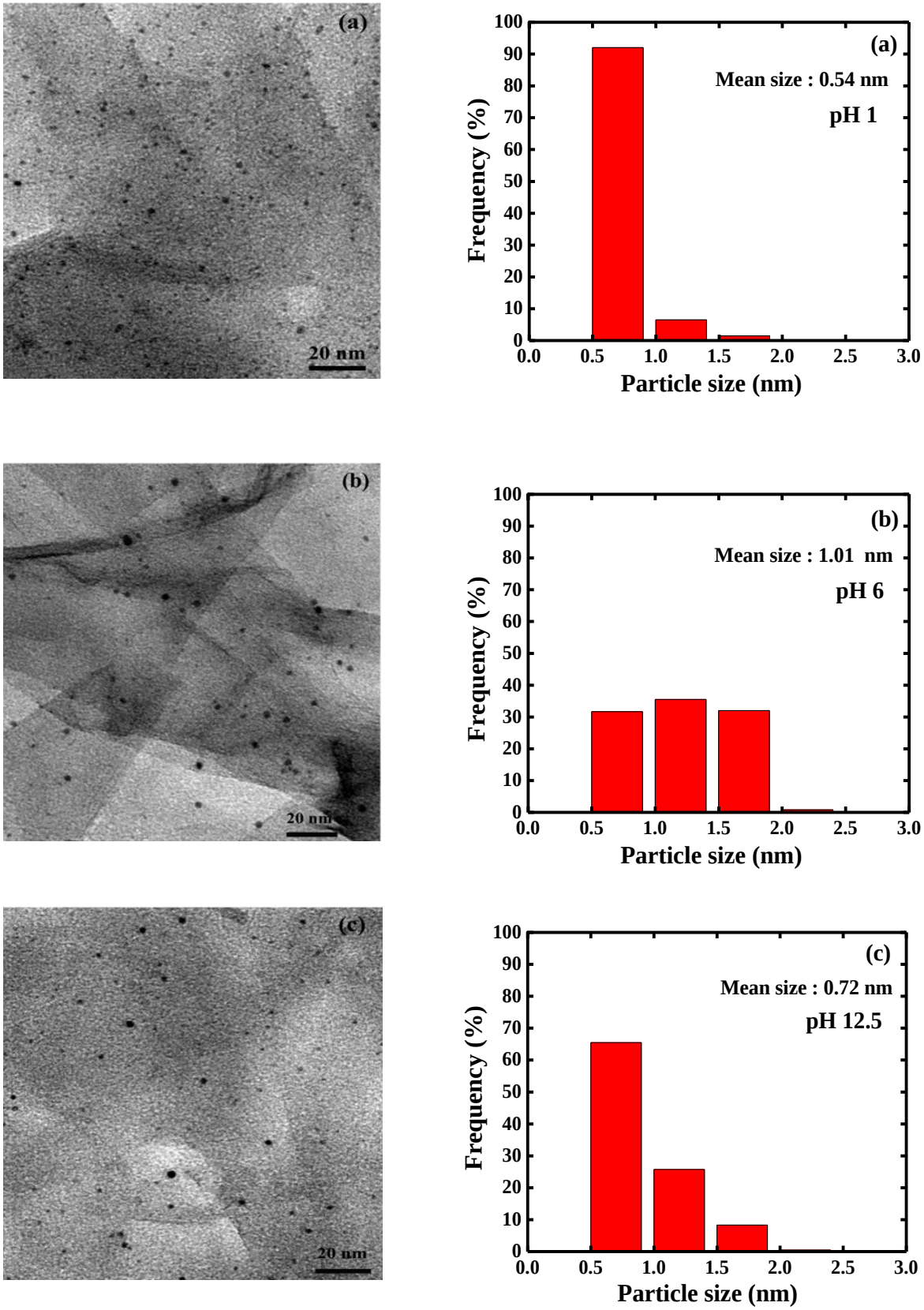

Figure 4.2 TEM images and histograms of 30 wt % Pt/GNS prepared at (a) pH 1, (b) pH 6, and (c) pH 12.5.

The mean cluster sizes were estimated by analyzing a few randomly chosen areas containing 650 clusters in magnified TEM images. It is found that the Pt subnano-clusters were well dispersed on GNS. The average diameters are 0.54, 1.01, and 0.72 nm for the Pt/GNS catalyst prepared at pH 1, 6, and 12.5 as summarized in Table 4.1.

Table 4.1 Average size of Pt clusters.

Catalysts	Cluster size of Pt (TEM) d (nm)
30 wt % Pt/GNS prepared at pH 1	0.54
30 wt % Pt/GNS prepared at pH 6	1.01
30 wt % Pt/GNS prepared at pH 12.5	0.72

It is clearly shown that very small Pt clusters (0.5–1 nm) are supported by GNS, which is consistent with the absence of the Pt XRD peaks. Note that several larger particles (1–2 nm) are observed in TEM, which have been also observed in addition to the Pt subnano-clusters in our previous study [5].

The numbers of Pt atoms in a single subnano-cluster were roughly estimated from the cluster sizes. Figure 4.3 shows possible structures of the Pt subnano-clusters with the size of 0.5–1 nm, assuming that the lattice constant of Pt is identical to that for bulk Pt.

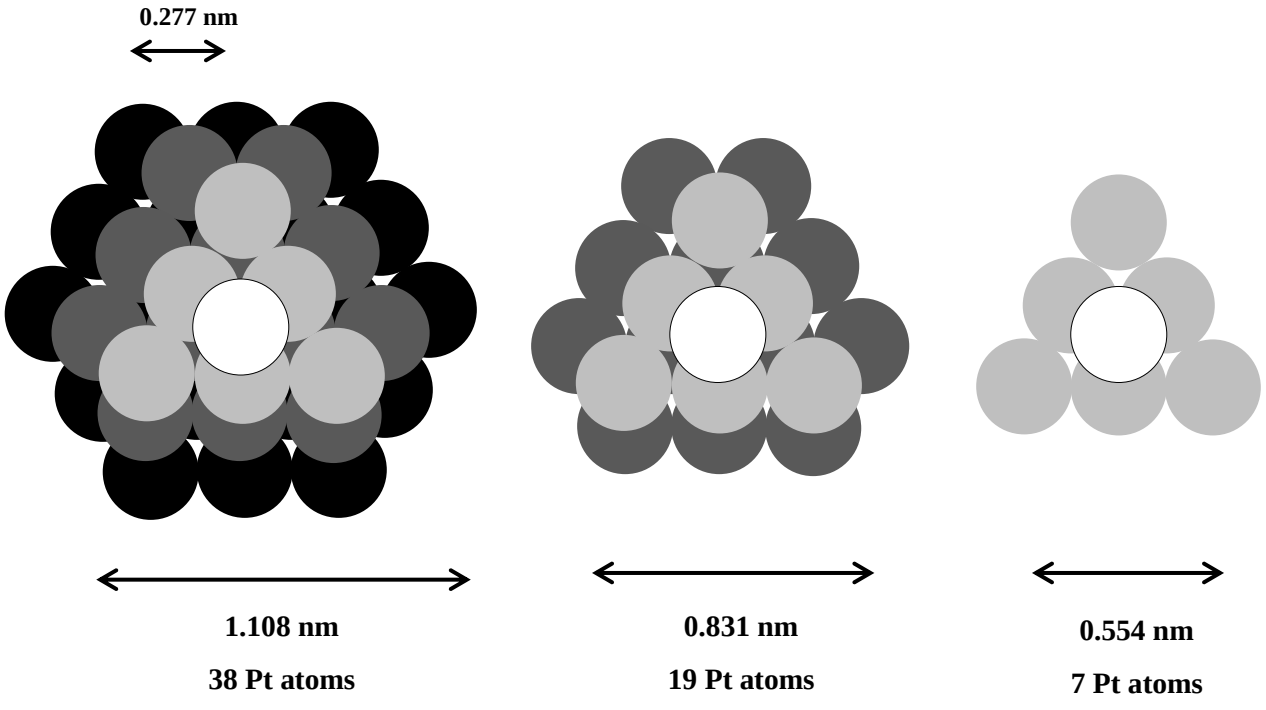

Figure 4.3 Number of Pt atoms included in Pt subnano-clusters.

The number of Pt atoms was thus estimated to be 5–40 in the subnano-clusters. As far as I know, Pt subnano-clusters have never been observed on the other carbon supports. The presence of them on GNS suggests a very strong interface interaction between Pt and GNS. In our research group, the interface interaction between Pt and carbon has been studied by surface science techniques separately [21,22].

4.3.2 Formation chemistry of Pt subnano-clusters

Generally, hexachloroplatinic acid (H_2PtCl_6) has been used as a catalyst precursor for the preparation of Pt catalysts supported on carbonaceous materials. In order to control the size of Pt particles using H_2PtCl_6, it is required to understand the chemistry of the catalyst preparations. I examined the effect of pH on the preparation of the Pt/GNS catalysts because chemistry of the H_2PtCl_6 precursor in the catalyst preparation should be sensitively changed under different pH. In particular, the exchange of Cl^- by OH^- in H_2PtCl_6 has been examined by XPS because the elimination of Cl^- from H_2PtCl_6 may be an important reaction step in the preparation of the Pt subnano-clusters.

Here, the procedures of the catalyst preparation are divided into three steps: step 1 is the preparation of the precursor solution using ethanol at different pH (1, 6, and 12.5) in the absence of GNS, step 2 is the reduction of the precursor solution by ethanol in the presence of GNS, and step 3 is the full reduction of Pt species attached on GNS by H_2. Figures 4.4–4.6 show the XPS results of samples after step 1, 2, and 3, respectively. Note that no GNS is used in step 1 (Figure 4.4), whereas GNS is used as a support material in steps 2 (Figure 4.5) and 3 (Figure 4.6).

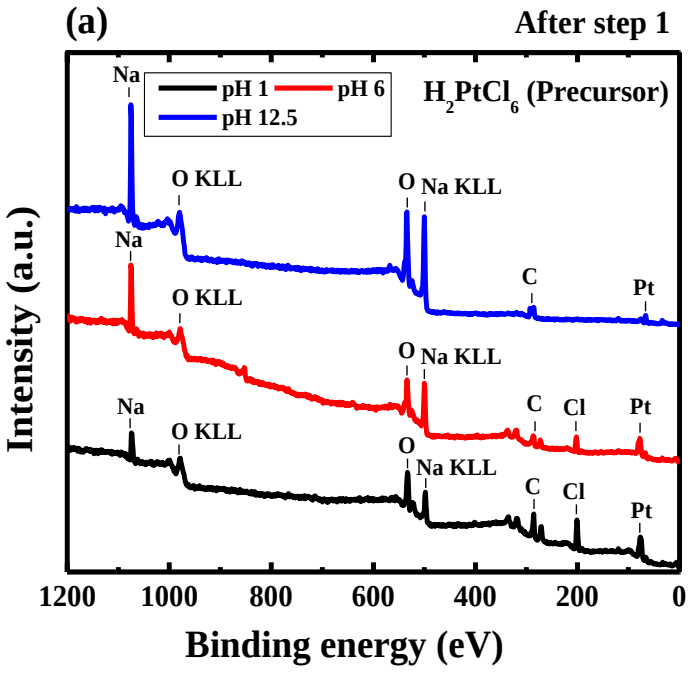

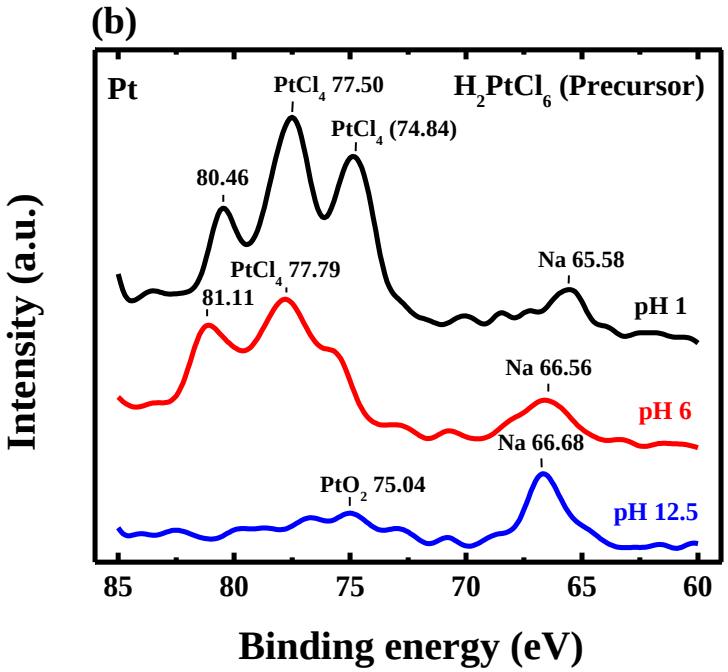

Figure 4.4 (a and b) XPS wide scan spectra of the samples after step 1.

After step 1 (Figure 4.4), the XPS peak due to Cl 2p was observed, which decreased in intensity with increasing pH (Figure 4.4a). At pH 1 and 6, the atomic ratios of Cl to Pt are 5.2 and 2.8 (Table 4.2), suggesting that $[PtCl_5(OH)]^-$ and $[PtCl_3(OH)]^-$ are mainly formed, respectively.

Table 4.2 Atomic ratio of samples (XPS measurement).

Samples	Cl/Pt	O/Pt	Na/Pt	C/Pt
30 wt % Pt/GNS prepared at pH 1				
step 1	5.2	2.8	2.0	–
step 2	–	18.8	–	34.1
step 3	–	14.3	–	68.1
prepared at pH 6				
step 1	2.8	6.7	1.0	–
step 2	–	19.2	–	36.6
step 3	–	13.9	–	85.4
prepared at pH 12.5				
step 1	0.4	9.2	0.4	–
step 2	–	19.3	–	37.3
step 3	–	15.1	–	84.3

On the other hand, the Cl 2p peak disappears for pH 12.5, suggesting that Cl^- in H_2PtCl_6 is replaced by OH^- to form $[Pt(OH)_6]^{2-}$ ions because of the high pH. Note that the valence of Pt in the complexes of $[PtCl_6]^{2-}$, $[PtCl_5(OH)]^{2-}$, and $[Pt(OH)_6]^{2-}$ are all assigned to be Pt^{4+} based on the Pt $4f_{7/2}$ peaks at 74.8–75.5 eV in Figure 4.4b, where the Pt $4f_{7/2}$ peak of $PtCl_4$ is known to appear at 75.5 eV in the literature [38]. On the other hand, the Pt 4f peak at around 80 eV for pH 1 and 6 is unknown because the information for that peak is not available in the literature [38]. This may be due to a charge-up effect in XPS because Pt complexes are insulator. The following reactions may thus occur at different pH as below:

Step 1

At pH 1,

$$[PtCl_6]^{2-} + OH^- \longrightarrow [PtCl_5(OH)]^- + Cl^-$$

At pH 6,

$$[PtCl_6]^{2-} + 3OH^- \longrightarrow [PtCl_3(OH)_3]^{2-} + 3Cl^-$$

At pH 12.5,

$$[PtCl_6]^{2-} + 6OH^- \longrightarrow [Pt(OH)_6]^{2-} + 6Cl^-$$

Here, it is possible that H_2O ligand is partially replaced by Cl^- instead of OH^-. The important point is that the replacement of Cl^- is controlled by pH. At pH 1, a Cl^- ligand is exchanged by OH^- (or H_2O). Then, at pH 6, more Cl^- ions are replaced than that at pH 1. It is known that $Na_2[Pt(OH)_6]$ is insoluble [39] so that the salt should be precipitated at pH 12.5, which is consistent with the intense Na peak in XPS (Figure 4.4a). The present results are also consistent with the results in the literature [39].

In step 2, GNS is added in the precursor solution mixed with ethanol. Here, I observed a significant shift in the Pt 4f peak for the catalyst samples obtained after the step 2 procedures. Figure 4.5b exhibits Pt $4f_{7/2}$ (73.3–73.5 eV) and Pt $4f_{5/2}$ (75.5–75.9 eV) peaks for Pt/GNS catalyst prepared at pH 1, 6 and 12.5.

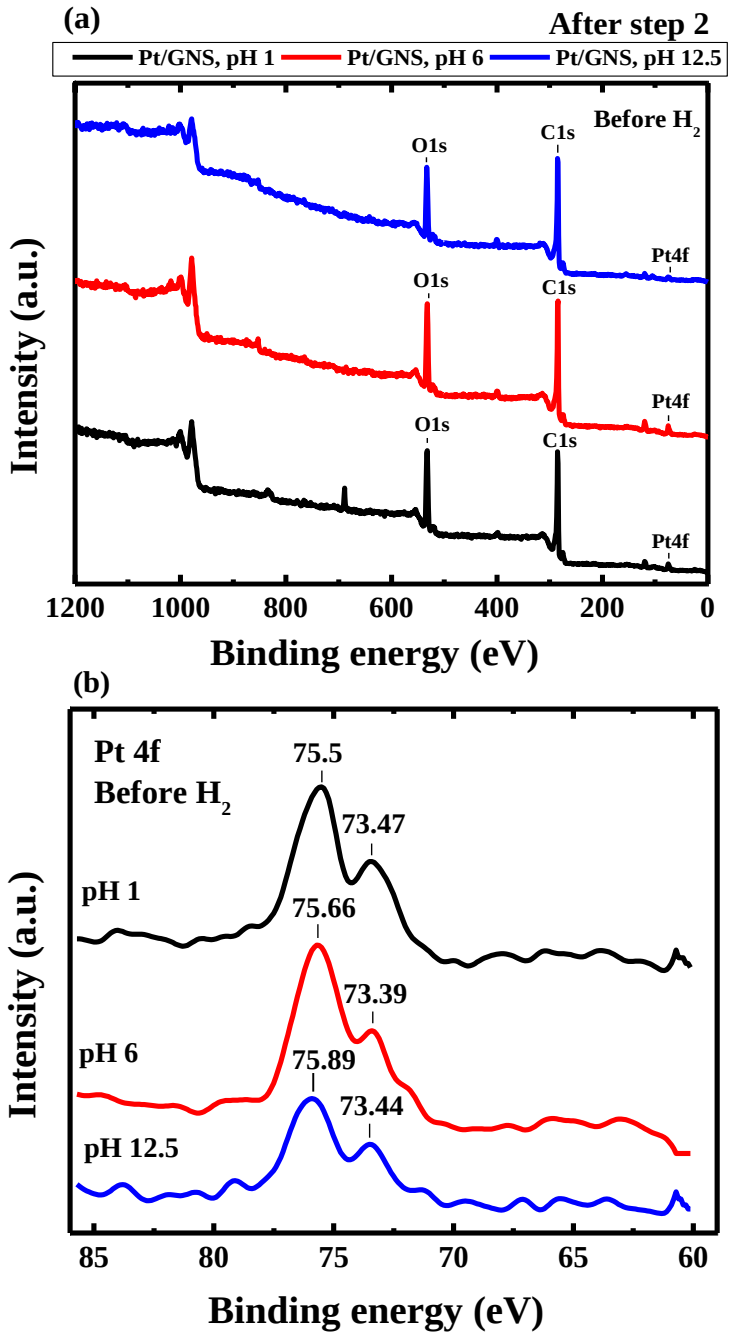

Figure 4.5 (a and b) XPS spectra of the samples after step 2.

It clearly shows that Pt 4f peaks shift to lower binding energies after step 2, however, which are higher than that of Pt^{0} (74.0 and 71.2 eV). In the literature [38], the Pt $4f_{7/2}$ binding energies of 73.3–73.5 eV agree with that of $Pt(OH)_2$ (72.36–73.81 eV). That means the valence state changes from Pt^{4+} to Pt^{2+}. This is very interesting because the presence of GNS apparently promotes the reduction of Pt^{4+} complexes by ethanol.

Step 2

+ GNS

Pt^{4+} ⟶ Pt^{2+}

+ Et–OH

Note that the XPS peaks of Cl and Na disappear after step 2 as shown in Figure 4.5a, suggesting that Pt^{2+} is bound with oxygen-containing ligands only. This is consistent with the atomic ratio of O to Pt (Table 4.2). It is thus concluded that PtO or $Pt(OH)_2$ particles are formed in step 2. The CO or COO species may be also formed as functional groups at the edges of GNS when treating GNS with H_2PtCl_6 acid and ethanol [40].

Finally, in step 3, it is found that Pt^{2+} is reduced to Pt^0 by H_2 reduction at 400 ^oC based on the XPS results of Pt 4f. Figure 4.6 shows XPS spectra for Pt/GNS after step 3.

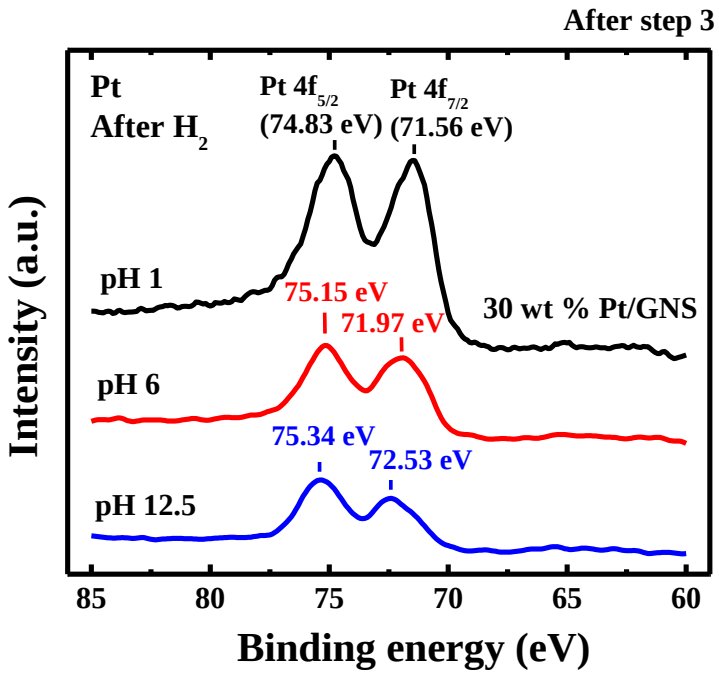

Figure 4.6 XPS spectra of the samples after step 3.

The results show that the binding energies of Pt 4f correspond to those for Pt metal (74.0 and 71.2 eV). That is, Pt^{2+} is fully reduced to Pt^0 in step 3.

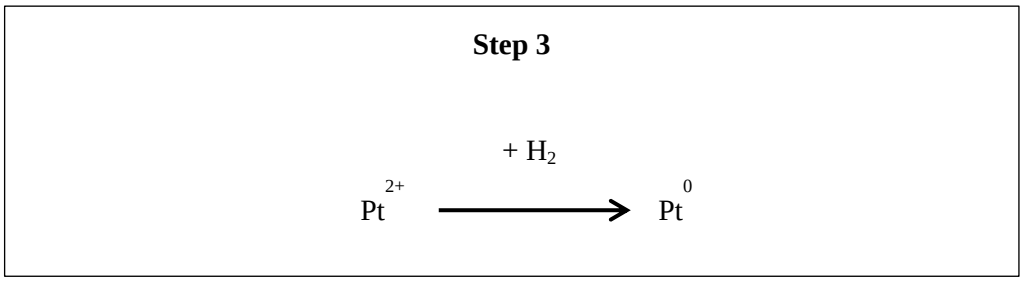

In Table 4.2, the atomic ratio of O to Pt for Pt/GNS after the H_2 reduction is smaller than that for Pt/GNS before the H_2 reduction. It also indicates the reduction of Pt species. Note that the binding energies of Pt 4f for the sample prepared at pH 1, 6 and 12.5 are little higher than that for metallic Pt, suggesting that Pt particles are interacted with graphene significantly via the π–d hybridization [15].

4.3.3 Mechanism of Pt subnano-clusters formation

In order to examine the mechanism of the Pt subnano-clusters formation on GNS, I then observed the catalyst samples after step 2 and step 3 by TEM as shown in Figure 4.7.

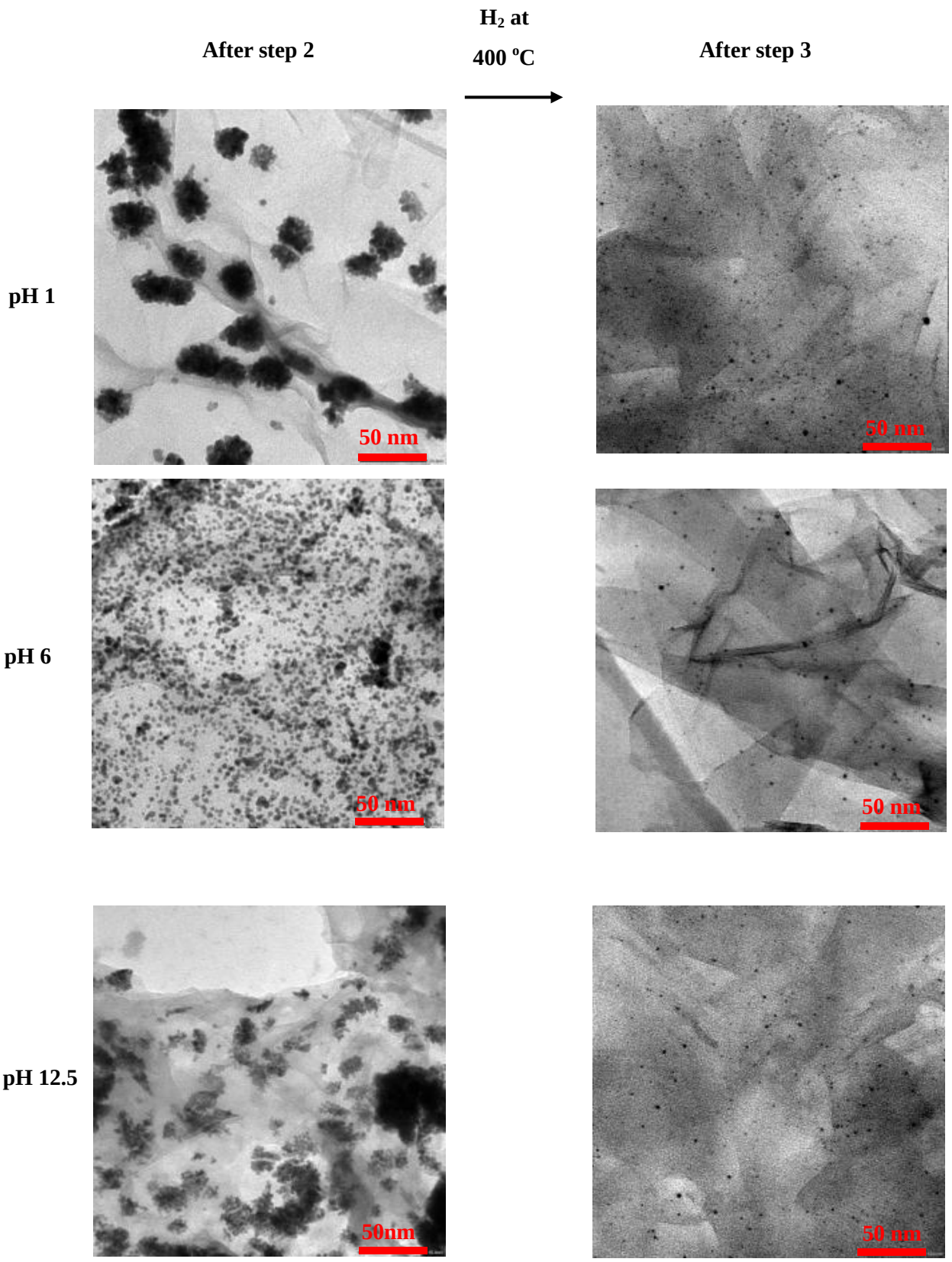

Figure 4.7 TEM images after steps 2 and 3 for Pt/GNS prepared at pH 1, 6, and 12.5.

For the sample after step 2 prepared at pH 1, large aggregates with sizes of 15–50 nm were observed, where the aggregates are composed of small particles with 3–6 nm. In contrast, at pH 6 and 12.5, dispersed particles with size of 2–7 nm were observed on GNS. The influence of pH condition is thus observed in step 2. Interestingly, after the H_2 reduction, these large particles prepared at any pH can be dispersed to form Pt subnano-clusters on GNS as shown in Figure 4.7. That is, during the reduction of the Pt^{2+}-containing complexes or salts by H_2, the Pt subnano-clusters are formed. The possible mechanism is schematically shown in Figure 4.8, which includes the reduction of Pt^{2+} into Pt metal occurring on the surface of Pt^{2+}-containing compounds, the migration of a single Pt atom on the GNS surface, and the formation of Pt subnano-clusters by the collision of the Pt atom.

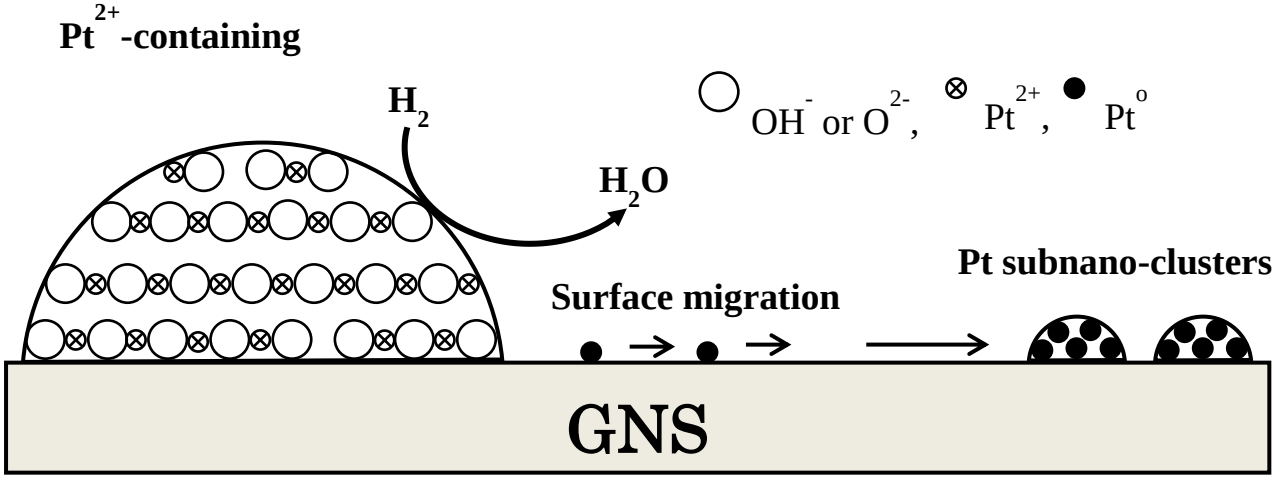

Figure 4.8 Formation mechanisms of Pt subnano-clusters.

I have also prepared Pt/GNS catalysts using a strong reductant of $NaBH_4$ instead of ethanol. However, no formation of Pt subnano-clusters was observed, where large Pt particles (2–5 nm) are mainly formed (Figure 6S, Appendix 1, Supporting Information). Only the preparation method by the gradual reduction via Pt^{4+} and Pt^{2+} species leads to the formation of Pt subnano-clusters (see Figures 5S–8S, Appendix 1, Supporting Information).

Question arises as to why Pt subnano-clusters are formed on graphene, but not on the other graphitic materials. I consider two factors, enthalpy and entropy factors. As for the enthalpy factor, the interface interaction between Pt and carbon via the π–d hybridization is significant for graphene due to the reactivity of graphene's π–conjugated states. The reactivity is different from that of the other graphitic materials. In graphite, two types of carbon are there, α and β carbon, where the former has carbon beneath in the under layer while the latter has no such a carbon. In scanning tunneling microscope (STM) measurements, only β-carbon can be imaged, suggesting overlapping of p_z orbital of α–carbon, i.e., some hybridization. In this sense, the two carbons are different in terms of electronic structure. In fact, an angle-resolved photoemission

spectroscopy (ARPES) study of HOPG has reported a band gap structure coexisting with the metal character due to the π–conjugated state [41]. Due to the absence of the hybridization of p_z orbital causing the band gap, the reactivity of graphene is expected to be significant compared to graphite. As the entropy factor, on the other hand, a large surface area of support materials should be generally required for a high dispersion of small particles. The prerequisite is satisfied for graphene supported Pt catalysts because of the large surface area. It is thus considered that the driving factors for the formation of Pt subnano-clusters are ascribed to the π–d hybridization between carbon and Pt as well as the large surface area of graphene.

Finally, the aggregates observed in TEM after step 2 are discussed. Considering the results of XPS, it is possible that the aggregates observed for pH 1 are $H_2[Pt(OH)_4]$ species, which are major species in the following equilibrium at low pH:

$$2H^+ + [Pt(OH)_4(H_2O)_4]^{2-} \longleftrightarrow H_2[Pt(OH)_4(H_2O)_4]$$

The neutrally charged property of $H_2[Pt(OH)_4(H_2O)_4]$ or $H_4[Pt(OH)_4]$ can explain the formation of the aggregates, where the attractive interaction in the aggregates is van der Waals interaction. That may be the reason for the formation of the aggregates at pH 1. On the other hand, for pH 6 and 12.5, the equilibrium of the $H_2[Pt(OH)_4(H_2O)_4]$ reaction should be shifted to the left hand side. As the results, negatively charged $[Pt(OH)_4(H_2O)_4]^{2-}$ or $[Pt(OH)_4]^{2-}$ ions will form, which then probably react with GNS. This model can explain i) the adsorption of Pt^{2+}-containing species on GNS (Figure 4.5b) and ii) the difference in the atomic ratio of O/Pt between steps 2 and 3, 4.5, 5.3, and 4.2 for pH 1, 6, and 12.5, respectively (Table 4.2), where the O/Pt ratio after step 3 may correspond to the residual oxygen at the edges of GNS. I consider that the particles shown in Figure 4.8 are composed of $Pt(OH)_2$ small crystals. I add supporting information about the XRD patterns of the sample after step 2 (Figure 9S, Appendix 1), which are too complex to identify the structures. This may be due to the formation of different kinds of Pt^{2+}-containing compounds with hydroxyl groups.

4.4 Conclusion

I have studied the formation process of Pt subnano-clusters on GNS from H_2PtCl_6 with ethanol at different pH. Aggregates of Pt^{2+}-containing compounds ranging from 2–30 nm in diameter are first attached on GNS by the partial reduction with ethanol. The Pt subnano-clusters are found to be formed in the reduction process of the Pt^{2+}-containing compounds by H_2 at 400 ^oC. I propose a formation model of the Pt subnano-clusters that Pt atoms formed by the reduction with H_2 migrate and collide with each other on GNS, leading to the formation of Pt subnano-clusters. The driving factors for the Pt subnano-clusters formation are ascribed to intense π–d hybridization between carbon and Pt as well as the large surface area of graphene.

References

[1] K. S. Novoselov, A. K. Geim, Science, **6**, 183–188 (2007).

[2] C. Lee, X. Wei, J. W. Kysar, J. Hone, Science, **321**, 385–388 (2008).

[3] A. A. Balandin, S. Ghosh, W. Bao, I. Calizo, D. Teweldebrhan, F. Miao, C. N. Lau, Nano Lett., **8**, 902–907 (2008).

[4] M. D. Stoller, S. Y. Park, J. An. Zhu, R. S. Ruoff, Nano Lett., **8**, 3498–3502 (2008).

[5] E. J. Yoo, T. Okata, T. Akita, M. Kohyama, J. Nakamura, I. Honma, Nano Lett., **9**, 2255–2259 (2009).

[6] B. Seger, V. P. Kamat, J. Phys. Chem. C., **19**, 7990–7995 (2009).

[7] S. Zhang, Y. Shao, H. Liao, M. H. Engelhard, G. Y. Geping, Y. L. Yuehe, ACS Nano, **5**, 1785–1791 (2011).

[8] Y. Li, L. Tang, J. Li, Electrochem. Comm., **11**, 846–849 (2009).

[9] Y. Xin, J. Liu, Y. Zhou, W. Liu, J. Gao, Y. Xie, Y. Yin, Z. Zou, J. Power Sources, **196**, 1012–1018 (2011).

[10] S. M. Choi, M. H. Seo, H. J. Kim, W. B. Kim, Carbon, **49**, 904–909 (2011).

[11] E. J. Yoo, T. Okada, T. Akita, M. Kohyama, I. Honma, J. Nakamura, J. Power Sources, **196**, 110–115 (2011).

[12] H. W. Ha, Y. I. Kim, S. J. Hwang, R. S. Ruoff, Electrochem. Sol. State Lett., **14**, B70–B73 (2011).

[13] Y. S. Yun, D. Kim, Y. Tak, H. J. Jin, Synth. Met., **161**, 2460–2465 (2011).

[14] M. H. Seo, S. M. Choi, H. J. Kim, W. B. Kim, Electrochem. Comm., **13**, 182–185 (2011).

[15] S. Marchini, S. Gunther, J. Wintterlin, Phys. Rev. B., **76**, 075429–1–175429 (2007).

[16] J. Nakamura, *Molecular Catalysts for Energy Conversion*, Eds. T. Okada, M. Kaneko, Springer series in Materials Science, **111**, 185–197 (2008).

[17] E. Antolini, Appl. Catal. B: Environ., **88**, 1–24 (2009).

[18] T. Matsumoto, T. Komatsu, K. Arai, T. Yamazaki, M. Kijima, H. Shimizu, Y. Takasawa, J. Nakamura, Chem. Commun., **7**, 840–841 (2004).

[19] T. Matsumoto, T. Komatsu, H. Nakano, K. Arai, Y. Nagashima, T. Yamazaki, M. Kijima, H. Shimizu, Y. Takasawa, Catal. Today, **90**, 277–281 (2004).

[20] E. J. Yoo, T. Okada, T. Kizuka, J. Nakamura, J. Power Sources, **180**, 221–226 (2008).

[21] T. Kondo, K. Izumi, K. Watahiki, Y. Iwasaki, T. Suzuki, J. Nakamura, J. Phys. Chem. C, **112**, 15607–15610 (2008).

[22] J. Oh, T. Kondo, D. Hatake, Y. Iwasaki, Y. Honma, Y. Suda, D. Sekiba, H. Kudo, J. Nakamura, J. Phys. Chem. Lett., **1**, 463–466 (2010).

[23] T. S. Ahmadi, Z. L. Wang, T. C. Green, A. Henglein, M. A. El-Sayed, Science, **272**, 1924–1926 (1996).

[24] S. R. Wang, W. J. Tseng, J. Nanopart. Res., **11**, 947–953 (2009).

[25] H. Bönnemann, R. M. Richards, Eur. J. Inorg. Chem., 2455–2480 (2001).

[26] T. Teranishi, M. Hosoe, T. Tanaka, M. Miyake, J. Phys. Chem. B, **103**, 3818–3827 (1999).

[27] B. Fang, N. K. Chaudhari, M. S. Kim, J. H. Kim, J. S. Yu, J. Am. Chem. Soc., **131**, 15330–15338 (2009).

[28] C. Y. Kim, S. H. Jeong, S. C. Yi, J. Ceramic Processing Research, **8**, 445–449 (2007).

[29] C. Bock, C. Paquet, M. Couillard, G. A. Botton, B. R. MacDougall, J. Am. Chem. Soc., **126**, 8028–8037 (2004).

[30] D. G. Duff, P. P. Edwards, B. F. G. Johnson, J. Phys. Chem., **99**, 15934–15944 (1995).

[31] H. Hirai, Y. Nakao, N. Toshima, K. Adachi, Chem. Lett., **5**, 905–910 (1976).

[32] N. Toshima, T. Yonezawa, New J. Chem., 1179–1201 (1998).

[33] Z. Liu, L. Hong, M. P. Tham, J. Power Sources, **161**, 831–835 (2006).

[34] X. Wang, I. M. Hsing, Electrochimica Acta, **47**, 2981–2987 (2002).

[35] C. L. Hui, X. G. Li, I. M. Hsing, Electrochimica Acta, **51**, 711–719 (2005).

[36] E. J. Yoo, J. Kim, E. Hosono, H. S. Zhou, T. Kudo, I. Honma, Nano Lett., **8**, 2277–2282 (2008).

[37] W. S. Hummers, R. J. Offeman, J. Am. Chem. Soc., **80**, 1339–1339 (1958).

[38] J. Moulder, W. F. Stickle, P. E. Sobol, K. D. Bomben, Handbook of X-ray Photoelectron Spectroscopy, Perkin Elmer Corporation, Minnesota, USA, 1992.

[39] W. A. Spieker, J. Liu, J. T. Miller, A. J. Kroph, J. R. Regalbuto, Appl. Catal. A. Gen., **232**, 219–235 (2002).

[40] A. S. Escribano, F. Coloma, F. R. Reinoso, Appl. Catal. A. Gen., **173**, 247–257 (1998).

[41] T. Ohta, A. Bostwick, J. L. McChesney, T. Seyller, K. Horn, E. Rotenberg, Phys. Rev. Lett., **98**, 206802, 1–4 (2007).

Chapter 5

Effect of N-doped graphene for Properties of Pt/N-doped graphene catalyst

In chapter 3, I have reported about the GNS as a support material for Pt/GNS catalyst. The results exhibited that free defect GNS has a good performance as a support material for Pt/GNS catalyst. However, the effect of graphene defect as a support material for Pt catalyst is not clearly understood. In this chapter, I describe the effect of N-doped graphene for Pt/N-doped graphene catalyst properties. The abstract of the Chapter 5 is as follows.

Nitrogen doping into graphene was carried out by heating GNS in ammonia to produce N-doped graphene (N-G). The N-G was used as a support material for Pt catalyst as well as a catalyst itself for half-cell cathode reaction of hydrogen fuel cell (H_2FC). It is found that the ORR electrocatalytic activity for N-G 900 (0.63 V versus RHE) is higher than GNS. It indicates that the incorporation of nitrogen in N-G may affect the ORR activities. XPS results exhibit the pyridinic N is the majority in N-G, where the pyridinic N refers to N atom bonds with two C atoms at the edges or defects of graphene. Interestingly, the Pt subnano-clusters were formed on all of Pt/N-G catalysts with Pt particle size (0.7–1.0 nm). It clearly indicates that the doping of nitrogen significantly influence π–d hybridization in terms of electronic structures.

5.1 Introduction

Graphene, a single layer of sp^2-bonded carbon atoms arranged in a honeycomb lattice, has been attracting much attention due to its fascinating properties [1], such as high surface area (2630 $m^2 g^{-1}$) [2], high thermal conductivity (~ 4840–5300 $W m^{-1} K^{-1}$) [3], fast charged carrier mobility (~ 200 000 $cm^2 V^{-1} s^{-1}$) [4], strong Young's modulus (~ 1 TPa) [5], and high carrier mobility (10^4 $cm^2 V^{-1} s^{-1}$ at room temperature) [1]. All these aspects make graphene material promising for various applications, including energy conversion and storage, electrocatalysis, sensors and electronics [6].

However, the absence of a band gap in perfect graphene does not allow switching of graphene-based transistors with a high enough on-off ratios. Hence, graphene has to be modified even when making basic devices and, even more, for manufacturing sophisticated circuits. Therefore, the defect in graphene can be hoped to alter its properties. It is well known that defects are not always stationary and that their migration can have an important influence on the properties of a defective crystal. The migration is generally governed by an activation barrier which depends on the defect type and increases exponentially with temperature. Defects can be done by using irradiation or chemical treatments. The chemical treatment, for instance chemical dopant may change the local electronic structure or inject charge into the electron system of sp^2-bonded carbon materials [7].

Aforementioned, the chemical doping is an important way to modulate the properties of graphene sheets. There are two means to chemically dope graphene: (i) the adsorption of gas, metal, or organic molecules to the graphene surface and (ii) substitution doping, which introduces heteroatoms, such as nitrogen atoms or boron atoms, into the carbon lattice of graphene. Substitution doping, which replaces some of carbon atoms in sp^2-network with foreign atoms such as nitrogen or boron, is more favorable than molecular doping from the viewpoint of structural robustness [8]. Both of these methods can modulate the electronic properties of graphene [6]. Doping nitrogen on carbon material is usually fulfilled via treatment of carbons by gaseous ammonia (NH_3), which it can enhance the conductivity of graphene [9] and incorporating different types of nitrogen into the carbon network would provide N-doped graphene with more functional groups for property design [10].

The N-doped graphene shows different properties compared with the pristine graphene. For instance, it exhibits high electrocatalytic activities for the oxygen reduction reaction (ORR). A possible approach to enhancing ORR activity is to introduce abundant defects and functional groups onto graphene to increase the number of catalytic sites. This is caused the nitrogen doping introduces spin density to the graphene and changes the atomic charge distribution on it. Note that, the catalytic active sites on the N-doped graphene have either high positive spin density or high positive atomic charge density [11]. That is why, this kind of activated region can participate in catalytic reactions directly, such as ORR, or anchor the metal nanoparticles used in the catalytic reaction [6]. Among the N-doped structure, the pyridinic N was reported

to play an important role in the enhanced ORR activity in acidic solution [12] and alkaline solution [13]. The computational study shows the graphene which contains N atoms at specific sites can exhibit metal-free catalytic activity [14]. Nevertheless, only a few of experimental studies have been reported so far about synthesis N-doped graphene, such as growth of N-doped graphene on Pt(111) surface [8] and synthesis of N-doped graphene by using chemical vapor deposition (CVD) method, whereas a metal catalyst (Cu or Ni) is used as substrate, then at high temperature, a carbon source gas mixed with a N-containing gas is introduced [6]. Thus, fabrication of N-doped graphene is strongly required.

The development of fuel cells as a clean-energy technology is largely limited by the prohibitive cost of the noble-metal catalysts which needed for catalyzing the ORR in fuel cells. The ORR taking place at the cathode of polymer-electrolyte-membrane fuel cells (PEMFC) has been attracting much attention because of the desire to elucidate its slow kinetics on electrocatalyst surfaces whereas this slow kinetics is one of the bottlenecks for achieving improved efficiencies in the fuel cell operation [15]. ORR catalysts based on precious metals such as platinum (Pt) or its alloys are routinely used in fuel cells because of their high activity and may promote the chemical reaction. The Pt nanoparticles supported by carbon nanostructures are a popular catalyst/support combination for many reactions including electricity generation using fuel cells [16]. However, Pt is expensive and susceptible to time-dependent drift and CO poisoning. Thus, developing inexpensive electrocatalysts with high catalytic activity will accelerate the process of fuel cell commercialization [17].

A low reduction oxygen rate at the cathode is one of the major challenges to overcome [18]. Although some theoretical work has been done on ORR pathways on N-doped graphene [11,19], the role of N-doped graphene for ORR activity remains unclear [17]. There are two strategies in order to improve the cathode long-term activity, namely enhancement of interaction between Pt and support materials and development of corrosion support material [20–22]. Therefore, the innovation to invent the high ORR catalytic activity is needed because it is recognized be able to improve catalyst stabilities and reducing Pt usage.

In this paper, I prepared the N-doped graphene (N-G) by the heat-treatment of GNS in ammonia, and studied the effect of N doping on the structure of graphene systematically. I also reported the role of graphene and N-G annealing temperature in ammonia on Pt/GNS and Pt/N-G for ORR activity. I focus on the electrochemical performance of N-G and Pt nanoparticles supported on N-G because this subject has not been studied yet in detail. Here, the N-G and Pt/N-G were characterized by X-ray photoelectron spectroscopy (XPS), X-ray diffraction (XRD), transmission electron microscope (TEM), and ORR measurement, respectively.

5.2 Experimental

5.2.1 Preparation of GNS, N-G, Pt/GNS and Pt/N-G catalysts

Graphite powder was used as a starting material. Graphene was prepared by the oxidation of graphite powder using the modified Hummers method [23]. Briefly, graphite powder (0.2 g), particle size 45 μm, (Wako Pure Chemical Industries, Ltd.) and sodium nitrate ($NaNO_3$) (0.16 g) were first stirred in concentrated sulphuric acid (95 wt % H_2SO_4) (6.7 mL) for 2 h while being cooled in an ice water bath. Then, potassium permanganate ($KMnO_4$) (0.9 g) was gradually added to form a new mixture. After 4 h in an ice water bath, the mixture was allowed to stand for 48 h at room temperature with gentle stirring. Thereafter, 20 mL of 5 wt % H_2SO_4 aqueous solution was added into the above mixture over 1 h with stirring. Then, 0.5 mL of H_2O_2 (30 wt % aqueous solution) was also added to the above liquid and the mixture was stirred for 2 h. After that, 20 mL of 3 wt % H_2SO_4/0.5 wt % H_2O_2 solutions was added into suspension and centrifuged (3000 rpm, 1 h). Subsequently, the product was dispersed in water and ultrasonicated for 5 h. This process affords material of oxidized graphene nanosheets (OGS) [24]. Finally, the OGS were reduced with hydrazine hydrate at room temperature for 48 h. This product was filtered and washed with distilled water and dried in air at RT for 24 h. The as-received powder is the so-called graphene nano sheets (GNS). The detail characterization of GNS can be seen in reference as I reported previously [25] and also was reported in Chapter 3. Nitrogen doped graphene was obtained by annealing GNS in pure ammonia (NH_3) (Sumitomo Seika Chemicals) under 0.2 MPa gas flow. The ammonia annealing of GNS was carried out in a homemade tube furnace with connected to gas tanks. Briefly, 100 mg GNS was put into boat glass and placed in the middle of tube furnace. Then, it was annealed by an ammonia stream 50 mL/min at 150, 300, 450, 600, 750, and 900 ^oC for 2 h in a furnace, respectively. The powder was collected and denoted as N-doped graphene 150–900 (N-G 150–900), respectively. Finally, they were characterized by XPS and XRD. For instance, the TEM image of N-G 600 can be seen in Appendix 1, Supporting Information (Figure 10S). It shows a ripple structure and consists of few layers. In addition, the Brunauer-Emmett-Teller (BET) surface area for GNS, and N-G 150–900, respectively are shown in Appendix 1, Supporting Information (Table 2S). It shows that the BET surface area of GNS (318 $m^2\ g^{-1}$) is lowest among the N-G 150–900 (340–630 $m^2\ g^{-1}$). It indicates that in the presence of ammonia on GNS may assist to increase the surface area of N-G.

Subsequently, the 20 wt % Pt catalysts were deposited onto GNS and N-G 150–900 using the precursor of [$H_2PtCl_6{\cdot}6H_2O$] (Alfa Aesar, A Johnson Matthey Company), respectively. Each of ethanol solution of the precursor was mixed with ethanol solution of GNS and N-G 150–900, respectively. After stirring solution for 3 h, each of the products was collected by filtration and was dried in air at 60 ^oC for 12 h. Each of them was then reduced by a hydrogen stream 25 mL/min at 400 ^oC for 2 h in a furnace, respectively. Finally, the catalysts were collected and denoted as 20 wt % Pt/GNS and 20 wt % Pt/N-G 150–900, respectively. The amount of Pt

on GNS and N-G 150–900 for 20 wt % Pt/GNS and Pt/N-G 150–900 catalysts were measured by thermogravimetric/differential thermal analysis (TG/DTA) (see the Appendix 1, Supporting Information, Figure 11S). It indicates that the Pt atoms of the catalyst precursor are well deposited on 20 wt % Pt/GNS and Pt/N-G 150–900 catalysts.

Then, the 20 wt % Pt/GNS and Pt/N-G 150–900 catalysts were characterized by XRD, TEM, XPS, and TG/DTA, respectively. XRD measurements were performed at room temperature employing a two circle diffractometer (PANalytical PW 3050 Philips X'pert Pro, Cu K_α radiation of 1.541 Å, without monochromator), installed at a line focus X-ray generator. A reflection free Si plate was used as a sample stage. Cu K_α radiation obtained by reflection from a singly bent HOPG crystal was used as the incident X-ray. Diffraction pattern was recorded using a solid state detector (PANalytical X'Celerator) with a scan speed of 0.05 deg. (in 2θ)/sec up to 90 degrees. XPS measurements were carried out using JEOL JPS 9010 TR (X-ray source Al K_α, 1486.6 eV; pass energy 50 eV, energy resolution 1.88 eV which was calibrated using Ag $3d_{5/2}$ by measuring a clean Ag sample, the uncertainty of binding energy ± 0.05 eV). TEM (JEOL JEM-1400 electron microscope was operated at 80 kV, resolution lattice image 0.20 nm, and resolution point image 0.38 nm. TG/DTA measurements were carried out using TG/DTA6300, Seiko Instruments Inc. (Reference: Pt; Air 200 mL/min; T measurement: 50–1000 ^oC; Rate: 10 ^oC/min), respectively.

5.2.2 Electrochemical measurement

The ORR activities of GNS, N-G 150–900, 20 wt % Pt/GNS, and 20 wt % Pt/N-G 150–900 catalysts, respectively were assessed by using cyclic voltammetry, and rotating ring disk electrode (RRDE) (PGSTAT PG12, AUTOLAB Potensiostat/Galvanostat) measurements in 0.1 M $HClO_4$. The catalyst ink was prepared by dispersing 1 mg catalyst in the mixture of 500 μL (1:50 in methanol) 5 wt % Nafion solutions (Aldrich), then the mixture of catalyst ink was sonicated for 60 minutes. Then, 10 μL of catalyst ink was transferred onto the polished glassy carbon disk (diameter = 5 mm, geometric area = 0.283 cm^2) and dried to form a thin catalyst layer. The catalysts loading on the glassy carbon for GNS, and N-G 150–900, respectively were 20 μg. On the other hand, the Pt loading on the glassy carbon for 20 wt % Pt/GNS, Pt/N-G 150–900, and Pt/CB commercial catalysts, respectively was 4 μg. The measurement setup was a typical three-electrode systems consist of a working electrode (glassy carbon), a Pt wire as a counter electrode, and a reversible hydrogen electrode (RHE) as a reference electrode. All measurements were performed at room temperature (~ 25 ^oC) using a fresh electrolyte solution (0.1 M $HClO_4$, Sigma-Aldrich). First, the catalyst on the working electrode was purged by bubbling nitrogen gas at 200 mL min^{-1} through 0.1 M $HClO_4$ for 20 minutes. Then, it was scanned at 0.05–1.0 V versus RHE for 50 cycles with scan rate 10 mV s^{-1} and rotation rate 500 rpm in N_2 to eliminate contaminant and de-oxygenates the environment. After that, the saturation gas was switched to O_2 for RRDE measurement, and the electrolyte was saturated for the same condition as CV measurement. The

RRDE polarization curves were obtained at 0.05–1.0 V versus RHE with scan rate 10 mV s^{-1} in O_2 saturated 0.1 M $HClO_4$.

For CO-stripping measurements, the amounts of Pt set on the working electrode are the same as those measured in ORR. Each of catalyst ink solutions for 20 wt % Pt/GNS, Pt/N-G 150–900, and Pt/CB commercial catalysts, respectively was loaded onto a glassy carbon disk electrode (0.28 cm^2) with diluted (1:50 in methanol) 5 wt % Nafion solution (Aldrich), respectively. Prior to the measurements, the working electrode was firstly purged by bubbling N_2 through the electrolyte solution of 0.1 M $HClO_4$ for 20 minutes, and then it was scanned at - 0.2 to 0.8 V versus Ag/AgCl for 50 cycles in nitrogen with scan rate 10 mV s^{-1} and rotation rate 500 rpm for cleaning and de-oxygenates the environment. Subsequently, CO was adsorbed to the surface of the working electrode by bubbling 3 % CO/H_2 into the electrolyte solution of 0.1 M $HClO_4$ at 60 ^oC for 60 minutes, while holding the working electrode potential at - 0.15 V versus Ag/AgCl. After 3 % CO/H_2 bubbling, the gas was switched to N_2 for 30 minutes and the potential was scanned from - 0.2 to 0.8 V versus Ag/AgCl to record the CO-stripping voltammogram at 60 ^oC with a scan rate of 10 mV s^{-1} [26–28].

As a reference, 20 wt % Pt/CB (Alfa Aesar, Johnson Mathew Company) was measured for comparison.

5.3 Results and Discussion

5.3.1 ORR of N-doped graphene

The ORR at the cathode of fuel cells plays a key role in controlling the performance of a fuel cell, and efficient ORR electrocatalysts are essential for practical applications of the fuel cells [29]. I performed the rotating ring disk electrode (RRDE) measurements to investigate ORR activity of GNS and N-G 150–900 in oxygen saturated 0.1 M $HClO_4$.

Figure 5.1 shows the onset potentials of GNS (0.41 V) and around 0.42–0.63 V versus RHE for N-G 150–900, respectively. It shows that the ORR activity of GNS is not significant different with N-G 150–600, however, the ORR electrocatalytic activity for N-G 750 and 900 is higher among GNS and N-G 150–600.

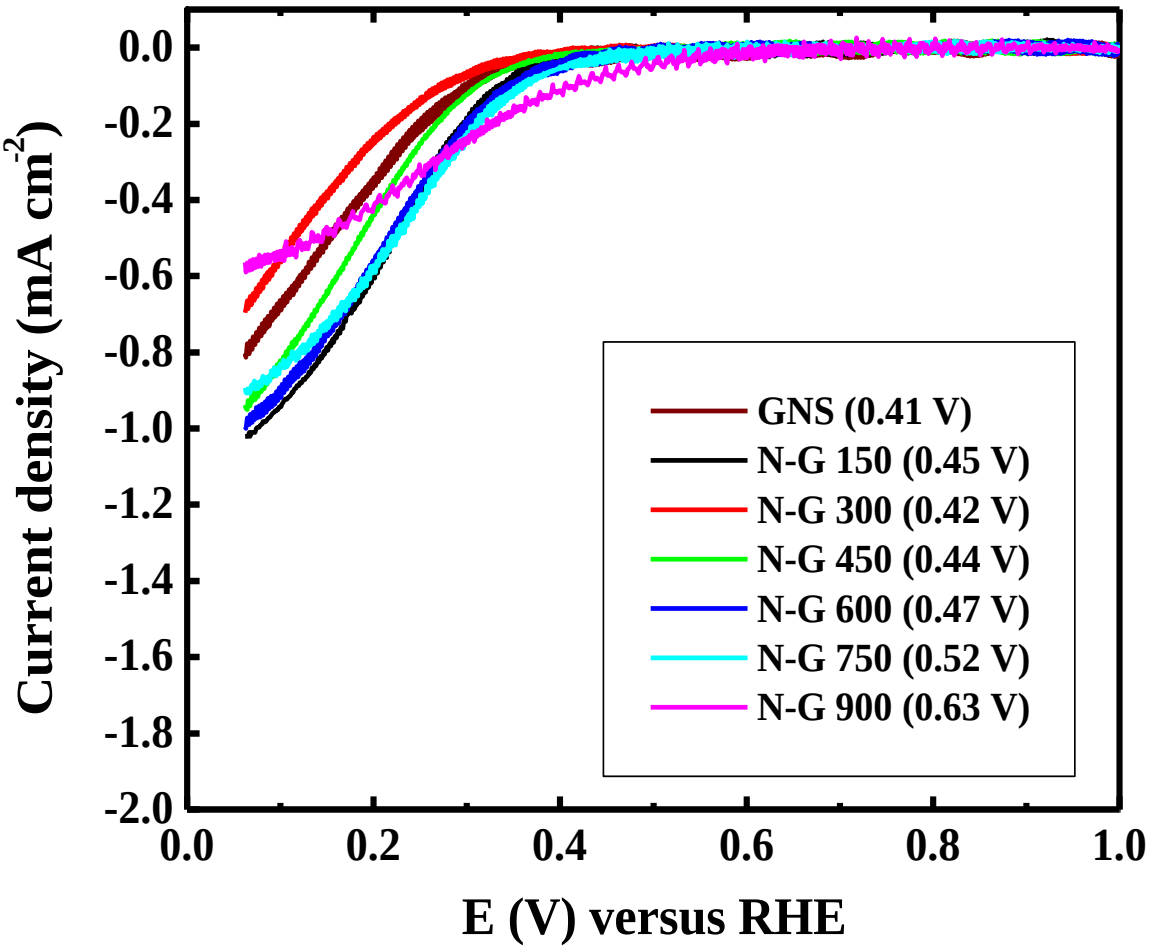

Figure 5.1 RRDE polarization curves of GNS and N-G 150–900 in O_2-saturated 0.1 M $HClO_4$ solution. Scan rate is 10 mV s^{-1}. For all the RRDE measurements, the loadings of GNS and N-G 150–900 are 20 μg.

It indicates that the pristine GNS has a poor ORR activity whereas N-G 900 exhibits significantly enhanced ORR activity. Thereby, the ORR activities of N-G 150–900 are affected by annealing temperature in ammonia.

5.3.2 XRD of N-doped graphene

Figure 5.2 shows the XRD patterns for graphite, GNS and N-G 150–900, respectively. The C(002) peaks appear at 26.6°, 24.4°, and around 25–26° (2θ) which correspond to the interlayer distances (d) 3.34, 3.64, 3.4–3.5 Å for graphite, GNS, and N-G 150–900, respectively. The broad peak and slight shifts of C(002) peaks from 26.6° to 24.4°, indicate that the graphene sheets are formed.

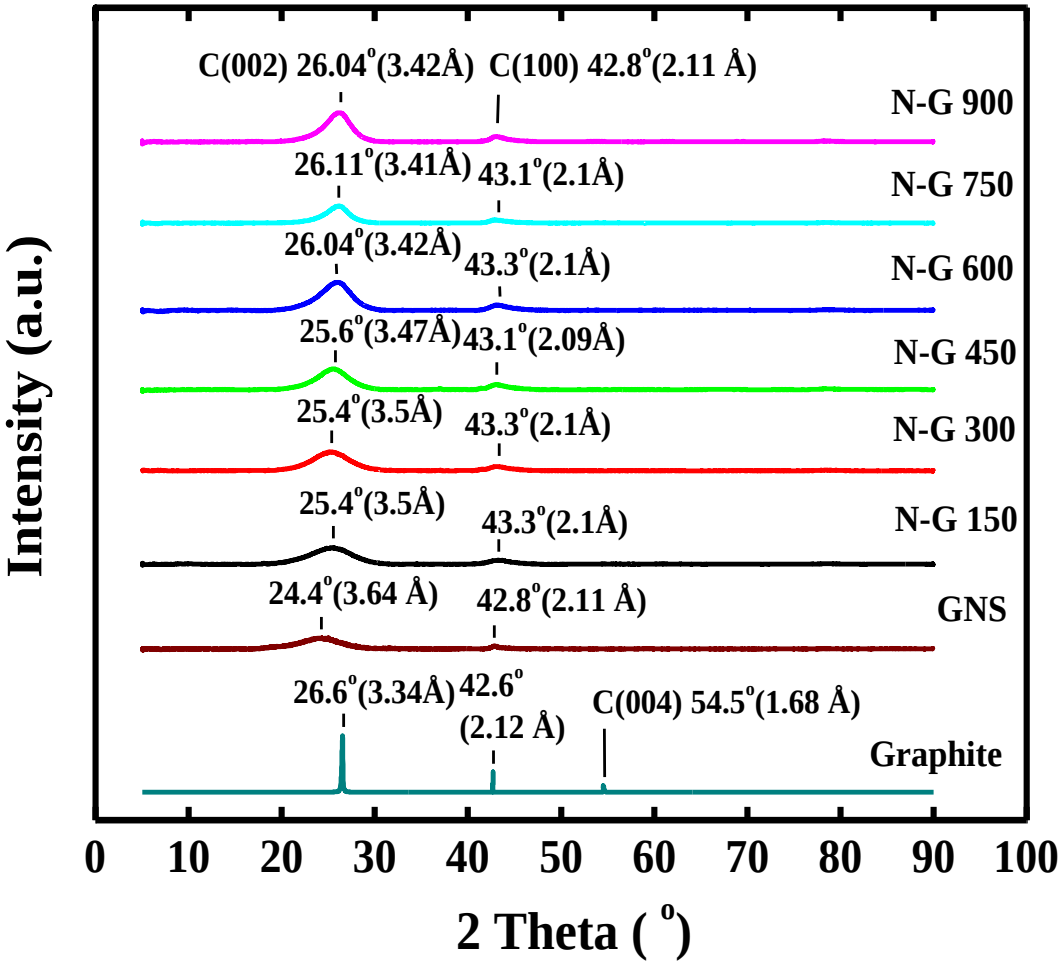

Figure 5.2 XRD patterns of graphite, GNS, and N-G 150–900.

Note that some graphitic species still remain with graphene sheets. It means a stacking of graphene. In the case of N-G 150–900, the C(002) peaks slightly shift compared to that of GNS. It means *d* of N-G is smaller than that of GNS. This data indicates that the nitrogen atoms are present in N-G. Furthermore, the *d* values of N-G tend to decrease with increasing annealing temperature in ammonia. It indicates that interlayer space for N-G is influenced by the annealing temperature.

5.3.3 XPS of N-doped graphene

XPS measurements were carried out to probe the presence of nitrogen atoms in the N-G structure. As shown in Figure 5.3, the N 1s peaks appear at around 400 eV for N-G 150–900. It indicates that nitrogen atoms exist on N-G structure.

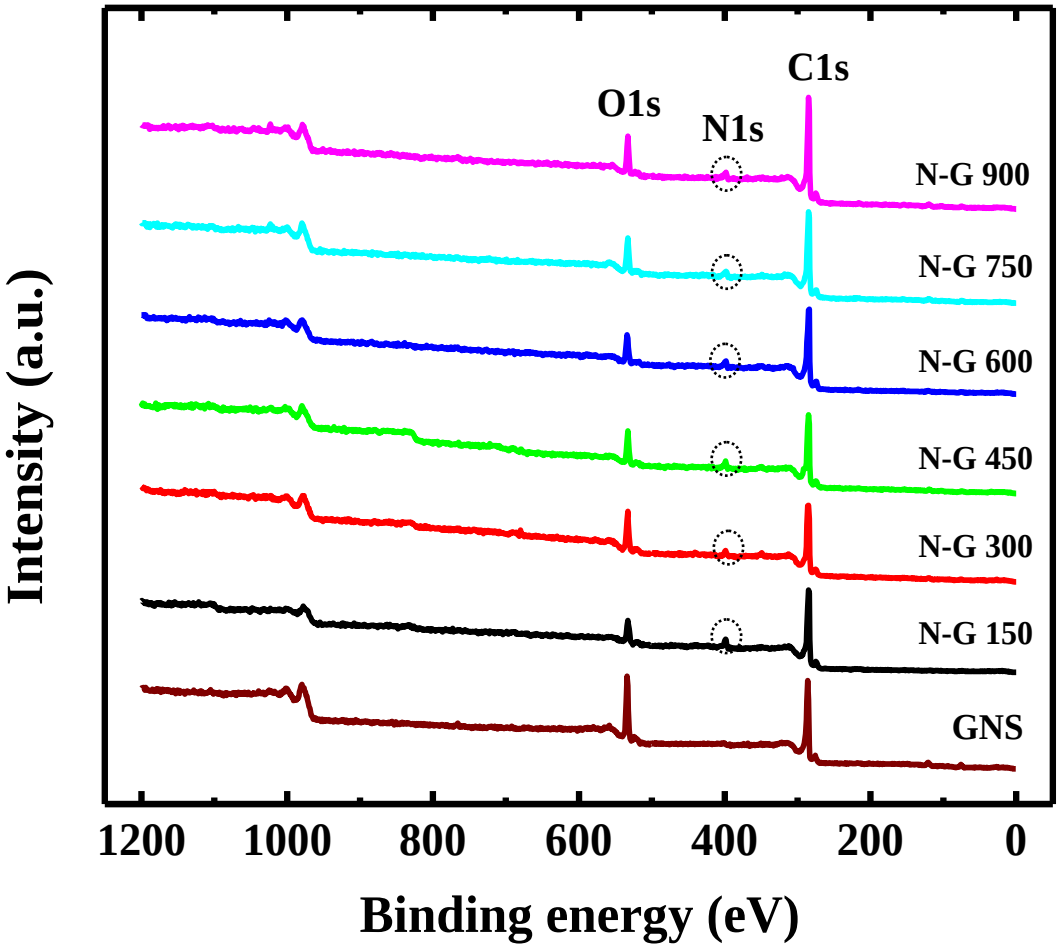

Figure 5.3 XPS spectra of GNS and N-G 150–900.

Furthermore, the N levels in N-G 150–900 are in a range of 3–5 %, with 150 ^{o}C annealing affording the highest N-doping level (5 %) (Figure 5.4a).

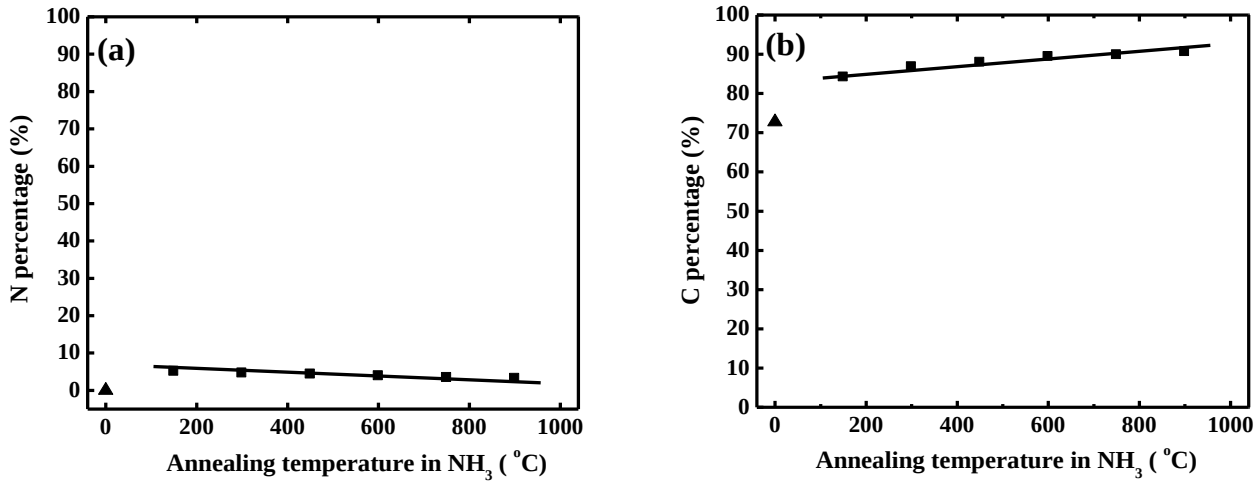

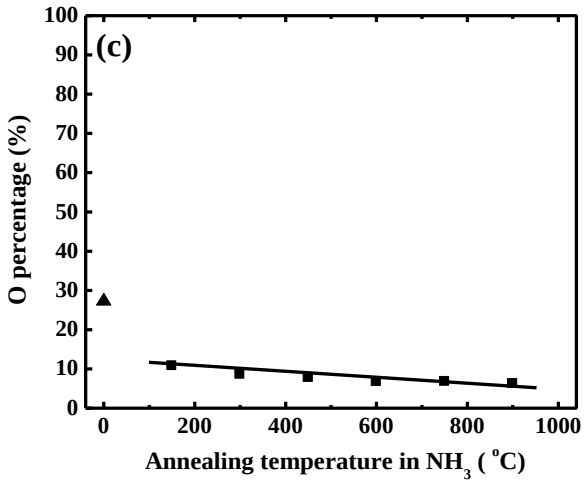

Figure 5.4 (a) C percentage, (b) O percentage, (c) N percentage for GNS (▲) and N-G 150–900 (■) detected by XPS measurement, respectively.

Moreover, the XPS spectra of C 1s peaks of N-G 150–900 shift to lower binding energies than that of GNS (Figure 5.5). This is probably due to the removal some functional groups in the pristine GNS by ammonia.

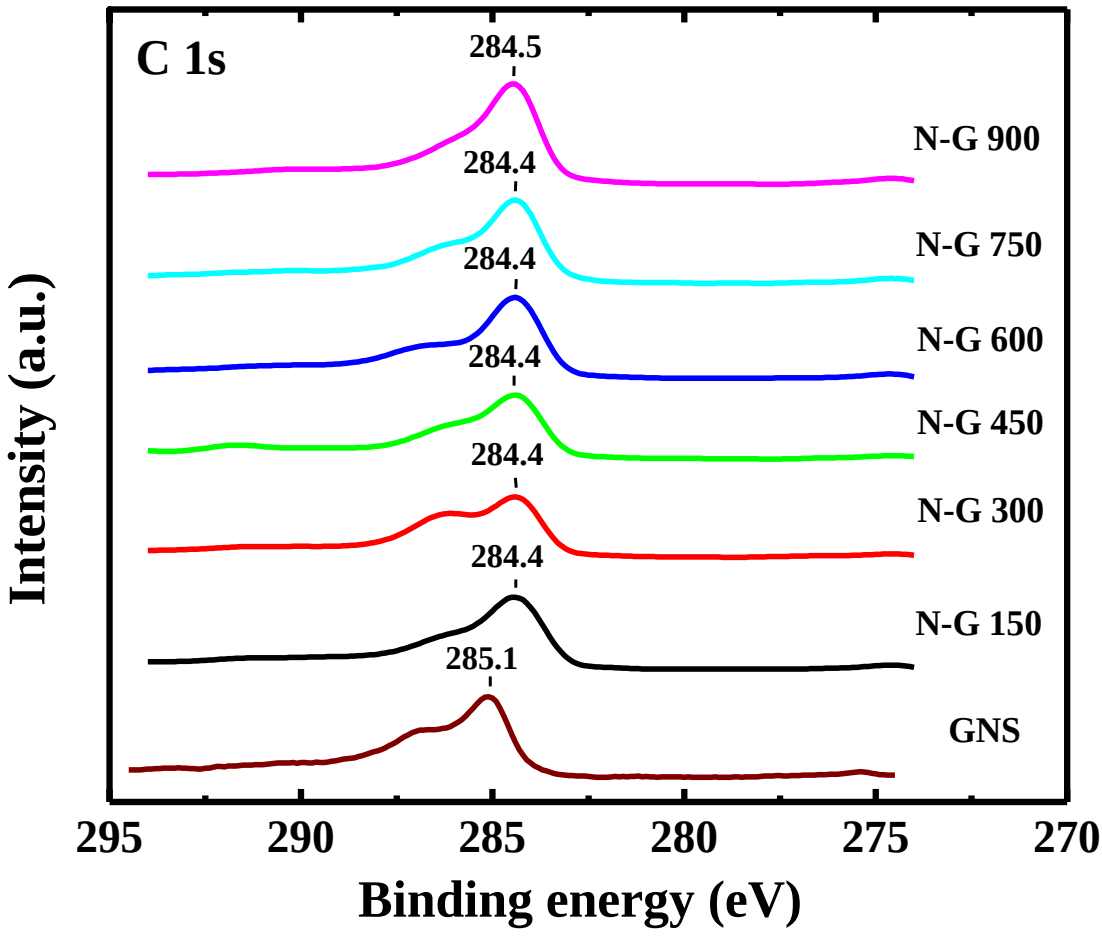

Figure 5.5 XPS spectra of C 1s peaks of GNS and N-G 150–900.

It suggests that an incorporation C-N. This result is consistent with XPS spectra of N 1 s (Figure 5.6).

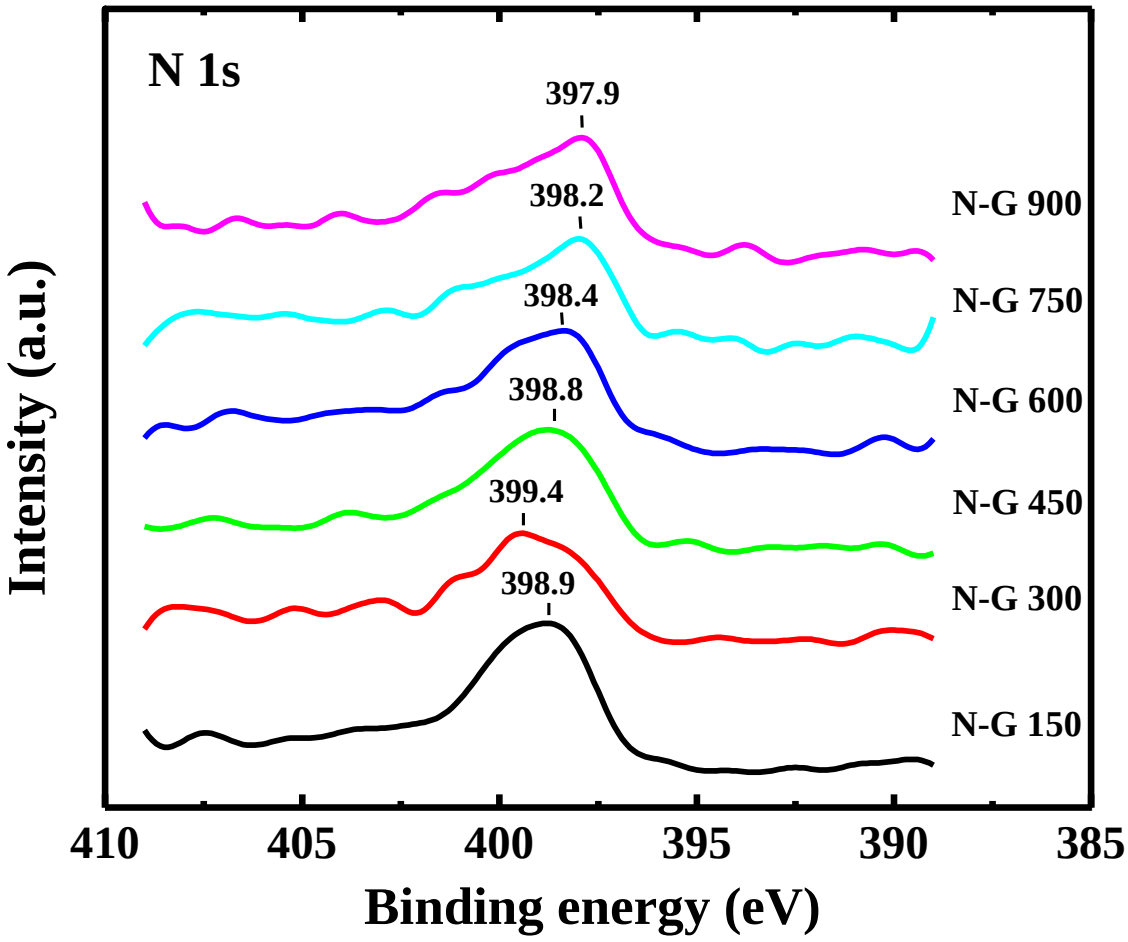

Figure 5.6 XPS spectra of N 1s peaks of N-G 150–900.

The N 1s peaks at 397–399 eV correspond to that of pyridinic N. The pyridinic N refers to N atom bonds with two C atoms at the edges or defects of graphene and contributes one p-electron to the π-system [9,30]. It indicates that nitrogen atoms of ammonia have been incorporated into the graphene hexagon rings to form C-N bonds and afford N-G [13]. The high resolution C 1s and N 1s XPS spectra of N-G 150–900 ^{o}C can be seen in Appendix 1, Supporting Information (Figures 12S and 13S). It indicates that pyridinic N is majority in N-G.

5.3.4 ORR of Pt/GNS, Pt/N-G 150–900, and Pt/CB

Figure 5.7 shows the polarization curves for the ORR on 20 wt % Pt/GNS, Pt/N-G 150–900, and Pt/CB commercial catalysts. It can be seen that the diffusion-limiting currents were obtained in the potential region below 0.4 V versus RHE. Both of the Pt/GNS and Pt/N-G catalysts show smaller limiting current in ORR than Pt/CB.

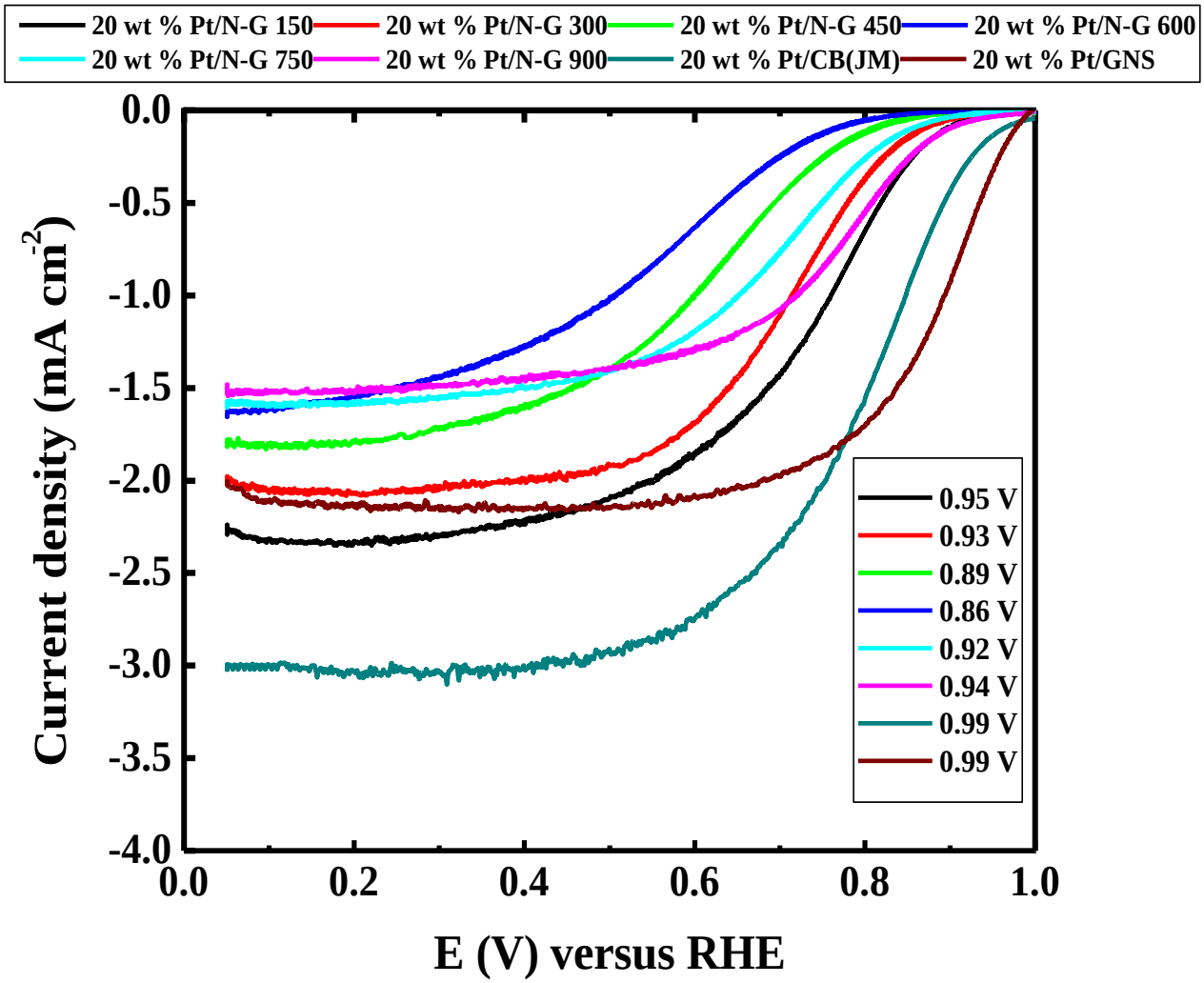

Figure 5.7 RRDE polarization curves of 20 wt % Pt/GNS, Pt/N-G 150–900, and Pt/CB commercial catalyst in O_2-saturated 0.1 M $HClO_4$ solution. Scan rate is 10 mV s^{-1}. For all the RRDE measurements, the Pt loading of catalysts are 4 μg for 20 wt % Pt/GNS, Pt/N-G 150–900, and Pt/CB commercial catalysts, respectively.

It is indicated that the diffusion limiting currents are affected by the structure of the catalyst supporting material [31]. The 20 wt % Pt/GNS exhibits the highest ORR activity from its onset potential (0.99 V versus RHE) and half wave potential ($E_{1/2} \approx 0.88$ V versus RHE) among the other catalysts. In the case of 20 wt % Pt/N-G 150–600, the ORR activities tend to decrease with increasing annealing temperature in ammonia. Their onset potentials are decreased from 0.95 to 0.86 V versus RHE for 20 wt % Pt/N-G 150 to Pt/N-G 600. Then, the onset potentials are increased from 0.92 to 0.94 V versus RHE for 20 wt % Pt/N-G 750 to 900. It indicates that the ORR activity of N-G is higher than N-G 300–750, but it is slight lower than N-G 150. The ORR mass activities were calculated at 0.9 V versus RHE. The current density was measured at 0.9 V versus

RHE are 0.99 and 0.97 mA cm^{-2} for 20 wt % Pt/CB commercial and Pt/GNS catalysts, respectively (Figure 5.8).

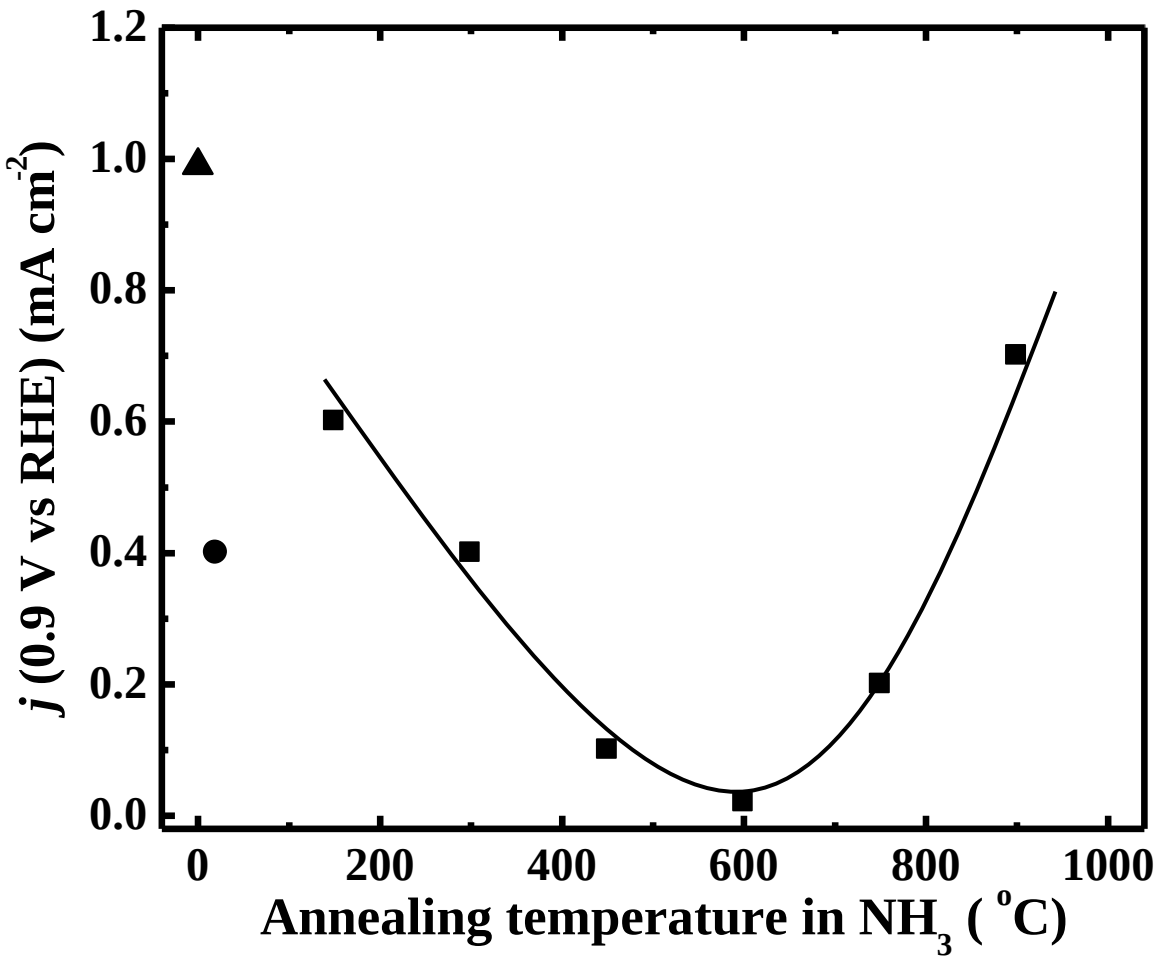

Figure 5.8 Current density at 0.9 V (mA cm^{-2}) versus annealing temperature in ammonia for 20 wt % Pt/GNS (▲), Pt/N-G 150–900 (■), and Pt/CB commercial catalyst (●).

On the other hand, the current densities are 0.6, 0.4, 0.1, 0.02, 0.2, and 0.7 mA cm^{-2} for 20 wt % Pt/N-G 150–900 catalysts, respectively. The current density results of 20 wt % Pt/N-G 150–900 are also consistent with their ORR data. The current densities are decreased with increasing annealing temperature ammonia for 20 wt % Pt/N-G 150–600. Then, their current densities increase with increasing annealing temperature ammonia for 20 wt % Pt/N-G 750–900. These data indicate that annealing temperature in ammonia affects the ORR activity for 20 wt % Pt/N-G 150–900 catalysts. However, the ORR activity of Pt/GNS is higher than that of Pt/N-G with its onset potential 0.99 to 0.86–0.95 V versus RHE for Pt/GNS and Pt/N-G catalysts, respectively. This is in accordance with the lowest oxidation potential peak of 20 wt % Pt/GNS among the Pt/N-G 150–900 and Pt/CB commercial catalysts as shown in CO-stripping data (Figure 5.9).

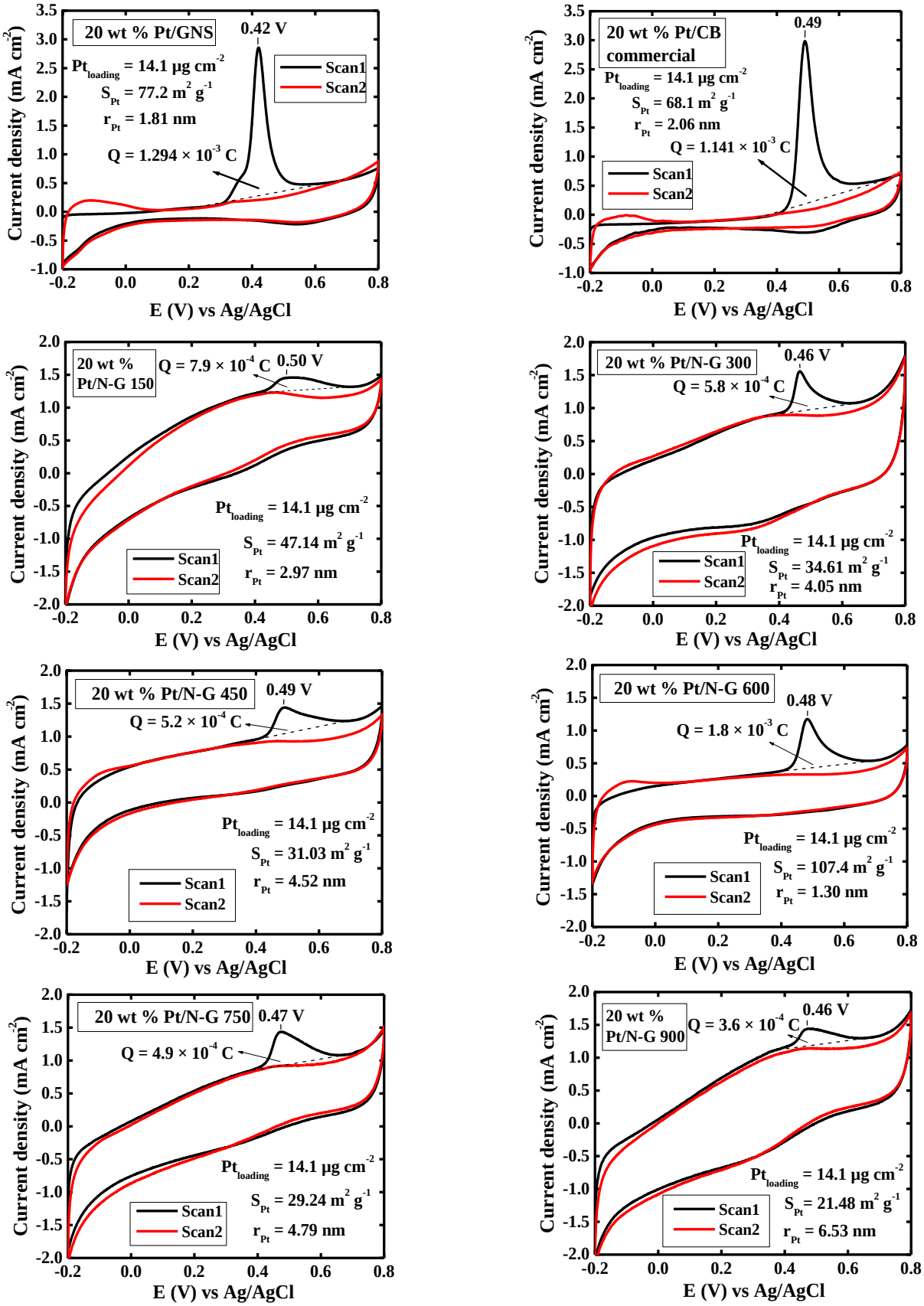

Figure 5.9 CO stripping voltammograms of 20 wt % Pt/GNS (▲), Pt/N-G 150–900 (■), and Pt/CB commercial catalyst (●).

The oxidation potential peaks are 0.42, 0.50, 0.46, 0.49, 0.48, 0.47, 0.46, and 0.49 V versus Ag/AgCl for 20 wt % Pt/GNS, Pt/N-G 150–900, and Pt/CB commercial catalysts, respectively. The oxidation potential peaks of Pt/N-G 150–900 are slight difference with Pt/CB. In contrast, Pt/GNS oxidation potential peak is significant shifted to lower potentials compared to Pt/N-G 150–900, and Pt/CB. These results are also consistent with the threshold voltages of the oxidation peaks (Figure 5.10).

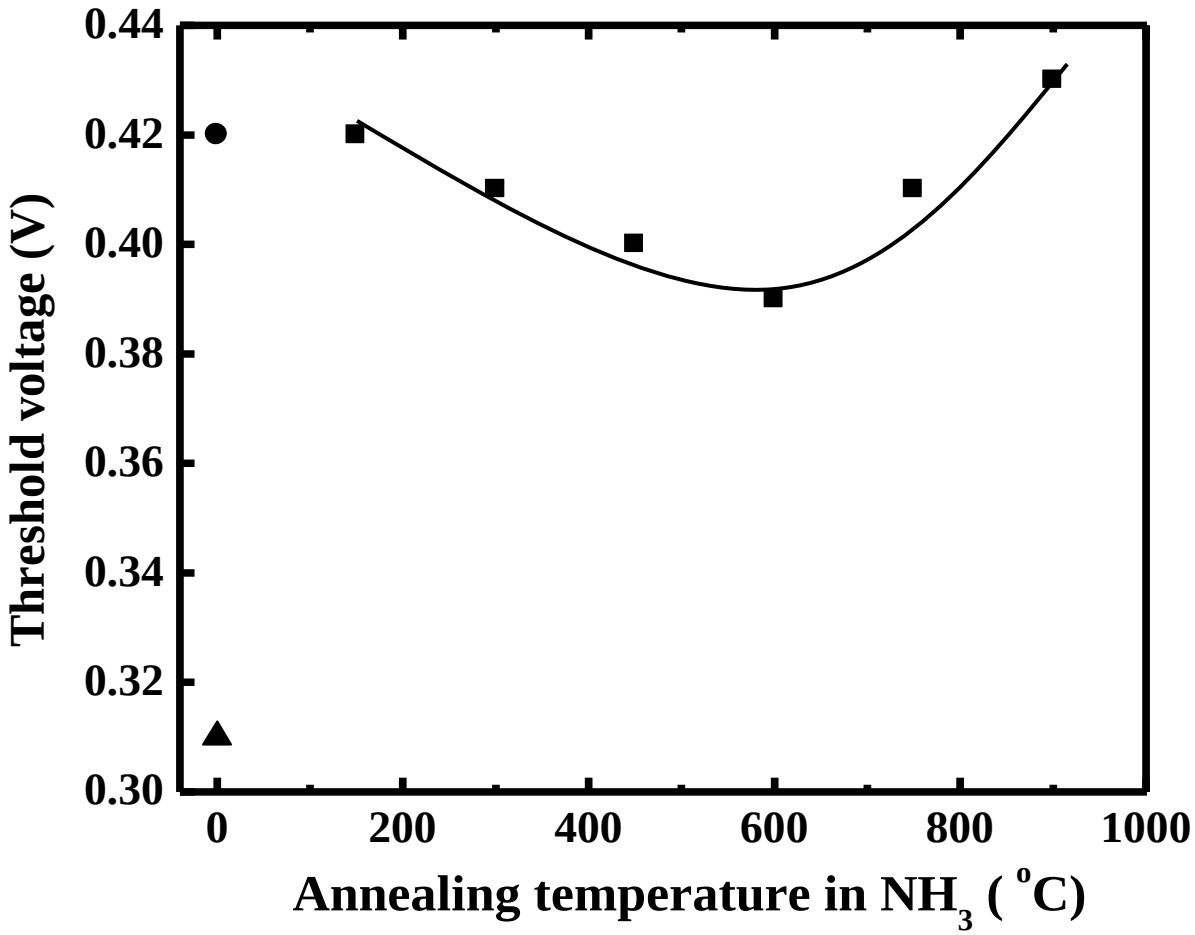

Figure 5.10 Threshold voltage versus annealing temperature in ammonia for 20 wt % Pt/GNS (▲), Pt/N-G 150–900 (■), and Pt/CB commercial catalyst (●).

It indicates that Pt/GNS shows the highest catalytic activity among the others. This is because the CO is more readily oxidized on Pt/GNS among those of Pt/N-G 150–900 and Pt/CB. It is believed that GNS as a support material plays the most important role in improving CO oxidation.

5.3.5 TEM of Pt/GNS, Pt/N-G 150–900, and Pt/CB

In order to further know effect of support material and annealing temperature in ammonia based on Pt particle size for Pt/GNS, Pt/N-G 150–900, and Pt/CB catalysts, I carried out TEM measurements. Figure 5.11

shows the TEM images with histograms of Pt particle size distributions by analyzing random chosen areas containing 600 particles in magnified TEM images for 20 wt % Pt/GNS, Pt/N-G 150–900, and Pt/CB commercial catalyst.

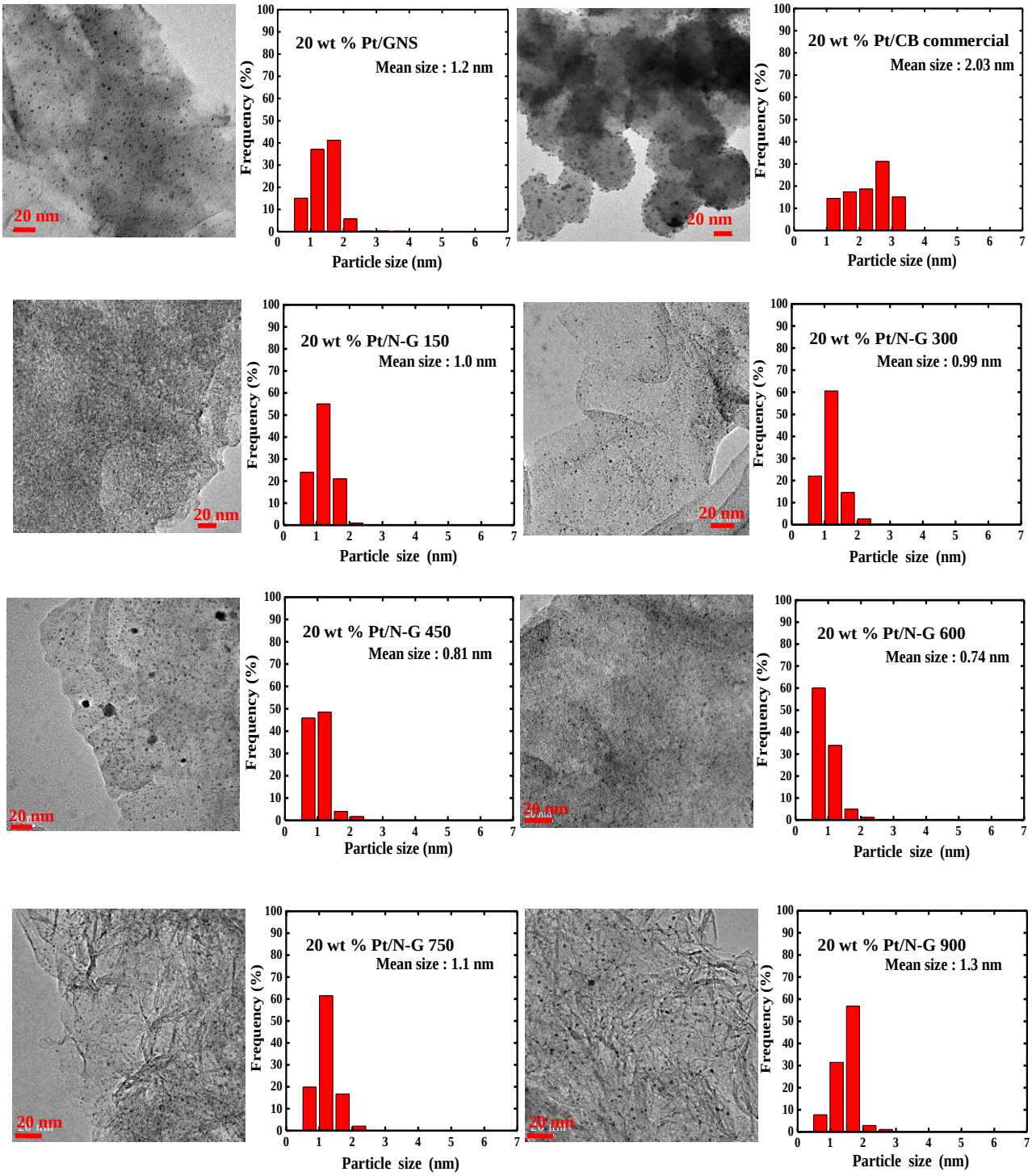

Figure 5.11 TEM images and histograms of 20 wt % Pt/GNS, Pt/N-G 150–900, and Pt/CB commercial catalyst.

Notice that the Pt particle size is estimated as < 5 nm. The high dispersion of Pt particles on GNS, N-G 150–900, and carbon black are clear as shown by TEM images. It is found that Pt subnano-clusters were formed on GNS and N-G 150–900. It should be noted that Pt subnano-clusters are not formed on carbon black. Thereby, GNS and N-G 150–900 play important role for Pt subnano-clusters formation. The average Pt particle sizes as a function of annealing temperature in ammonia estimated by TEM are shown in Figure 5.12.

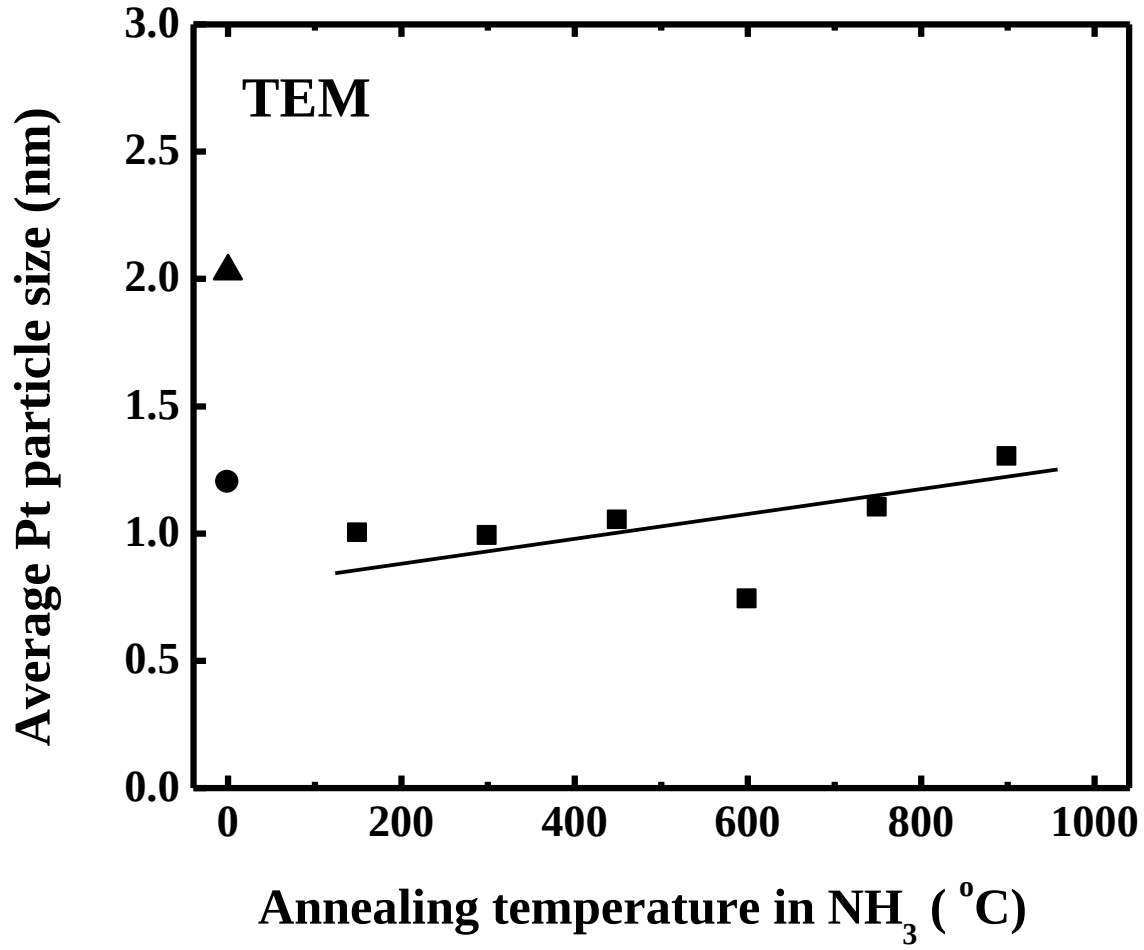

Figure 5.12 Average Pt particle size (nm) estimated by TEM versus annealing temperature in ammonia for 20 wt % Pt/GNS (▲), Pt/N-G 150–900 (■), and Pt/CB commercial catalyst (●).

It shows that the average size of Pt particle on N-doped graphene is smaller among those of GNS and CB. It indicates that the support material has important role to affect the Pt particle size. In the case of Pt/N-G catalysts, the average size of Pt tends to decrease with increasing annealing temperature ammonia from 150–600 ^{o}C, and then it gradually increases with increasing annealing temperature ammonia from 750 and 900 ^{o}C. It means Pt particle size of Pt/N-G catalyst is affected by annealing temperature in ammonia.

5.3.6 XRD of Pt/GNS, Pt/N-G 150–900, and Pt/CB

Figure 5.13 shows XRD patterns for 20 wt% Pt/N-G, Pt/GNS, and Pt/CB commercial catalyst.

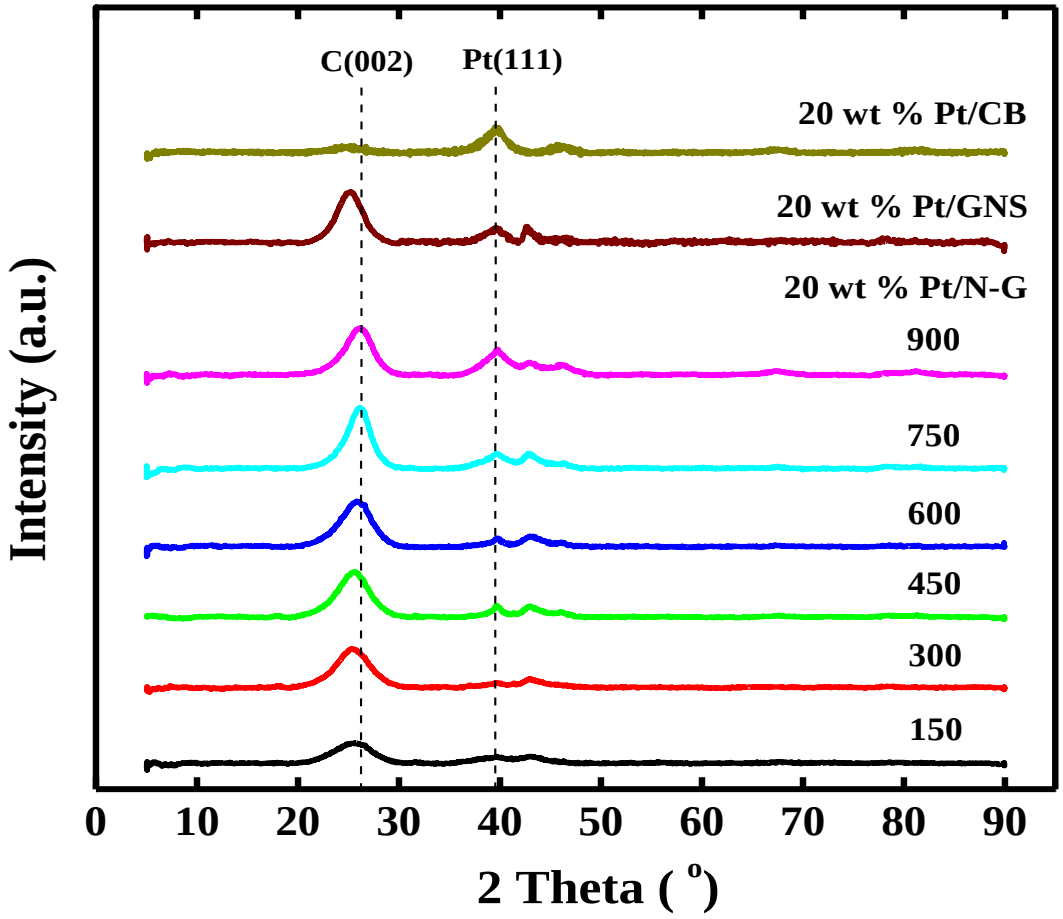

Figure 5.13 XRD patterns for 20 wt % Pt/GNS, Pt/N-G 150–900, and Pt/CB commercial catalyst.

The 2θ Bragg angle peaks appear at around 25 and 39°, which correspond to C(002) and Pt(111). The C(002) peaks of Pt/GNS and Pt/N-G 150–900 catalysts are sharp and broad. The C(002) peaks of Pt/N-G catalysts are slightly shifted to higher 2θ Bragg angles (lower lattice parameters) than the C(002) peak of Pt/GNS catalyst. It indicates that nitrogen atoms are incorporated in graphene. The Pt(111) peaks of Pt/GNS and Pt/N-G 150–900 are relatively smaller in intensity compared to Pt/CB. It suggests that the crystallinity of Pt is smaller than Pt/CB. On the other hand, all of the Pt(111) peaks for Pt/N-G and Pt/GNS are weak and broad. The weak and broad peaks indicate that Pt subnano-clusters were formed [25]. In the case of Pt/N-G, the Pt(111) peaks of Pt/N-G 150 and 300 are very weak and broad, and then gradually become sharper with increasing annealing temperature in ammonia for Pt/N-G 450–900. It indicates that the particle sizes are different with annealing temperature in ammonia. Therefore, I estimated the Pt particle size by using Scherrer equation [32]. As shown in Figure 5.14, the Pt particle size tends to increase with increasing annealing temperature in ammonia for 20 wt % Pt/N-G 150–900.

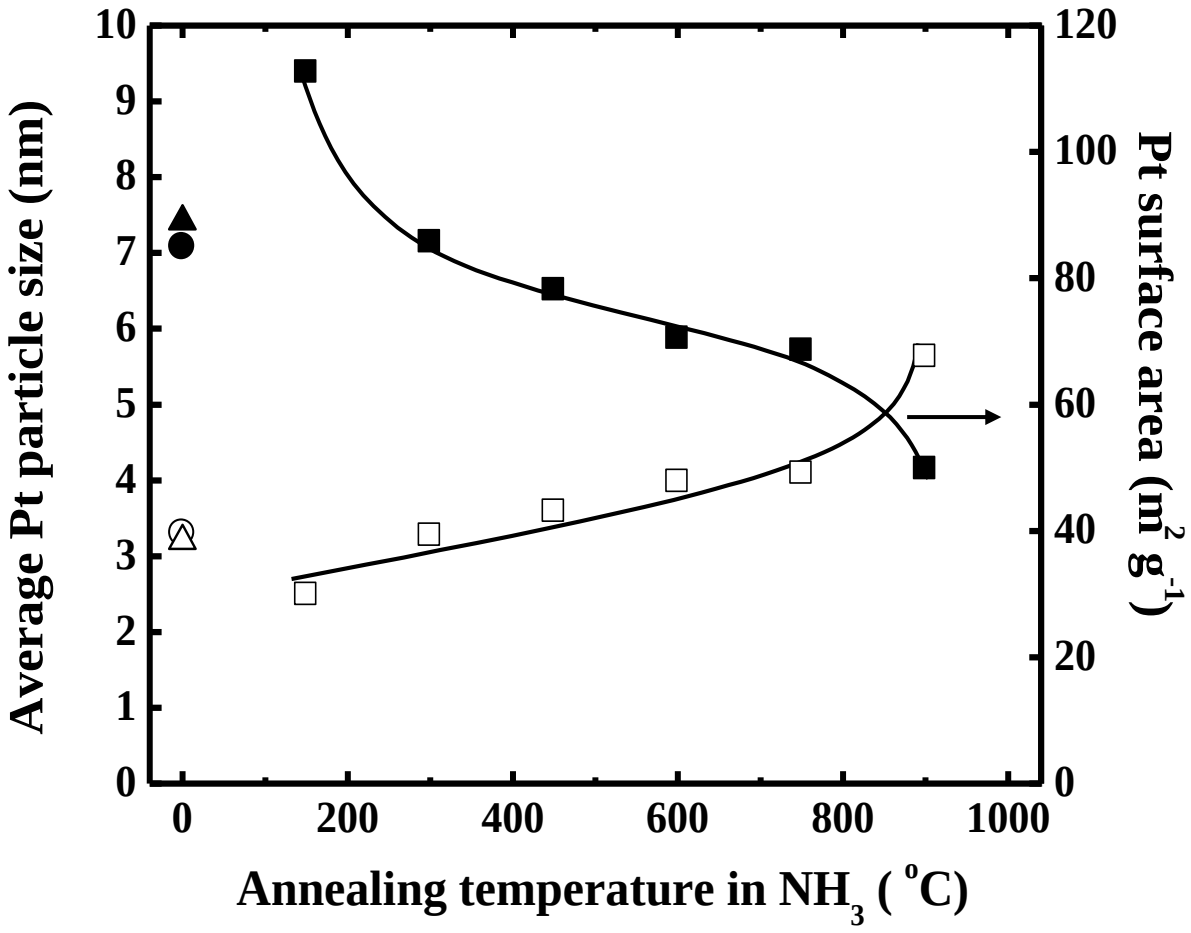

Figure 5.14 Average Pt particle size (nm) (□, left axis) and Pt surface area (m^2 g^{-1}) (■, right axis) estimated by XRD as a function of annealing temperature in ammonia for 20 wt % Pt/N-G. The results for 20 wt % Pt/GNS are shown (△ and ▲), and Pt/CB commercial catalyst (○ and ●).

The Pt particle size is around 2–6 nm for Pt/N-G. However, the Pt particle size is similar with those of Pt/GNS and Pt/CB for 20 wt % Pt/N-G 150 and 300 and the Pt particle size of Pt/N-G 450–900 is larger than that of Pt/N-G 150 and 300. It indicates that the Pt particle size is affected by annealing temperature in ammonia.

5.3.7 XPS of Pt/GNS, Pt/N-G 150–900, and Pt/CB

The Pt 4f XPS spectra for 20 wt % Pt/N-G 150–900, Pt/GNS, and Pt/CB commercial catalyst are shown in Figure 5.15.The binding energy (BE) of Pt/CB is 71.4 eV. It is close to the BE of bulk Pt (71.2 eV) [33]. It indicates that interaction between Pt and CB is weak. In contrast, the BE of Pt/N-G and Pt/GNS shift to higher BE than that of Pt/CB. The BE shifts to higher BE should be related with the Pt electronic state.

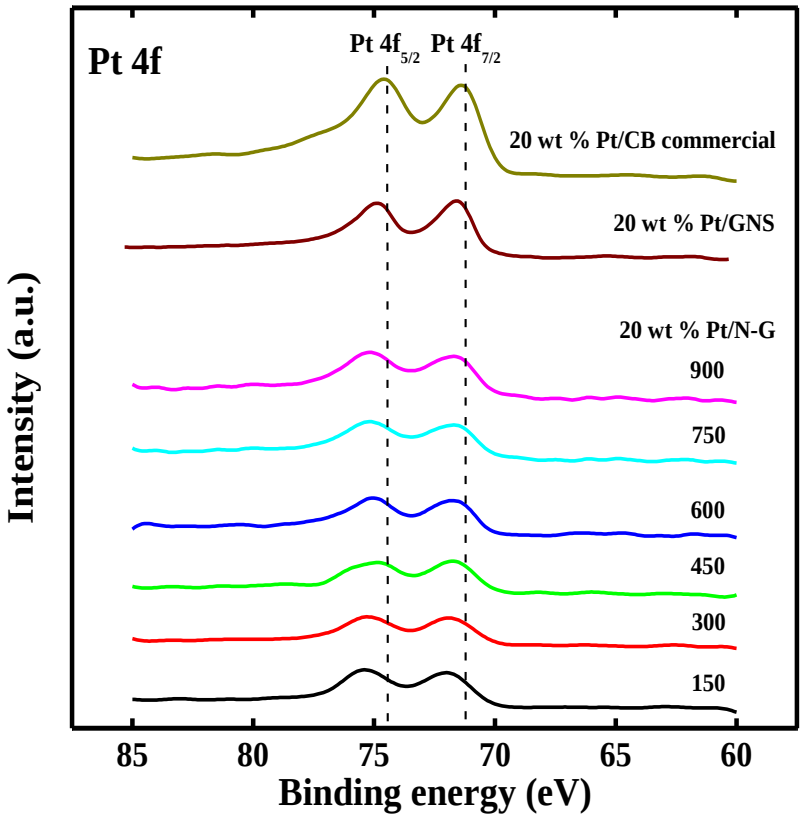

Figure 5.15 XPS spectra for 20 wt % Pt/GNS, Pt/N-G 150–900, and Pt/CB commercial catalyst.

That is, a strong interaction between Pt and GNS and N-G. In the case of 20 wt % Pt/N-G, it is found that the Pt 4f peaks shift to lower BE with increasing annealing temperature in ammonia. The Figure 5.16 shows the tendency of Pt 4f binding energy with annealing temperature in ammonia.

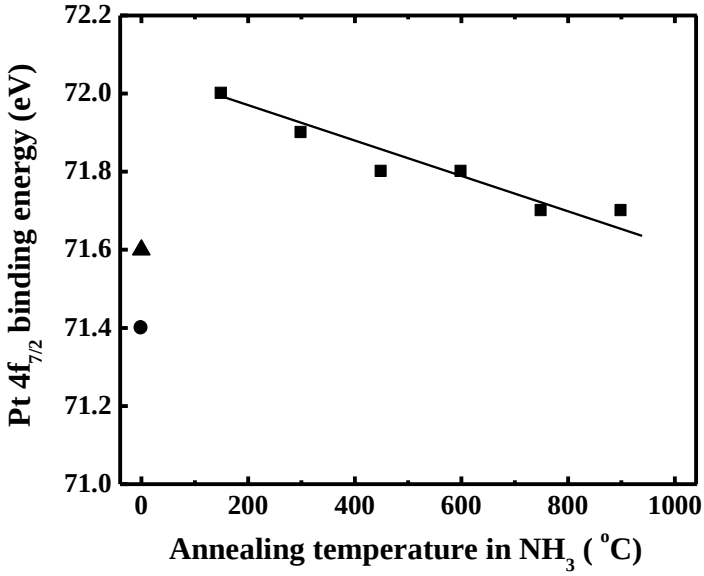

Figure 5.16 Pt $4f_{7/2}$ binding energy (eV) versus annealing temperature in ammonia for 20 wt % Pt/N-G 150–900 (■), Pt/GNS are shown (▲), and Pt/CB commercial catalyst (●).

It clearly shows that the maxima BE of Pt 4f (72.0 eV) is shifted to lower BE with increasing annealing temperature in ammonia. This is probably due to the Pt particle size effect on N-G. The atomic ratio of Pt to C estimated by XPS for 20 wt % Pt/N-G 150–900, Pt/GNS, and Pt/CB commercial catalyst are summarized in Table 3S (Appendix 1, Supporting Information). In the case of 20 wt % Pt/N-G 150–900, it shows that the atomic ratio of N to C slightly decreases with increasing annealing temperature in ammonia. It indicates that the amount of N on N-G is affected by annealing temperature. However, the atomic ratio of Pt to C is not significantly decreased with increasing annealing temperature in ammonia.

5.4 Conclusion

Nitrogen doping into graphene was carried out by heating GNS in ammonia to produce N-doped graphene (N-G). The N-G was used as a support material for Pt catalyst as well as a catalyst itself for half-cell cathode reaction of hydrogen fuel cell (H_2FC). It is found that the ORR electrocatalytic activity for N-G 900 (0.63 V versus RHE) is higher than GNS. It indicates that the incorporation of nitrogen in N-G may affect the ORR activities. XPS results exhibit the pyridinic N is the majority in N-G, where the pyridinic N refers to N atom bonds with two C atoms at the edges or defects of graphene. Interestingly, the Pt subnano-clusters were formed on all of Pt/N-G catalysts with Pt particle size (0.7–1.0 nm). It clearly indicates that the doping of nitrogen significantly influence π–d hybridization in terms of electronic structures.

References

[1] K. S. Novoselov, A. Geim, S. V. Morozov, D. Jiang, Y. Zhang, S. V. Dubonos, I. V. Grigorieva, A. A. Firsov, Science, **306**, 666–669 (2004).

[2] M. D. Stoller, S. Park, Y. Zhu, J. An, R. S. Ruoff, Nano Lett., **8**, 3498–3502 (2008).

[3] A. A. Balandin, S. Ghosh, W. Bao, I. Calizo, D. Teweldebrhan, F. Miao, C. N. Lau, Nano Lett., **8**, 902–907 (2008).

[4] K. I. Bolotin, K. J. Sikes, Z. Jiang, M. Klima, G. Fudenberg, J. Hone, P. Kim, H. L. Stormer, Solid State Commun., **146**, 351–355 (2008).

[5] C. Lee, X. Wei, J. W. Kysar, J. Hone, Science, **321**, 385–388 (2008).

[6] H. Wang, T. Maiyalagan, X. Wang, ACS Catal., **2**, 781–794 (2012).

[7] F. Banhart, J. Kotakoski, A. V. Krasheninnikov, ACS Nano, **5**, 26–41 (2011).

[8] G. Imamura, K. Saiki, J. Phys. Chem. C., **115**, 10000–10005 (2011).

[9] L. S. Zhang, X. Q. Liang, W. G. Song, Z. Y. Wu, Phys. Chem. Chem. Phys., **12**, 12055–12059 (2010).

[10] X. Q. Wang, J. S. Lee, Q. Zhu, J. Liu, Y. Wang, S. Dai, Chem. Mater., **22**, 2178–2180 (2010).

[11] L. Zhang, Z. Xia, J. Phys. Chem. C, **115**, 11170–11176 (2011).

[12] K. R. Lee, K. U. Lee, J. W. Lee, T. B. Ahn, S. I. Woo, Electrochem. Commun., **12**, 1052–1055 (2010).

[13] L. Qu, Y. Liu, J. B. Baek, L. Dai, ACS Nano, **4**, 1321–1326 (2010).

[14] T. Ikeda, M. Boero, S. F. Huang, K. Terakura, M. Oshima, J. Ozaki, J. Phys. Chem. C, **112**, 14706–14709 (2008).

[15] Y. Wang, P. B. Balbuena, J. Phys. Chem. B, **109**, 14896–14907 (2005).

[16] C. Wang, M. Waje, X. Wang, J. M. Tang, R. C. Haddon, Y. S. Yan, Nano Lett., **4**, 345–348 (2004).

[17] L. Zhang, J. Niu, L. Dai, Z. Xia, Langmuir, **28**, 7542–7550 (2012).

[18] A. Kongkanand, S. Kuwabata, G. Girishkumar, P. Kamat, Langmuir, **22**, 2392–2396 (2006).

[19] L. Yu, X. Pan, X. Gao, P. Hu, X. Bao, J. Catal., **282**, 183–190 (2011).

[20] Y. Shao, S. Zhang, R. Kou, X. Wang, C. Wang, S. Dai, V. Viswanathan, J. Liu, Y. Wang, Y. H. Lin, J. Power Sources, **195**, 1805–1811 (2010).

[21] S. Donthu, M. Cai, M. Ruthkosky, I. Halalay, Chem. Commun., 4203–4205 (2009).

[22] Q. Zhu, S. Zhou, X. Wang, S. Dai, J. Power Sources, **193**, 495–500 (2009).

[23] W. S. Hummers, R. E. Offeman, J. Am. Chem. Soc., **80**, 1339 (1958).

[24] S. Stankovich, D. A. Dikin, G. H. B. Dommett, K. M. Kohlhaas, E. J. Zimney, E. A. Stach, R. D. Piner, S. T. Nguyen, R. S. Ruoff, Nature, **442**, 282–286 (2006).

[25] R. Siburian, J. Nakamura, J. Phys. Chem. C, **116**, 22947–22953 (2012).

[26] J. B. Joo, P. Kim, W. Kim, Y. Kim, J. Yi, J. Appl. Electrochem., **39**, 135–140 (2009).

[27] T. Vidakovic, M. Christov, K. Sundmacher, Electrochim. Acta, **52**, 5606–5613 (2007).

[28] O. V. Cherstiouk, P. A. Simonov, E. R. Savinova, Electrochim. Acta, **48**, 3851–3860 (2003).

[29] K. Gong, F. Du, Z. Xia, M. Durstock, L. Dai, Science, **323**,760–764 (2009).

[30] X. Li, H. Wang, J. T. Robinson, H. Sanchez, G. Diankov, H. Dai, J. Am. Chem. Soc., **131**, 15939–15944 (2009).

[31] D. He, K. Cheng, H. Li, T. Peng, F. Xu, S. Mu, M. Pan, Langmuir, **28**, 3979–3986 (2012).

[32] A. Pozio, M. De Francesco, A. Cemmi, F. Cardellini, L. Giorgi, J. Power Sources, **105**, 13–19 (2002).

[33] J. Moulder, W. F. Stickle, P. E. Sobol, K. D. Bomben, Handbook of X-ray Photoelectron Spectroscopy, Perkin Elmer Corporation, Minnesota, USA, 1992.

Chapter 6

Support material effect for Pt catalytic activity at cathode

In this study, the GNS and N-G were used as supporting materials to deposit Pt particles in order to investigate the support material effect for ORR activity. The ORR activity of Pt/GNS is higher than Pt/N-G catalysts. This suggests that the modification of π states by the N-doping change the properties of the interaction between Pt and carbon. The interaction between Pt and graphene is considered to be π–d hybridization. Therefore, one can control the electronic structure of graphene and Pt by doping of some elements.

- Chapter 6 -

6.1 Introduction

Polymer electrolyte membrane fuel cell (PEMFC) are being developed as electrical power sources for vehicles and portable applications as an alternative to conventional internal combustion engines, secondary batteries, and other conventional power sources [1]. Recently, the design of cheap and stable fuel cell catalysts for ORR is main challenge [2]. This is caused catalysts exhibit great influence on both the cost and the durability of PEMFC [3]. The platinum (Pt) nanoparticles supported on carbon black (Pt/CB) are most used for ORR catalysts. It has outstanding catalytic and electrical properties [4]. Therefore, much of the art and science of catalysts development for the ORR rely on both the fundamental understanding of the reaction at the Pt electrolyte interface and the optimization of the catalytic properties of the Pt surface [5]. However, Pt price is expensive and also it is limited natural resources [6]. Therefore, it is a prerequisite to decrease the usage of Pt and enhance the catalytic activity of Pt in order to achieve a competitive low cost of fuel cell.

The catalyst support materials exhibit great influence on the cost, performance, and durability of PEMFC. For instance, carbon-supported precious metal nanoparticles (e.g., Pt, Au, Pd, and Rh) are widely used in heterogeneous catalysis and electrocatalysis [7]. The support materials are necessary to obtain a high dispersion, narrow distribution of Pt and Pt-alloy nanoparticles and also can interplay with catalytic metals, which is the prerequisite to obtain the high catalytic performance of catalysts [1]. Commonly, the catalyst support materials require high specific surface area, high conductivity, low combustive reactivity under both dry and humid air conditions at low temperatures (150 ^{o}C or less), high electrochemical stability under fuel cell operating conditions, easy to recover Pt in the used catalyst [1,8], and the interaction between catalytic metals and the support materials [9]. This is because the interaction between the support and metal catalyst can modify the electronic structure of catalytic metals which in turn changes the catalytic activity [10]. However, the weak interaction between metal and carbon supports results in a severe sintering/agglomeration of catalytic metal nanoparticles and consequently decreases the active surface area, which leads to the degradation of performance under long-term operations [7]. Many researchers have reported novel carbon support materials, such as carbon nanohorns [11], carbon nanocoils [12], carbon nanotube (CNT) [13], graphite nanofibers (GNFs) [14], and carbon black [15] for PEMFC applications. Some papers also reported that nitrogen-doped carbon nanotube (N-CNT) with metal catalysts or without metals exhibit enhancement catalytic activity toward ORR [16]. They showed promising results toward fuel cell electrode reactions: ORR and methanol oxidation reaction (MOR). But, in term of activity, cost and durability, current catalysts can still not satisfy the requirements of target PEMFC [17]. Therefore, many efforts are still necessary to find the novel catalytic metals and support materials.

Graphene sheets, a two-dimensional carbon material with single (or a few) atomic layer has attracted great attention for both fundamental science and applied research. This is caused it has large surface area

(2630 m^2 g^{-1}) [18], and high carrier mobility (10^4 cm^2 V^{-1} s^{-1} at room temperature) [19]. Recently, graphene as a supporting material for Pt catalyst is believed to improve catalytic activity for hydrogen oxidation reaction (HOR) and methanol oxidation reaction (MOR). However, the controversial results regarding the ORR activity for Pt/GNS compare to Pt/CB commercial catalyst. Moreover, fuel cell tests with Pt/GNS catalysts as cathode materials showed a considerably lower performance than that of the cell with Pt/CB as cathode catalyst [20].

In this chapter, I studied the effect of support materials; those are graphene nano sheet (GNS) and nitrogen doped GNS (N-G) on Pt catalyst for cathode hydrogen fuel cell. I focus about the ORR catalytic activity of Pt/GNS, Pt/N-G and Pt/CB commercial catalyst as reference. Because, ORR at the cathode of fuel cells plays a key role in controlling the performance of a fuel cell, and the efficiency of ORR electrocatalysts are essential for fuel cells practical applications [21]. Thereby, I can know the support material effect for ORR catalytic activity based on Pt catalyst.

6.2 Experimental

6.2.1 Preparation of support materials and catalysts

In this experiment, I prepared two kinds support materials, namely graphene nano sheets (GNS) and nitrogen doped GNS (N-G). Subsequently, Pt atoms were deposited on GNS and N-G, respectively. GNS was prepared by the oxidation of graphite powder using the modified Hummers method [22]. Briefly, graphite powder (0.2 g), particle size 45 μm, (Wako Pure Chemical Industries, Ltd.) and sodium nitrate ($NaNO_3$) (0.16 g) were first stirred in concentrated sulphuric acid (95 wt % H_2SO_4) (6.7 mL) for 2 h while being cooled in an ice water bath. Then, potassium permanganate ($KMnO_4$) (0.9 g) was gradually added to form a new mixture. After 4 h in an ice water bath, the mixture was allowed to stand for 48 h at room temperature with gentle stirring. Thereafter, 20 mL of 5 wt % H_2SO_4 aqueous solution was added into the above mixture over 1 h with stirring. Then, 0.5 mL of H_2O_2 (30 wt % aqueous solution) was also added to the above liquid and the mixture was stirred for 2 h. After that, 20 mL of 3 wt % H_2SO_4/0.5 wt % H_2O_2 solutions was added into suspension and centrifuged (3000 rpm, 1 h). Subsequently, the product was dispersed in water and ultrasonicated for 5 h. This process affords material of oxidized graphene nano sheets (OGS) [23]. Finally, the OGS were reduced with hydrazine hydrate at room temperature for 48 h. This product was filtered and washed with distilled water and dried in air at RT for 24 h. The as-received powder is called graphene nano sheets (GNS). The detail characterization of GNS can be seen in reference as I reported previously [24] and also can be seen in Chapter 3 and 5.

Nitrogen-doped GNS (N-G) was obtained by annealing GNS in pure ammonia (NH_3) (Sumitomo

Seika Chemicals) under 0.2 MPa gas flow. The ammonia annealing of GNS was carried out in a homemade tube furnace with connected to gas tanks. Briefly, 100 mg GNS was put into boat glass and placed in the middle of tube furnace. Then, it was annealed by an ammonia stream 50 mL/min at 900 ^{o}C for 2 h in a furnace, respectively. The powder was collected and denoted as N-doped GNS 900 (N-G). Finally, they were characterized by transmission electron microscopy (TEM), X-ray photoelectron spectroscopy (XPS) and X-ray diffraction (XRD). The TEM image of N-G can be seen in Appendix 1, Supporting Information (Figure 14S). It shows that N-G has a ripple and wrinkle structure. In addition, the surface area of GNS and N-G was determined by the Brunauer Emmett and Teller (BET) adsorption method (Table 4S, Appendix 1, Supporting Information) are 318 and 594 m^2 g^{-1}, respectively. It indicates that in the presence of ammonia on GNS may assist to increase the surface area of N-G. Furthermore, the existence of N atoms in N-G was investigated by XPS measurements. As shown in Figure 15S (Appendix 1, Supporting Information), the appearance peak at around 399–400 eV, indicating the existence of N atoms on N-G structure. In addition, the level and types of N atoms on N-GNS as measured by XPS are shown in Figures 16S–18S (Appendix 1, Supporting Information), respectively. They are also evidence that N incorporation in N-G structure. This is also consistent with the atomic ratio data (Table 5S, Appendix 1, Supporting Information). It exhibits that the nitrogen are presence on N-G.

In order to prepare 20 wt % Pt/GNS, the calculated amount of Pt precursor $H_2PtCl_6 \cdot 6H_2O$ (Alfa Aesar, A Johnson Matthey Company) were dissolved in 50 mL ethanol. Subsequently, each of ethanol solution of the precursor was mixed with ethanol solution of GNS. After stirring solution for 3 h, the product was collected by filtration and dried in air at 60 ^{o}C for 12 h. It was then reduced by a hydrogen stream 25 mL/min at 400 ^{o}C for 2 h in a furnace. Finally, the catalysts were collected and denoted as 20 wt % Pt/GNS. Further, the 20 wt % Pt/N-G catalyst was prepared as same as Pt/GNS catalyst preparation. The amount of Pt on GNS and N-G were measured by thermogravimetric/differential thermal analysis (TG/DTA) (see in Appendix 1, Supporting Information, Figure 19S). This data shows that the Pt atoms of the catalyst precursor are well deposited on 20 wt % Pt/GNS and Pt/N-G catalysts.

Furthermore, the 20 wt % Pt/GNS and Pt/N-G catalysts were characterized by XRD, TEM, XPS, and TG/DTA, respectively. XRD measurements were performed at room temperature employing a two circle diffractometer (PANalytical PW 3050 Philips X'pert Pro, Cu K_α radiation of 1.541 Å, without monochromator), installed at a line focus X-ray generator. A reflection free Si plate was used as a sample stage. Cu K_α radiation obtained by reflection from a singly bent HOPG crystal was used as the incident X-ray. Diffraction pattern was recorded using a solid state detector (PANalytical X'Celerator) with a scan speed of 0.05 deg. (in 2θ)/sec up to 90 degrees. Figure 20S (Appendix 1, Supporting Information) shows the XRD patterns for 20 wt % Pt/GNS, Pt/N-G, and Pt/CB commercial catalyst. The Pt(111) peaks for Pt/GNS and Pt/N-G are weak and broad. The weak and broad peaks indicate that Pt subnano-clusters were formed, as previous reported [24]. In addition the Pt particle size and surface area for Pt/GNS, Pt/N-G and Pt/CB can be

seen in Figure 21S, Appendix 1, Supporting Information. XPS measurements were carried out using JEOL JPS 9010 TR (X-ray source Al K_{α}, 1486.6 eV; pass energy 50 eV, energy resolution 1.88 eV which was calibrated using Ag $3d_{5/2}$ by measuring a clean Ag sample, the uncertainty of binding energy ± 0.05 eV). TEM (JEOL JEM-1400 electron microscope was operated at 80 kV, resolution lattice image 0.20 nm, and resolution point image 0.38 nm. TG/DTA measurements were carried out using TG/DTA6300, Seiko Instruments Inc. (Reference: Pt; Air 200 mL/min; T measurement: 50–1000 ^{o}C; Rate: 10 ^{o}C/min), respectively.

6.2.2 Electrochemical measurement

The ORR activities of GNS, N-G, 20 wt % Pt/GNS and Pt/N-G catalysts, respectively were assessed by using cyclic voltammetry (CV), and rotating ring disk electrode (RRDE) (PGSTAT PG12, AUTOLAB Potensiostat/Galvanostat) measurements in 0.1 M $HClO_4$. The catalyst ink was prepared by dispersing 1 mg catalyst in the mixture of 500 μL (1:50 in methanol) 5 wt % Nafion solutions (Aldrich), then the mixture of catalyst ink was sonicated for 60 minutes. Then, 10 μL of catalyst ink was transferred onto the polished glassy carbon disk (diameter = 5 mm, geometric area = 0.283 cm^2) and dried to form a thin catalyst layer. The catalysts loading on the glassy carbon are 20 μg for both GNS and N-G. The rotating ring disk electrode (RRDE) polarization curves of GNS and N-G in O_2-saturated 0.1 M $HClO_4$ solution are shown in Figure 22S, Appendix 1, Supporting Information. It shows that the ORR activity of N-GNS is significant different with GNS. It indicates that the improvement ORR activity of N-G is probably due to the N incorporate in N-G structure.

On the other hand, the Pt loading on the glassy carbon for 20 wt % Pt/GNS, Pt/N-G, and Pt/CB commercial catalysts, respectively was 4 μg. The CV measurement was carried out by using a typical three-electrode systems consist of a working electrode (glassy carbon), a Pt wire as a counter electrode, and a reversible hydrogen electrode (RHE) as a reference electrode. All measurements were performed at room temperature (~ 25 ^{o}C) using a fresh electrolyte solution (0.1 M $HClO_4$, Sigma-Aldrich). First, the catalyst on the working electrode was purged by bubbling nitrogen (N_2) gas at 200 mL min^{-1} through 0.1 M $HClO_4$ for 20 minutes. Then, it was scanned at 0.05–1.0 V versus RHE for 50 cycles with scan rate 10 mV s^{-1} and rotation rate 500 rpm in N_2 to eliminate contaminant and de-oxygenates the environment. After that, the saturation gas was switched to oxygen (O_2) for RRDE measurement, and the electrolyte was saturated for the same condition as CV measurement. The RRDE polarization curves were obtained at 0.05–1.0 V versus RHE with scan rate 10 mV s^{-1} in O_2 saturated 0.1 M $HClO_4$.

For CO stripping measurements, notice that, the Pt loadings on the working electrode are the same as those measured in ORR. Briefly, each of catalyst ink solutions for 20 wt % Pt/GNS, Pt/N-G, and Pt/CB commercial catalysts, respectively was loaded onto a glassy carbon disk electrode (0.28 cm^2) with diluted

(1:50 in methanol) 5 wt % Nafion solution (Aldrich), respectively. Prior to the measurements, the working electrode was firstly purged by bubbling N_2 through the electrolyte solution of 0.1 M $HClO_4$ for 20 minutes, and then it was scanned at - 0.2 to 0.8 V versus Ag/AgCl for 50 cycles in N_2 with scan rate 10 mV s^{-1} and rotation rate 500 rpm for cleaning and de-oxygenates the environment. Subsequently, CO was adsorbed to the surface of the working electrode by bubbling 3 % CO/H_2 into the electrolyte solution of 0.1 M $HClO_4$ at 60 ^oC for 60 minutes, while holding the working electrode potential at - 0.15 V versus Ag/AgCl. After 3 % CO/H_2 bubbling, the gas was switched to N_2 for 30 minutes and the potential was scanned from - 0.2 to 0.8 V versus Ag/AgCl to record the CO stripping voltammogram at 60 ^oC with a scan rate of 10 mV s^{-1} [25–27]. The CO stripping voltammograms of 20 wt % Pt/GNS, Pt/N-G, and Pt/CB can be seen in Appendix 1, Supporting Information (Figure 23S). It shows the surface areas of Pt are 77.2, 21.5, and 68.1 m^2 g^{-1} for Pt/GNS, Pt/N-G, and Pt/CB, respectively. This data indicates that the surface area of Pt is affected by supporting material. In addition, the CO stripping data also can be used to know catalytic activity of catalyst, based on potential of CO oxidation. As shown in Figure 24S, Appendix 1, Supporting Information, the threshold voltage of Pt/GNS (0.31 V) is lower compare to Pt/N-G (0.42 V) and Pt/CB (0.43 V versus Ag/AgCl). It indicates that Pt/GNS is more readily oxidized CO compare to among Pt/N-G and Pt/CB. It means the catalytic activity of Pt/GNS is highest among the others. This is probably caused the strong interaction between Pt and GNS.

As a reference, 20 wt % Pt/CB (Alfa Aesar, Johnson Mathew Company) was measured for comparison.

6.3 Results and Discussion

6.3.1 ORR of Pt/GNS, Pt/N-G, and Pt/CB commercial catalyst

Figure 6.1 shows the ORR activities for 20 wt % Pt/GNS, Pt/N-G, and Pt/CB commercial catalyst. It clearly shows that the diffusion-limiting currents (below 0.4 V versus RHE) for all the catalysts. However, their diffusion limiting currents are different, depending on support material. This data indicates the catalyst support material affects the diffusion limiting currents values [28]. The ORR activity of Pt/GNS is higher than those of Pt/N-G and Pt/CB commercial catalyst. Further, the Pt/GNS shows the higher ORR activity, corresponding to its onset potential (0.99 V) than Pt/N-G (0.94 V versus RHE). Even the amount of Pt is similar; nevertheless, the ORR activity of catalyst is different. It indicates the Pt electronic structures of each catalyst are different as effect of supporting material.

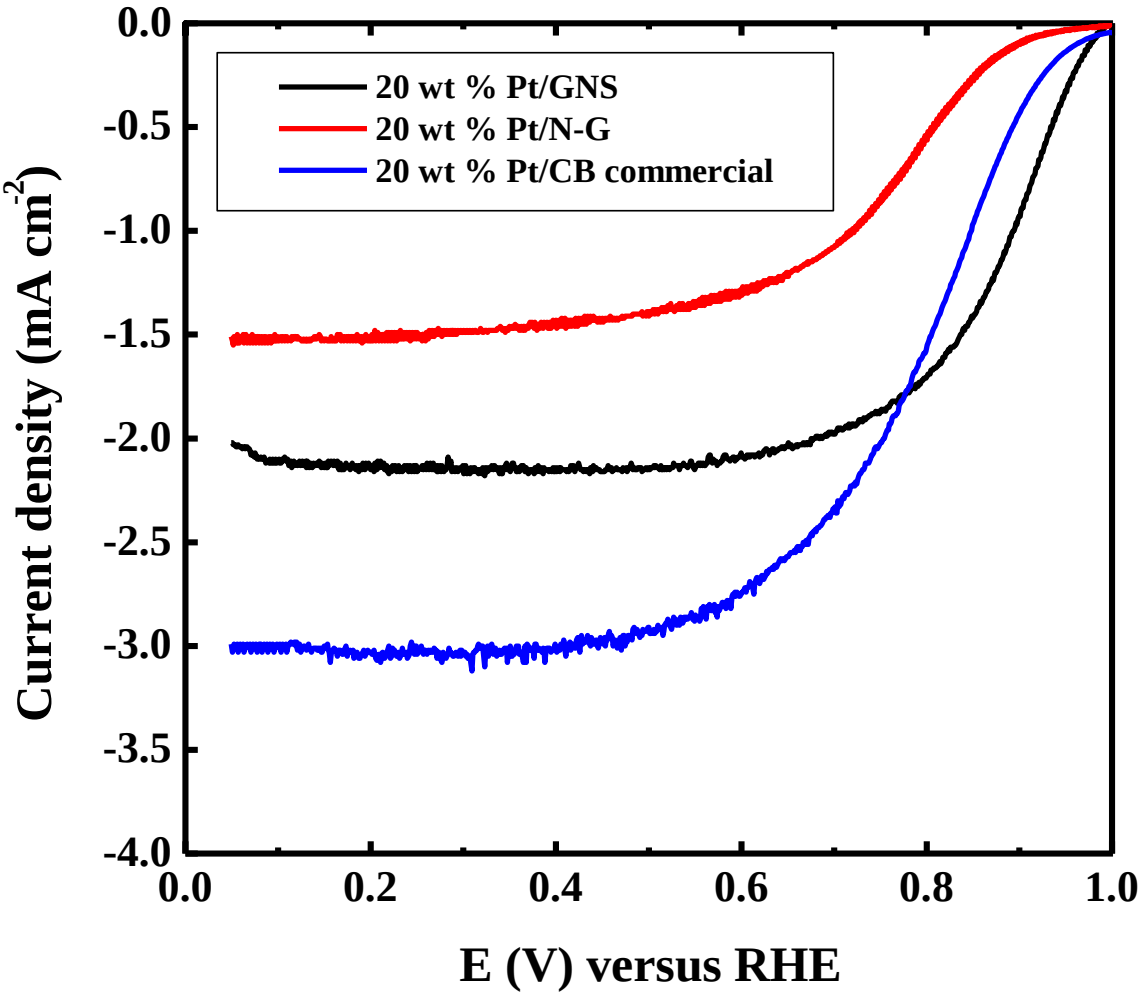

Figure 6.1 RRDE polarization curves of 20 wt % Pt/GNS, Pt/N-G, and Pt/CB commercial catalys in O_2-saturated 0.1 M $HClO_4$ solution. Scan rate is 10 mV s^{-1}. For all the RRDE measurements, the Pt loading of catalysts are 4 μg for 20 wt % Pt/GNS, Pt/N-G, and Pt/CB commercial catalyst, respectively.

This data is consistent with the results of the current density whereas was measured at 0.9 V versus RHE (Table 6.1).

Table 6.1 Current density, average Pt particle size, and BE of Pt 4f for samples.

Samples	*j* (0.9 V vs RHE) (mA cm^{-2})	Average Pt particle size (nm) (TEM measurement)	BE of Pt 4f (eV)
20 wt % Pt/GNS	0.9	1.2	71.6
20 wt % Pt/N-G	0.1	1.3	71.7
20 wt % Pt/CB	0.4	2.03	71.4

It clearly shows that the current densities of Pt/GNS, Pt/N-G and Pt/CB are 0.9, 0.1, and 0.4 mA cm^{-2}, respectively. This data also shows that Pt/GNS is higher ORR activity than Pt/N-G. It is caused the support material effect. For the ORR, the too high reactivity of the support material impedes reaction by blocking the active sites with strong adsorbed intermediates, while too low reactivity hinders the dissociation of O–O bond and charge transfer [29].

6.3.2 TEM

The TEM images and histograms of 20 wt % Pt/GNS, Pt/N-GNS, and Pt/CB commercial catalysts are shown in Figure 6.2.

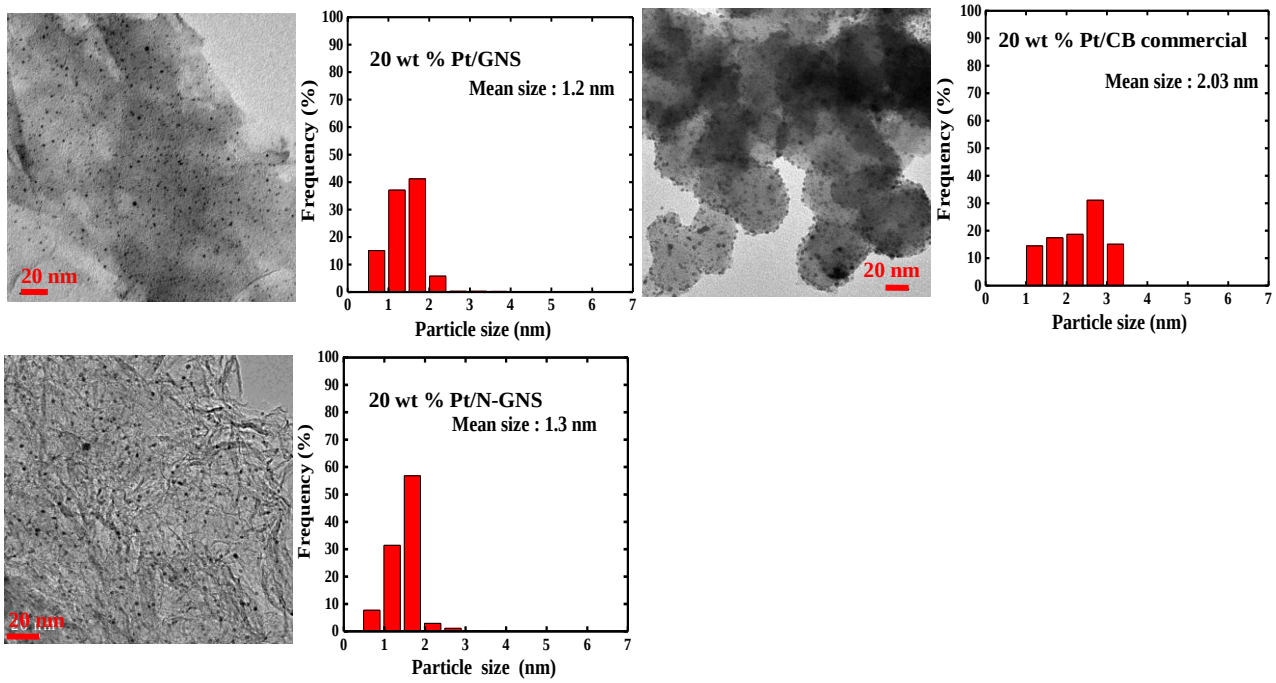

Figure 6.2 TEM images and histograms of 20 wt % Pt/GNS, Pt/N-G, and Pt/CB commercial catalyst, respectively.

The Pt particle size distributions were analyzed with random chosen areas containing 600 particles in magnified TEM images. The Pt particle size only was estimated base on Pt particles (< 5 nm). As shown in TEM images, the Pt particles are good dispersing on GNS, N-G, and CB. The average Pt particle size of Pt/GNS, Pt/N-G, and Pt/CB are 1.2, 1.3, and 2.03 nm, respectively (Table 6.1). Interestingly, the Pt subnano-clusters were only formed on GNS and N-G, but not on CB. It means the GNS and N-G as supporting materials may play important role on formation of Pt subnano-clusters. The Pt subnano-clusters are much more formed on Pt/GNS than that of Pt/N-G. It is responsible causing the ORR activity of Pt/GNS is higher than Pt/N-G.

6.3.3 XPS

Figure 6.3 shows the Pt 4f XPS spectra for 20 wt % Pt/GNS, Pt/N-G, and Pt/CB commercial catalyst.

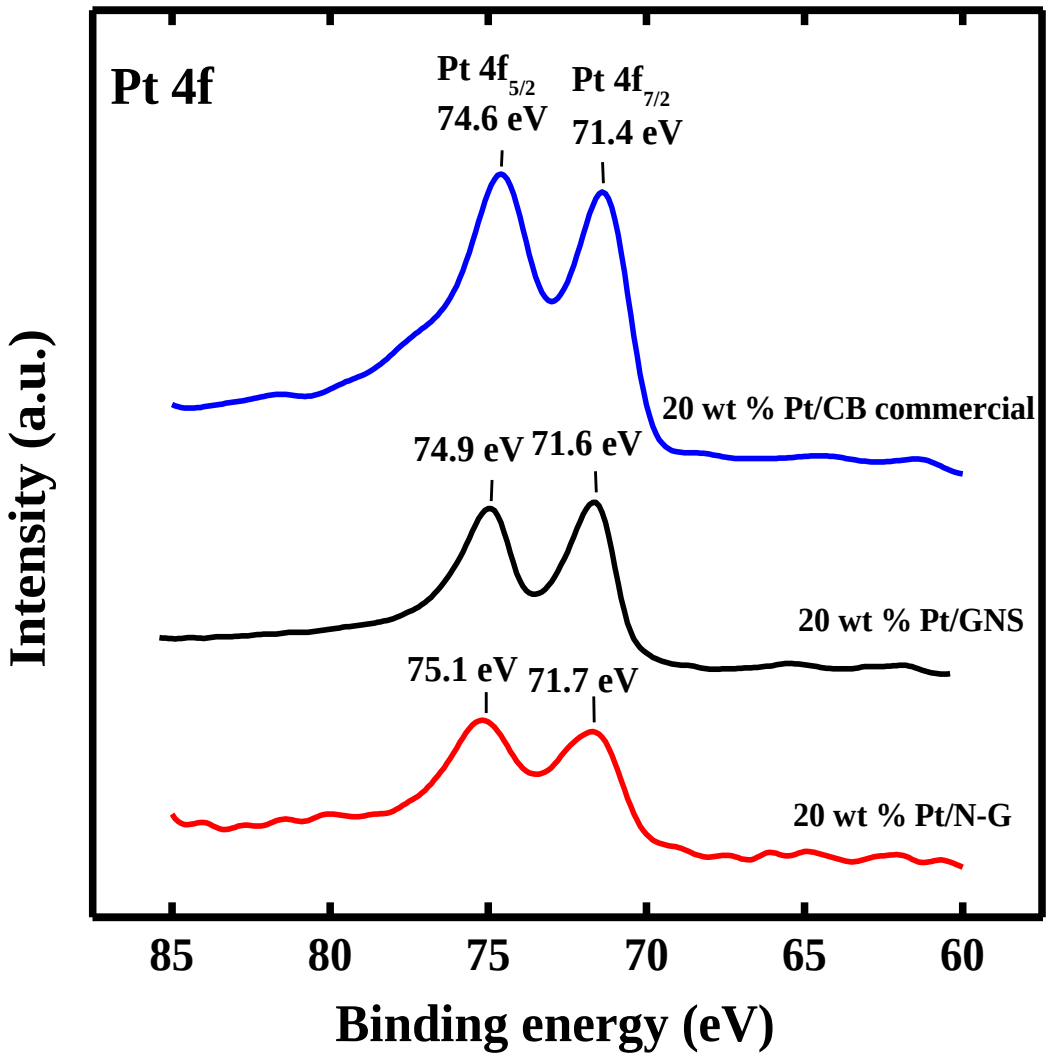

Figure 6.3 XPS spectra for 20 wt % Pt/GNS, Pt/N-G, and Pt/CB commercial catalyst.

The binding energies (BEs) are 71.6, 71.7, and 71.4 eV for Pt/GNS, Pt/N-G, and Pt/CB, respectively (Table 6.1). The BE of Pt on Pt/CB is close to the bulk Pt (71.2 eV) [30], indicating the weak interaction between Pt and CB. Interestingly, the BEs of Pt on Pt/GNS and Pt/N-G shift to higher binding energy compare to Pt/CB. It indicates that GNS and N-G significantly influence the π–d interaction in terms of Pt electronic structure. Therefore, the GNS and N-G can be expected to modify the Pt electronic structure. This is also the reason why the ORR activity of Pt/GNS is highest among the others, because the strong interaction between Pt and GNS, probably π–d interaction.

6.4 Conclusion

In this study, the GNS and N-G were used as supporting materials to deposit Pt particles in order to investigate the support material effect for ORR activity. The ORR activity of Pt/GNS is higher than Pt/N-G catalysts. This suggests that the modification of π states by the N-doping change the properties of the interaction between Pt and carbon. The interaction between Pt and graphene is considered to be π–d hybridization. Therefore, one can control the electronic structure of graphene and Pt by doping of some elements.

References

[1] Y. Shao, J. Liu, Y. Wang, Y. Lin, J. Mat. Chem., **19**, 46–59 (2009).

[2] H. A. Gasteiger, N. M. Markovic, Science, **324**, 48–49 (2009).

[3] H. A. Gasteiger, S. S. Kocha, B. Sompalli, T. F. Wagner, Appl. Catal. B. Environ., **56**, 9–35 (2005).

[4] Z. Peng, H. Yang, Nano Today, **4**, 143–164 (2009).

[5] N. M. Markovic, T. J. Schmidt, V. Stamenkovic, P. N. Ross, Fuel Cells, **1**, 105–116 (2001).

[6] D. J. Berger, Science, **286**, 49–50 (1999).

[7] R. Kou, Y. Shao, D. Mei, Z. Nie, D. Wang, C. Wang, V. V. Viswanathan, S. Park, I. A. Aksay, Y. Lin, Y. Wang, J. Liu, J. Am. Chem. Soc., **133**, 2541–2547 (2011).

[8] Y. Shao, G. Yin, Y. Gao, J. Power Sources, **171**, 558–566 (2007).

[9] J. G. Zhou, X. T. Zhou, X. H. Sun, R. Y. Li, M. Murphy, Z. F. Ding, X. L. Sun, T. K. Sham, Chem. Phys. Lett., **437**, 229–232 (2007).

[10] Y. Shao, J. Sui, G. Yin, Y. Gao, Appl. Catal., B, **79**, 89–99 (2008).

[11] T. Yoshitake, Y. Shimakawa, S. Kuroshima, H. Kimura, T. Ichihashi, Y. Kubo, D. Kasuya, K. Takahashi, F. Kokai, M. Yudasaka, S. Iijima. Physica B, **323**, 124–126 (2002).

[12] K. W. Park, Y. E. Sung, S. Han, Y. Yun, T. Hyeon, J. Phys. Chem. B, **108**, 939–944 (2004).

[13] Y. Y. Shao, G. P. Yin, J. J. Wang, Y. Z. Gao, P. F. Shi, J. Power Sources, **161**, 47–53 (2006).

[14] C. A. Bessel, K. Laubernds, N. M. Rodriguez, R. T. K. Baker, J. Phys. Chem. B, **105**, 1115–1118 (2001).

[15] J. Wang, G. Yin, Y. Shao, S. Zhang, Z. Wang, Y. Gao, J. Power Sources, **171**, 331–339 (2007).

[16] C. L. Sun, L. C. Chen, M. C. Su, L. S. Hong, O. Chyan, C.Y. Hsu, K. H. Chen, T. F. Chang, L. Chang, Chem. Mater., **17**, 3749–3753 (2005).

[17] Y. Y. Shao, G. P. Yin, Z. B. Wang, Y. Z. Gao, J. Power Sources, **167**, 235–242 (2007).

[18] M. D. Stoller, S. Park, Y. Zhu, J. An, R. S. Ruoff, Nano Lett., **8**, 3498–3502 (2008).

[19] K. S. Novoselov, A. Geim, S. V. Morozov, D. Jiang, Y. Zhang, S. V. Dubonos, I. V. Grigorieva, A. A. Firsov, Science, **306**, 666–669 (2004).

[20] E. Antolini, Applied Catalysis B: Environmental, **123–124**, 52–68 (2012).

[21] O. V. Cherstiouk, P. A. Simonov, E. R. Savinova, Electrochim. Acta, **48**, 3851–3860 (2003).

[22] W. S. Hummers, R. E. Offeman, J. Am. Chem. Soc., **80**, 1339 (1958).

[23] S. Stankovich, D. A. Dikin, G. H. B. Dommett, K. M. Kohlhaas, E. J. Zimney, E. A. Stach, R. D. Piner, S. T. Nguyen, R. S. Ruoff, Nature, **442**, 282–286 (2006).

[24] R. Siburian, J. Nakamura, J. Phys. Chem. C, **116**, 22947–22953 (2012).

[25] J. B. Joo, P. Kim, W. Kim, Y. Kim, J. Yi, J Appl. Electrochem., **39**, 135–140 (2009).

[26] T. Vidakovic, M. Christov, K. Sundmacher, Electrochim. Acta, **52**, 5606–5613 (2007).

[27] O. V. Cherstiouk, P. A. Simonov, E. R. Savinova, Electrochim. Acta, **48**, 3851–3860 (2003).

[28] D. He, K. Cheng, H. Li, T. Peng, F. Xu, S. Mu, M. Pan, Langmuir, **28**, 3979–3986 (2012).

[29] M. Shao, A. Peles, K. Shoemaker, Nano Lett., **11**, 3714–3719 (2011).

[30] J. Moulder, W. F. Stickle, P. E. Sobol, K. D. Bomben, Handbook of X-ray Photoelectron Spectroscopy, Perkin Elmer Corporation, Minnesota, USA, 1992.

Chapter 7

Conclusions and Future studies

This study was performed to control the particle size of Pt on GNS in a region from sub-nanometer to a few nanometers. The controlling average of Pt particle size can be prepared by changing Pt loading on GNS. Then, I can clarify relationship among the Pt particle size, catalytic activity, and the electronic structure of Pt on GNS by XRD, XPS, TEM and electrochemical measurements. Interestingly, Pt subnano-clusters are formed on GNS, which has never been observed for the other graphitic supports. It exhibited the outstanding properties, such as large surface area, high electrocatalytic activity and strong interaction between Pt and graphene. Subsequently, the formation of Pt subnano-clusters on GNS is needed to clarify. The mechanism of formation for Pt subnano-clusters on GNS was proposed based on catalyst preparation at different pH. Finally, I study about defect of graphene. It can be prepared by annealing of GNS in ammonia at various annealing temperature to produce N-doped graphene. The effect of N-doped graphene as a supporting material for Pt catalyst also was evaluated by XRD, XPS, TEM and electrochemical measurements. As results of this study, I have found that the catalytic activity and electronic state of Pt is affected by supporting material.

Here I present the conclusions of this thesis and the outlook for the future studies.

7.1 Conclusions

1) Size Control to a Sub-nanometer Scale in Platinum Catalysts on Graphene

In this study, controlling the particle size of Pt on GNS in a region from sub-nanometer to a few nanometers have been successfully prepared by changing Pt loading on GNS from 10 to 70 wt %. At a low loading of 10 wt %, Pt subnano-clusters are formed on GNS shows large surface area of 170 $m^2 g^{-1}$. The 10 wt % Pt/GNS catalyst also exhibits the best performance in the electro-oxidation of adsorbed CO. Therefore,

Pt subnano-clusters can be expected as excellent electro-oxidation catalysts. An increase in loading of Pt leads to an increase in particle size of Pt, resulting in the lower activities for electro-oxidation of adsorbed CO. Core level of Pt in the electronic structure for Pt subnano-clusters are shifted to higher binding energies, indicating chemical interaction between Pt and graphene. The modification of catalytic properties and the electronic structure is ascribed to the interface interaction between Pt and graphene via π–d hybridization.

2) Formation Process of Pt Subnano-Clusters on Graphene Nano Sheets

The formation process of Pt subnano-clusters on GNS from H_2PtCl_6 with ethanol at different pH has been studied. The formation mechanism of Pt subnano-clusters composed of 5–40 Pt atoms on GNS has been studied by XRD, XPS, and TEM. The exchange of Cl^- ion by OH^- ion and the reduction of Pt^{4+} to Pt^{2+} are examined by XPS in the reduction of an H_2PtCl_6 catalyst precursor by ethanol at different pH. Aggregates of Pt^{2+}-containing compounds ranging from 2 to 30 nm in diameter are first attached on GNS by the partial reduction with ethanol. The Pt subnano-clusters are found to be formed in the reduction process of Pt^{2+}-containing compounds by H_2 at 400 ^oC. A formation model of the Pt subnano-clusters is proposed that Pt atoms formed by the reduction with H_2 migrate and collide with each other on GNS, leading to the formation of Pt subnano-clusters. The driving factors for the Pt subnano-clusters formation are ascribed to intense π–d hybridization between carbon and Pt as well as the large surface area of graphene.

3) Effect of N-doped graphene for Properties of Pt/N-doped graphene catalyst

Nitrogen doping into graphene was carried out by heating GNS in ammonia to produce N-doped graphene (N-G). The N-G was used as a support material for Pt catalyst as well as a catalyst itself for half-cell cathode reaction of hydrogen fuel cell (H_2FC). It is found that the ORR electrocatalytic activity for N-G 900 (0.63 V versus RHE) is higher than GNS. It indicates that the incorporation of nitrogen in N-G may affect the ORR activities. XPS results exhibit the pyridinic N is the majority in N-G, where the pyridinic N refers to N atom bonds with two C atoms at the edges or defects of graphene. Interestingly, the Pt subnano-clusters were formed on all of Pt/N-G catalysts with Pt particle size (0.7–1.0 nm). It clearly indicates that the doping of nitrogen significantly influence π–d hybridization in terms of electronic structures.

4) Support material effect for Pt catalytic activity at cathode

In this study, the GNS and N-G were used as supporting materials to deposit Pt particles in order to investigate the support material effect for ORR activity. The ORR activity of Pt/GNS is higher than Pt/N-G catalysts. This suggests that the modification of π states by the N-doping change the properties of the interaction between Pt and carbon. The interaction between Pt and graphene is considered to be π–d hybridization. Therefore, one can control the electronic structure of graphene and Pt by doping of some elements.

7.2 Future studies

As mentioned above, I showed that activity of Pt catalyst can be controlled by controlling the Pt particle size and depend on supporting material. It was also suggested that especially the flat graphene surface affect the electronic state of Pt catalyst. However, there are still many problems to elucidate a catalyst support effect in the application of fuel cell field and also directly evidence interaction between Pt and support material is needed. Finally, I will briefly discuss the outlooks for future studies on support effect.

1) Evaluation of catalyst by using carbon monoxide-temperature program desorption (CO-TPD) measurement is needed in order to direct evidence the interaction between metal catalyst and support material. In addition, in the same time, the catalytic activity of catalyst also can be estimated.

2) Investigation of the local density of states (LDOS) at Fermi energy (E_F) of Pt/GNS by using the scanning tunneling microscopy (STM) and spectroscopy (STS) techniques is needed. STS involves observation of changes in constant-current topography with tip-sample bias, local measurement of the tunneling current versus tip-sample bias (I-V) curve. Thereby, the difference in the electronic state of Pt monolayer and bulk Pt may be clarified by using this method.

Acknowledgements

First of all, I would like to thankful, Prof. Junji Nakamura as my supervisor, for having patience, giving inspiration, constant encouragement throughout my study and earnest review for the creation of this thesis. I was granted the unique opportunity and golden chance to learn a wide range of experimental and comfortable learning process, travelling with discussion, attending many conferences, working and studying with much collaboration from a wide range of scientists with expertise in many different aspects of catalysis research. Over the three years, I have grown substantially as a student and a scientist under Prof. Nakamura guidance, supports and providing a good laboratory environment and facilities, to which I am eternally grateful. Much appreciation and gratitude goes to Assistant Professor Takahiro Kondo (University of Tsukuba) for helping and guidance me with fruitful discussion during doctoral program and also his earnest review of my publications.

I wish to express my sincere appreciation to my Ph.D committees, Professor Hiroaki Suzuki (University of Tsukuba), Professor Junichi Fujita (University of Tsukuba), and Associate Professor Hiromasa Goto (University of Tsukuba) for their fruitful comments and suggestions, which have been exceedingly helpful during the writing process of this thesis and to my work in the degree committee.

During the past three years, I had the benefit of working closely with some extraordinary students. I was able to learn the basics of catalysis research and the usage of equipment from several particularly helpful students: Masataki Sakurai, Hiromitsu Nogi, Dr. Yoshihiro Nemoto (NIMS), Dr. Shinichi Ito (University of Tsukuba), Nitta-San, Obuchi-San, Soukura-San, Akasu-San, and all of the others member of Nakamura Laboratory, I am extremely grateful for your love, cooperation, valuable discussions, and very precious experience in my life.

I am also thankful to Ministry of Education and Culture, Republic of Indonesia for scholarship supporting during my doctoral program.

Finally, I would like to thank my dear family. To my father, Pdt. Drs. R.A. Siburian, my wife, Efi Srivita Sinambela, M. Si and our daughters, Madeline Hanatasya Siburian and Nathania Yosefin Siburian, for their unfailing love, patience, perseverance, and encouragement enable me to really concentrate on my study.

February 2013

Institute of Material Science

University of Tsukuba

Rikson Asman Fertiles Siburian

List of Publications

1. R. Siburian, J. Nakamura, Formation process of Pt subnano–clusters on graphene nanosheets
   J. Phys. Chem. C **116** (2012) 22947–22953.

2. R. Siburian, T. Kondo, J. Nakamura, Size Control to a Sub-Nanometer Scale in Platinum Catalysts on Graphene, J. Phys. Chem. C (2013), DOI**:** 10.1021/jp311852j (in press).

3. R. Siburian, T. Kondo, J. Nakamura, Support effect in cathode catalytic activity of Pt/GNS, J. Phys. Chem. C 2013 (to be submitted).

4. R. Siburian, 中村潤児、グラフェンを用いた燃料電池電極触媒（著書）
   NTS 出版「グラフェンが拓く材料の新領域-物性・作製から実用化まで-」
   p192-p199 (2012).

List of Presentations

1. R. Siburian, J. Nakamura, Effect of pH on the preparation of Pt/Graphene Nano Sheets for CO-Tolerant Anode Catalyst, 14th International Association of Colloid and Interface Scientists, Conference (International conference), May 13-18, 2012, Sendai, Japan.

Appendix 1

Supporting Information

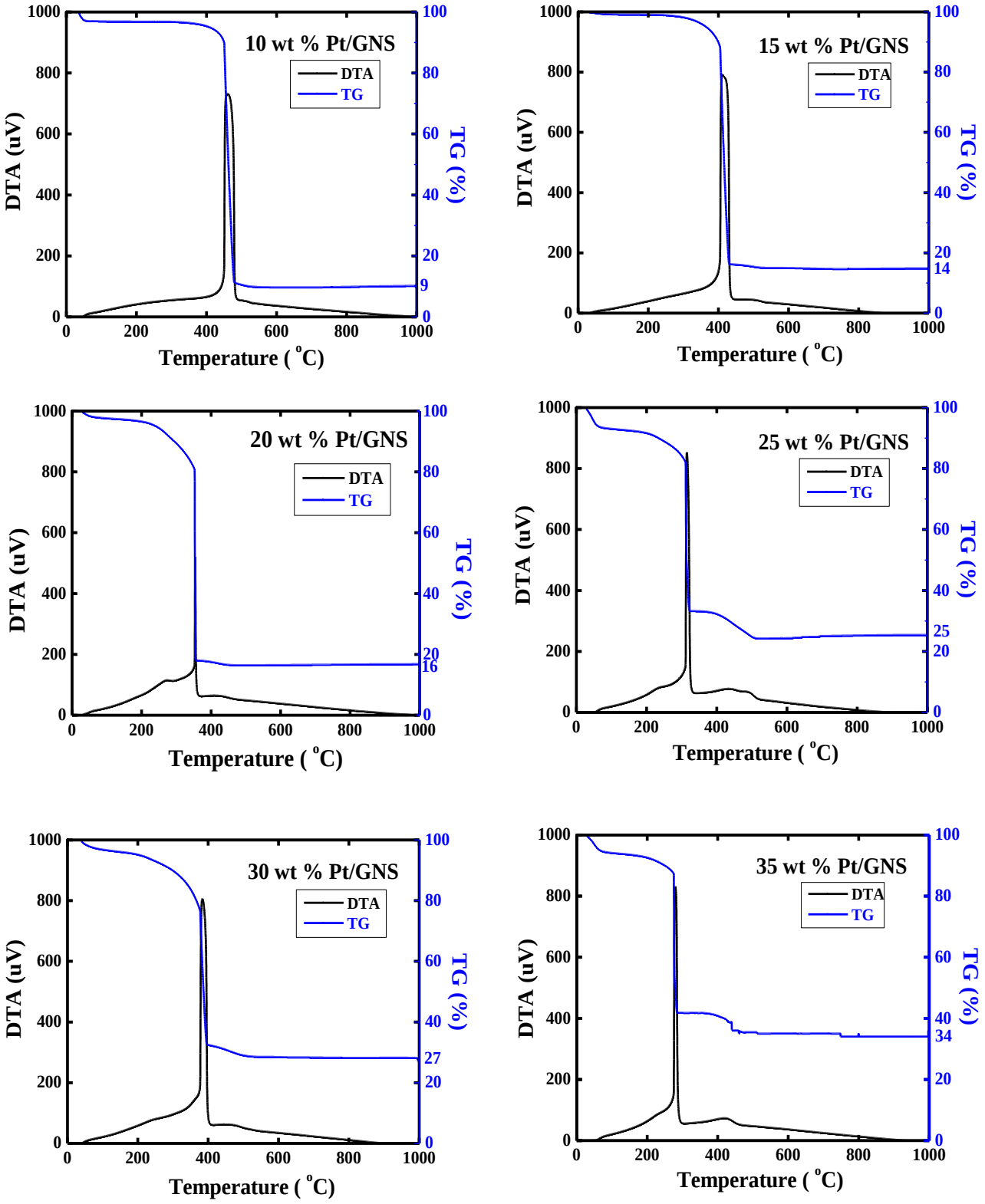

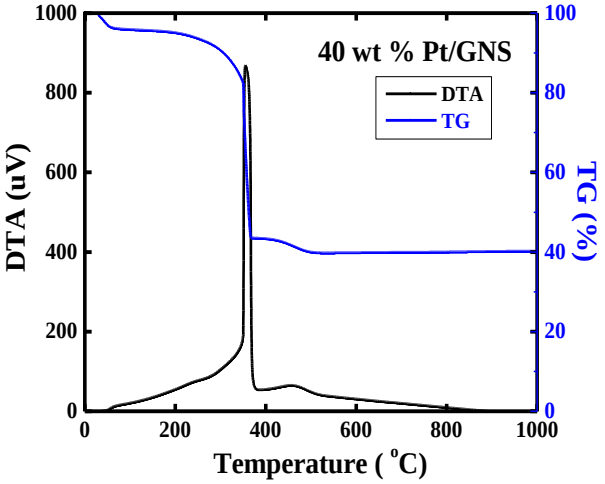
40 wt % Pt/GNS
DTA
TG
DTA (uV)
TG (%)
Temperature (°C)
1000
800
600
400
200
0
100
80
60
40
20
0
0
200
400
600
800
1000

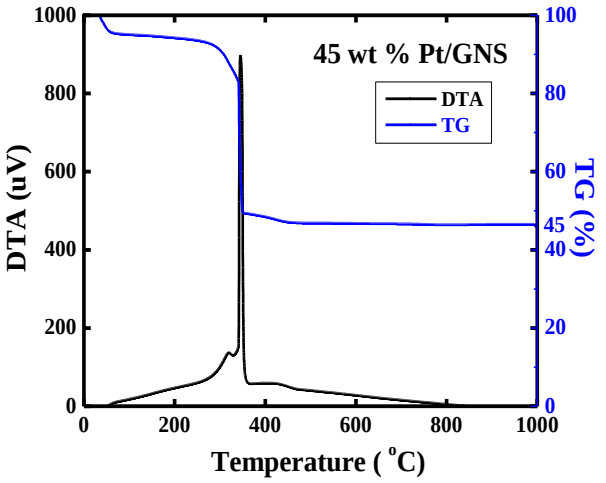
45 wt % Pt/GNS
DTA
TG
DTA (uV)
TG (%)
Temperature (°C)
1000
800
600
400
200
0
100
80
60
45
40
20
0
0
200
400
600
800
1000

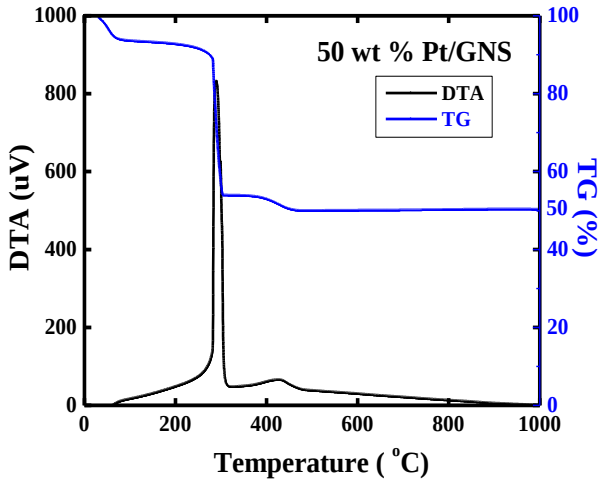
50 wt % Pt/GNS
DTA
TG
DTA (uV)
TG (%)
Temperature (°C)
1000
800
600
400
200
0
100
80
60
50
40
20
0
0
200
400
600
800
1000

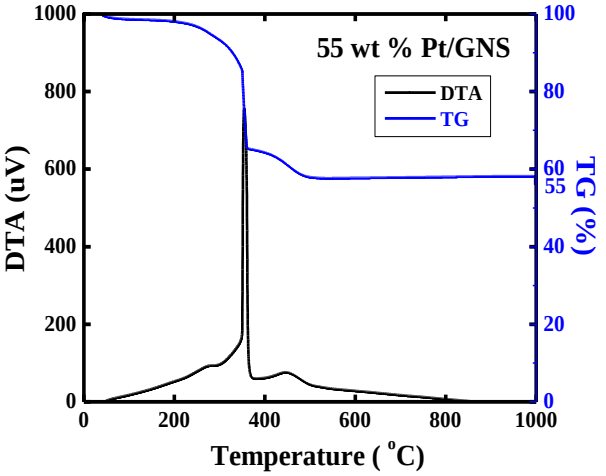
55 wt % Pt/GNS
DTA
TG
DTA (uV)
TG (%)
Temperature (°C)
1000
800
600
400
200
0
100
80
60
55
40
20
0
0
200
400
600
800
1000

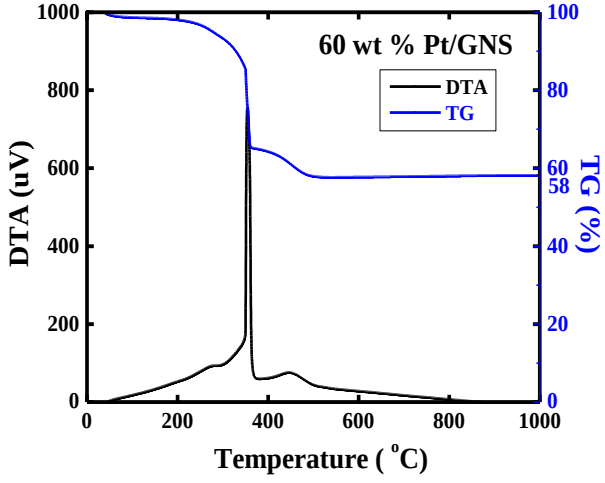
60 wt % Pt/GNS
DTA
TG
DTA (uV)
TG (%)
Temperature (°C)
1000
800
600
400
200
0
100
80
60
58
40
20
0
0
200
400
600
800
1000

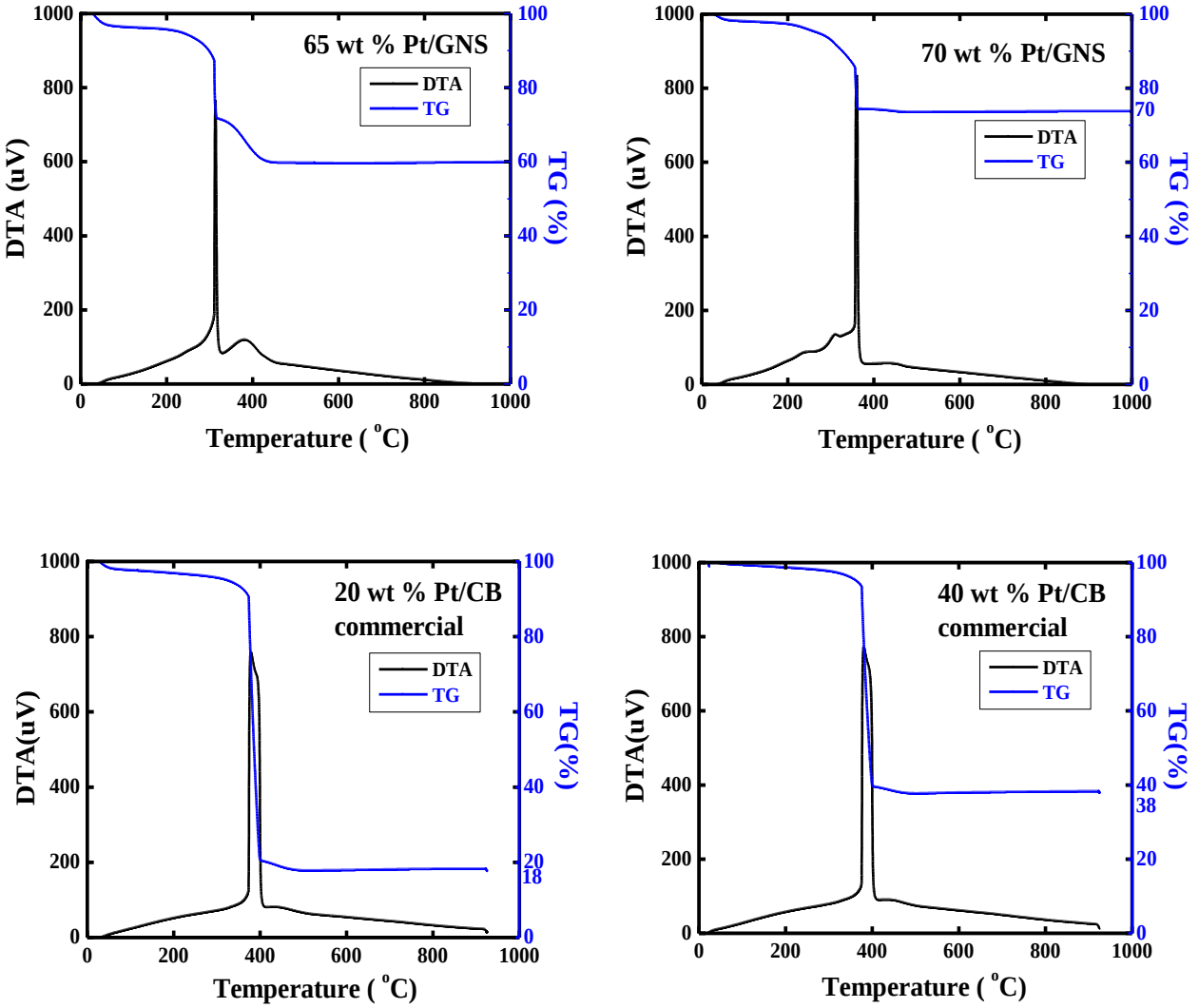

Figure 1S. TG/DTA thermograms for 10–70 wt % Pt/GNS and 20 and 40 wt % Pt/CB commercial catalysts.

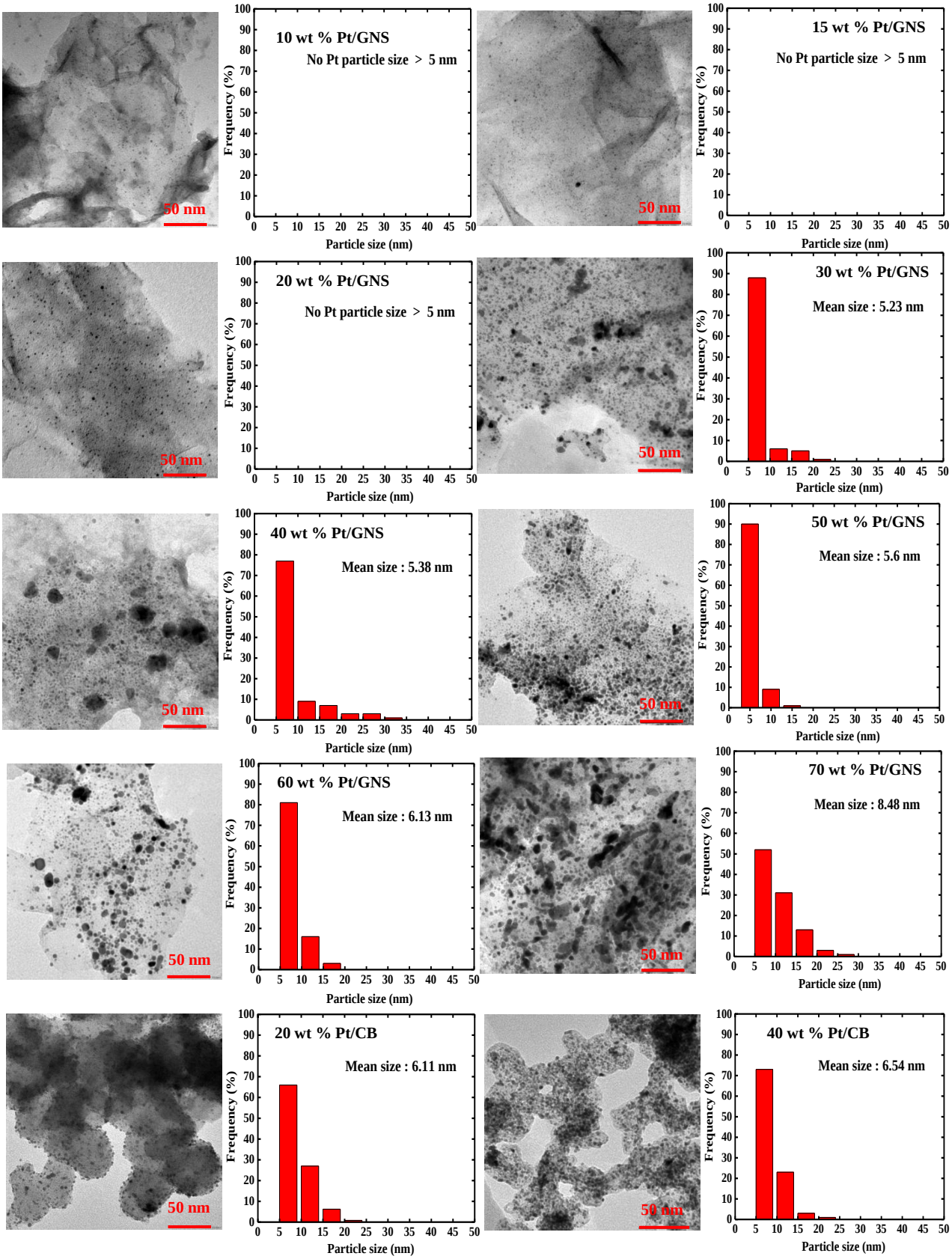

Figure 2S. TEM images and histograms of 10–70 wt % Pt/GNS. The results for 20 and 40 wt % Pt/CB commercial catalysts are also shown.

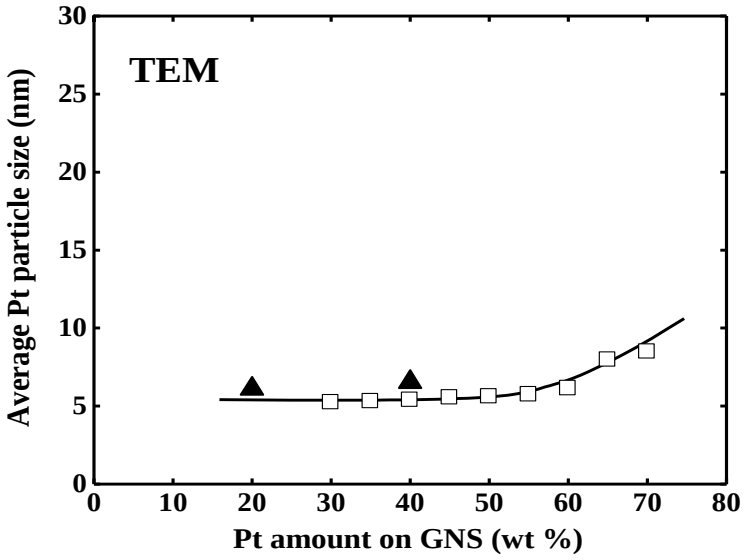

Figure 3S. Average Pt particle size (nm) estimated by TEM versus Pt amount on GNS (□). The results for 20 and 40 wt % Pt/CB commercial catalysts (▲) are also shown.

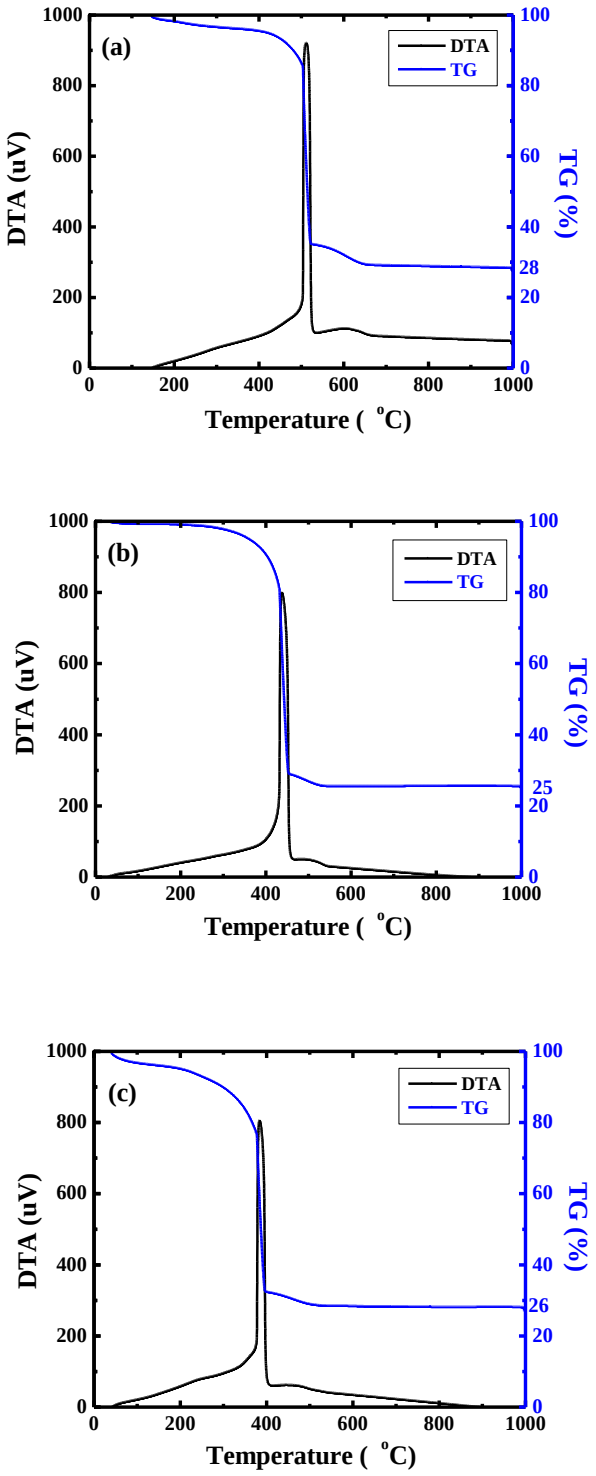

Figure 4S. TG/DTA thermograms of Pt/GNS, prepared at (a) pH 1, (b) pH 6, and (c) pH 12.5, respectively.

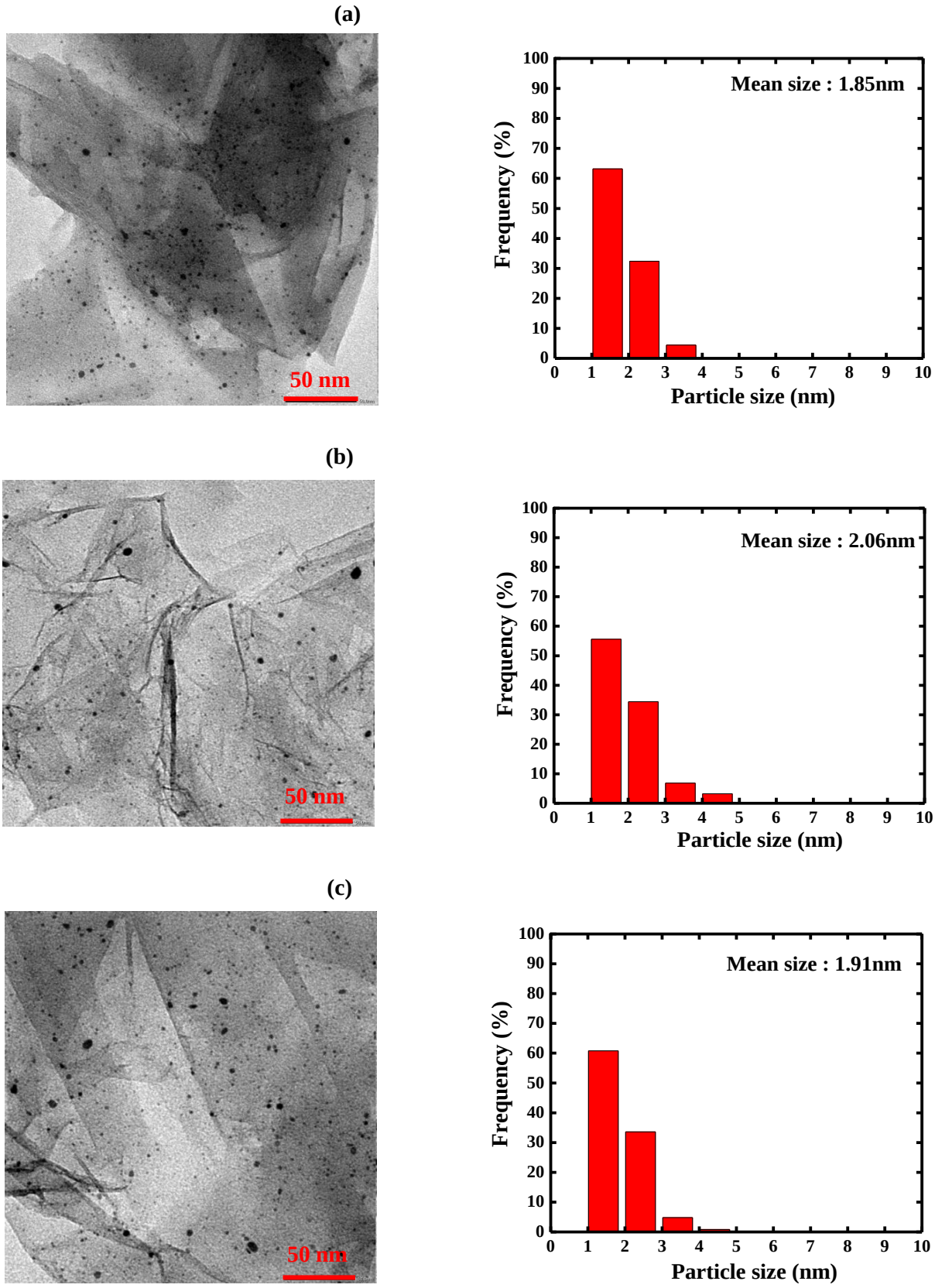

Figure 5S. (a–c) TEM images and histograms for 30 wt % Pt/GNS catalyst prepared at pH 1, 6, and 12.5 in aqueous solution and reduced with H_2 (400 ^{o}C, 2h), respectively.

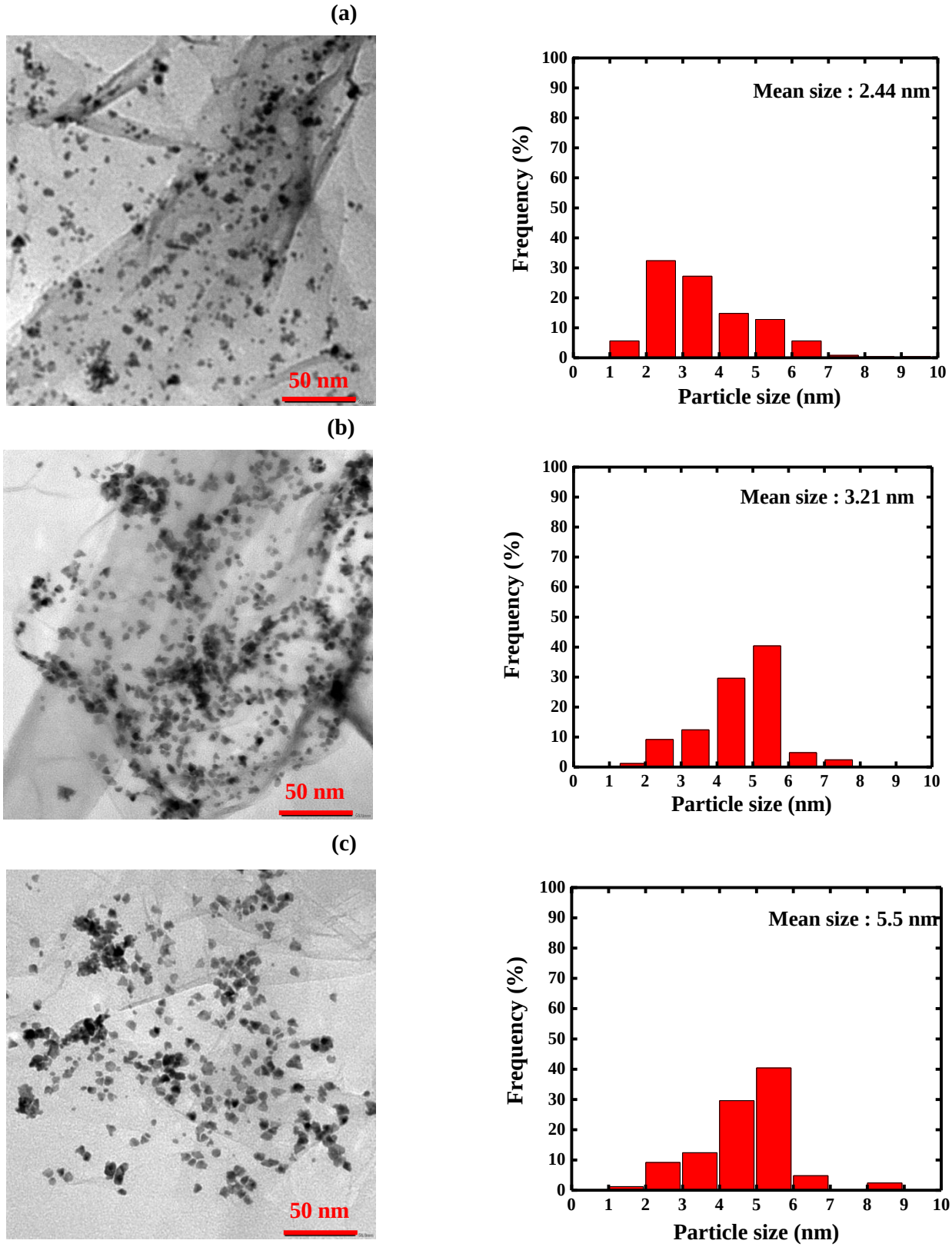

Figure 6S. (a–c) TEM images and histograms for 30 wt % Pt/GNS catalyst prepared at pH 1, 6, and 12.5 in aqueous solution and reduced with 0.01 M $NaBH_4$, respectively.

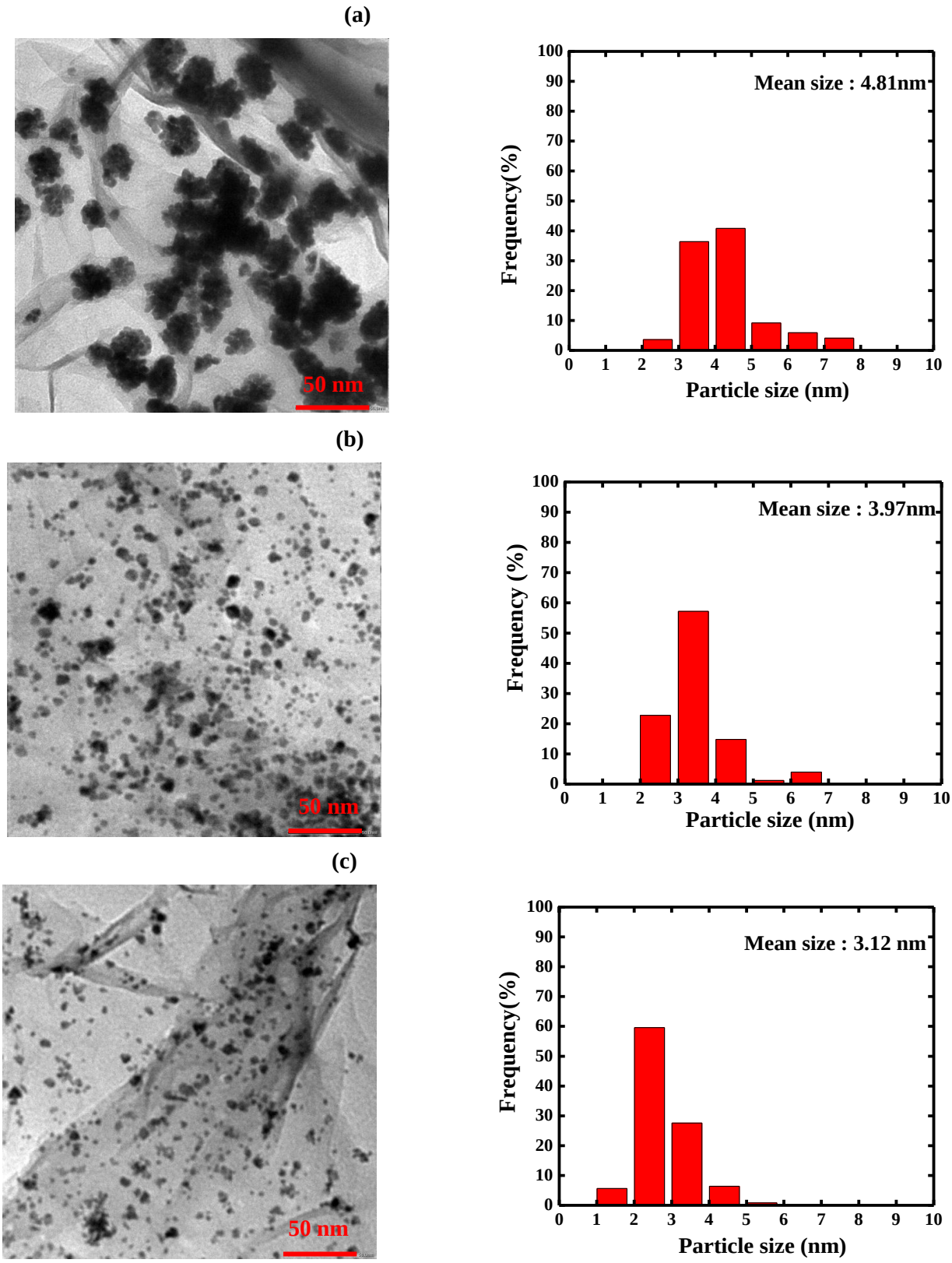

Figure 7S. (a–c) TEM images and histograms for 30 wt % Pt/GNS catalyst prepared at pH 1, 6, and 12.5 in ethanol solution and reduced with 0.01 M $NaBH_4$, respectively.

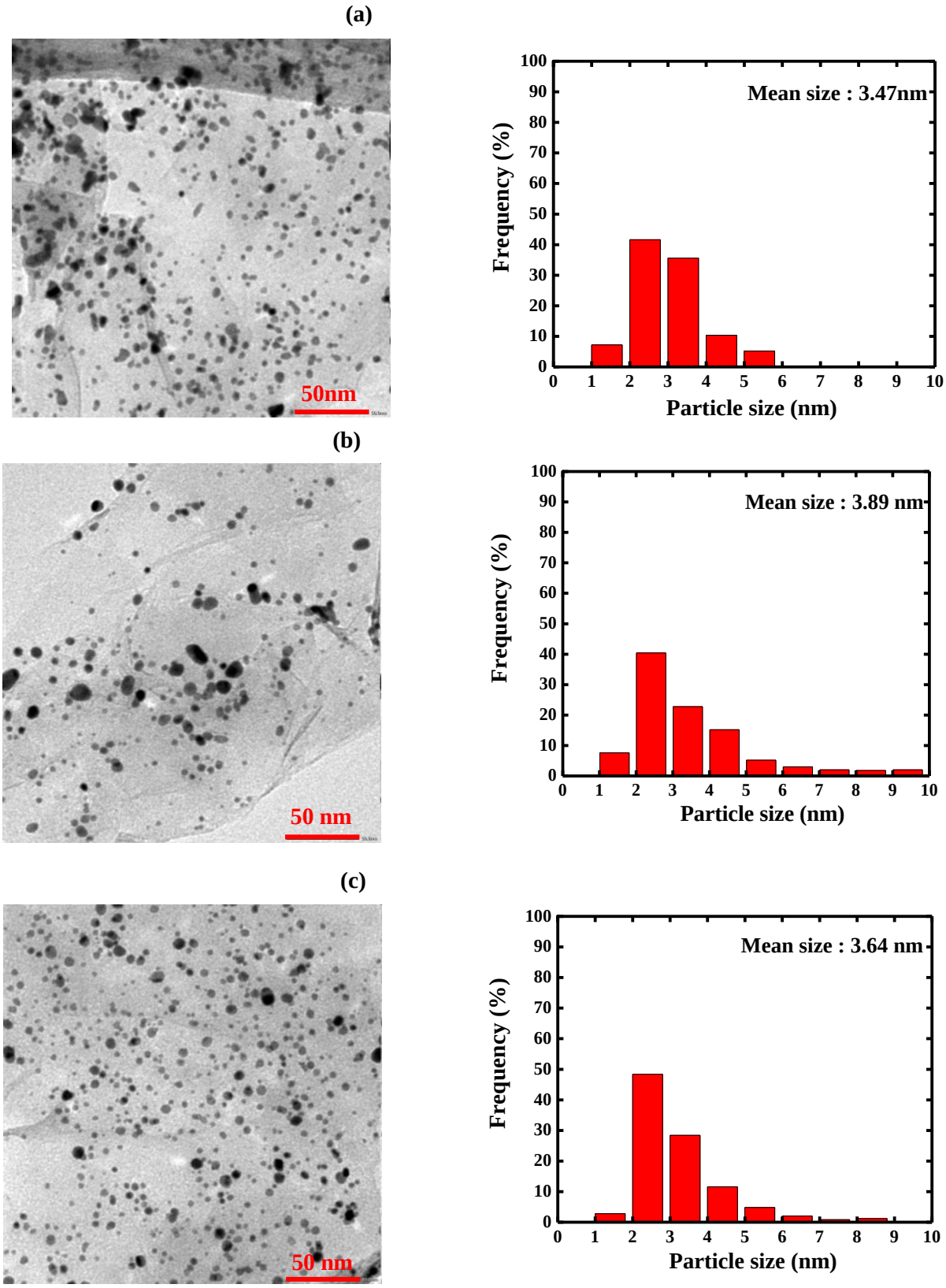

Figure 8S. (a–c) TEM images and histograms for 30 wt % Pt/GNS catalyst prepared at pH 1, 6, and 12.5 in ethanol solution, reduced with 0.01 M $NaBH_4$ and heat treatment in H_2 (400 ^oC, 2h), respectively.

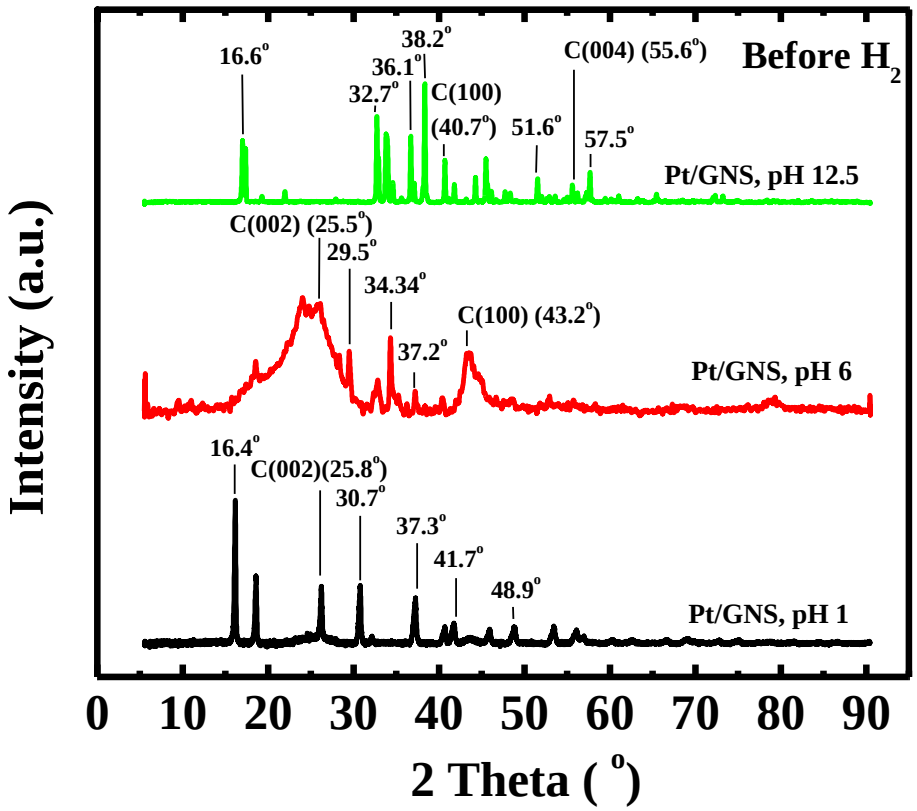

Figure 9S. XRD patterns of the samples after step 2.

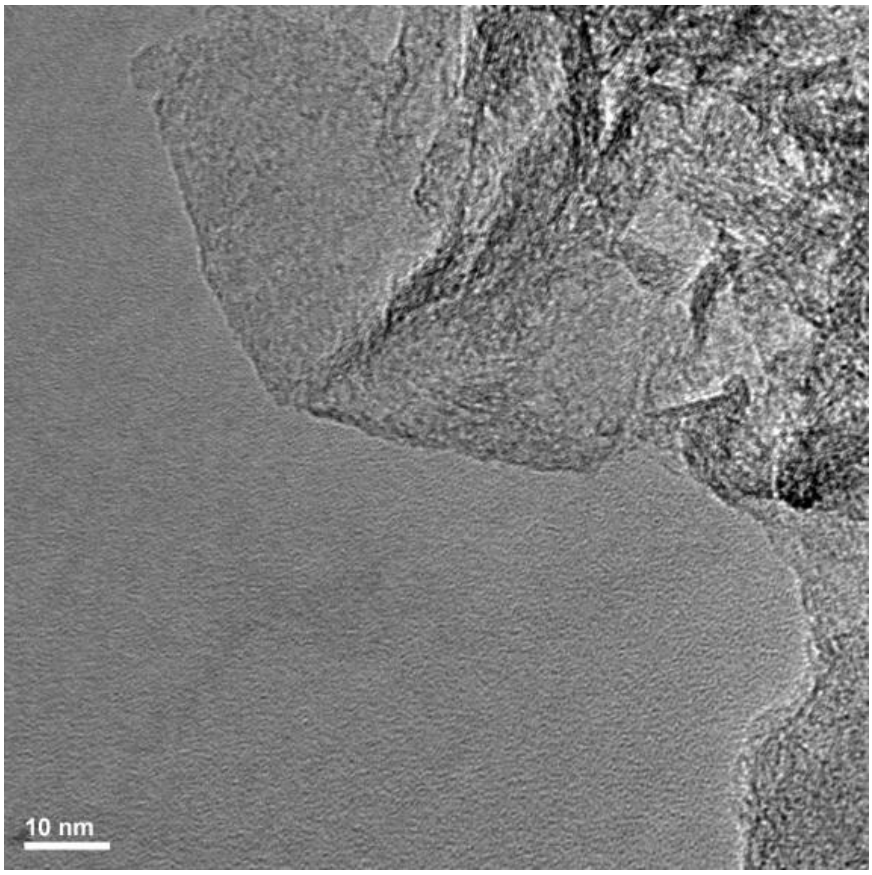

Figure 10S. TEM image of N-G 600.

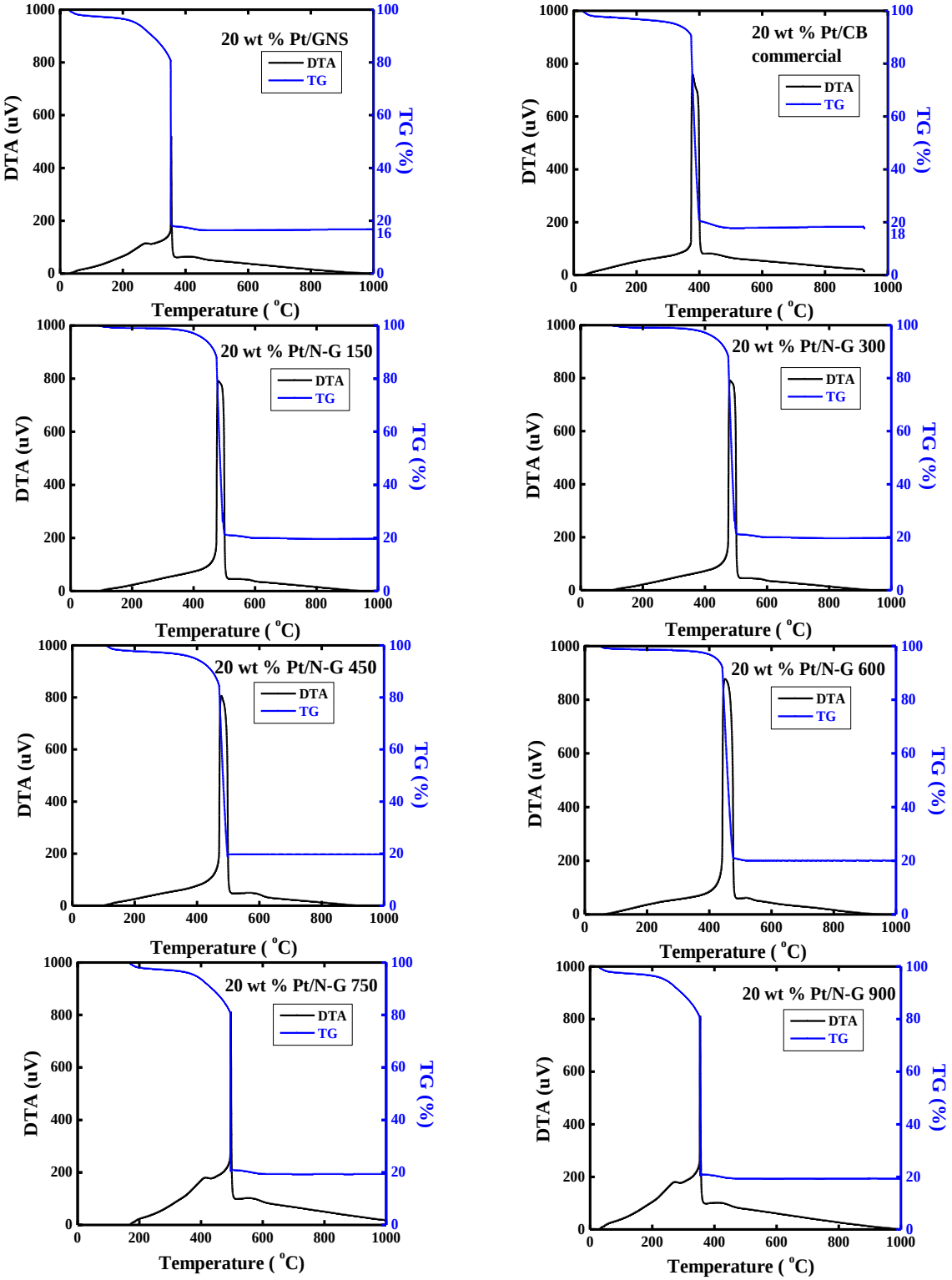

Figure 11S. TG/DTA thermograms of 20 wt % Pt/GNS, Pt/N-G 150–900, and Pt/CB commercial catalyst.

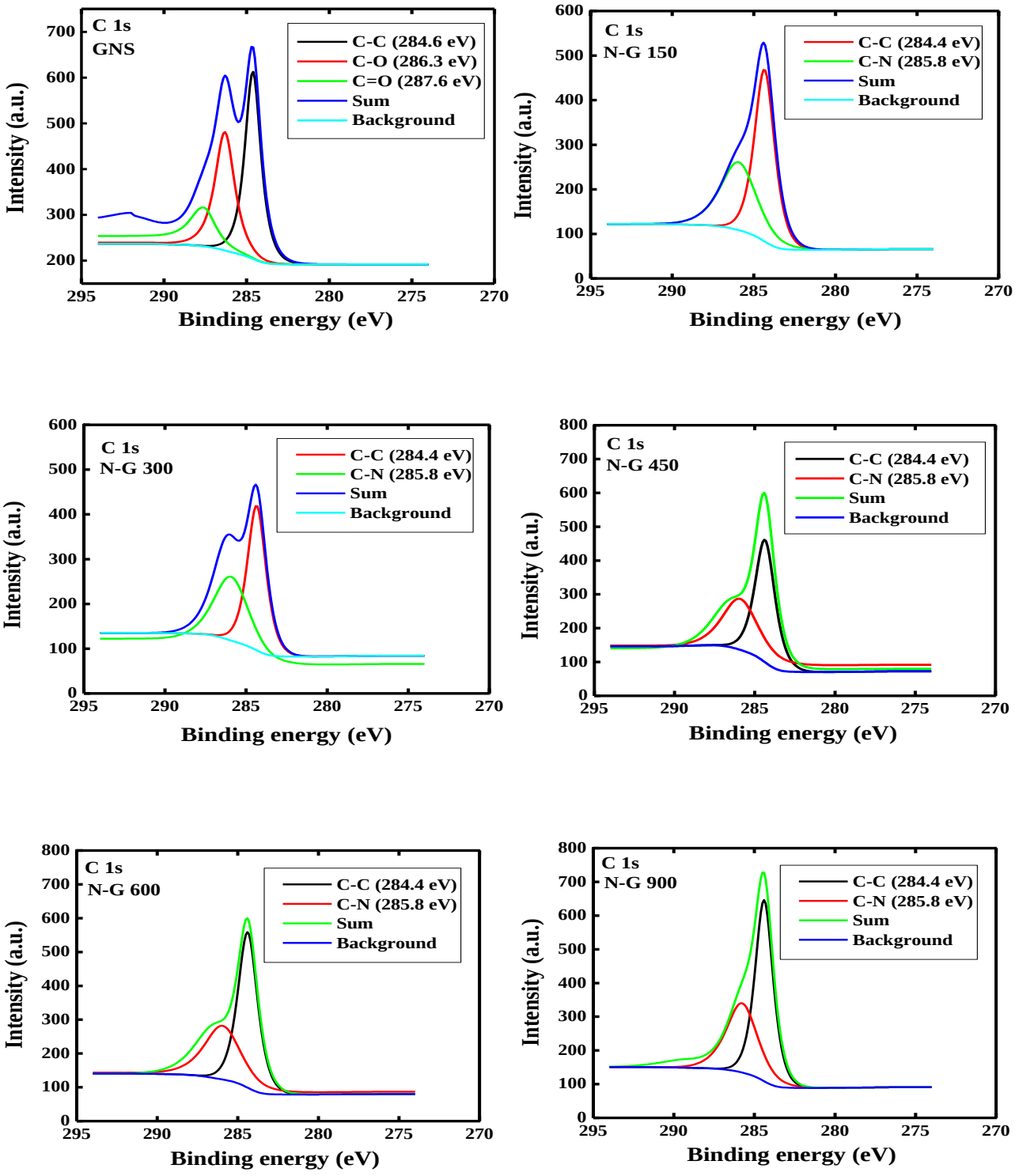

Figure 12S. High resolution of C 1s XPS spectra for GNS and N-G 150–900.

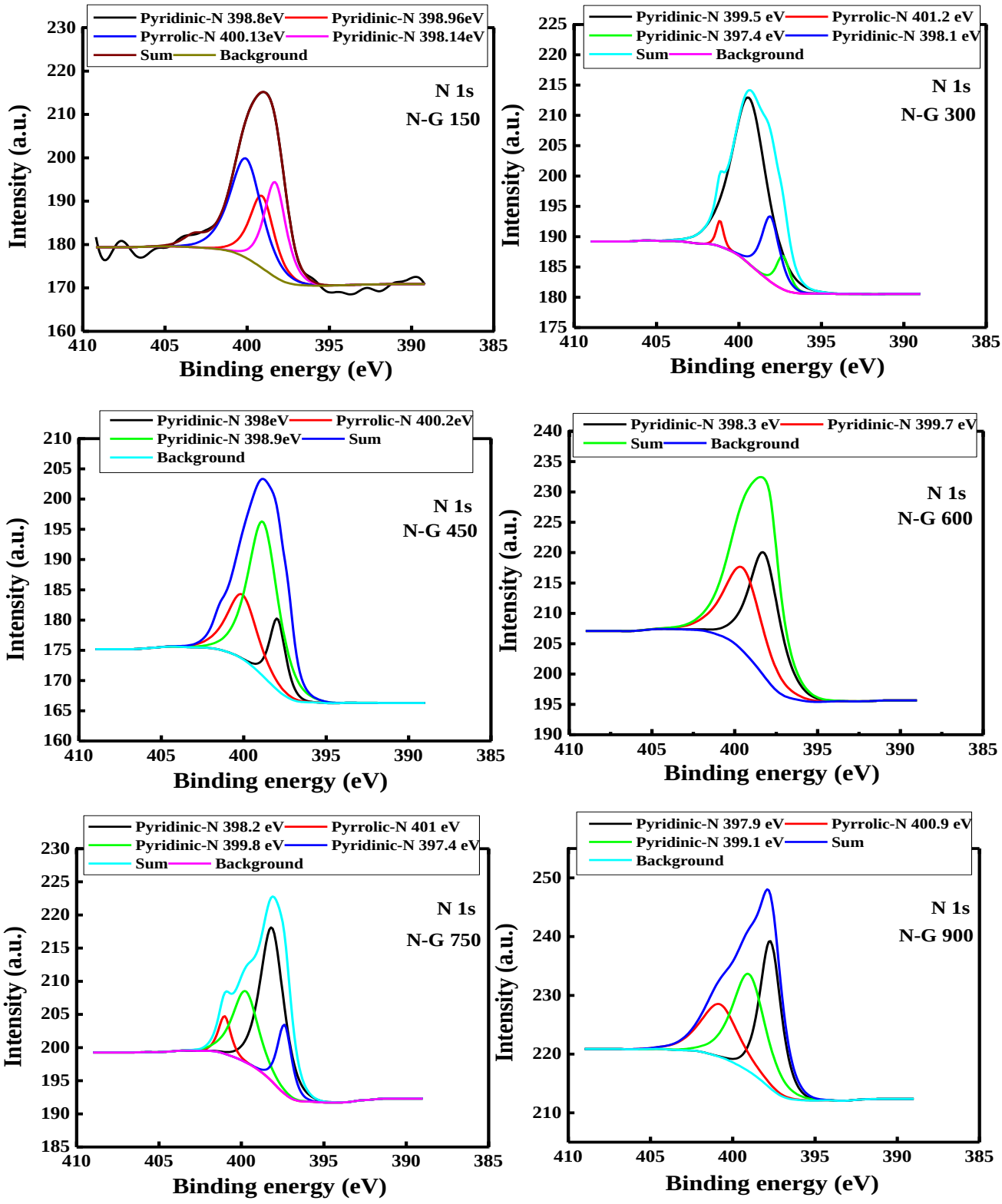

Figure 13S. High resolution of N 1s XPS spectra for N-G 150–900.

Figure 14S. TEM image of N-G.

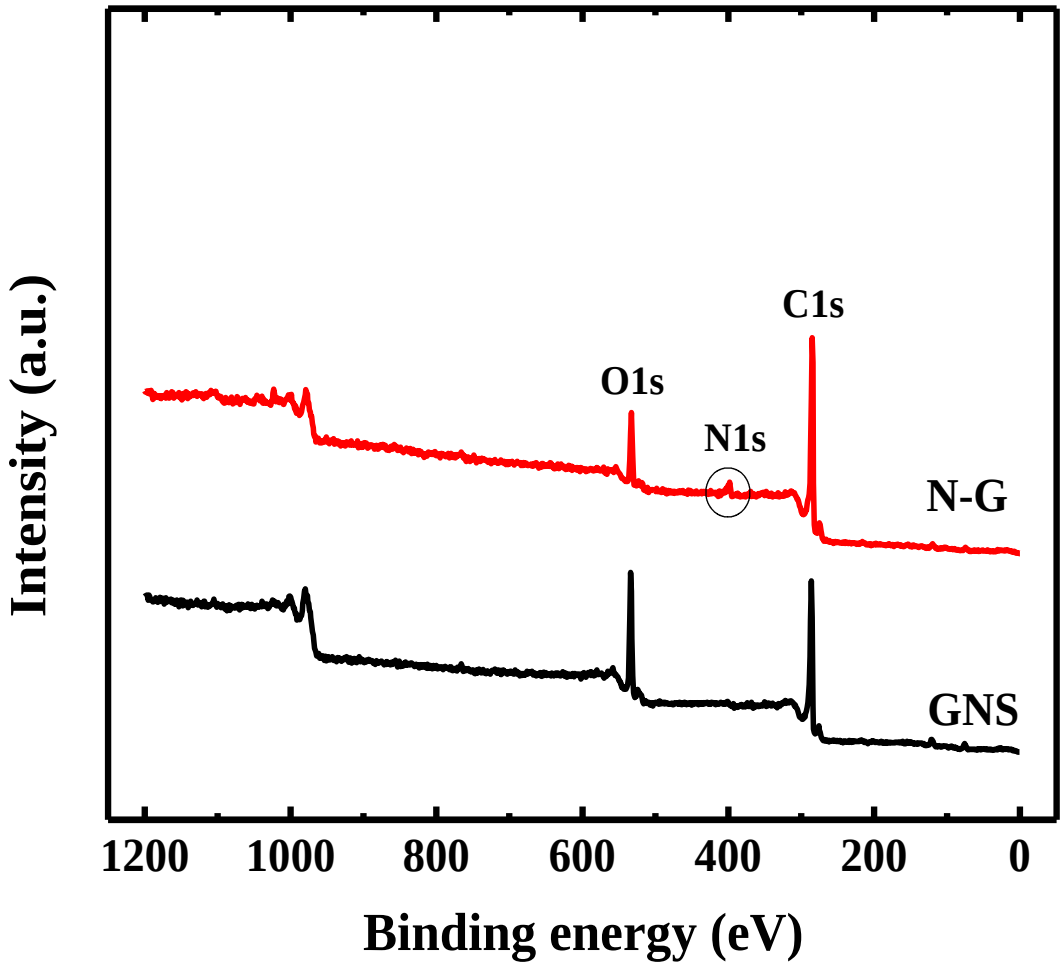

Figure 15S. XPS spectra of GNS and N-G.

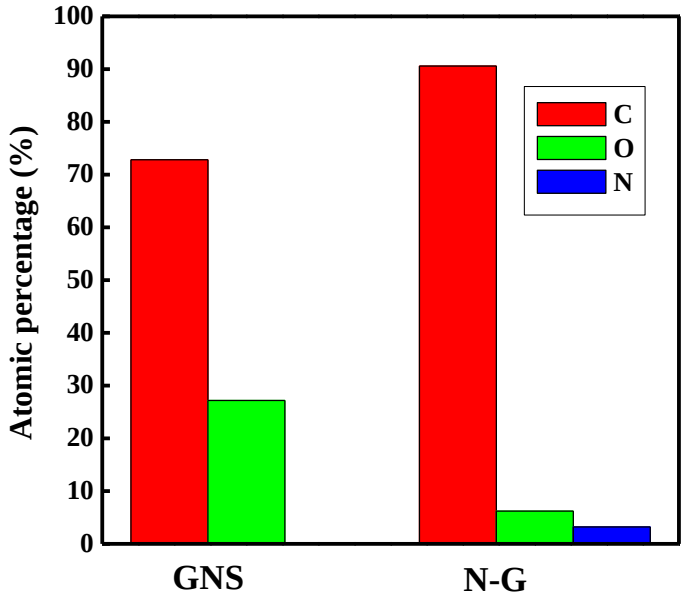

Figure 16S. Atomic percentages of GNS and N-G (XPS measurement).

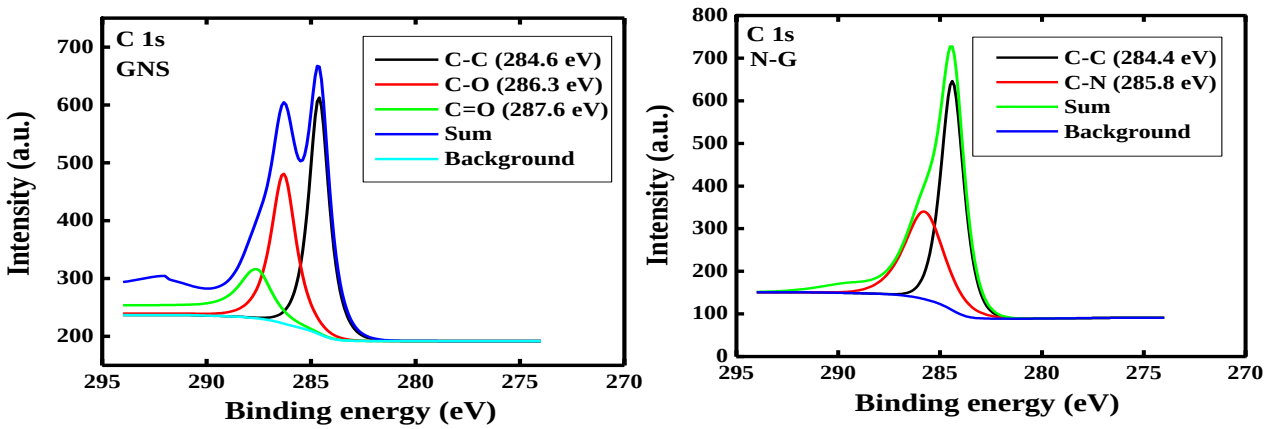

Figure 17S. High resolution of C 1s XPS spectra for GNS and N-G.

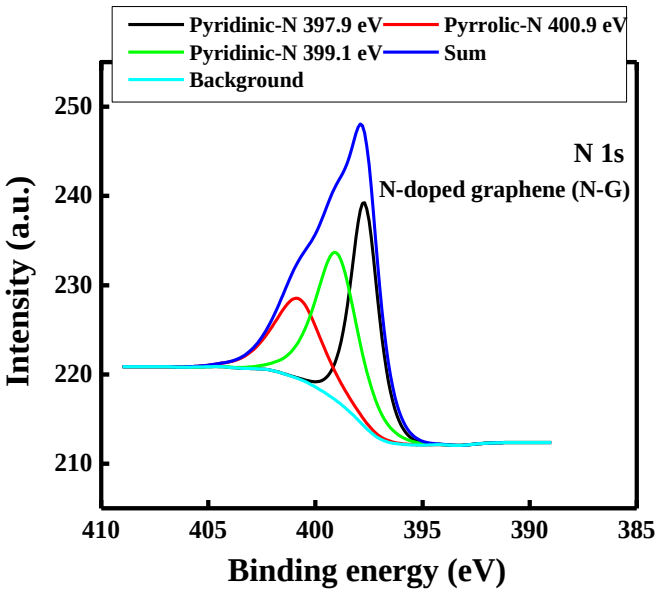

Figure 18S. High resolution of N 1s XPS spectra for N-G.

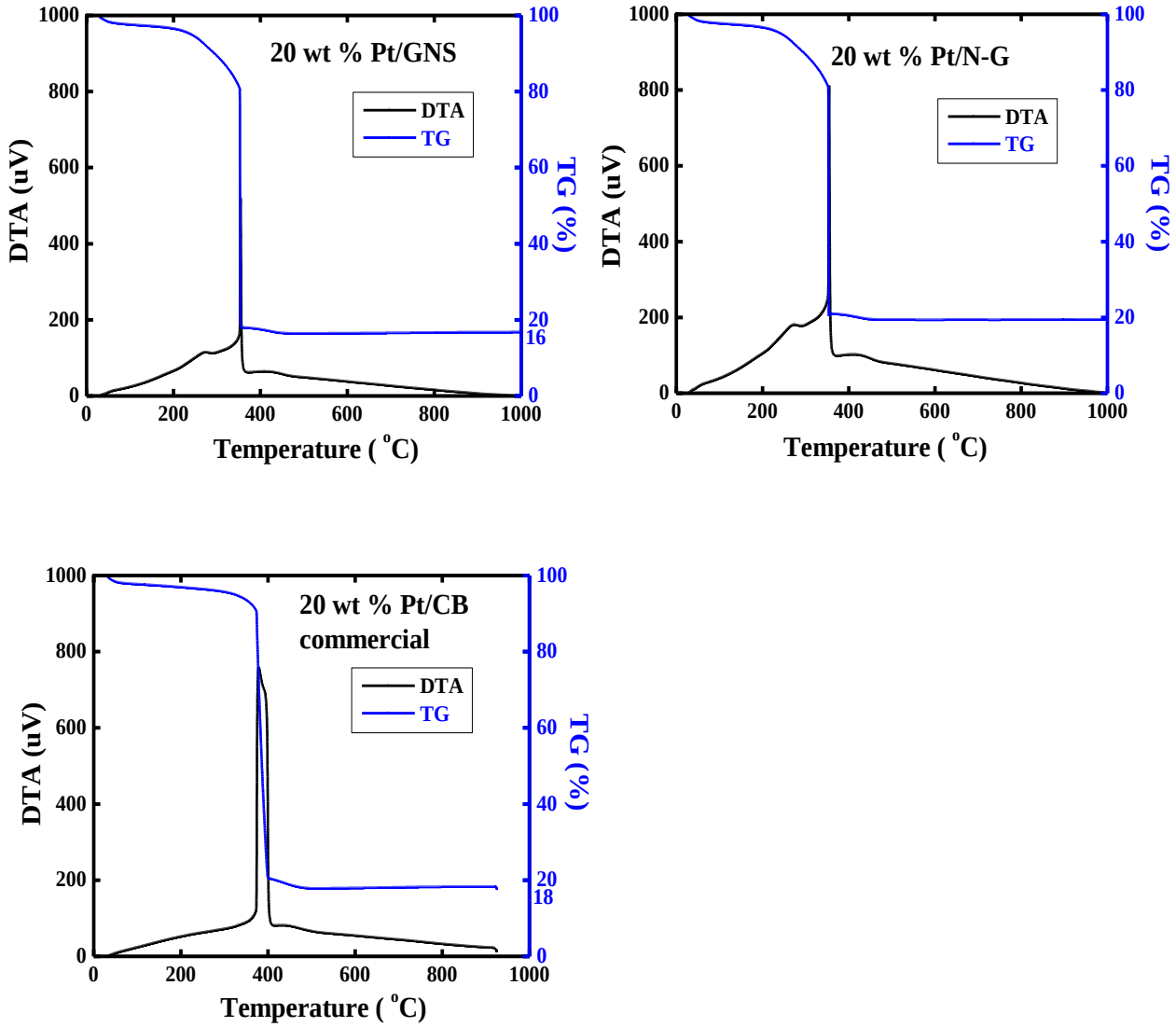

Figure 19S. TG/DTA thermograms of 20 wt % Pt/GNS, Pt/N-G, and Pt/CB commercial catalyst.

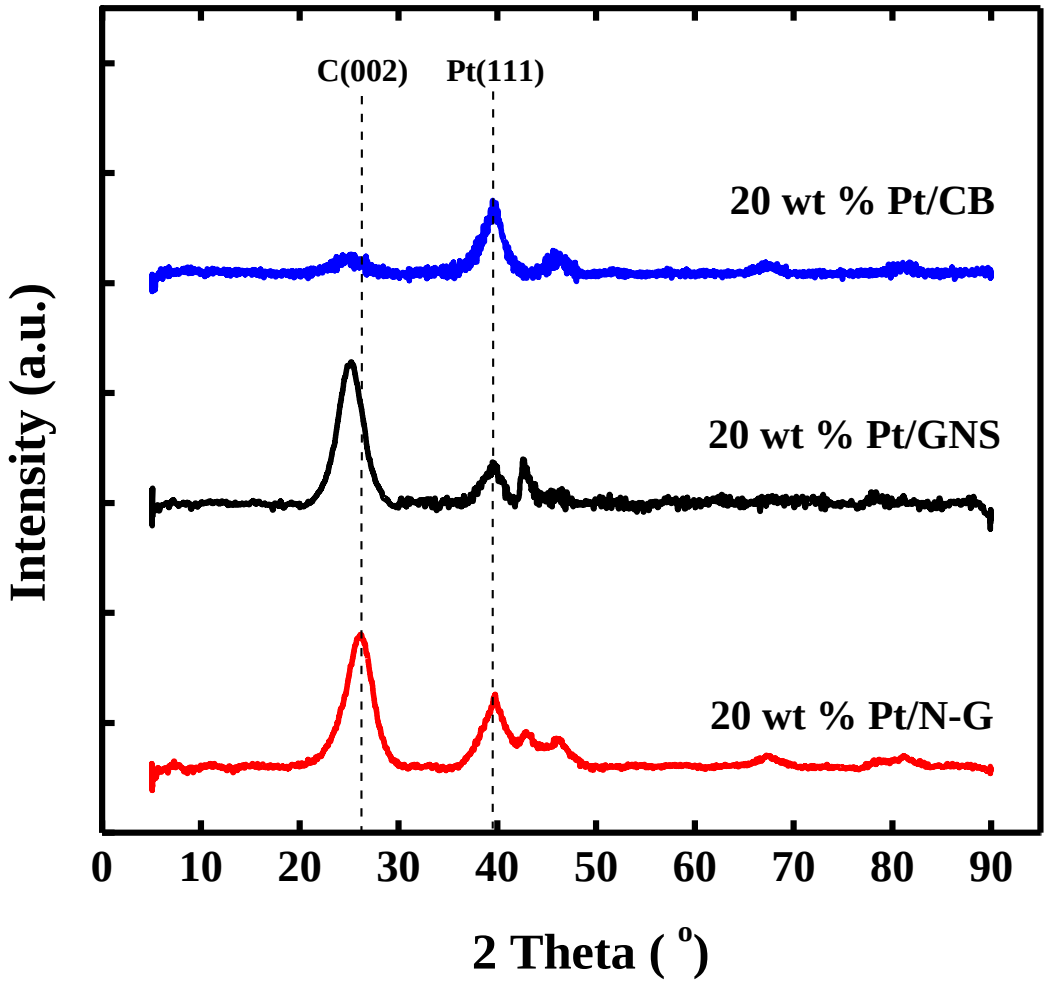

Figure 20S. XRD patterns for 20 wt % Pt/GNS, Pt/N-G, and Pt/CB commercial catalyst.

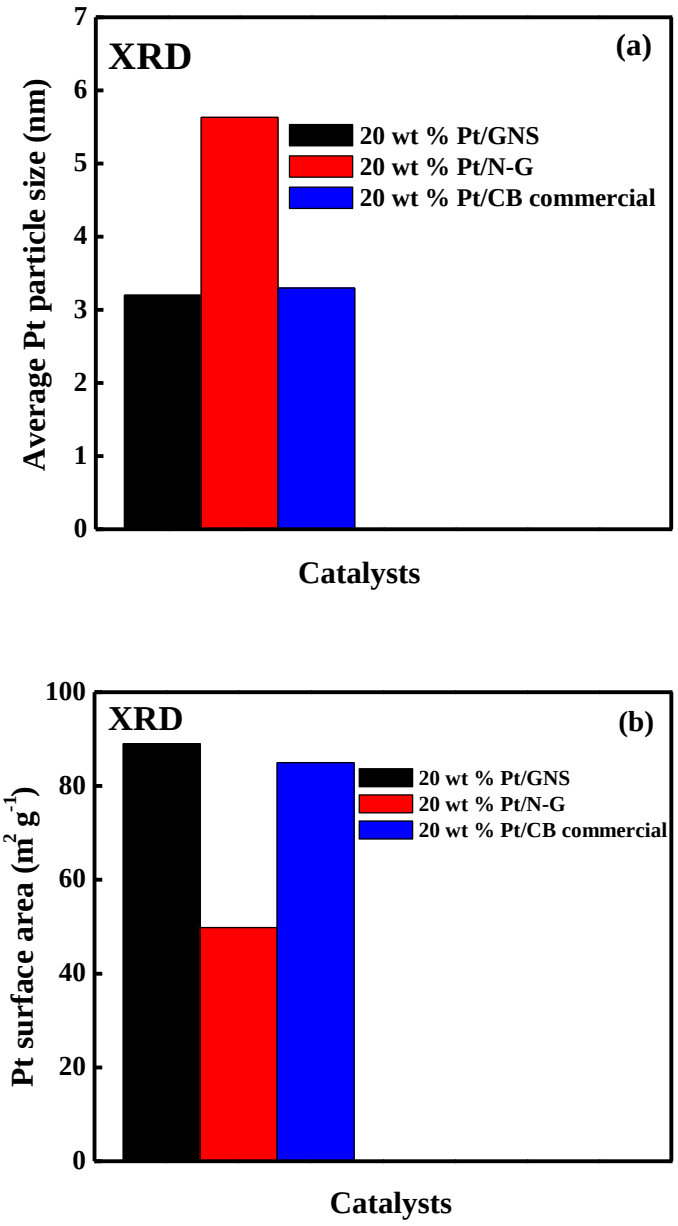

Figure 21S. (a) The average of Pt particle size and (b) Pt surface area of Pt/GNS, Pt/N-G, and Pt/CB, respectively.

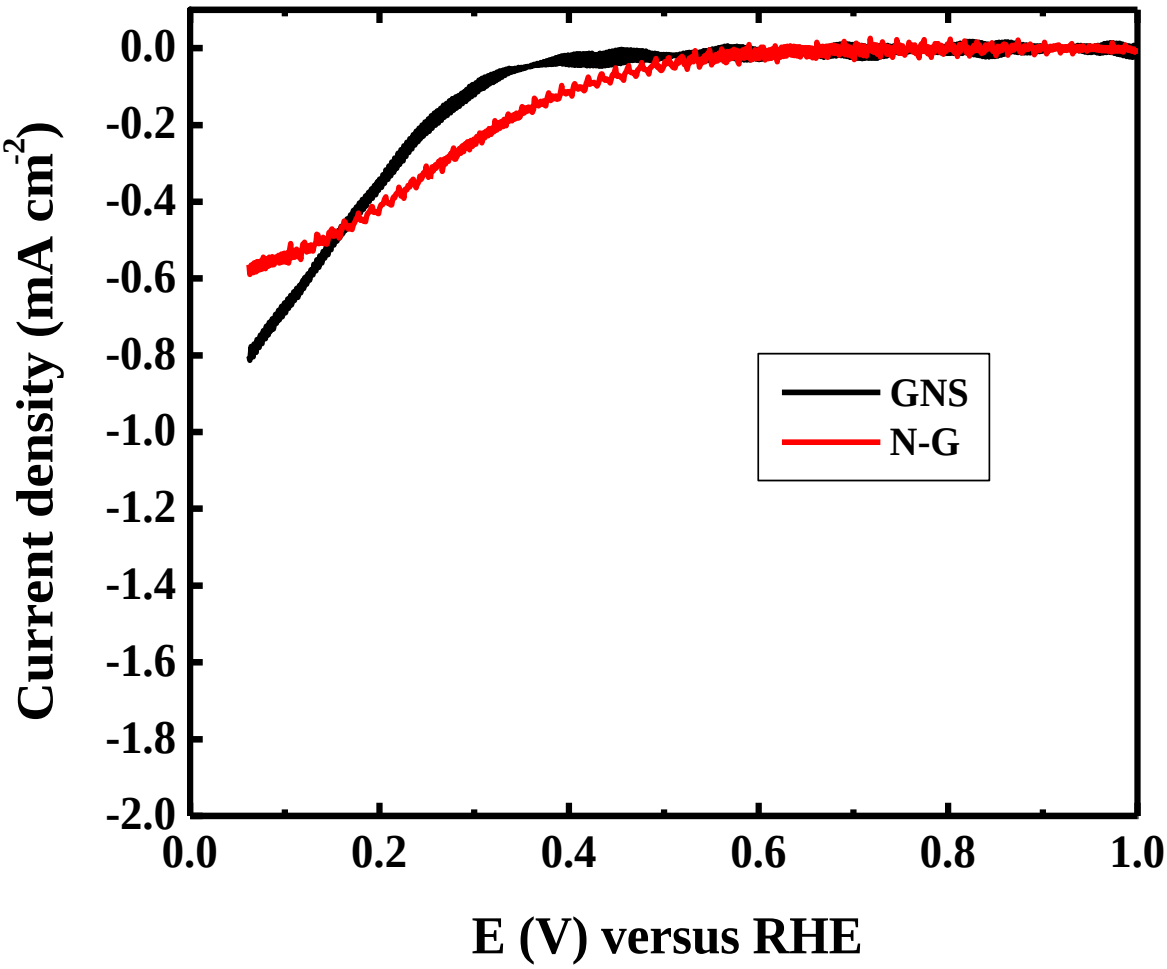

Figure 22S. RRDE polarization curves of GNS and N-G in O_2-saturated 0.1 M $HClO_4$ solution. Scan rate is 10 mV s^{-1}. For all the RRDE measurements, the loading of GNS and N-GNS are 20 μg.

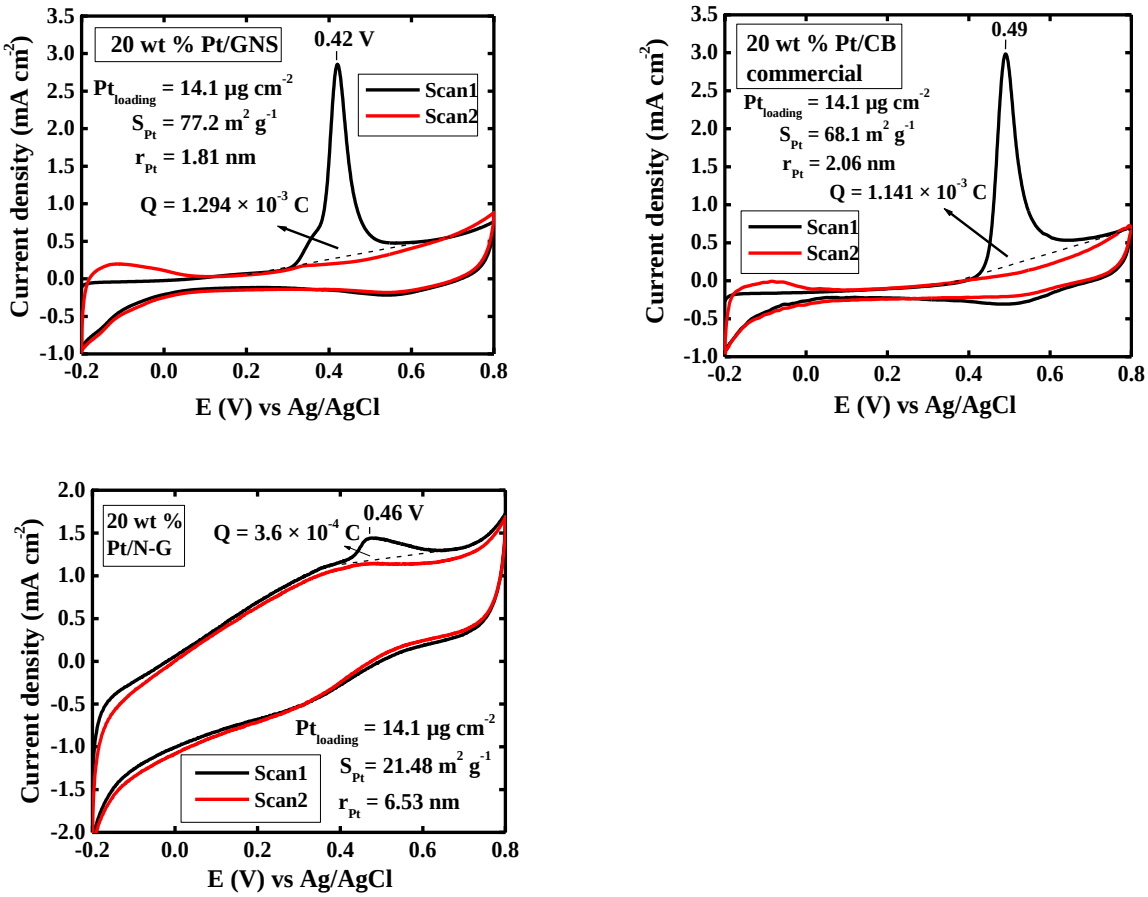

Figure 23S. CO stripping voltammograms of 20 wt % Pt/GNS, Pt/N-G, and Pt/CB commercial catalyst.

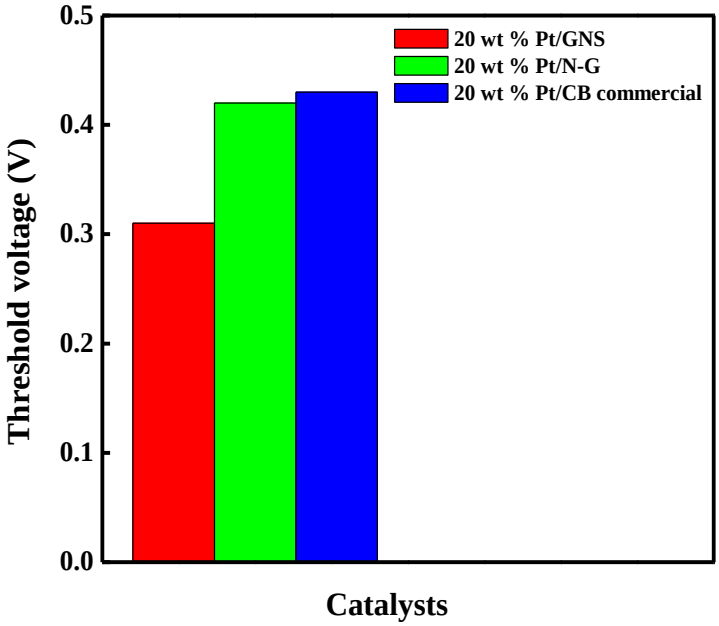

Figure 24S. Threshold voltage versus annealing temperature in ammonia for 20 wt % Pt/GNS, Pt/N-G, and Pt/CB commercial catalyst.

Table 1S. Atomic ratio of samples (XPS measurement).

Samples	C (%)	O (%)	Pt (%)	C/Pt	Pt/C
10 wt % Pt/GNS	62.9	33.6	2.4	26.2	0.04
15 wt % Pt/GNS	56.2	32.2	3.6	15.6	0.06
20 wt % Pt/GNS	55.5	32.6	3.9	14.2	0.07
25 wt % Pt/GNS	63.3	32.7	4.0	15.8	0.06
30 wt % Pt/GNS	59.6	35.8	4.6	12.9	0.08
35 wt % Pt/GNS	59.2	35.9	4.9	17.5	0.05
40 wt % Pt/GNS	59.2	35.8	4.9	12.1	0.08
45 wt % Pt/GNS	59.0	35.8	5.2	11.3	0.08
50 wt % Pt/GNS	53.1	34.5	5.4	9.8	0.10
55 wt % Pt/GNS	57.8	36.4	5.7	10.1	0.09
60 wt % Pt/GNS	57.5	36.4	6.1	9.4	0.11
65 wt % Pt/GNS	57.9	35.9	6.2	9.3	0.11
70 wt % Pt/GNS	56.8	36.5	6.7	8.5	0.12
20 wt % Pt/CB commercial	61.9	33.9	4.2	14.7	0.06
40 wt % Pt/CB commercial	60.2	35.0	4.8	12.5	0.08

Table 2S. Surface area of samples (BET measurement).

Samples	S_{BET} **(m^2 g^{-1})**
N-doped graphene (N-G)	
150	340
300	400
450	452
600	630
750	389
900	594
GNS	318

Table 3S. Atomic ratio of samples (XPS measurement).

Samples	**C (%)**	**O (%)**	**N (%)**	**Pt (%)**	**C/N**	**Pt/C**
20 wt % Pt/N-G						
150	86.9	8.3	3.8	1.0	22.9	0.01
300	84.2	11.9	2.9	1.0	29.0	0.01
450	91.7	3.8	3.6	0.9	25.5	0.01
600	91.9	3.9	3.4	0.8	27.0	0.009
750	92.1	4.2	2.8	0.9	32.9	0.01
900	88.7	7.9	2.7	0.7	32.8	0.008
20 wt % Pt/GNS	55.5	32.6	-	3.9	-	0.07
20 wt % Pt/CB commercial	61.9	33.9	-	4.2	-	0.06

Table 4S. Surface area of samples (BET measurement).

Samples	S_{BET} (m^2 g^{-1})
GNS	318
N-G	594

Table 5S. Atomic ratio of samples (XPS measurement).

Samples	C (%)	O (%)	N (%)	Pt (%)	C/N	Pt/C
20 wt % Pt/GNS	55.5	32.6	-	3.9	-	0.07
20 wt % Pt/N-G	88.7	7.9	2.7	0.7	32.8	0.008
20 wt % Pt/CB commercial	61.9	33.9	-	4.2	-	0.06

Appendix 2

Outline of Thesis

Chapter 1 Introduction

Nowadays, the population is approximately seven billions and is estimated to grow to nine billion by 2050, and about ten billion by 2100. With the rapid increase in population and economic development around the world, the demand for energy is surging. Energy is the lifeblood of technological and economic development. Therefore, the secure, reliable and affordable energy supplies are fundamental to economic stability and development. The total global energy use exceeds 350 quadrillion British thermal units (Btus) per year, which is equivalent to over 170 million barrels of oil each day. The global energy consumption main draws from 86 % three primary fossil fuels sources; those are 33 % petroleum oil, 23 % natural gas, and 30 % coal [3]. However, there are some disadvantages of fossil fuels (i) pollution and (ii) the fossil fuels are not renewable resources. It means they will deplete one day. The cheaper alternative energy has become more important especially at a time where we are facing a global recession. Recently, polymer electrolyte membrane fuel cells (PEMFCs) have increasingly received worldwide attention because of their potential application in transportation and in stationary and portable electronics. Commercialization of fuel cells and deployment in these early market applications is expected to lead to further improvement in performance, durability, and cost. The fuel cell is also more efficient in its conversion of chemical energy to electrical energy than present technologies. Together, these features suggest that fuel cells can reduce the problems associated with petroleum based energy production, which include air pollution, greenhouse-gas emissions, and economic dependence on petroleum. For this reason, industrial developers and world governments have shown great interest in developing fuel cell power sources. Fundamentally, the performance of fuel cells system is directly related to the material properties. Therefore, material technology plays a pivotal role in the development of electrochemical energy conversion and storage systems. Among the various materials, which have been investigated in these electrochemical devices, carbon materials are of great interest owing to their abundance, stability and relative environmental-friendliness. In particular, the excellent chemical stability across a wide temperature range in either acidic or basic media makes carbon materials extremely attractive for use as electrodes in electrochemical energy devices. The graphene as a new carbon material has fascinated many researchers, especially as based material for fuel cells and capacitors. It has been demonstrated to possess a high specific surface area, good chemical stability and outstanding electrical properties. It is thus expected to be one of the best suitable base-materials for developing alternative energy sources. In this study, I reported a recent significant progress of graphene as a supported material for Pt based fuel cell catalyst. The Pt subnano-clusters were formed on graphene nano sheets (GNS) with the superior catalytic activity and strong interaction between Pt and graphene probably via π–d interaction. The aims of this study are (i) to control the Pt particle size on GNS in a region from sub-nanometer to a few nanometer and also to clarify relationship among Pt particle size, catalytic activity and electronic structure of Pt on GNS, (ii) to study the formation process of Pt subnano-clusters on GNS, (iii) to know effect of annealing temperature of GNS in ammonia for Pt/N-GNS catalysts properties, and (iv) to clarify support material effect for oxygen reduction activity based on Pt catalyst. Base on the results of this study, I can improve electrocatalytic activity of Pt catalyst and reduce Pt usage by using GNS as a supporting material.

Chapter 2 Method of Study

In the chapter 2, the basic theory about apparatus which was used to characterize the support materials and catalysts is described. Those are X-ray photoelectron spectroscopy (XPS), X-ray diffraction (XRD), transmission electron microscope (TEM), and electrochemistry. XPS is a widely used to investigate the elemental and chemical composition of solid surface. The photoelectron spectrum provides much information on electron binding energy, shift in binding energy (chemical shift), and concentration of elements. XPS is thus extensively applied to research in solid state physics and solving the problems related

to surfaces and interfaces. The principle of XPS is based on the interaction between an electromagnetic wave and a material (atoms). The process of photoelectron emission from a solid is divided into three stages (three step model): First, X-rays are absorbed by atoms, and photoelectrons are emitted (photoelectron emission process), Next, part of the photoelectrons generated within a solid move toward the surface (electron attenuation length (escape depth)), and Finally, the photoelectrons which have reached the surface are emitted into a vacuum (work function). XPS is one of a number of surface analytical techniques that bombard the sample with photons, electrons or ions in order to excite the emission of photons, electrons or ions. The main components of a XPS instrument are the X-ray source, the electron energy analyzer, the electron detector and an efficient pumping system for the high vacuum requirement.

XRD is a rapid analytical technique primarily used for phase identification of a crystalline material and can provide information on unit cell dimensions. Because the wavelength of the X-rays is comparable to the size of the atoms, they are ideally suited for the probing the structure arrangement of atoms and molecules in a wide range of materials. XRD is a versatile, non-destructive analytical technique that reveals detailed information about the chemical composition and type of molecular bond of crystalline phase. It is an efficient technique to expose the crystallographic structure of natural and manufactured materials and a technique in which analytical results are correlated with references and standards of ICDD. In addition, the other advantages of XRD are precise phase determination of solid materials; the X-ray spectra generated provide a structural fingerprint of the unknown, determination of material characteristic and the highest quality and reproducibility. The concept of X-ray diffraction can be described by the Bragg's Law $n\lambda = 2d \sin\theta$. X-ray diffractometers consist of three basic elements: an X-ray tube, a sample holder, and an X-ray detector. X-rays are generated in a cathode ray tube by heating a filament to produce electrons, accelerating the electrons toward a target by applying a voltage, and bombarding the target material with electrons. XRD is most widely used for the identification of unknown crystalline materials (e.g. minerals, inorganic compounds). Determination of unknown solids is critical to studies in geology, environmental science, material science, engineering and biology. The other applications include: characterization of crystalline materials, identification of fine-grained minerals such as clays and mixed layer clays that are difficult to determine optically, determination of unit cell dimensions and measurement of sample purity.

In a TEM, electrons penetrate a *thin* specimen and are then imaged by appropriate lenses. The TEM has proved invaluable for examining the ultrastructure of metals. For example, crystalline defects known as dislocations were first predicted by theorists to account for the fact that metals deform under much lower forces than calculated for perfect crystalline array of atoms. The instrument of TEM divided into three sections, those are (i) the illumination system comprise the electron gun, together with two or more condenser lenses that focus the electrons onto the specimen. Its design and operation determine the diameter of the electron beam (often called the “illumination”) at the specimen and the intensity level in the final TEM image, (ii) the specimen stage allows specimens to either be held stationary or else intentionally moved, and also inserted or withdrawn from the TEM. The mechanical stability of the specimen stage is an important factor that determines the spatial resolution of the TEM image, and (iii) the imaging system contains at least three lenses that together produce a magnified image (or a diffraction pattern) of the specimen on a fluorescent screen, on photographic film, or on the monitor screen of an electronic camera system.

Electrochemistry is the science which deals with the consequences of the transfer of electric charge from one phase to another. An electrochemical reaction is a heterogeneous process which involves electron transfer across a phase boundary or interface. Electrochemical phenomena and processes are useful for the quantitative and qualitative chemical analysis of various substances and media, including liquids, gases, and solids.. It is very convenient that electrical signals are used for the perturbation: current, potential, and that the result again is obtained as an electrical signal. Voltammetry is a widely electrochemical technique to measure the current as a function of the varied potential, i.e. cyclic voltammetry (CV) and linear sweep voltammetry (LSV). CV has the further attraction of providing information not only on the thermodynamics of redox processes but also on the kinetics of heterogeneous electron-transfer reactions and coupled chemical reactions. In cyclic voltammetry, mass transport of the reducible or oxidizable electroactive species occurs only by diffusion. This is measured with suitable equipment and recorded as a characteristic current-voltage curve-a cyclic voltammogram. The Pt surface area can be estimated by electrochemical stripping of carbon monoxide (CO) for an adsorbed monolayer. It is generally assumed that CO is bonded linearly to a single metal surface atom. Thus, the electro oxidation of an adsorbed monolayer of CO may be used for Pt surface area measurement.

Chapter 3 Size Control to a Sub-Nanometer Scale in Platinum Catalysts on Graphene

Recently, graphene nano sheets (GNS) have been applied to a support material for low-temperature fuel cell catalysts. The combination of the large surface area (theoretical value of 2630 m^2 g^{-1}), high conductivity (1250 S m^{-1}), unique graphitized basal plane structure, and potential low manufacturing cost makes GNS a promising candidate as low-temperature fuel cell catalyst support. Platinum clusters on graphene have attracted considerable attention in theoretical studies because modification in the electronic structure of Pt is expected, which may lead to an enhancement in the catalytic activity. On the other hand, in our group, Pt subnano-clusters are found to be formed on GNS, which are composed of 5–40 Pt atoms. They showed a high CO tolerance as an anode catalyst in H_2-O_2 polymer electrolyte fuel cells (PEFCs). The high CO tolerance has been ascribed to the interface interaction between Pt and graphene. The reason why our group can synthesize Pt subnano-clusters is due to the preparation method. The importance in the study of graphene supported Pt catalysts lies in a control in the electronic structure of Pt by taking advantage of the Pt-C interaction, which probably varies as a function of Pt particle size. It is thus an interesting subject in experimental studies how to control the particle size of Pt on graphene at a sub-nanometer scale, which may further control the catalytic activity of Pt. If it is possible, the Pt subnano-cluster on graphene will be a new type of Pt catalyst, whose electronic structure can be controlled by the Pt-C interaction. In this study, we have first tried to control the particle size of Pt on GNS in a region from sub-nanometer to a few nanometers. We have successfully controlled the average particle size of Pt by changing loading of Pt on GNS. Then we have studied the relationship among the Pt particle size, the catalytic activity, and the electronic structure of Pt on GNS by X-ray diffraction (XRD), transmission electron microscope (TEM), electrochemical measurements, and X-ray photoelectron spectroscopy (XPS). The size controlled Pt catalysts supported by GNS are prepared by changing loading of Pt at 10–70 wt % using an impregnation method was investigated. We found that at a low loading of 10 wt %, Pt subnano-clusters are formed showing high surface area of 170 m^2 g^{-1}. The 10 wt % Pt/GNS catalyst exhibits the best performance in the electro-oxidation of adsorbed CO. Therefore, Pt subnano-clusters can be expected as excellent electro-oxidation catalysts. An increase in loading of Pt leads to an increase in particle size of Pt, resulting in the lower activities for electro-oxidation of adsorbed CO. Core level of Pt in the electronic structure for Pt subnano-clusters are shifted to higher binding energies, indicating chemical interaction between Pt and graphene. The interaction is explained by π–d hybridization.

Chapter 4 Formation Process of Pt Subnano-Clusters on Graphene Nano Sheets

Platinum (Pt) catalysts supported by GNS have been applied for methanol oxidation reaction (MOR), hydrogen oxidation reaction (HOR), and oxygen reduction reaction (ORR). In the case of MOR, HOR and ORR, Pt/GNS catalysts exhibited higher catalytic activities compared to Pt/carbon black (CB). It has been also reported that the CO-tolerance of Pt/GNS anode catalysts is superior to that of Pt/CB. The improved catalytic performance of Pt/GNS can be explained by the interface interaction between graphene and Pt, probably, via π–d hybridization. It should be noted that Pt subnano-clusters are found to be formed on GNS, which have never been observed for the other graphitic supports. That is, the sizes of Pt particles for Pt/CB range from 1 to 10 nm. The Pt subnano-cluster formation suggests that the interface interaction seems to be intense for graphene compared to the other graphitic carbon. However, the formation mechanism of the Pt subnano-clusters on GNS has not been clarified yet. The approach taking advantage of the interface interaction for the preparation of Pt electrode catalysts is promising from viewpoints of reducing Pt usages. The aim of this study is to clarify the formation process of Pt subnano-clusters on GNS during the catalyst preparation. We prepared Pt/GNS catalysts using an H_2PtCl_6 precursor at different pH, in which the formation process of Pt subnano-clusters on GNS was examined by X-ray diffraction (XRD), X-ray photoelectron spectroscopy (XPS), transmission electron microscope (TEM), and thermogravimetric/differential thermal analysis (TG/DTA). The formation mechanism of Pt subnano-clusters composed of 5–40 Pt atoms on graphene nanosheets (GNS) has been studied by X-ray diffraction (XRD), X-ray photoelectron spectroscopy (XPS), and transmission electron microscope (TEM). The exchange of Cl^- ion by OH^- ion and the reduction of Pt^{4+} to Pt^{2+} are examined by XPS in the reduction of an H_2PtCl_6 catalyst precursor by ethanol at different pH. XPS and TEM results show that particles of Pt^{2+}-containing compounds with the sizes of 2–7 nm are first

formed on GNS by the reduction of H_2PtCl_6 with ethanol, which are then fully reduced to Pt subnano-clusters by H_2 at 400 ^oC. The proposed mechanism for the subnano-cluster formation includes two pivotal surface reactions: the reduction of Pt^{2+}-particles into isolated Pt atoms by H_2 on the GNS surface, followed by the formation of Pt subnano-clusters by collision of the Pt single atom migrating on GNS.

Chapter 5 Effect of N-doped graphene for Properties of Pt/N-doped graphene catalyst

Graphene, a single layer of sp^2–bonded carbon atoms arranged in a honeycomb lattice, has been attracting much attention due to its fascinating properties, such as high surface area (2630 m^2 g^{-1}), high thermal conductivity (~ 4840–5300 W m^{-1} K^{-1}), fast charged carrier mobility (~ 200 000 cm^2 V^{-1} s^{-1}), strong Young's modulus (~ 1 TPa), and high carrier mobilities (10^4 cm^2 V^{-1} s^{-1} at room temperature). All these aspects make graphene material promising for various applications, including energy conversion and storage, electrocatalysis, sensors and electronics. However, the absence of a band gap in perfect graphene does not allow switching of graphene-based transistors with a high enough on-off ratios. Hence, graphene has to be modified even when making basic devices and, even more, for manufacturing sophisticated circuits. Therefore, the defect in graphene can be hoped to alter its properties. It is well known that defects are not always stationary and that their migration can have an important influence on the properties of a defective crystal. The migration is generally governed by an activation barrier which depends on the defect type and increases exponentially with temperature. Defects can be done by using irradiation or chemical treatments. The chemical treatment, for instance chemical dopant may change the local electronic structure or inject charge into the electron system of sp^2-bonded carbon materials. The results show that the ORR electrocatalytic activity for N-G 900 (0.63 V versus RHE) is higher than GNS. It indicates that incorporation nitrogen in N-G may affect the ORR activities of N-G 900. XPS results exhibit that the pyridinic N is the majority including in N-G, where the pyridinic N refers to N atom bonds with two C atoms at the edges or defects of graphene and contributes one *p* electron to the π system of graphene. Interestingly, the Pt subnano-clusters were formed in Pt/N-G catalysts with Pt particle size (0.7–1.0 nm). It also exhibits a strong interaction between Pt and N–G. However, the ORR activity of Pt/N–G is lower than that of Pt/GNS catalysts. It is clearly indicated that the doping of nitrogen significantly influence the π–d hybridization in terms of electronic structures.

Chapter 6 Support material effect for Pt catalytic activity at cathode

Polymer electrolyte membrane fuel cells (PEMFC) are being developed as electrical power sources for vehicles and portable applications as an alternative to conventional internal combustion engines, secondary batteries, and other conventional power sources. Recently, the design of cheap and stable fuel cell catalysts for oxygen reduction reaction (ORR) is main challenge. This is caused catalysts exhibit great influence on both the cost and the durability of PEMFC. The platinum (Pt) nanoparticles supported on carbon black (Pt/CB) are most used for ORR catalysts. It has outstanding catalytic and electrical properties. Therefore, much of the art and science of catalysts development for the ORR rely on both the fundamental understanding of the reaction at the Pt electrolyte interface and the optimization of the catalytic properties of the Pt surface. However, Pt price is expensive and also it is limited natural resources. Therefore, it is a prerequisite to decrease the usage of Pt and enhance the catalytic activity of Pt in order to achieve a competitive low cost of fuel cell. The support materials are necessary to obtain a high dispersion, narrow distribution of Pt and Pt-alloy nanoparticles and also can interplay with catalytic metals, which is the prerequisite to obtain the high catalytic performance of catalysts. This is because the interaction between the support and metal catalyst can modify the electronic structure of catalytic metals which in turn changes the catalytic activity. In this study, GNS and N-G were used as support materials to deposited Pt particles in order to investigate the support material effect for ORR activity. The ORR activity of Pt/GNS is highest among Pt/N-G and Pt commercial catalyst. This suggests that π states in the conjugated system determine the properties of the interaction between Pt and carbon. The interaction between Pt and graphene is considered to be π–d hybridization. Therefore, the graphene as a support material usage is more significant for Pt catalyst in term of oxygen reduction activity as well as the core level of Pt 4f.